



3 1176 00160 5584

NASA CR-164,288

NASA-CR-164288  
19810015462

# The Telecommunications and Data Acquisition Progress Report 42-62

January and February 1981

N. A. Renzetti  
Editor

April 15, 1981

National Aeronautics and  
Space Administration  
  
Jet Propulsion Laboratory  
California Institute of Technology  
Pasadena, California

LIBRARY

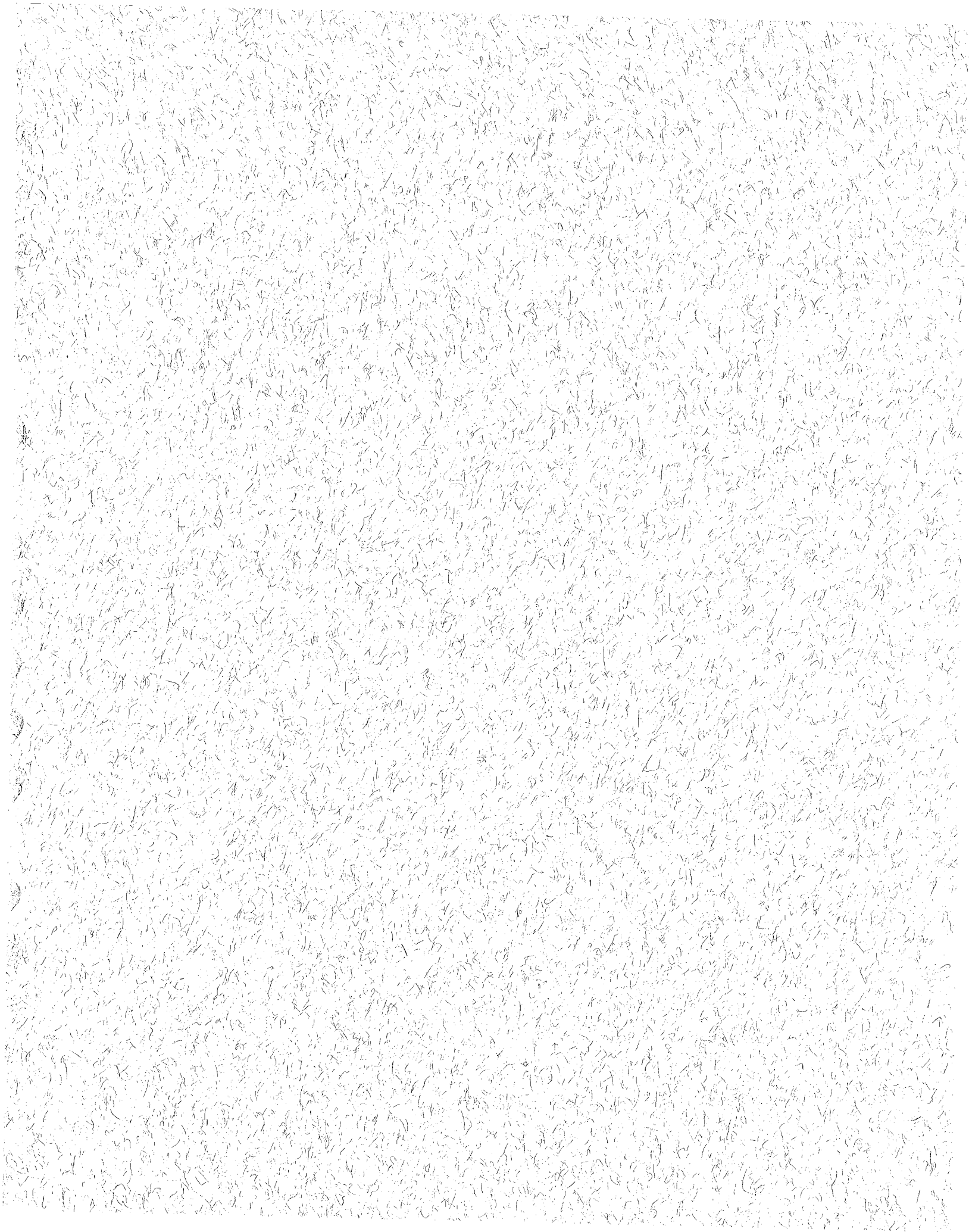
APR 15 1981

LANGLEY RESEARCH CENTER  
LIBRARY, NASA  
HAMPTON, VIRGINIA



NF01744

FOR REFERENCE



# The Telecommunications and Data Acquisition Progress Report 42-62

January and February 1981

N. A. Renzetti  
Editor

April 15, 1981

National Aeronautics and  
Space Administration

**Jet Propulsion Laboratory**  
California Institute of Technology  
Pasadena, California

*N81-23997#*

The research described in this publication was carried out by the Jet Propulsion Laboratory, California Institute of Technology, under contract with the National Aeronautics and Space Administration.

## Preface

This publication was formerly entitled *The Deep Space Network Progress Report*. Although the practice of reporting progress in the development and operations of the Deep Space Network continues, the report has been expanded to include developments in Earth-based radio technology as applied to other research programs. These programs are:

- (1) Geodynamics: For several years, the laboratory has been developing radio interferometry at microwave frequencies for application to geodetic measurements. This branch of telecommunications technology is now being applied to the study of geodynamics.
- (2) Astrophysics: The deep space stations, individually and in pairs as an interferometer, have been used by radio astronomers for astrophysics research by direct observations of radio sources.
- (3) An activity closely related to radio astronomy's use of the deep space stations is NASA's continuing program of radio search for extraterrestrial intelligence in the microwave region of the electromagnetic spectrum.

Each succeeding issue of this report will present material in some, but not all, of the following categories:

Radio Astronomy  
Search for Extraterrestrial Intelligence  
Radio Interferometry at Microwave Frequencies

Geodetic Techniques Development  
Spacecraft Navigation  
Orbiting Very Long Baseline Interferometry

Deep Space Network

Description  
Program Planning  
Planetary and Interplanetary Mission Support  
Advanced Systems  
Network and Facility Engineering and Implementation  
Operations  
Spacecraft Radio Science  
Planetary Radar  
Energy

In each issue, there will be a report on the current configuration of one of the seven DSN systems (Tracking, Telemetry, Command, Monitor and Control, Test Support, Radio Science, and Very Long Baseline Interferometry).

The work described in this report series is either performed or managed by the Telecommunications and Data Acquisition organization of JPL.



# Contents

## RADIO ASTRONOMY

<b>Radio Astronomy</b> .....	1
R. D. Shaffer, P. R. Wolken, and A. E. Niell	
NASA Code 311-03-21-00	

## RADIO INTERFEROMETRY AT MICROWAVE FREQUENCIES

### GEODETIC TECHNIQUES DEVELOPMENT

#### ORION

<b>A Frequency and Timing Subsystem for the ORION Mobile Unit</b> .....	3
P. A. Clements	
NASA Code 692-40-20-00	
<b>ORION—Microwave Water Vapor Radiometer Subsystem Design</b> .....	10
R. P. McKinney and N. I. Yamane	
NASA Code 692-40-20-00	

## THE DEEP SPACE NETWORK ADVANCED SYSTEMS

### Tracking and Ground-Based Navigation

<b>Posterior Error Probability in the Mu-II Sequential Ranging System</b> .....	15
C. W. Coyle	
NASA Code 310-10-60-10	
<b>Frequency Standard Test Facility Data Acquisition and Processing System</b> .....	22
L. J. Knapp	
NASA Code 310-10-62-18	
<b>A Four-Way Distribution Amplifier for Reference Signal Distribution</b> .....	31
Y. V. Lo	
NASA Code 310-10-62-23	
<b>Station Stability Measurement</b> .....	35
E. N. Sosa	
NASA Code 310-10-62-25	

### Communications

<b>High Speed Front End of the Multimegabit Telemetry Demodulator-Detector</b> .....	43
E. R. Wechsler	
NASA Code 310-20-67-22	
<b>ISPM X-Band Uplink Technology Demonstration. Part I. Overview</b> .....	50
T. A. Komarek, J. G. Meeker, and R. B. Miller	
NASA Code 310-20-64-50	

<b>End-to-End Quality Measure for Transmission of Compressed Imagery Over a Noisy Coded Channel</b> .....	63
V. N. Korwar and P. J. Lee NASA Code 310-20-67-57	
<b>Calculation of Atmospheric Loss From Microwave Radiometric Noise Temperature Measurements</b> .....	73
C. Stelzried and S. Slobin NASA Code 310-20-65-15	
<b>Maximizing Throughput Over an Average-Power-Limited and Band-Limited Optical Pulse Position Modulation Channel</b> .....	81
D. Zwillinger NASA Code 310-20-67-59	
<b>Optimum Design of Hybrid Phase Locked Loops</b> .....	87
P. Lee and T. Yan NASA Code 310-20-67-13	

#### Network Data Processing and Productivity

<b>The Reliability of Multistate, Multioutput Systems</b> .....	96
E. J. Subelman NASA Code 310-40-73-06	
<b>New Results on Antenna Arraying: Part 1</b> .....	105
L. J. Deutsch, R. L. Miller, and S. A. Butman NASA Code 310-40-74-51	

### NETWORK AND FACILITY ENGINEERING AND IMPLEMENTATION

#### Network

<b>34-Meter Antenna-Subreflector Translations to Maximize RF Gain</b> .....	112
M. S. Katow NASA Code 311-03-41-02	
<b>A Decoding Failure Test for the Transform Decoder of Reed-Solomon Codes</b> .....	121
R. L. Miller, T. K. Truong, and I. S. Reed NASA Code 311-03-43-20	

#### Ground Communications

<b>Radio Frequency Interference Protection of Communications Between the Deep Space Network and Deep Space Flight Projects</b> .....	125
D. W. H. Johnston NASA Code 311-06-50-00	

### OPERATIONS

#### Network Operations

<b>DSN Scheduling System</b> .....	132
R. Durham NASA Code 311-03-13-50	

## ENERGY

<b>Computer-Simulated Building Energy Consumption for Verification of Energy Conservation Measures in Network Facilities</b> .....	142
B. Plankey NASA Code 311-03-41-08	
<b>Reporting Capabilities and Management of the DSN Energy Data Base</b> .....	147
R. D. Hughes and S. T. Boyd NASA Code 311-03-41-08	



# Radio Astronomy

R. D. Shaffer and P. R. Wolken  
Deep Space Network Operations Section

A. E. Niell  
Tracking Systems and Applications Section

*This article reports on the activities of the Deep Space Network in support of Radio and Radar Astronomy Operations during September through December 1980. The article concentrates on a report of an experiment selected for use of the DSN by the Radio Astronomy Experiment Selection Panel: that of VLBI observations of the energetic galactic object SS-433.*

## I. Introduction

Deep Space Network (DSN) 26-, 34- and 64-meter-antenna stations are utilized in support of experiments in three categories: NASA Office of Space Science (OSS), Radio Astronomy Experiment Selection (RAES), and Host Country.

## II. Radio Astronomy Operations

### A. NASA OSS Category

During this period, support of Planetary Radio Astronomy (OSS196-41-73) and Pulsar Rotation Constancy (OSS188-41-55-09) observations continued at their previous levels. In addition, the Southern Hemisphere Interferometer (OSS188-41-55-16) made considerable use of DSS 42/43.

### B. RAES Panel Category

1. RA 175 (SS-433). This activity continues to be supported at intervals of approximately 40 days, and was recently

extended by the RAES panel for another year. The following is a brief summary of the history of the study of SS-433, including a report of the progress made in the VLBI observations of it.

SS-433 is not a newly discovered object. It can be historically traced as an optical variable from plates dating back to 1929. But the SS-433 name was not bestowed until much later. Observed as a red, 14th-magnitude star, its distinguishing bright hydrogen emission spectrum caught the attention of Stephenson and Sanduleak, of Case Western Reserve University, who were compiling a catalog of stars with this particular characteristic. It is the 433rd object in that catalog.

Since the mid-1970's a series of coincidental observations focused new attention on SS-433. Several satellites identified X-ray sources in about the same location. An unresolved variable radio source was also noted in this region. Still another discovery in this approximate location was that of a supernova remnant (SNR) identified as W50. Bruce Margon of

UCLA and his associates closed the historical loop of observation by doing modern optical photometry and spectroscopy of SS-433 as part of a program of observing visible counterparts of galactic radio sources.

Margon's data showed an incredible tripling of emission lines, which shifted rapidly and drastically. Identification of the lines revealed the tripling effect: a zero-velocity emission accompanied by both large red- and blue-shifted variable components. Analysis of this phenomenon, based on the doppler effect, implied velocity maxima of  $50,000 \text{ km s}^{-1}$  redshift and  $\sim 35,000 \text{ km s}^{-1}$  blueshift, changing at a rate of  $30,000 \text{ km s}^{-1}$  in 40 days, which confirms the earliest lightcurve period as  $164 \pm 3$  days. When radial velocity (measured as  $Z = \Delta\lambda/\lambda$ ) is plotted against time, a very striking and obvious condition is noticed: a smooth sinusoid about a  $Z$  of  $+0.04$ . This effect could most simply be explained by a binary star system having an orbital period of 164 days. However, such a system would need to have a total mass equal to about one percent of the entire galaxy in order to exhibit the orbital velocities implied by the red- and blue-shifted spectra. Another possible explanation might be that some of the observed SS-433 characteristics are similar to those of a quasar. This explanation requires that SS-433 be a very remote object, which is not backed up by other observational evidence. Another model was needed.

As more news of SS-433 was disseminated, more and more models proliferated. However, one model seems to best explain the observed phenomena: the so-called kinematic model proposed by B. Margon and his associates at UCLA. This model postulates an object, as yet unidentified, which is ejecting jets of matter in opposite directions along an axis which is itself inclined to an axis of precession. The central object and twin beams account for the doppler shifts and triple emission lines, while the precession of the ejection axis gives a 164-day period. Since the geometry of this scheme is quite specific, forecasts of observations could be made with regard to discrete events such as convergence and crossing of the spectral emission lines. This very event was observed as predicted by Margon in 1979, lending further credence to this model.

Radio observations have determined variations in 2.7 GHz flux densities from 0.5 Jy to 1.6 Jy within a 15-day interval as well as variations in flux density of 140 mJy at 8.1 GHz over four days. An angular diameter of 0.1 arcsec at 8.1 GHz has also been measured.

Yet to be addressed is the relationship between SS-433 and its surrounding neighborhood, the SNR W50. Recent multi-station VLBI experiments undertaken as RA-175 have uncovered some startling results. The position angles of the elongated radio source, greater than 0.1 arcsec, were within 10 degrees of the position angle of W50's apparent bulges. This implies a physical connection between SS-433 and W50.

The features observed in SS-433 — a small active radio core connected by relativistic jets to extended radio lobes — lend support to the suggestion that we are observing the same phenomenon that powers quasars and radio galaxies but on a scale that is a billion times smaller.

Radio results thus far are not discordant with the kinematic optical model. Observations of variations in the separation angle have revealed a separation rate between the radio elongations comparable to that of the optical jets. Measurement of the change in structure shows that radio emission propagates outward from SS-433 in radio "blobs." Assuming these "blobs" travel at the speed of the optical jets,  $0.26c$ , the distance derived is 5 kpc (15,000 ly), which is about one and a half times further than previous estimates to W50. In this, the Goldstone/OVRO baseline is in an orientation peculiarly well-suited for observing the east-west SS-433 jet. Furthermore, the sensitivity of DSN stations for detecting the flux density as well as the unique baselines available to optimize the precision of position angle measurements for variations serves to ensure that the DSN will retain an important position as a major resource for this project.

### C. Host Country Operations

Host country operations were limited to support of pulsar observations in Australia.

# A Frequency and Timing Subsystem for the ORION Mobile Unit

P. A. Clements

Communications Systems Research Section

*JPL is building a mobile surveying instrument in support of the NASA crustal dynamics program. This instrument will measure the length and direction of the distance between sites on the Earth's surface. This is done using Very Long Baseline Interferometry techniques operating at microwave frequencies using extragalactic radio sources (QUASARS). One of the subsystems is the Frequency and Timing Subsystem. The frequency standard used is a hydrogen maser, which is the most stable operational frequency standard in the world today. It is also a device which is sensitive to its environment, so great care must be taken in installation and operation. An important part of the subsystem is a sophisticated automatic system to monitor frequency stability and accumulated clock error.*

## I. Introduction

A special-purpose Frequency and Timing Subsystem (FTS) is needed for the Operational Radio Interferometry Observation Network (ORION) Mobile Station, (Ref. 1) which is being designed and built by JPL. The ORION mobile station is a part of the ORION System. This system employs Very Long Baseline Interferometry (VLBI) techniques to create a surveying instrument capable of determining the length and direction between two points on the Earth's surface to a precision of 5 centimeters over a distance of up to 5000 kilometers.

## II. Functional Requirements Imposed on the FTS

The Functional Requirement Document (FRD) for the ORION mobile unit includes the following requirements on the FTS:

Frequency performance:

- (1) Stability of  $1 \times 10^{-14} \Delta f/f$  for averaging time of  $>60$  seconds.
- (2) Isolation of  $>60$  dB between ports
- (3) Output level of 13 dBm  $\pm 3$  dB in 50 ohms

Frequency distribution: There are four output ports required for the other subsystems in the ORION mobile unit. The Phase Calibrator Subsystem (PCS), one port, and the Data Acquisition Subsystem (DAS) three ports. Both of these other subsystems require 5 MHz. The FTS will provide ports at the FTS cabinet which will supply these frequencies. System cables will interconnect these ports to the other subsystems.

Epoch time: The time of year to the second will be available (day, hour, minute, and second). This time is needed so it can be entered into the computer when it is turned on, which

occurs when the ORION mobile unit is put into the operational mode.

**Timing pulse distribution:** There is one output port required for the DAS. This timing pulse will establish time of second to within 1 microsec. It is not required that the pulse be exactly on the second, but that the offset be known to within 1 microsec with respect to the United States Naval Observatory (USNO). The FTS will supply this port at the FTS cabinet. A system cable will interconnect it to the DAS. This timing pulse will be 1 pulse per sec (PPS), at least 4 V peak into 50 ohms.

**Performance monitoring:** Certain parameters will be measured to ascertain that the FTS is operating as required, such information will be provided to the unit computer through RS232C interfaces.

**Power:**

- (1) Certain parts of the FTS will need to operate continuously. Therefore dc power must be provided during transit of the ORION mobile unit. The allowable FTS budget is 300 W.
- (2) The portion of the FTS that runs on ac power will use 105-130 Vac, 1 phase, 48-63 Hz at less than 890 W.

The FTS will be usable and meet all specifications in less than four hours after arrival at an operational site.

### III. Satisfaction of the Requirements

All of the functional requirements can be met. However, a hydrogen maser is a delicate instrument that requires special attention. The best results are obtained in a laboratory environment with everything kept in proper adjustment. Even with the most sophisticated environmental controls and careful operational procedures, it is difficult to obtain laboratory performance in a mobile van.

Establishing epoch time synchronized with USNO to less than 1 microsec is a nontrivial task. Present methods require the use of a traveling atomic cesium clock with several calibrations per year. This is combined with careful record keeping to give time synchronization to the sub-microsec level. The new satellite systems (Transit, Nova and Navstar) offer promise of a partially automatic timekeeping capability between the 10 to 1 microsec level, depending on the system utilized.

## IV. Description of the FTS

### A. The Basic Subsystem

To meet these requirements an FTS design was proposed. The basic part of the FTS consists of a hydrogen maser frequency standard, a distribution amplifier, and a clock

(Fig. 1). These three devices are powered continuously using the mobile unit's dc or ac power, which allows the FTS to provide the performance to specifications within four hours after arrival on site. (There is the withstanding mode during which no power is available and all equipment is to be shut down. This is discussed later in this paper.)

**1. The frequency standard.** The primary source of a stable frequency for the FTS is a hydrogen maser frequency standard (Refs. 2-4). The hydrogen maser is the most stable operational frequency standard in the world today (for averaging times of  $>1$  sec). It is the only frequency standard available that can possibly meet the ORION system frequency stability requirements. Like all frequency standards the hydrogen maser is susceptible to vibration, changes in temperature, magnetic fields and barometric pressure. The superior stability of the hydrogen maser makes these influences very apparent, so great care must be taken any time a hydrogen maser is installed in a system.

**2. The distribution amplifier.** The distribution amplifier has a 5-MHz input signal from the hydrogen maser. Its output consists of several 5-MHz signals which are all coherent with the input. The isolation between any two output ports is 60 dB minimum. Furthermore, the amplifier must not degrade the hydrogen maser stability. All of the levels at the four output ports will be 13 dBm  $\pm 3$  dB into a 50-ohm termination. (An amplifier with these capabilities is not readily available.) Presently there are four candidates — two commercial and two noncommercial. A tradeoff study will be made during the first quarter of 1981. All of these amplifier types will be tested on a HP5390A frequency stability analyzer. The selection will be based on technical performance and cost.

**3. The clock.** The third part of the basic system is the clock. There are other clocks in the FTS (described later in this document) but this is the primary clock and will be known as the FTS clock. The FTS clock has one 5-MHz input from the distribution amplifier and hydrogen maser. It has two outputs: (1) the time of year and (2) four 1-PPS ports. These 1-PPS outputs have time of second information to the nearest microsec. The time of year to the second is available to the computer through a RS232C interface. One of the functions of the FTS clock is to provide a knowledge of time with respect to USNO within 1 microsec. The stability and offset of that signal will determine the accumulated clock error. With a hydrogen maser the maximum accumulated clock error should be approximately 1 microsec per month (which is  $\Delta T/T \approx 4 \times 10^{-13}$ ).

### B. Time and Frequency Comparison

In order to meet the requirement to monitor the FTS and to have knowledge of the FTS clock time to 1 microsec with

respect to USNO, additional components are needed in the FTS. These components form two systems; one is the time comparison equipment, the other is the phase comparison equipment. These two systems are available only when 120 Vac power is operating.

**1. Time comparison.** The accumulated clock error rate on the FTS clock should be  $4 \times 10^{-13} \Delta T/T$ , which is large enough to require frequent calibrations of the FTS clock. In order to have knowledge of time to microsec level, it is necessary to use some sort of high-precision time transfer. Several methods exist to accomplish this (Ref. 5). For the ORION FTS, the following four time transfer methods are being considered:

- (a) Traveling atomic clock.
- (b) Loran-C.
- (c) Transit or Nova satellite.
- (d) Global positioning satellite (NAVSTAR).

All four of these methods will be considered and a tradeoff study will be made. The method selected should be determined by June 1981. Some obvious considerations for this selection are listed below:

- (a) The cost of the traveling clock to maintain submicrosec clock accuracy.
- (b) The unavailability of Loran-C throughout the world (particularly the southern hemisphere).
- (c) The new and relatively untried aspects of satellites for time synchronization to submicrosec accuracy.
- (d) Ability to meet the system requirements for time synchronization.

This same accumulated clock error data will be used to determine the long-term (>10 days) frequency stability of the hydrogen maser. This information will be used to help determine the need for maintenance.

**2. Phase comparison.** The purpose of the phase comparison system is to give immediate information on the output frequency of the hydrogen maser. Another frequency standard, a rubidium vapor unit, is needed so that the hydrogen maser can be compared to it. The 5-MHz signals from the rubidium unit and the hydrogen maser are compared in a phase comparator; the analog output is read and digitized by an analog-to-digital converter. The data are then sent to the mobile unit computer for analysis. This analysis can quickly detect any severe frequency offset between the two frequency standards, and also provide stability information on the rubidium.

There are two additional uses for the rubidium frequency standard. The rubidium frequency standard has a built-in digital clock, and with this backup clock FTS time to the microsec can be recovered in the event of the failure of the FTS clock. The rubidium standard could also be used as the FTS frequency standard in the event the hydrogen maser is unavailable (Ref. 6).

## V. Operation of the FTS

### A. Modes of Operations

**1. Operating mode.** This is when the mobile unit is on site and operating or preparing to operate. The ac power is being supplied, the van is air conditioned and the computer is operating.

**2. Transit mode.** This is when the mobile unit is being moved from one site to another; dc power is being supplied to only the hydrogen maser compartment. This powers the compartment air conditioner, hydrogen maser and necessary auxiliary equipment. The other subsystems are not operating.

**3. Withstanding mode.** This mode exists when the mobile unit subsystems cannot be supplied power. All of the equipment must be shut down. (A hydrogen maser must be shut down using a procedure specified by the manufacture. If the hydrogen maser is shut down it must be supplied high voltage pump power to prevent damage.) This is an undesirable situation but one which must be planned for. If the hydrogen maser is shut down it will require several weeks to restabilize it after it is restarted. It will take a considerable effort to reestablish the time of the FTS clock, which means, of course, that the four-hour requirement to operational status is no longer applicable.

### B. Operation

The ORION mobile unit personnel have a minimum number of tasks to perform. Some of the tasks that must be accomplished by the mobile unit personnel are listed below:

- (1) Erect the antenna for the time comparison system. This should be a several-minute operation and it should involve no connections or disconnections of cables.
- (2) Reconfigure the FTS. This would occur only if there were a failure in a major part of the FTS.
- (3) Reestablish FTS clock time. If time were lost on the FTS clock a time transfer would have to be made from the rubidium clock.
- (4) Setup time comparison system. All of the possible time comparison systems will use a time interval counter. This will have to be put into operation.

- (5) Evaluate the real-time monitor functions to verify performance.

## **VI. FTS Requirements of Other Subsystems**

### **A. Monitor and Control**

The following functions must be performed by the monitor and control subsystem:

- (1) A constant record of time offset between the FTS clock and the external clock needs to be kept. Furthermore, long-term records need to be kept to establish the performance of the frequency standard. "Long term" is meant to be several months to one or two years.
- (2) Operating data on the hydrogen maser consist of the many operating parameters provided by the hydrogen maser microprocessor. The data should be available when requested by the ORION mobile computer unit and should be included within the regular reporting procedures.
- (3) Phase offset data between the hydrogen maser and the rubidium frequency standard will be used to check on the immediate operation of the hydrogen maser and so must be available at the ORION mobile computer unit.

### **B. Power Requirements**

The FTS requires 28 Vdc power at approximately 9 A. This power is required continuously except when ac power is applied or when the mobile unit is in the withstanding mode.

During the operating mode, the FTS requires 120 Vac power at about 6 A.

### **C. Space Requirements**

The compartment that holds the hydrogen maser and the other continuously operated components of the FTS must be at least 170 cm wide, 220 cm long, and 225 cm tall. The remaining equipment in the FTS will fit in less than 150 cm of cabinet height.

### **D. Vibration Protection**

A vibration dampening device needs to be installed between the hydrogen maser and the mobile unit structure. This will protect the physics unit during transit of the mobile unit. Because the design of a vibration dampening device is so dependent on the weight mounting hole locations and center of gravity location of the hydrogen maser unit, it was decided to make it a part of the FTS.

### **E. Antennas**

If the time comparison system uses an antenna, it will need to be mounted on top of the electronics van. The time comparison will need to have an unobstructed view of the sky, and yet it must not interfere with the movement of the van.

### **F. Temperature**

Perhaps the most critical requirement to achieve the stability performance of the FTS is that ambient temperature surrounding the hydrogen maser must be stable to 0.1°C during operation and for 48 hours prior to operation.

## References

1. Brunn, D. L., Wu, S. C., Thom, E. H., McLaughlin, F. D., and Sweetser, B. M., "ORION Mobile Unit Design," in *The TDA Progress Report 42-60*, Jet Propulsion Laboratory, Pasadena, Calif., Dec. 15, 1980.
2. Ramsey, N. F., "The Atomic Hydrogen Maser," Eighth Annual Precision Time and Timing Applications and Planning Meeting, Nov. 30 – Dec. 2, 1976, p. 183, NASA/Goddard Space Flight Center, Greenbelt, Md.
3. Reinhardt, V. S., Peters, H. E., and Burnbaum, L. A., "Field Operable Hydrogen Maser Design," Eighth Annual Precision Time and Timing Applications and Planning Meeting, Nov. 30 – Dec. 2, 1976, p. 197, NASA/Goddard Space Flight Center, Greenbelt, Md.
4. Dachel, P. R., Meyer, R. F., Petty, S. M., and Sydnor, R. L., "Hydrogen Maser Frequency Standards for the Deep Space Net," Eighth Annual Precision Time and Timing Applications and Planning Meeting, Nov. 30 – Dec. 2, 1976, p. 213, NASA/Goddard Space Flight Center, Greenbelt, Md.
5. Putkovich, K., "High Precision Time Transfer Methods," Seventh Annual Precision Time and Timing Applications and Planning Meeting, Dec. 2-4, 1975, p. 323, NASA/Goddard Space Flight Center, Greenbelt, Md.
6. MacDoran, P. F., Thomas, J. B., Ong, K. M., Fliegel, H. F., and Morabito, D. D., "Radio Interperometric Geodesy Using a Rubidium Frequency System," Seventh Annual Precision Time and Timing Applications and Planning Meeting, Dec. 2-4, 1975, p. 439, NASA/Goddard Space Flight Center, Greenbelt, Md.

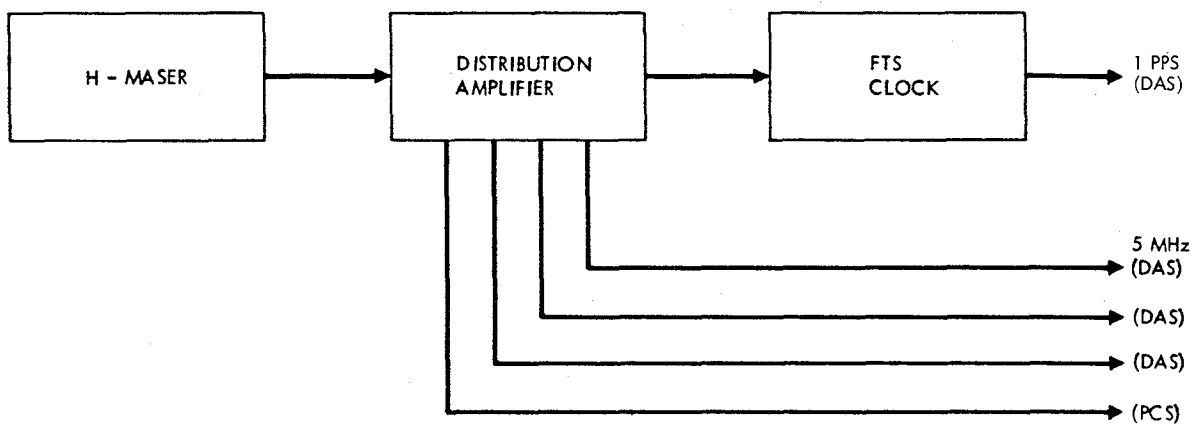


Fig. 1. The basic frequency and timing system

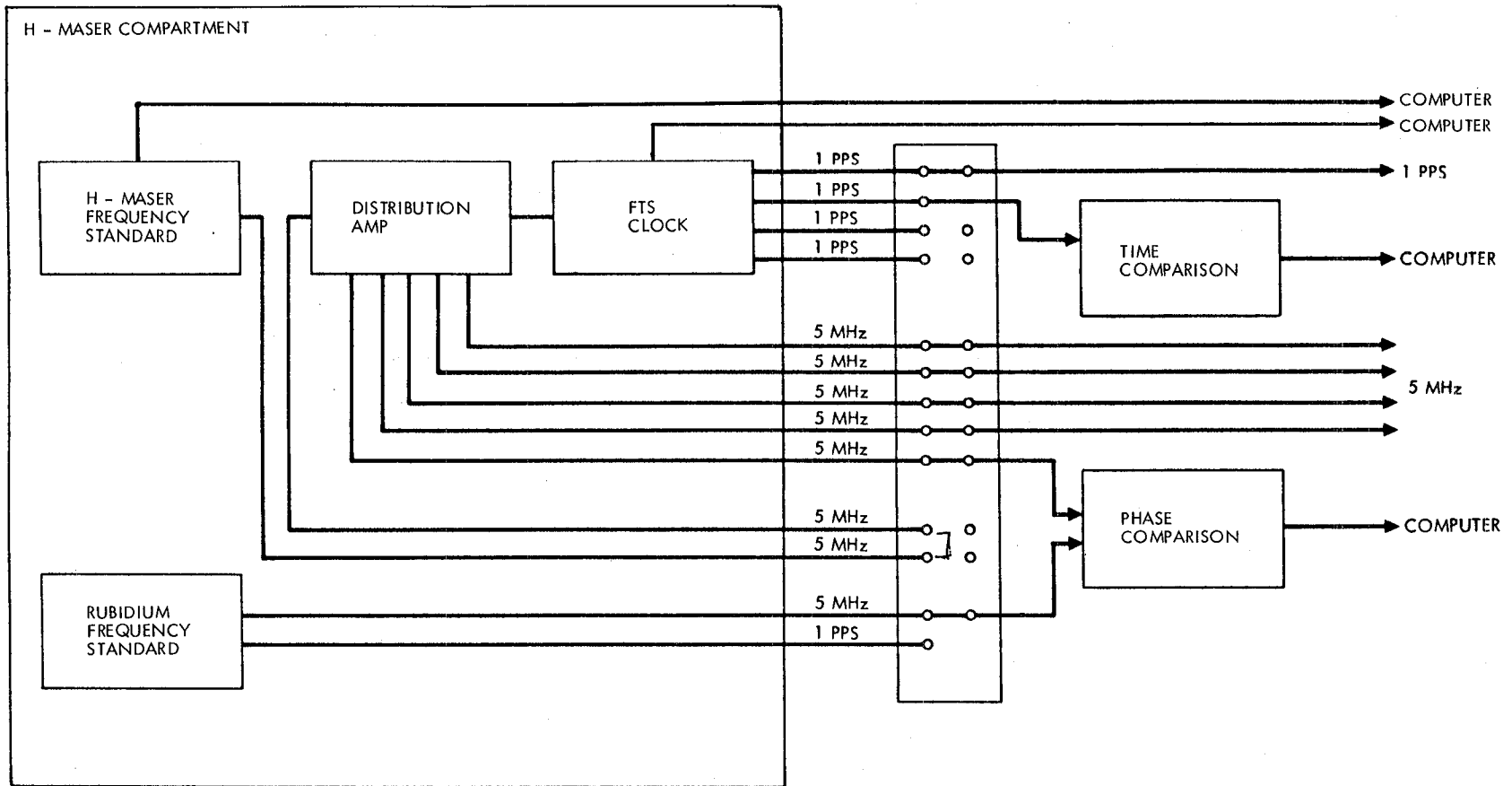


Fig. 2. The complete frequency and timing system

# ORION — Microwave Water Vapor Radiometer Subsystem Design

R. P. McKinney and N. I. Yamane  
Microwave Observational Systems Section

*Electrical path delay caused by atmospheric water vapor may be a limiting error source for geodetic measurements made with very long baseline interferometry. Direct measurement of atmospheric water vapor is necessary to obtain path delay correction required by the ORION project. A dual-channel water vapor radiometer is described which operates at frequencies near the 22-GHz water vapor line and is capable of collecting data that will permit calculation of path delay with 2-cm accuracy.*

## I. Introduction

The ORION Microwave Water Vapor Radiometer (WVR) will collect radiometric data to permit subsequent calculation of the line-of-sight path delay to radio waves caused by tropospheric water vapor. The data shall be of quality such that the calculation of path delay can be made with an error of less than  $\pm 2$  cm, a criterion of the overall system requirement.

## II. Background

Microwave interferometric systems operating over long baselines on the earth's surface are sensitive to path delay errors induced by tropospheric water vapor. The total delay can vary from 3 to 150 cm for surface ambient temperatures of 0 to 50°C (for a surface temperature below -10°C, tropospheric water vapor will be negligible). Overall system errors from this source can be reduced to between 10 and 15 cm by using estimation techniques based on historical measurements of water vapor or models based on the measurement of surface meteorology. Reduction of path delay error below the

10-15 cm range requires measurements of tropospheric water vapor along the line-of-sight of the interferometer receiving antenna.

## III. History

The Jet Propulsion Laboratory has been active in the design and fabrication of passive microwave radiometers for remote sensing of water vapor and atmospheric temperature for many years. During the early 1970's, radiometers were developed and successfully launched on the Nimbus E, Nimbus F, and Tiros series of weather satellites. Extensive work was also done in developing data reduction algorithms. In 1974, a JPL team used the prototype scanning multifrequency radiometer (SCAMS) from Nimbus F to demonstrate that water vapor in the atmosphere can be measured with ground-based remote sensing. Data from this test were compared with other data (Ref. 1) and the results indicated the radiometer yielded data that could enable calculation of the water-vapor-induced delay with an accuracy of  $\pm 2$  cm.

A similar prototype water vapor radiometer (WVR) was integrated with a microprocessor to perform data collection functions and communication with a host computer. This prototype WVR was used as a support instrument on the long baseline program (Astronomical Radio Interferometric Earth Surveying, ARIES) project that was being conducted by JPL.

Another JPL team used the algorithms developed earlier for spacecraft instruments to generate software necessary to operate the WVR microprocessor. The WVR also had stand-alone capability via an RS232 serial data interface. The software generates all control and data taking functions on request from the host computer or RS232-compatible data terminal.

Results from the ARIES prototype were evaluated and a decision was then made to fabricate four WVR's for use on the Very Long Base Interferometer (VLBI) project. Several improvements were made, including better thermal control, use of a very low side-lobe corrugated horn antenna, and improved calibration load stability. The improved WVR's were built and the design was documented with formal drawings. An improved version of the software was also developed and integrated with the Mark III Data System. An additional unit was built to the formal drawings for ARIES II and served as a check of the documentation; all discrepancies have been corrected.

## IV. WVR Subsystem Functional Description

### A. General Description

The ORION Water Vapor Radiometer will be a modified version of the ARIES WVR, designed for the mobile operations environment. These descriptions and requirements are for the WVR. The functions and interface of the WVR are shown in Fig. 1. The WVR will be installed in the reflector of the ORION antenna and the pointing will be aligned within  $\pm 1$  degree. Microwave radiation will be measured at two frequencies. One of the frequencies will be on the lower frequency skirt of the water vapor emission line at approximately 21 GHz. The other frequency will be off the emission line at approximately 31 GHz. The 31-GHz channel is twice ( $\times 2$ ) as sensitive to liquid water as the 21-GHz, but it is only five tenths ( $\times 0.5$ ) as sensitive as the 21-GHz to water vapor. This will permit calculation of both liquid water and water vapor by using combined data from both channels. Each frequency will have its own horn antenna and receiver system, and will operate simultaneously. The rationale for the frequency selection is discussed extensively in Ref. 2. A block diagram of the WVR is shown in Fig. 2.

### B. WVR Assemblies

There are three assemblies to the WVR: (1) Radiometer Electronics Assembly, (2) Power Supply Assembly, and

(3) Data and Control Assembly. Each is in a separate package for ease of installation and repair as well as thermal design considerations.

**1. Radiometer Electronics Assembly.** The Radiometer Electronics Assembly consists of an antenna, Dicke-switched super-heterodyne receiver and associated circuitry for each channel. Incoming microwave radiation is collected by two low side-lobe corrugated horn antennas. The output of each antenna is fed to a port of a 5-port latching ferrite switch. The radiometer is switched between the antenna port and a reference load (Dicke-switching scheme) at a frequency of 1 kHz. The signal from the output port of the ferrite switch is mixed with a local oscillator (tuned to the center frequency of each channel and passed through an IF filter and amplifier). The signal is then detected by the first detector and the resulting video signal is amplified. The video signal is synchronously detected using the same 1-kHz reference previously used to drive the ferrite switch. The detected signal is integrated (low-pass filtered) and amplified to provide an analog output voltage proportional to the difference in signals at the switch ports. Internal calibration of the WVR is done by switching from the antenna port to each of two ports having microwave termination loads held at fixed temperatures, one at 310 K and the other at 373 K. Internal calibration is performed each time a data set is taken. This calibration will be supplemented by doing "tipping curve" calibrations, which require movement of the entire antenna subsystem for each tipping curve calibration sequence. Tipping curve sequences are planned at two-hour intervals. The sequence will be controlled by the host computer. The use of tipping curves to remove instrument error is discussed in Ref. 2. Temperature of the loads as well as other critical components will be measured using platinum temperature sensors. The Radiometer Electronics Assembly also contains the ferrite switch drivers, and heater controllers.

The Radiometer Electronics Assembly is housed in a thermally insulated enclosure that provides protection from the elements and thermal stability. Heaters are provided to stabilize the internal temperature of the enclosure and electronics. Electrical power to the Radiometer Electronics Assembly is controlled remotely from the control and data assembly.

**2. Power Supply Assembly.** The Power Supply Assembly provides all necessary voltage to operate the WVR electronics assembly from 117 V rms  $\pm 10\%$ , 60-Hz, 1 $\phi$  commercial power. Independent power supplies are used for each channel and separate ground returns are used for maximum dc isolation between channels.

Housing of the power supplies in a separate enclosure permitted better thermal stability in the Radiometer Electronics Assembly and allowed more freedom in mounting the subsystem. The power supply assembly is equipped with tem-

perature-controlled heaters to assure reliable operation in low-temperature environments.

**3. Control and Data Assembly.** The Control and Data Assembly consists of a microprocessor system and associated circuitry, including analog I/O circuits, multiplexer, 12-bit A to D converter, memory, and an RS232 serial digital interface circuit. A local control panel is also included for checkout, testing, and troubleshooting of the subsystem. Internal power supplies provide all voltages necessary to operate the Control and Data Assembly from 117 V rms  $\pm 10\%$ , 60-Hz, 1 $\phi$  commercial power. During normal operation, all WVR functions will be controlled by external commands from the host computer.

The Control and Data Assembly will accept, digitize, and collect both analog data and monitor signals from the Radiometer Electronics Assembly. It will then format, buffer, and transmit the data on command to the host computer. There are provisions for only limited processing and memory in the Control and Data Assembly due to the limitations of the microprocessor. Conversion of antenna temperatures to path delay will be performed by the host computer.

## V. ORION WVR Design

The previously described WVR was the ORION baseline design which was basically an add-on system with stand-alone capability. The ORION WVR is to be an integral part of the total ORION system, and necessary design revisions were made. The previous WVR's were mounted on a separate positioner that was controlled by the microprocessor, but this was not necessary for ORION because the WVR is located with the main ORION antenna and positioned by it. The narrow beamwidth of the radiometer antennas allowed the placing of the WVR at the rear of the main antenna looking through a hole in the antenna reflector without interference from the subreflector. When the positioner was removed from the WVR, the microprocessor was deleted and its remaining data and control functions assigned to the Monitor and Control Subsystem.

Mechanical design of the WVR has been revised and design changes were made in several areas to improve structural strength of the WVR to the main antenna interface.

## VI. Current Design Status

Preliminary thermal analysis had indicated that the Radiometer Electronics and Power Supply Assemblies would operate normally over the specified ambient temperature range for ORION. Subsequent temperature qualification testing revealed a problem with the Power Supply Assembly at low temperature. The problem was solved by redesigning the heat sink and heater layout. The units operated satisfactorily on retest. Humidity and barometric tests have not been performed, and are not planned. Vibration and shock tests have not been performed and are not planned. Preliminary examination of available reliability data for the WVR subsystem indicates compliance with overall mean time between failure requirement.

The formal drawings for the WVR have been redlined to show corrections except for the Data and Control Assembly. Release of the redline corrections is not currently planned due to lack of funds. The functional requirements design review (Level D) has been completed and the Functional Design Requirements (FDR) document prepared. A preliminary Detail Design Specification (DDS) has been completed. The detail design review (Level E), release of the FDR, and completion of the final DDS is dependent upon revision of the Data and Control Assembly design, which is not currently planned due to lack of funds. Preliminary test procedures have been completed except for the Data and Control Assembly. The installation, maintenance and operation manual are planned for FY 82.

## VII. Conclusions

The WVR design will meet functional requirements of the ORION system to provide calculation of path delays with an accuracy of  $\pm 2$  cm. Minor mechanical design changes and interface modification are required before finalization of design. Project management has indicated that drawings currently completed in "redline" form are sufficiently developed to assure completion as scheduled.

## References

1. Winn, F. B., et al., "Atmospheric Water Vapor Calibrations: Radiometer Techniques," in *The Deep Space Network Progress Report 42-32*, pp. 38-49, Jet Propulsion Laboratory, Pasadena, Calif., April 15, 1976.
2. Claflin, E. S., et al., "Microwave Radiometric Measurements of Water Vapor Path Delay: Data Reduction Techniques," in *The Deep Space Network Progress Report 42-48*, pp. 22-30, Jet Propulsion Laboratory, Pasadena, Calif., Dec. 15, 1978.

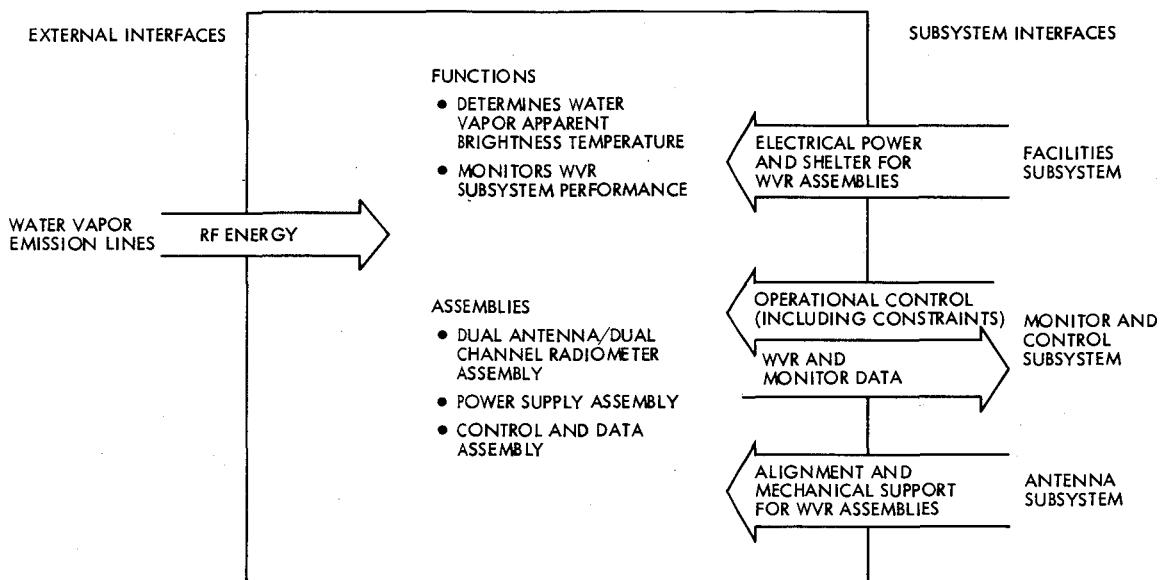


Fig. 1. ORION Water Vapor Radiometer Subsystem, function and interfaces

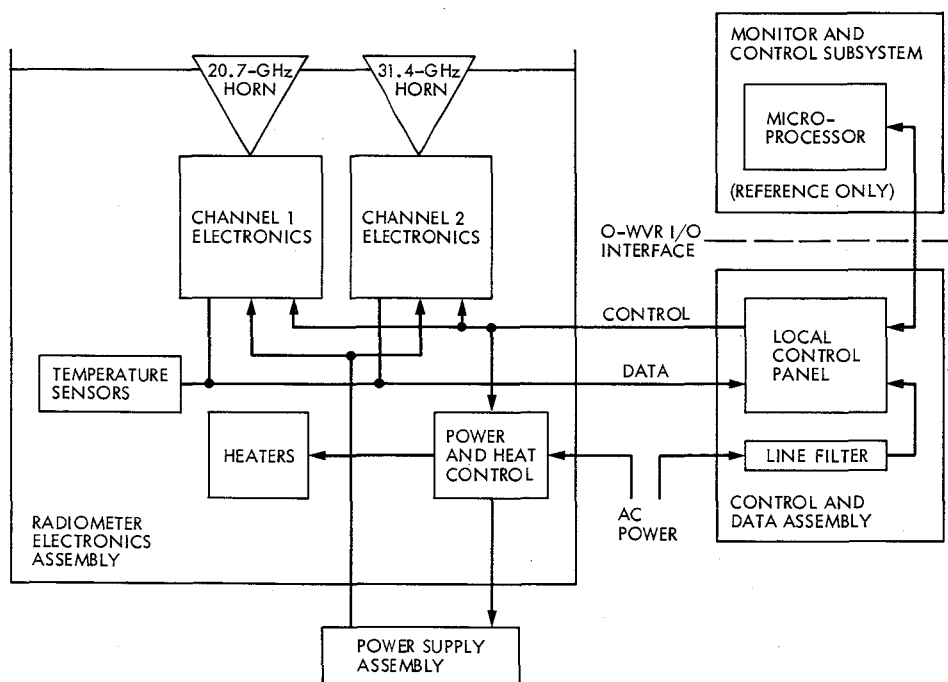


Fig. 2. ORION Water Vapor Radiometer, overall block diagram

# Posterior Error Probability in the Mu-II Sequential Ranging System

C. W. Coyle

Communications Systems Research Section

*An expression is derived for the posterior error probability in the Mu-II Sequential Ranging System. An algorithm is developed which closely bounds the exact answer and can be implemented in the machine software. A computer simulation is provided to illustrate the improved level of confidence in a ranging acquisition using this figure of merit as compared to that using only the prior probabilities. In a simulation of 20,000 acquisitions, with an experimentally determined threshold setting, the algorithm detected 90 percent of the actual errors and made false indications of errors on 0.2 percent of the acquisitions.*

## I. Introduction

In the interest of economizing on the acquisition time in the Mu-II Ranging System, it is desirable to find an upper bound on the error probability in a range determination, given suitable estimates of the signal and noise levels and the entire set of receiver correlator outputs. A complete description of this ranging machine can be found in Ref. 1.

The Mu-II operates by receiving a sequence of square waves, each member of the sequence having twice the period of the previous one (Fig. 1). The highest frequency component provides the required precision, while each subsequent component is used to resolve the remaining ambiguity, which is equal to the previous component's period. Upon correlation of each component with a locally generated reference, the receiver shifts the local reference in an attempt to force the next component onto a peak of its triangular correlation curve. A

quadrature output is also produced by correlation of the signal with a 90-deg shifted version of the reference.

An initial assumption made here is that the  $2\pi$  modulus phase delay of the first (highest resolution) component was measured exactly ( $\tau$  in Fig. 1). For the second component, and for all subsequent components, a binary decision must be made as to whether the in-phase correlator output is at a positive or negative peak, as discussed in Ref. 2. It is the probability of correctness of this set of decisions that will be examined here.

## II. A General Expression for the Posterior Probability

If  $\bar{R}$  is a vector of all in-phase correlator outputs  $I_n$  and all quadrature correlator outputs  $Q_n$ , the posterior probability that all decisions were made correctly is, by Bayes's rule,

$$\begin{aligned}
P(\text{correct}|\bar{R}) &= \frac{P(\bar{R}|\text{correct}) P(\text{correct})}{P(\bar{R})} \\
&= \frac{P(\bar{R}|\text{correct}) P(\text{correct})}{P(\bar{R}|\text{correct}) P(\text{correct}) + P(\bar{R}|\text{incorrect}) P(\text{incorrect})} \\
&= \left[ 1 + \frac{P(\text{incorrect}) P(\bar{R}|\text{incorrect})}{P(\text{correct}) P(\bar{R}|\text{correct})} \right]^{-1}
\end{aligned} \tag{1}$$

As nothing is known about the transmitted vector,  $P(\text{correct}) = 2^{-N}$  and  $P(\text{incorrect}) = 1 - 2^{-N}$ , giving

$$P(\text{correct}|\bar{R}) = \left[ 1 + (2^N - 1) \frac{P(\bar{R}|\text{incorrect})}{P(\bar{R}|\text{correct})} \right]^{-1} \tag{2}$$

$P(\bar{R}|\text{correct})$  is simple to compute because, given that components were received correctly, the means of all the  $Q_n$  are zero. The probability that component  $n$  will yield output values  $Q_n, I_n$  is

$$P_n(I_n, Q_n | S_0) = P_n(\bar{R}_n | S_0) \tag{3}$$

where  $S_0$  is the mean of  $I_n$ . By the receiver decision rule,  $S_0$  will have a sign equal to the sign of  $I_n$ .

These probabilities are mutually independent when conditioned on a sequence of correct decisions, so

$$P(\bar{R}|\text{correct}) = \prod_{n=1}^N P_n(\bar{R}_n | S_0) \tag{4}$$

$P(\bar{R}|\text{incorrect})$  is much more difficult to determine. This is because the location of the mean for a given component depends on the sequence of prior errors. The mean will, in general, be located off the  $I$  axis. This probability can be expanded as

$$\begin{aligned}
P(\bar{R}|\text{incorrect}) &= \sum_{\text{all } \bar{S}} P(\bar{R}|\bar{S}) P(\bar{S}) \\
&= \sum_{\text{all } \bar{S}} \prod_{n=1}^N P(\bar{R}_n|\bar{S}) P(\bar{S}),
\end{aligned} \tag{5}$$

where  $\bar{S}$  is an  $N$  bit binary sequence other than the sequence chosen by the receiver. As there are  $2^N - 1$  equally likely sequences  $\bar{S}$ ,  $P(\bar{S}) = (2^N - 1)^{-1}$ . The desired expression is then

$$P(\text{correct}|\bar{R}) = \left[ 1 + \sum_{\text{all } \bar{S}} \prod_{n=1}^N \frac{P_n(\bar{R}_n|\bar{S})}{P_n(\bar{R}_n|S_0)} \right]^{-1} \tag{6}$$

To evaluate each  $P_n(\bar{R}_n|\bar{S})$ , the position of the mean for component  $n$  is determined by assuming  $\bar{S}$  to be the correct sequence and comparing this with the sequence produced by the receiver, thus making known the nature and location of all errors in the receiver decision under this hypothesis.

### III. Development of a Useful Bound

Evaluating the sum in Eq. (6), with its  $2^N - 1$  terms, each containing  $N$  factors, is clearly impractical for the usual values of  $N$  (often  $> 10$ ) encountered. In order to be useful as an indicator of performance in the Mu-II, a lower bound must be found for (6) which is simple to compute but sufficiently tight to be meaningful. At this point, we observe that all of the  $\bar{R}_n$  are Gaussian random variables of equal variance with probability densities of the form

$$\begin{aligned}
p_n(\bar{R}_n|\bar{\mu}_n) &= (2\pi\sigma^2)^{-1} \exp \left\{ -\frac{1}{2\sigma^2} \left[ (Q_n - \mu_{nq})^2 \right. \right. \\
&\quad \left. \left. + (I_n - \mu_{ni})^2 \right] \right\}
\end{aligned} \tag{7}$$

where  $\bar{\mu}_n$  is the mean vector resulting from the specified condition on  $P_n(\bar{R}_n)$ . This substitution makes (6) become

$$P(\text{correct}|\bar{R}) = \left[ 1 + \sum_{\bar{S}} \prod_n F_n(\bar{S}) \right]^{-1} \tag{8}$$

where

$$\begin{aligned}
F_n(\bar{S}) &= \exp \left\{ \frac{1}{2\sigma^2} \left[ m^2 - (\mu_{ni}^2 + \mu_{nq}^2) \right. \right. \\
&\quad \left. \left. + 2(I_n \mu_{ni} + Q_n \mu_{nq} - |I_n| m) \right] \right\}
\end{aligned} \tag{9}$$

Here,  $(\mu_{ni}, \mu_{nq})$  is the mean vector derived for  $P_n(\bar{R}_n|\bar{S})$  and  $m$  is the magnitude of  $S_0$ . The  $(\mu_{ni}, \mu_{nq})$  are the component means seen by the receiver if its decision was incorrect and the  $\bar{S}$  under consideration is correct.

The  $2^N - 1$  possible sequences  $\bar{S}$  can be classified into types. Each type is denoted by the number of agreements with receiver decisions before a disagreement occurs. Thus, if there are  $N$  components, there will be  $N$  types of decision sequences, numbered from 0 to  $N - 1$ . (A sequence with  $N$  agreements corresponds to the receiver decision and the set  $\bar{S}$  specifically excludes this case.) It is easy to see that there will be  $2^{N-p-1}$  members of a type  $p$  sequence.

Now, if there are  $p$  agreements before a disagreement, the first  $p$  values of  $(\mu_{ni}, \mu_{nq})$  will be simply  $(S_0, 0)$  and the first  $p$  values of  $F_n(\bar{S})$  will, using (9), be unity. Component  $p + 1$  will still have its mean on the  $I$  axis, specifically at  $(-S_0, 0)$ . For  $n = p + 2$ , the vector  $(\mu_{ni}, \mu_{nq})$  becomes either  $(0, m)$  or  $(0, -m)$ , because of error at component  $p + 1$  shifts the mean onto the  $Q$  axis. The value of  $F_{p+2}(\bar{S})$  can be upper bounded by always choosing the sign of  $m$  to minimize the distance between the mean and  $\bar{R}_n$ . Using (9),

$$F_{p+1}(\bar{S}) = \exp\left\{\frac{-2m}{\sigma^2} |I_{p+1}|\right\} = \bar{F}_{p+1}, \quad (10)$$

and

$$F_{p+2}(\bar{S}) \leq \exp\left\{\frac{-m}{\sigma^2} [ |I_{p+2}| - |Q_{p+2}| ]\right\} = \bar{F}_{p+2}. \quad (11)$$

Equation (8) can now be lower bounded by

$$P(\text{correct}|\bar{R}) \geq \left[ 1 + \sum_{p=0}^{N-1} G_p \right]^{-1} \quad (12)$$

where  $G_p$  is an upper bound on the sum of products over a particular  $\bar{S}$  type:

$$G_p \leq 2^{N-p-1} \bar{F}_{p+1} \bar{F}_{p+2} \prod_{n>p+2} F_n(\bar{S}), \quad (13)$$

where all factors with subscripts greater than  $N$  are taken equal to unity.

A simplifying approximation can be used to determine the  $F_n(\bar{S})$  when  $n > p + 2$ . Upper bounds on these can be computed by choosing, for each component, a mean vector  $(\mu_{ni}, \mu_{nq})$  that will result in the largest possible value of  $F_n$ . Such worst case values are independent of  $\bar{S}$  and need only be computed once for each component.

Such a bound can be obtained by realizing that the possible means associated with a particular sequence  $\bar{S}$  are confined to a locus of points as shown in Fig. 2. (Ref. 2). Attention has been restricted to the first quadrant as would be done in practice by using the absolute values of  $I_n$  and  $Q_n$ . For  $\bar{R}_n$  in the shaded region bordering the  $I$  axis, the nearest possible mean (the one that will maximize  $F_n$ ) is the point  $(m, 0)$ . If  $\bar{R}_n$  is in the shaded region bordering the  $Q$  axis, the nearest mean is the point  $(0, m)$ . For all other  $\bar{R}_n$ , the nearest mean is the intersection of the locus of means with a perpendicular passing through  $\bar{R}_n$ , yielding a vector  $(\mu_{ni}, \mu_{nq})$  where

$$\begin{aligned} \mu_{ni} &= \frac{1}{2} [m - (|Q_n| - |I_n|)] \\ \mu_{nq} &= \frac{1}{2} [m + (|Q_n| - |I_n|)]. \end{aligned} \quad (14)$$

Using Eq. (9)

$$\text{a) } F_n = 1 \text{ for } |I| > m \text{ and } |Q| < |I| - m,$$

$$\text{b) } F_n = \exp\left[\frac{m}{\sigma^2} (|Q_n| - |I_n|)\right]$$

for  $|Q| > m$  and  $|I| < |Q| - m$

$$\text{c) } F_n = \exp\left\{\frac{1}{4\sigma^2} [(m - |I_n|) + |Q_n|]^2\right\} \text{ otherwise.} \quad (15)$$

It is apparent from (13) that the  $F_n$  need not be computed for  $n < 3$ .

An improvement in the tightness of the bound can be realized by taking into account the discrete nature of the possible locations for the means. It is clear that the first component can only have a mean at  $(m, 0)$ . Each subsequent component has  $2^{n-2} + 1$  possible means equally spaced along the line joining  $(m, 0)$  and  $(0, m)$ . In general, the location of these will be given by

$$\mu'_{ni} = mi/2^{n-2} \quad (16)$$

and

$$\mu'_{nq} = m - \mu'_{ni} = m(1 - i/2^{n-2}),$$

$$n > 1 \quad i = 0, 1, 2, \dots, 2^{n-2}.$$

An upper bound on  $F_n$  is found by again dropping a perpendicular from  $\bar{R}_n$  to the diagonal locus of means. In general, this intersection will not satisfy (16). It is easily seen that the nearest mean satisfying (15) is found by choosing a value for  $i$  that will minimize  $|\mu_{ni} - \mu'_{ni}|$ . Substituting values from (14) and (16),

$$i_n = \frac{\mu'_{ni}}{m} 2^{n-2} \left. \vphantom{i_n} \right\} \begin{array}{l} \text{rounded to} \\ \text{nearest integer} \end{array} \quad (17)$$

$$= \left( 1 + \frac{|I_n| - |Q_n|}{m} \right) 2^{n-3} \quad n > 1$$

The resulting  $\mu'_{ni}$  and  $\mu'_{nq}$  can be inserted into (9) and the result

$$F_n = \exp \left( \frac{m}{\sigma^2} \left\{ (1 - i_n 2^{2-n}) \left[ i_n m 2^{2-n} - (|I_n| - |Q_n|) \right] \right\} \right) \quad (18)$$

for  $n > 1$  can be used in place of (15c).

This expression will provide noticeable reductions in the  $F_n$  compared with (15c), especially for low values of  $n$  where the nearest  $\mu'_{ni}$  is often far from  $\mu_{ni}$ .

To reiterate the procedure of finding a bound for  $P(\text{correct}|\bar{R})$ ,

- (a) Compute a set of  $F_n$  ( $n = 3, 4, \dots, N$ )

from

$$F_n = 1 \quad \text{for } |I| > m \text{ and } |Q| < |I| - m$$

$$F_n = \exp \left[ \frac{m}{\sigma^2} (|Q_n| - |I_n|) \right] \quad \text{for } |Q| > m \text{ and } |I| < |Q| - m$$

$$F_n = \exp \left( \frac{m}{\sigma^2} \left\{ (1 - i_n 2^{2-n}) \left[ i_n m 2^{2-n} - (|I_n| - |Q_n|) \right] \right\} \right) \quad (19)$$

Otherwise,

where

$$i_n = \left( 1 + \frac{|I_n| - |Q_n|}{m} \right) 2^{n-3}$$

rounded to the nearest integer.

- (b) Compute a set of  $\bar{F}_n$  ( $n = 1, 2, \dots, N$ )

from

$$\bar{F}_n = \exp \left\{ \frac{-2m}{\sigma^2} |I_n| \right\}. \quad (20)$$

- (c) Compute a set of  $\bar{\bar{F}}_n$  ( $n = 2, 3, \dots, N$ )

from

$$\bar{\bar{F}}_n = \exp \left\{ \frac{-m}{\sigma^2} (|I_n| - |Q_n|) \right\} \quad (21)$$

- (d) Compute a set of  $N-1$  products

$$G_p = 2^{N-p-1} \bar{F}_{p+1} \bar{\bar{F}}_{p+2} \prod_{n>p+2} F_n \quad p=0, \dots, N-1. \quad (22)$$

The result is then given as

$$P(\text{correct}|\bar{R}) \geq \left[ 1 + \sum_{p=1}^{N-1} G_p \right]^{-1}. \quad (23)$$

## IV. Simulation

A computer program was developed to simulate a ranging acquisition by generating a random binary vector, suitably corrupted with Gaussian noise. The vector was sequentially detected, care being taken to properly shift the means of subsequent components when a detection error was made. A modified version of the algorithm found in Ref. 3 was used.

The simulation consisted of 20,000 trial acquisitions, each with 10 lower frequency components. The value of  $m/\sigma$  was 3.5, for a postcorrelation SNR of 7.9 dB. Using Ref. 2, the prior probability of a correct acquisition was determined to be approximately 0.998. The expected number of errors over the sample is then about 40. The number of errors that actually occurred was 39. Various thresholds were considered and an error was assumed to have occurred when the algorithm returned a number below threshold. Table 1 summarizes the results.

It is important to note that all the undetected errors (with the exception of one additional at 0.01 threshold) occurred on

the last component of the acquisition. Such an error is particularly difficult to detect because there is no following component from which to observe the shift of the mean onto the  $Q$  axis. If the rest of the components were received reliably, the error probability will be essentially that of the last component, as if it were the only one transmitted. This probability will never be less than 0.5. The problem could be circumvented by transmitting one more code component than is necessary to resolve the range ambiguity. The received component could then be used to check the reliability of the previous decision but would not be used in the range calculation.

The reason why it is possible to detect virtually all errors even with a rather low threshold is found in the behavior of the probability bound for "marginal" acquisitions. In such cases the number returned by the algorithm is often considerably less than the actual probability of being correct. Thus it becomes necessary to experimentally determine a threshold setting for the signal-to-noise ratios of interest. When an error was actually made in the simulation on any but the last component, the algorithm reacted very strongly by returning values almost always below 0.01 and typically less than  $10^{-5}$ .

Overall, the average figure of merit for the 20,000 trials was 0.991. It is assumed that an average over the true posterior probabilities would converge to the prior correctness probability, 0.998.

## V. Conclusion

It should be possible to reduce the integration time for receiving the lower frequency components if this algorithm is used to determine a figure of merit for each acquisition. Such a reduction may be of importance for very long distance ranging when signal power is low and integration times are correspondingly long.

Also, during superior solar conjunction, a ranging acquisition should be performed in as short a time as possible to reduce the change of bursts of noise interfering strongly with the signal. Ranging via several short acquisitions has been seen to be effective in such highly dynamic noise situations (Ref. 4). It is expected that the posterior error probability bound would be a very useful figure of merit given the resulting low signal-to-noise ratios.

## References

1. Martin, W. L., and Zygielbaum, A. I., *Mu-II Ranging*, Technical Memorandum, 33-768, Jet Propulsion Laboratory, Pasadena, Calif., May 15, 1977.
2. Goldstein, R. M., "Ranging With Sequential Components," in *Space Programs Summary*, 37-52, Vol. II, pp. 46-49, Jet Propulsion Laboratory, Pasadena, Calif., July 31, 1968.
3. Timor, U., *Sequential Ranging with the Viterbi Algorithm*, JPL Technical Report 32-1526, Vol. II, pp. 75-79, Jet Propulsion Laboratory, Pasadena, Calif., April 15, 1971.
4. Zygielbaum, A. I., "Near Sun Ranging," in *The Deep Space Network Progress Report* 42-41, pp. 43-50, Jet Propulsion Laboratory, Pasadena, Calif., October 15, 1977.

**Table 1. Performance of the figure of merit algorithm for various threshold settings**

Threshold	Errors detected	Errors not detected	False error indications
0.99	39	0	579
0.9	38	1	236
0.8	38	1	183
0.7	37	2	140
0.6	36	3	113
0.5	35	4	91
0.4	35	4	79
0.3	35	4	68
0.2	35	4	53
0.1	35	4	37
0.01	34	5	16

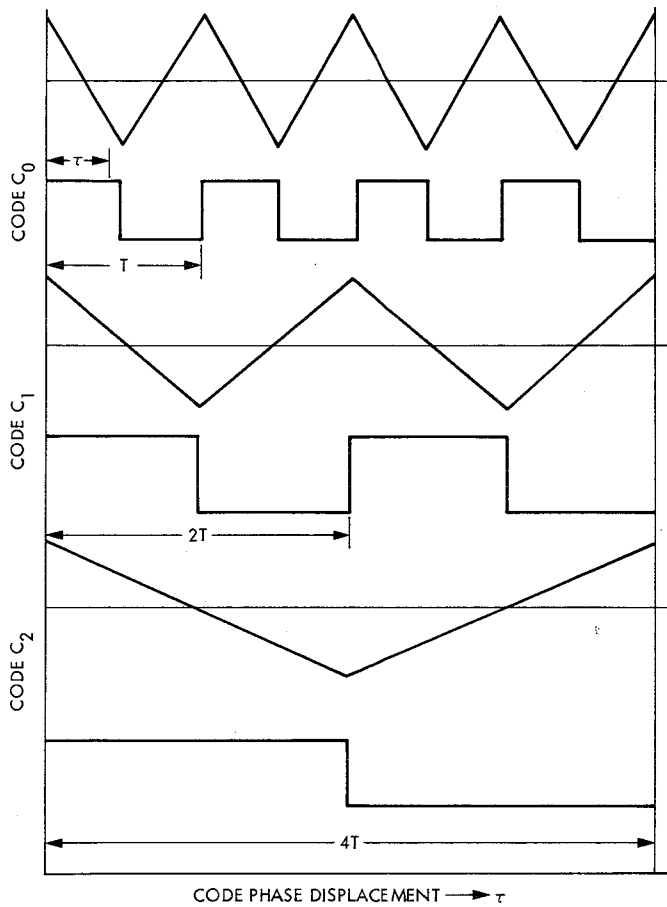


Fig. 1. Transmitted codes with respective correlation functions. The measured phase of the highest frequency component is  $\tau$

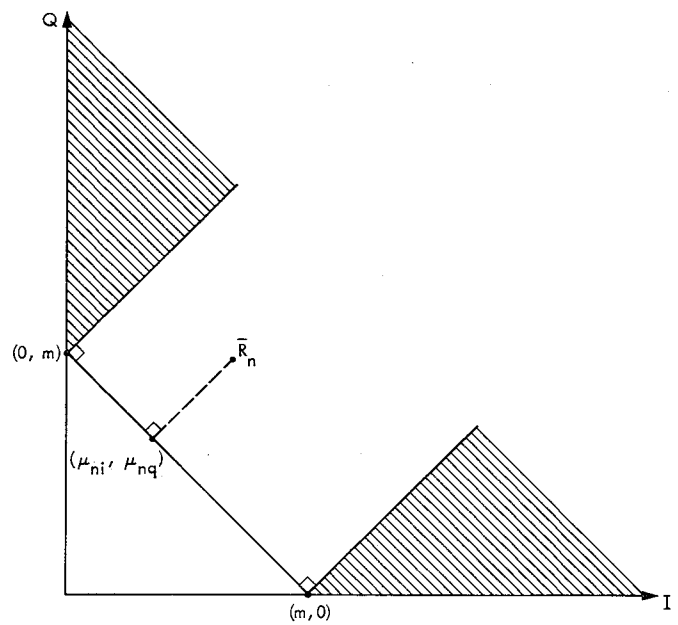


Fig. 2. Determining the nearest possible mean to the received vector  $\bar{R}_n$

# Frequency Standard Test Facility Data Acquisition and Processing System

L. J. Knapp

Communications Systems Research Section

*The Interim Frequency Standards Test Facility tests all frequency standards used in the Deep Space Network. It is also the central testing facility for testing all ultrastable hydrogen maser frequency standards. This proposed data acquisition/processing system was designed to support the IFSTF, by acquiring and processing the large amounts of data generated there.*

## I. Introduction

With the increased testing of frequency standards at the Interim Frequency Standards Test Facility (IFSTF), a need has been demonstrated to automate the data acquisition and reduction for the numerous tests that are performed. This article describes the proposed Data Acquisition and Processing System designed for this effort.

## II. Proposed System

In the proposed system (Fig. 1), analog and digital test data are read by the Hewlett-Packard 9835B controller at user-defined time intervals (i.e., 1, 10, 60 sec). The raw data are then time-tagged (a time code from the TRAK clock) and stored on external memory (disk) for later reduction/processing and/or archival storage.

The data reduction and processing is performed by a Hewlett-Packard 9845B desk-top computer. The acquisition of

the raw data from the disk is time-shared via the HP-9835B controller. Data reduction and/or processing can be accomplished immediately or on request from the user. The output generated can be lists, graphs, and/or plots of one channel or a combination of many.

The proposed system has been divided into seven phases (Figs. 2-8). After each phase has been completed and tested, it will be installed at the IFSTF for further evaluation.

## III. Conclusion

Presently, retrieving statistical and historical data has been limited by manpower, channel monitoring capabilities, and time. This proposed system has the capability of monitoring up to 6 units (frequency standard, oscillator, synthesizer) with a total of 300 channels in real-time. This will greatly increase the statistical and historical data needed for analysis.

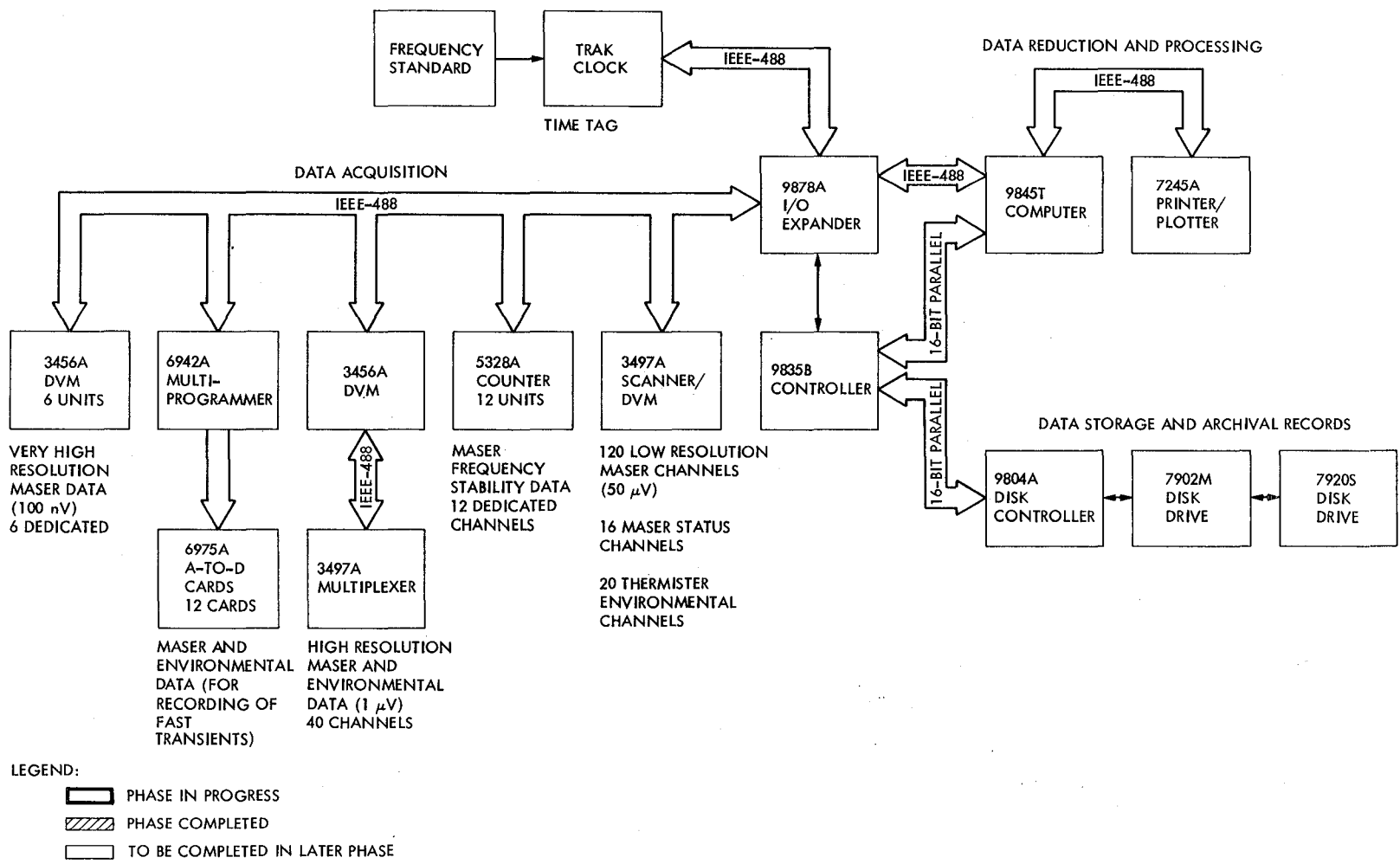
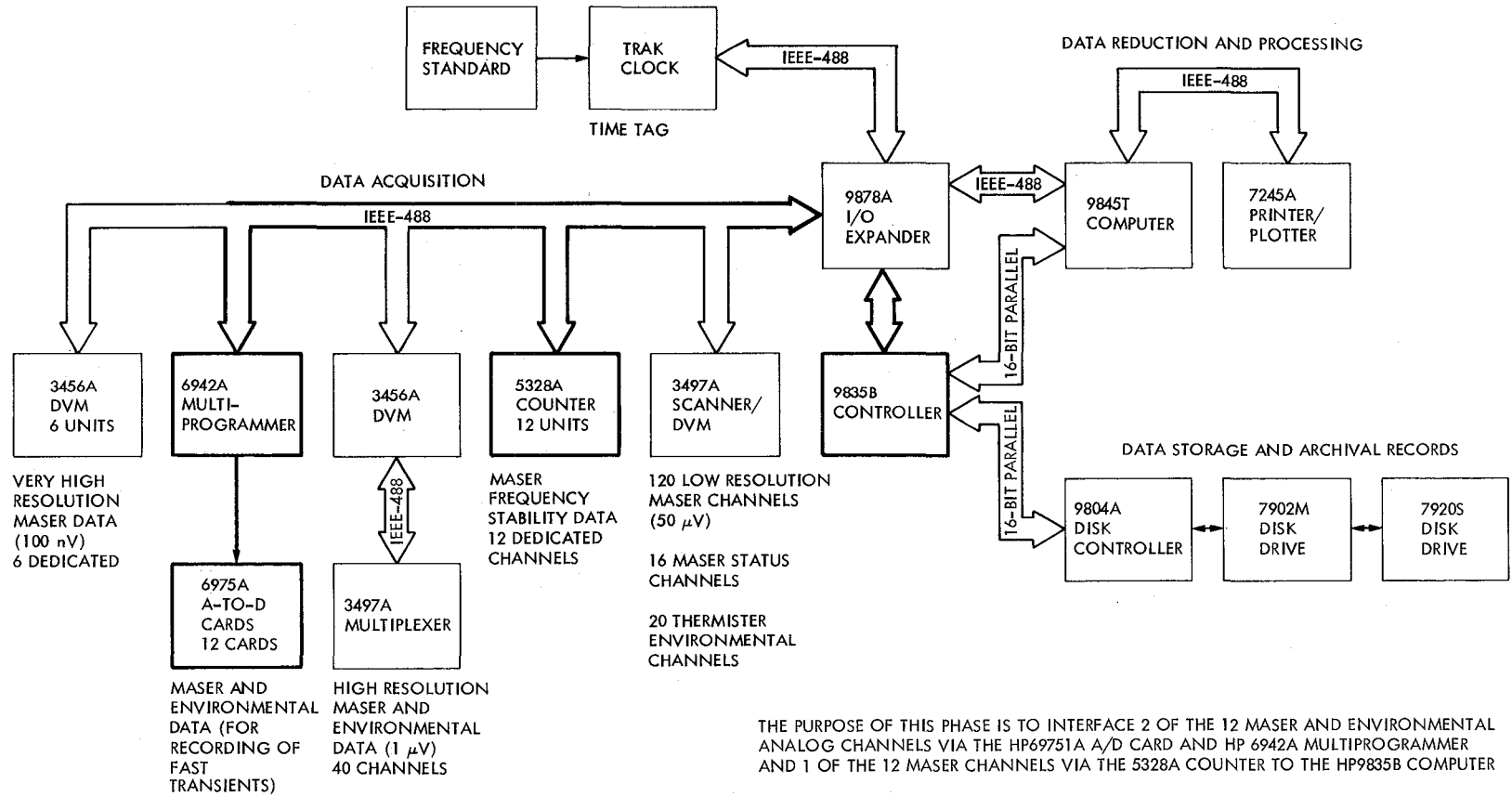


Fig. 1. Overall data acquisition system



LEGEND:

- PHASE IN PROGRESS
- PHASE COMPLETED
- TO BE COMPLETED IN LATER PHASE

THE PURPOSE OF THIS PHASE IS TO INTERFACE 2 OF THE 12 MASER AND ENVIRONMENTAL ANALOG CHANNELS VIA THE HP69751A A/D CARD AND HP 6942A MULTIPROGRAMMER AND 1 OF THE 12 MASER CHANNELS VIA THE 5328A COUNTER TO THE HP9835B COMPUTER

Fig. 2. Data acquisition system, phase 1

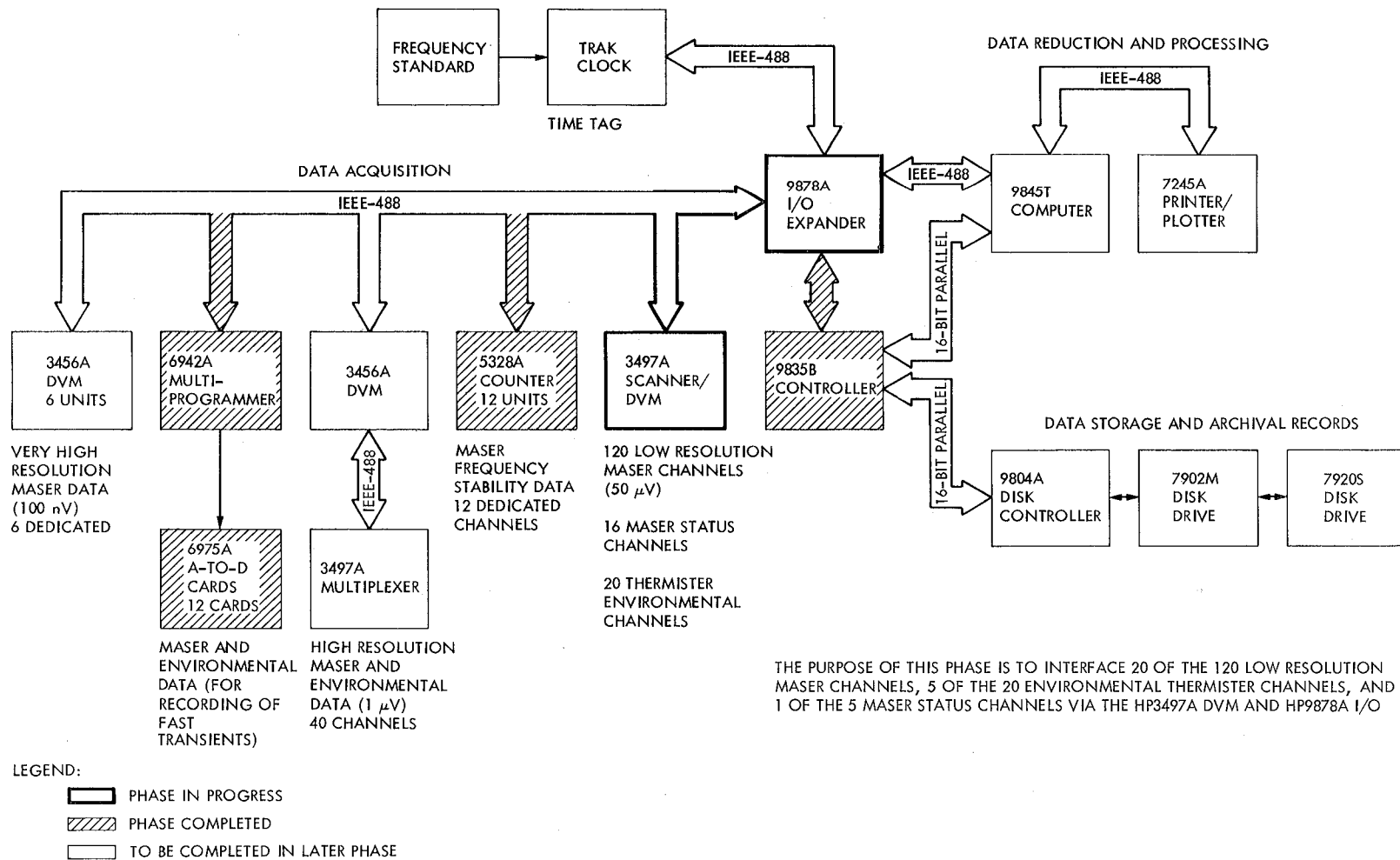


Fig. 3. Data acquisition system, phase 2

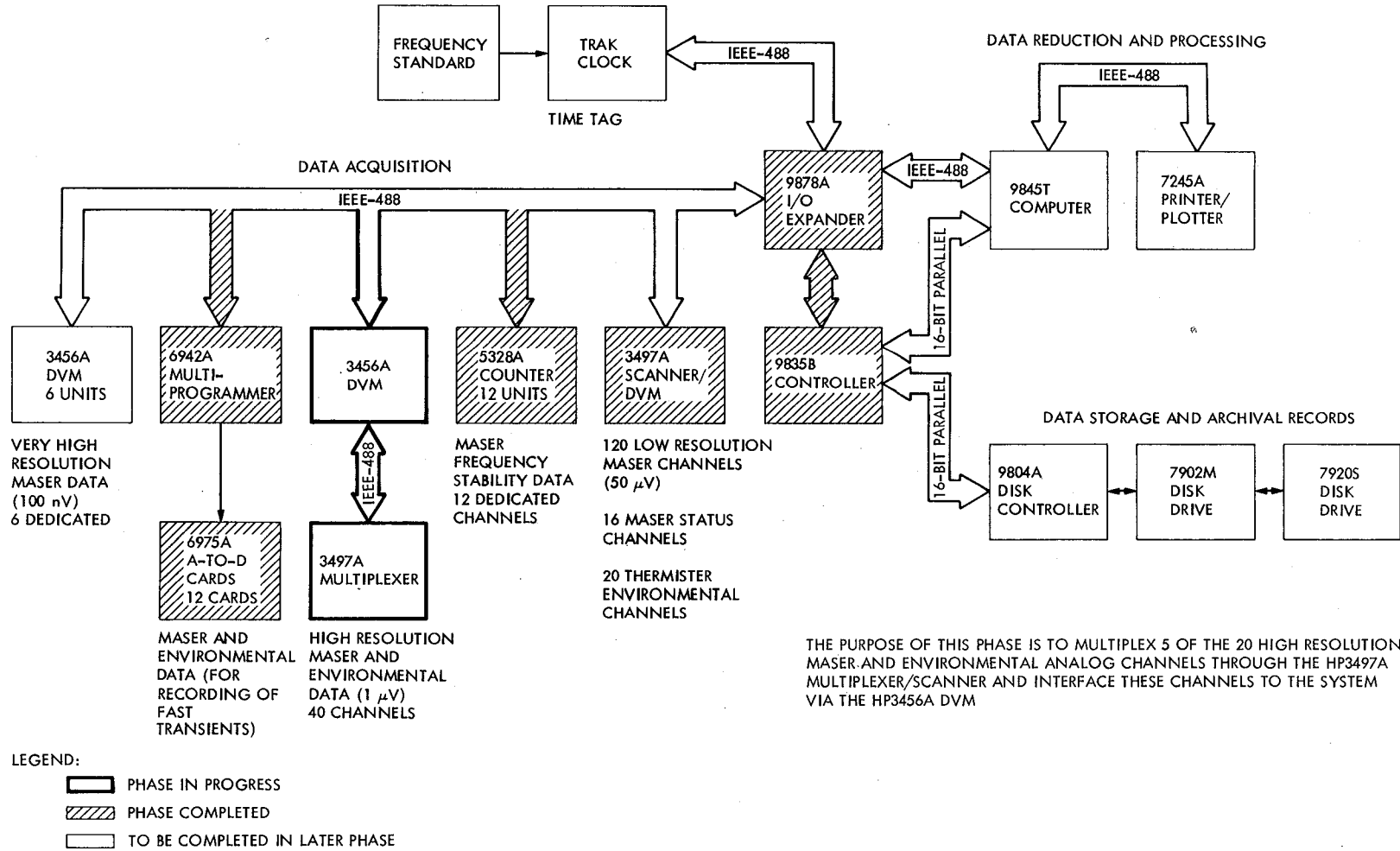


Fig. 4. Data acquisition system, phase 3

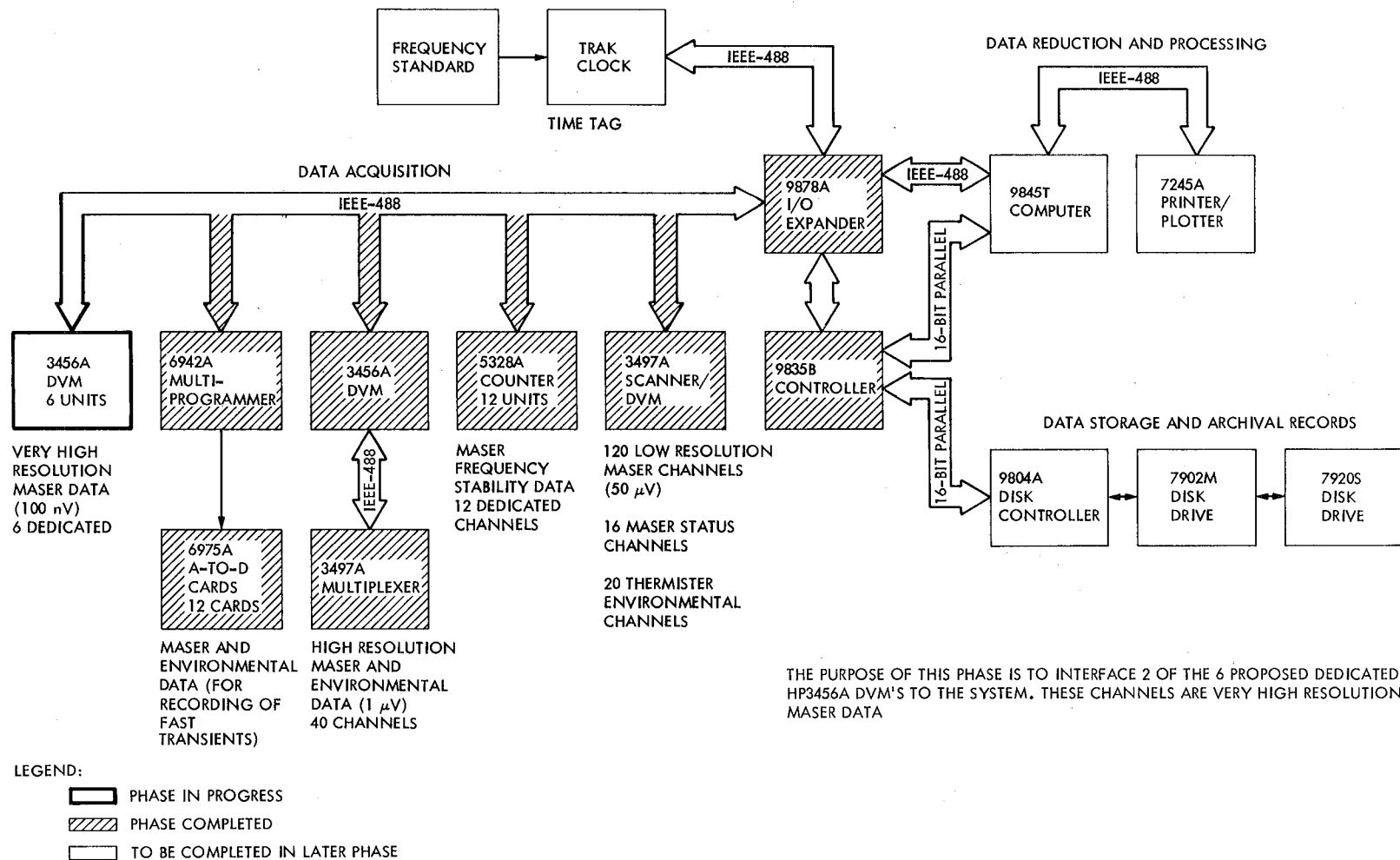


Fig. 5. Data acquisition system, phase 4

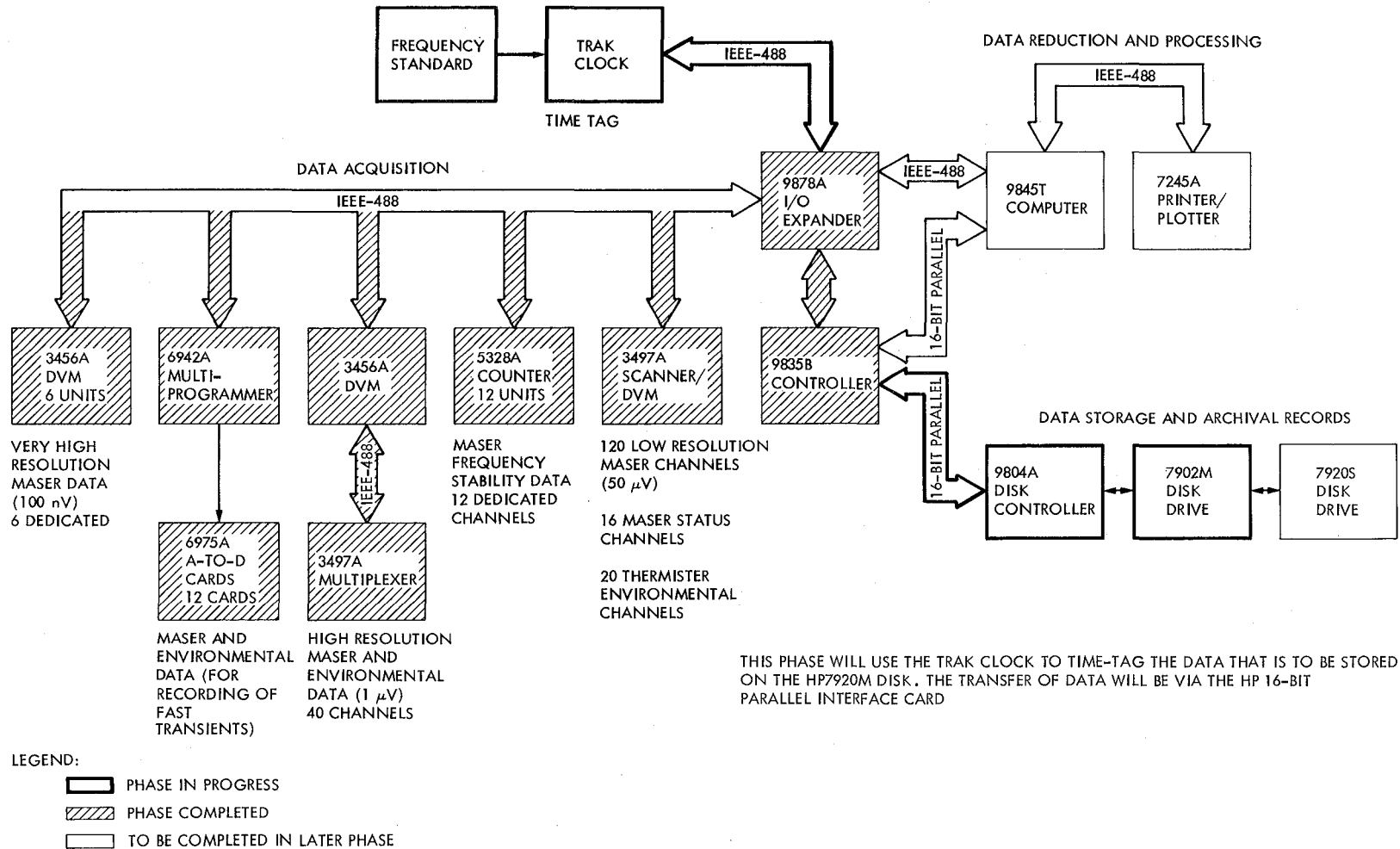
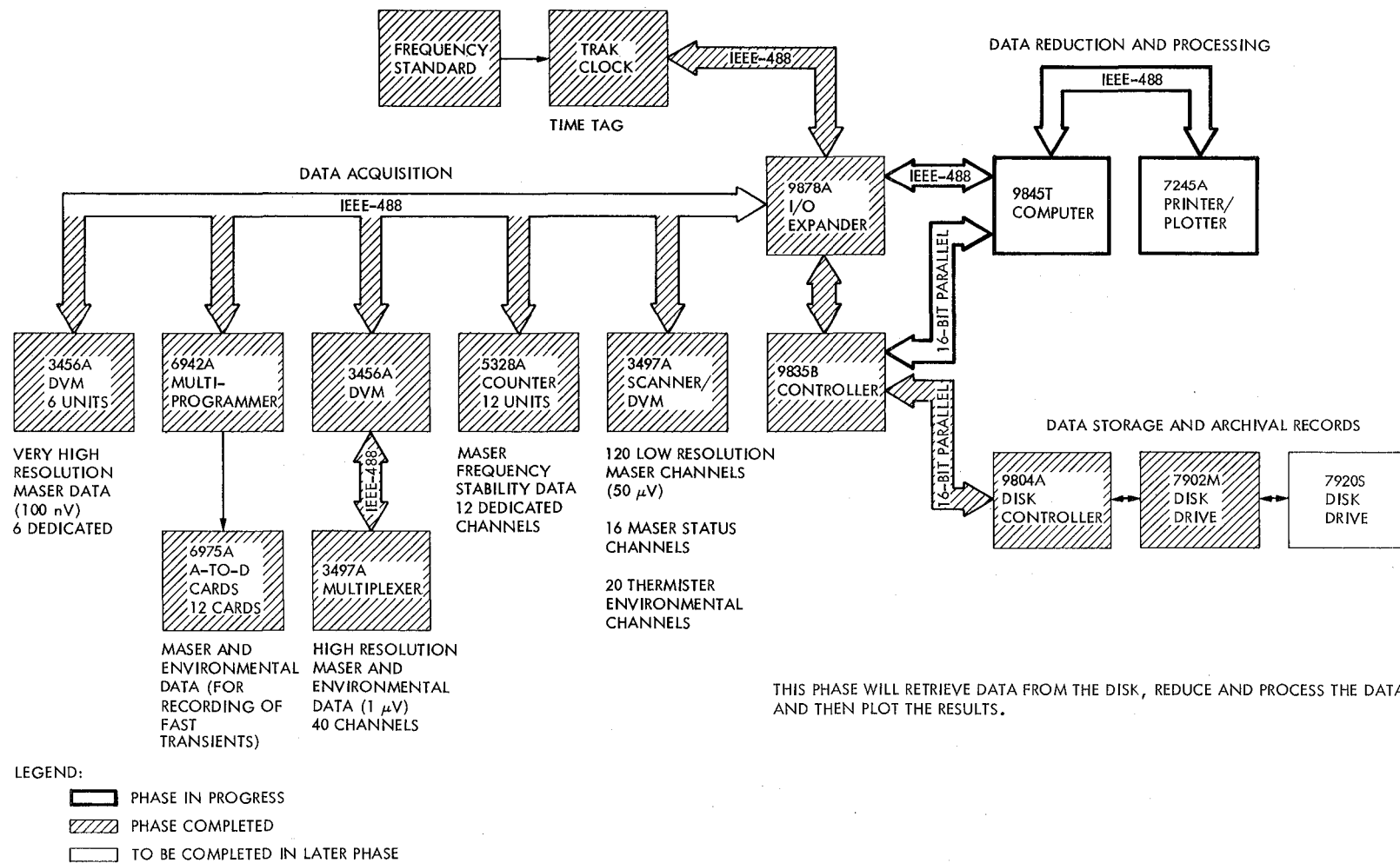


Fig. 6. Data acquisition system, phase 5



THIS PHASE WILL RETRIEVE DATA FROM THE DISK, REDUCE AND PROCESS THE DATA, AND THEN PLOT THE RESULTS.

Fig. 7. Data acquisition system, phase 6

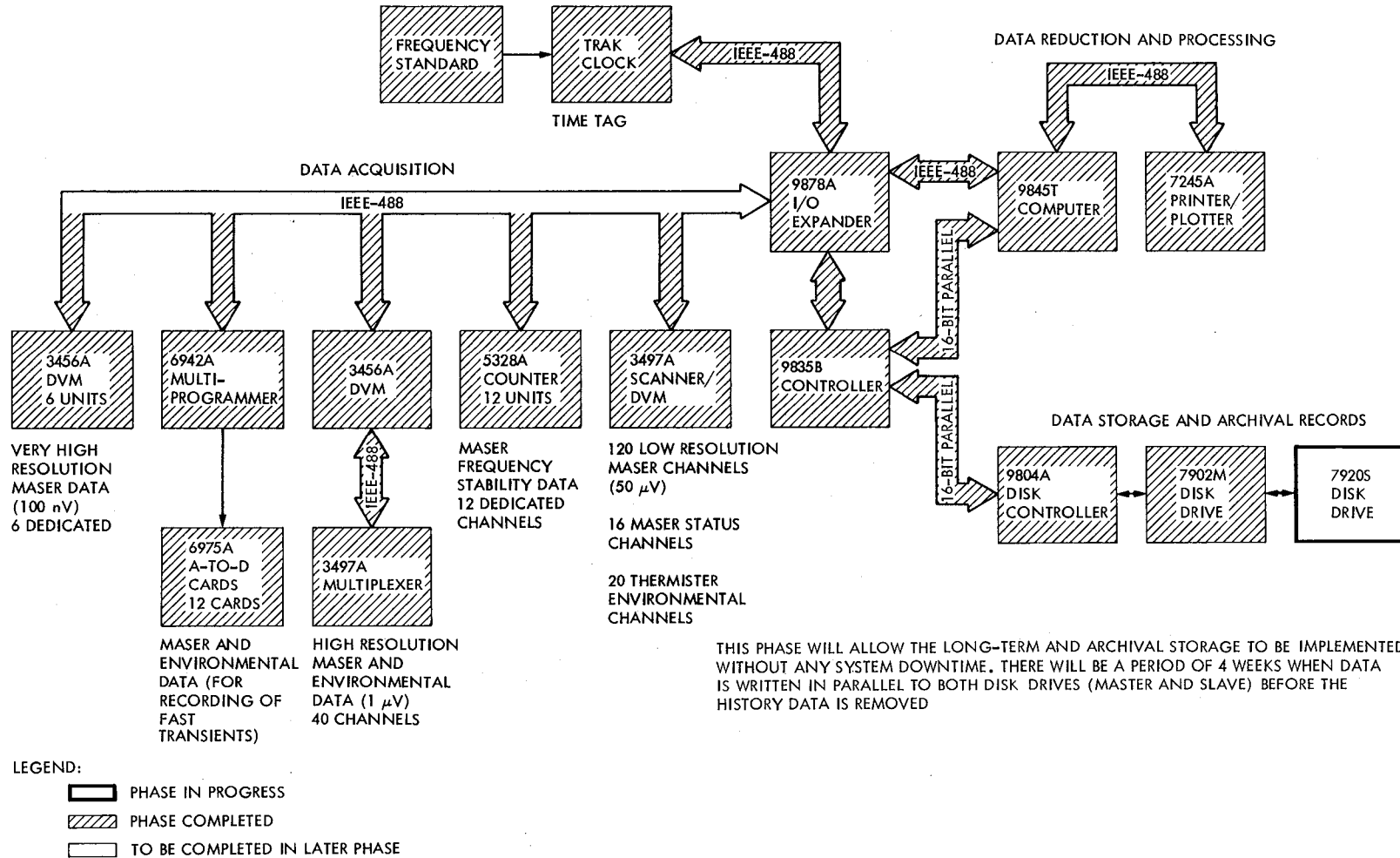


Fig. 8. Data acquisition system, phase 7

# A Four-Way Distribution Amplifier for Reference Signal Distribution

Y. V. Lo

Communications Systems Research Section

*This article presents the design and construction of a four-way distribution amplifier. It has 100 dB isolation between any two output ports, and it will be used to distribute multiple reference signals.*

## I. Introduction

A four-way distribution amplifier with up to 100 dB isolation and with low phase noise of  $-140$  dBc in a 1 Hz bandwidth 10 Hz from a 100 MHz signal has been developed. It will be used in the stabilized optical fiber distribution system (Ref. 1) to provide multiple outputs.

This article describes the design and overall construction of the amplifier. Optimizing techniques and performance are discussed.

## II. Description

As shown in the block diagram (Fig. 1), the distribution amplifier consists of five isolation amplifiers (Ref. 2), one power amplifier, a matching network and one four-way power splitter. The matching network is used to maximize isolation.

The isolation amplifier (Fig. 2) is an in-house design. It contains a complementary common emitter stage followed by a complementary emitter follower. This combination provides maximum output to input isolation for a two-stage amplifier, and better efficiency than can be obtained with a single-ended

design. Input and output ports of the isolation amplifier are capacitively coupled, and the impedances are adjusted to  $50 \Omega$ .

The power stage is a commercial wideband amplifier with output power up to 22 dBm. It has a gain of 10 dB. Input and output VSWR are typically better than 1.5:1. DC power consumption is about 1.32 watts.

The power splitter is also a commercial unit chosen to achieve the maximum isolation between different output ports. It has a bandwidth of 200 MHz.

## III. Isolation

Maximum isolation between output to output and output to input ports of any power splitter can be achieved by providing the optimum impedance at the input port. With the four-way power splitter connected as shown in the block diagram (Fig. 1), tests have demonstrated that 100 dB isolation is obtainable between either the opposite or the adjacent output ports, but not both simultaneously.

In order to obtain 100 dB isolation between all four output ports, a four-way power splitter can be made out of three

two-way power splitters, and then an optimum input match can be provided for each of them. A single four-way power splitter was used in the prototype amplifier and the output to output isolation was compromised by adjusting the input impedance of the power splitter until the same isolation is obtained between all output ports. The isolation is thus reduced to -92 dB, and this method requires fewer components than the use of three two-way splitters.

The particular power amplifier used was chosen for its low VSWR and small reactance at its output port. Consequently, a low Q matching-circuit (Fig. 3) can be constructed which will transform the power amplifier output impedance to the optimum input impedance of the power splitter.

In order to determine the optimum matching impedance for best isolation, a tunable matching network was designed to match a 50  $\Omega$  source to a range of load impedances. This matching network was applied between the four-way power splitter and the power amplifier. The tuning elements were adjusted for best isolation over a small bandwidth at the desired frequency. In order to get a wideband isolation characteristic, a low Q circuit was substituted for the tunable matching network.

## IV. Tests

Tests to determine isolation, gain, VSWR, phase noise and maximum power output have been conducted on the amplifier. The results of these tests are shown in Figs. 4 through 9.

The distribution amplifier has an isolation of 92 dB between any two output ports. It has an isolation of 132 dB from any one output port back to the input. A 3 dB gain is obtained over a bandwidth of 250 MHz. The input and output VSWRs are optimized at 100 MHz. Power spectral density of phase noise (Ref. 3) is -140 dBc in a 1-Hz bandwidth, 10 Hz from a 100 MHz signal. Power output at 5% harmonic distortion is 14 dBm. The total dc power consumption is 4 watts.

## V. Conclusion

The distribution amplifier described has excellent isolation, low phase noise, low VSWR, wide bandwidth, and good efficiency. It is well-suited to distribute ultra-stable reference frequencies to multiple users. The techniques described may be useful in other applications requiring high isolation, wide bandwidth and low phase noise.

## References

1. Lutes, G., "Optical Fibers for the Distribution of Frequency and Timing References," in *Proceedings of the Twelfth Annual Precise Time and Time Interval Applications and Planning Meeting*, a meeting held at the Goddard Space Flight Center, Greenbelt, Maryland, December 2-4, 1980.
2. Lutes, G., "Frequency Generation and Control: Distribution Amplifiers for the Hydrogen Maser Frequency Standard," in *The Deep Space Network, Space Programs Summary 37-61*, Vol. II, pp. 68-72, Jet Propulsion Laboratory, Pasadena, California, January 31, 1970.
3. Meyer, R., and Sward, A., "Frequency Generation and Control: The Measurement of Phase Jitter," in *The Deep Space Network, Space Programs Summary 37-64*, Vol. II, pp. 55-58, Jet Propulsion Laboratory, Pasadena, California, August 31, 1970.



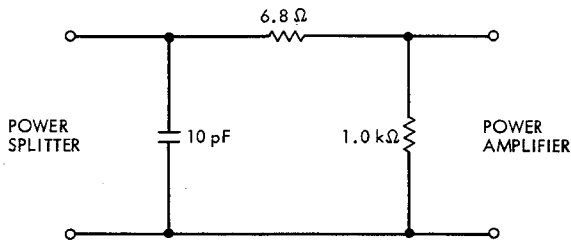


Fig. 3. Matching network

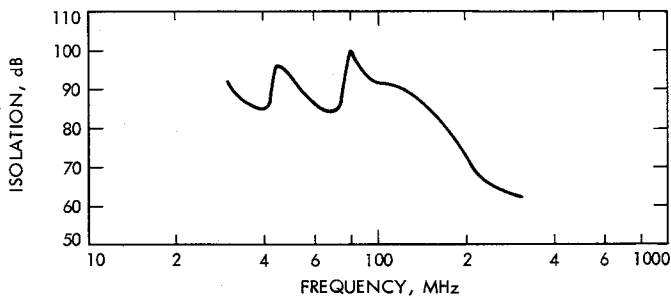


Fig. 4. Typical isolation characteristic of the distribution amplifier (between any two output ports)

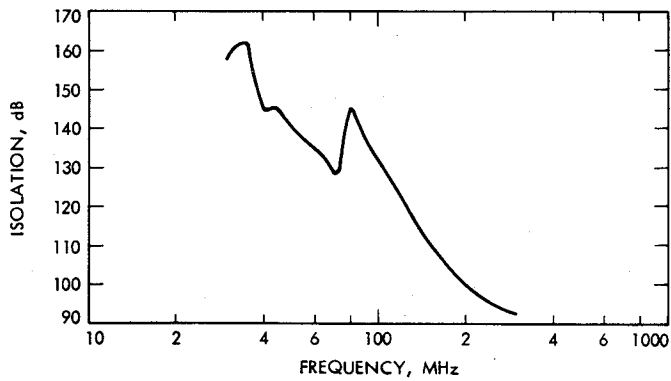


Fig. 5. Typical isolation characteristic of the distribution amplifier (from any one output port to input)

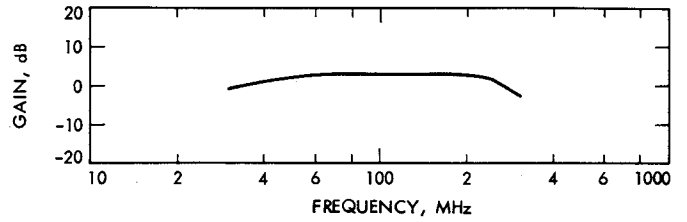


Fig. 6. Gain characteristic for the distribution amplifier

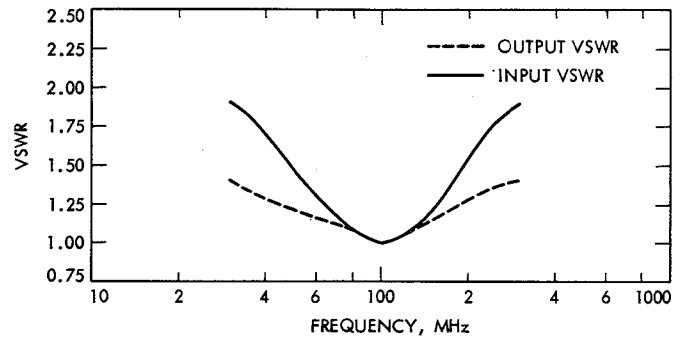


Fig. 7. Input and output VSWR of the distribution amplifier

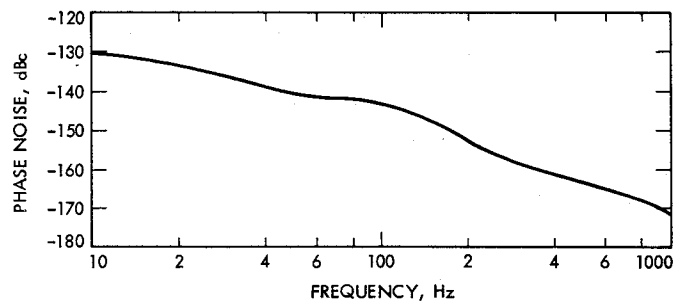


Fig. 8. Power spectral density of phase noise vs frequency of the distribution amplifier (single side band)

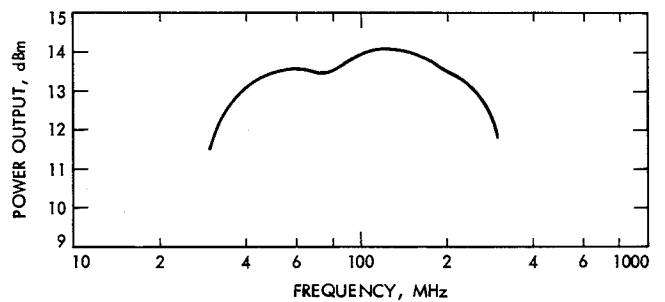


Fig. 9. Power output corresponding to 5% harmonic distortion for the distribution amplifier

# Station Stability Measurement

E. N. Sosa

Radio Frequency and Microwave Subsystems Section

*Methods and instrumentation are being developed to determine the frequency stability of Deep Space Stations. The efforts are presently focused on the verification of the stability of the X-band uplink and other RF and microwave subsystems which contribute to the overall stability of the system. The measurement methodology is presented as well as frequency stability data generated with the development measurement system. The system characteristics are highlighted and the potential areas where improvements could be made are discussed.*

## I. Introduction

The measurement of frequency stability has been of concern in the DSN since the implementation of the hydrogen masers. Highly stable reference signals derived from the hydrogen maser degrade as these are distributed and processed throughout the station. In addition, requirements for greater tracking accuracies and space-charged particle calibrations have given impetus to the development of an X-band uplink with much-improved short- and long-term frequency stabilities that need to be verified in the station. A method, described below, is being developed to determine the overall stability of a Deep Space Station (DSS) by measuring the contributions of key elements of the RF and microwave subsystems. Previously, it was not possible to make these measurements on the station site, and components could be measured only by special laboratory techniques. The new method described below is presently being used for measuring the frequency stability of a Block III receiver in Compatibility Test Area (CTA) 21. After completion of the tests at CTA 21, the stability measurement equipment will be transported to Goldstone for measurements at DSS 13, which will have the X-band uplink capability. The

outcome of these measurements at DSS 13 will be the demonstrated frequency stability of the overall system as a function of operating modes and conditions.

The approach for measuring frequency stability at the station utilizes recently developed commercial instrumentation in conjunction with specially built frequency translators to interface the key RF and microwave assemblies in the DSS with the measurement equipment. This approach was selected after an investigation of the state of the art in the measurement of frequency stability. The commercial instrumentation chosen as the initial development tool was the Hewlett-Packard Frequency Stability Analyzer, Model HP5390A. The basis for the selection was performance, availability, and portability. It was necessary, however, to experimentally assess the HP5390A system capabilities with respect to ultrastable sources such as the hydrogen masers. Evaluation test results obtained at JPL's Interim Frequency Standards Test Facility (IFSTF) are presented below after a discussion of the measurement methodology. Finally, the initial frequency stability data obtained at CTA 21 on Block III receiver are presented.

## II. Measurement Methodology

Stability (or instability) refers to the degree to which a signal departs from a nominal value over a designated time interval. The generally accepted method of determining frequency stability in the time domain is by the two-sample deviation (or the square root of the Allan Variance). The theory and justification for the two-sample deviation is well-understood (Ref. 1), and it is sufficient here to state only the working equation. The two-sample fractional frequency deviation,  $\sigma_{\Delta f/f}(N, \tau)$ , is given by

$$\sigma_{\Delta f/f}(N, \tau) = \frac{1}{2N} \sqrt{\sum_{i=1}^N \left( \frac{\Delta f_{i+1}}{f_o} - \frac{\Delta f_i}{f_o} \right)^2} \quad (1)$$

in which  $\tau$  is the time interval over which the RMS deviation of the signal from the carrier is measured,  $N$  is the number of samples to be averaged,  $f_o$  is the nominal frequency,  $\Delta f_{i+1}$  and  $\Delta f_i$  denote the two contiguous samples of frequency deviation averaged over the time period,  $\tau$ . To get meaningful stability data with the above working expression one requires a sufficiently large number of statistical samples, typically 100 samples for values of  $\tau < 10$  seconds and 25 samples for values of  $\tau \sim 10^3$  seconds. The large number of samples and long averaging times imply that the measured deviation includes the effects of noise, spurious signals, and short-term drifts. These effects become important considerations with respect to the measurement equipment. The components of the measurement system have been selected for their high stability, thereby minimizing noise and spurious signals. However, because there are some temperature-sensitive components that may affect the measurements, especially in a field environment, the use of temperature-stabilized ovens to control these components has been considered to eliminate temperature-related drifts. The measurement equipment components are described in the paragraphs below.

The standard method of measuring the frequency stability of a signal in the time domain is illustrated in Fig. 1. The beat frequency,  $f_b$ , is filtered, amplified, and measured with a period counter over an interval of time,  $\tau$ . The commercially available Hewlett-Packard System (HP5390A) uses a similar method, and comprises five major components: a mixer/amplifier unit, a high-resolution reciprocal counter, a measurement storage plug-on unit, a desk-top calculator, and a printer/plotter output device. Communication and control between the various instruments is provided by a digital interface bus. A block diagram of the HP5390A system is shown in Fig. 2. The measurement process is controlled via software supplied with the system. The key features of the HP5390A system are that it is compact, portable, and that it uses the

generally accepted algorithm for calculating fractional-frequency deviation.

The technique developed for making the stability measurements at any DSS utilizes the HP5390A in conjunction with a synthesizer and a frequency translator to provide stable offsettable signals. The block diagram illustrating this method is shown in Fig. 3. The salient feature of this technique is that a large number of signals with different frequencies can be measured without requiring different reference oscillators. For example, at the DSS 13 receiver, the anticipated number of points to be measured is twelve. Each of these points has a different frequency over the range 10 kHz to 8400 MHz. The synthesizer depicted in Fig. 3 covers a narrow frequency range (10 kHz-1200 MHz), and frequency translators especially designed for the frequencies of interest are used to provide the frequencies above 1200 MHz. The use of the synthesizer and the frequency translators allows the overall system to be independent and totally portable.

The key set of measurements at DSS 13 will be performed on the exciter which is being developed for the X-band uplink. This exciter will have greater phase stability (Ref. 2) than its predecessors and will require the measurement system to have a fractional-frequency deviation noise floor lower than  $1 \times 10^{-15}$  for sampling times of 1000 seconds. This noise floor level is the most difficult requirement that must be met by the measurement system.

In order to make meaningful measurements and to determine that a noise floor  $< 1 \times 10^{-15}$  can be achieved, it is necessary to fully characterize the HP5390A system along with the synthesizer and frequency translators, so that measurement errors will not be introduced inadvertently by any component. To this extent, efforts have been made to characterize synthesizers and translator components with respect to frequency instabilities. In addition, the HP5390A system and synthesizers have been tested at JPL's Interim Frequency Standard Test Facility against the equipment used for measuring the stability of hydrogen masers. The following section describes the tests performed and the results obtained.

## III. Experimental Results

To ascertain the capabilities of this initial development system, use was made of JPL's Interim Frequency Standard Test Facility (IFSTF), which is equipped to make two-sample  $\Delta f/f$  deviation measurements. Hydrogen masers with well-known stability characteristics were used as the reference oscillators. A series of tests was made, and data measured with the HP5390A system were directly compared with those measured with the IFSTF equipment that provided the standard.

The most stringent test that the HP5390A was subjected to was the measurement of two hydrogen masers. One of these masers (DSN2) was used as the reference oscillator, and the other one (DSN3) was used as the test oscillator. The test setup used is that shown in Fig. 2. The objective of this test was to obtain the measurement capability of the HP5390A when operating with very stable inputs and at its limit with respect to the smallest allowable offset frequency (1 Hz). A 1-Hz frequency offset was the largest frequency difference that could be obtained between two hydrogen masers. In addition, the measurement bandwidth of the IFSTF equipment is fixed at 1 Hz, and measurements with larger frequency offsets cannot be easily made. To make the HP5390A system comparable with the IFSTF equipment, a 1-Hz low-pass filter was externally connected to the mixer/amplifier module of the HP5390A. The measurements were taken simultaneously and the results are shown in Fig. 4 where the two-sample deviation is plotted as a function of  $\tau$ , the sampling time interval.

It is evident from the plots that a significant discrepancy exists at all values of  $\tau$  to 1000 seconds. The data shown in Fig. 4 are somewhat typical in that all the  $\Delta f/f$  deviations measured with HP5390A system were usually 25 to 50 percent higher than the deviations measured with the IFSTF equipment. For example, a simultaneous test was performed with the two measurement systems on a cesium maser. The DSN3 hydrogen maser was used as the reference oscillator. In this particular application, the measurement was made at least two orders of magnitude above the noise floor of the HP5390A and data discrepancies between the two systems were not expected. The results of this test are shown in Fig. 5. In this case also a discrepancy between the two systems is noted, and it is about 25 percent.

A systematic discrepancy of the type exhibited by the aforementioned tests is acceptable providing all possible uses of the equipment are known, and providing the system is calibrated for each particular use. Another proviso is that the cause for the discrepancy must be known in order to ascertain whether it truly is systematic. An experiment that sheds light on this subject was performed and points to future improvements to the HP5390A system.

The experiment performed was essentially a repeat of the first test described above. In other words, the setup shown in Fig. 4 was used except that the mixer/amplifier of the HP5390A was disconnected, and instead the mixer/amplifier of the IFSTF equipment was used. The results of this stability test are shown in Fig. 6. In this case, the systematic measurement discrepancy was eliminated and the IFSTF data points are within the repeatability of the HP5390A system. Error bars are shown on the data points taken with the HP5390A system

“as is” to show that the new data is beyond the measurement error.

The above test data point to the HP5390A's mixer/amplifier unit as being noisier and/or wider in bandwidth than the IFSTF's mixer/amplifier. This aspect will be investigated as soon as possible because the outcome will quickly transform the measurement system from a developmental stage to a field-ready system capable of standard test-laboratory accuracies.

Other tests performed at the Interim Frequency Standard Test Facility were to characterize the stability of various synthesizers to determine their noise floor. Comparative data are shown in Fig. 7, which depicts the frequency stability of three Dana synthesizers and one from Hewlett-Packard (Model 8662A). These plots exhibit only the contribution of the synthesizers since these are data measured with the IFSTF test equipment. The lower noise floor generally exhibited by the HP8662A makes this synthesizer the indicated one for use in the station stability measurement systems, except for measurements of the X-band uplink. The noise floor of the HP8662A synthesizer is higher ( $4 \times 10^{-15}$ ) than the requirement for the X-band uplink exciter. For the X-band uplink measurements the synthesizer will be deleted, and only frequency translators (multipliers) will be used. In practice, by proper selection, phase-locked multipliers exhibit greater frequency stability than the hydrogen maser. Thus, the noise floor expected for the X-band uplink measurements is essentially that shown in Fig. 4 for the HP5390A. In addition, significant margin can be obtained by improving the mixer/amplifier unit.

After the selection of the HP8662A synthesizer for use in conjunction with the HP5390A Frequency Stability Analyzer for the less stringent requirements, the two were tested as a system. This test would confirm the method shown in Fig. 3 and also establish its noise floor. This is particularly true because the frequency translators will have a significantly lower noise floor than that of the synthesizer. The signal source selected for this test was that from the hydrogen maser, DSN2. The test setup for this measurement along with the test results are shown in Fig. 8. The discrepancies between the two sets of data are attributed partly to the fact that the tests cannot be absolutely simultaneously conducted and partly due to the repeatability of both systems.

To affirm the notion of portability and on-site measurements, fractional-frequency deviation tests have been performed at CTA 21 using the method shown in Fig. 3. These are only initial measurements but they lend credence to the correctness of the application. As the specially designed frequency translators are built and tested, more test points will be measured until DSS 13 is fully characterized. The key test

points of the Block III receiver and X-band uplink exciter are delineated in Table 1. In the table, the expected two-sample, fractional-frequency deviations are also given, as well as the noise floor expected from the frequency translators. The initial experimental data acquired at CTA 21 on a Block III receiver are presented in the table. The estimated value of  $1 \times 10^{-13}$  for  $\tau = 1000$  seconds is an extrapolation from the measured data. New table entries of measured stability will be made as the different points in the receiver and exciter are measured. It is important to stress that the preceding efforts and those to take place at CTA 21 are preparatory to the actual measurements to be taken at DSS 13. However, the above experiments and the data generated from them give sufficient confidence that meaningful measurements of frequency stability can be made on the DSS 13.

#### IV. Conclusion

The investigation to determine the frequency stability of a Deep Space Station has led to a method for making stability measurements at the station site. The method will measure the fractional-frequency deviations of the key components of the

RF and microwave subsystems. The goal is to identify the assemblies or subsystems that must be improved to obtain balanced system performance consistent with the X-band uplink stability and that of the hydrogen maser frequency standard.

The method utilizes a synthesizer and specially built frequency translators in conjunction with the HP5390A Frequency Stability Analyzer. Calibration tests have been performed on the HP5390A system and HP8662A synthesizer, and the results indicate that the system is capable of measuring the frequency stabilities expected in the Block III receiver and exciter subsystems. The frequency stability measurement system as delineated above is currently in use, testing a Block III receiver in CTA 21. The stability measurements at DSS 13 will be performed when the special frequency translators are built and tested. With respect to improved performance of the measurement system, it has been determined that by improving the mixer/amplifier unit, the present system can make a leap from its present developmental stage to a field-ready system capable of standard test-laboratory accuracies. The exploitation of this measurement capability will aid in improving DSN capability.

### Acknowledgment

The author would like to acknowledge and thank Richard L. Sydnor, Supervisor, Time and Frequency Systems Research, for the support given to this project. A special note of thanks is extended to Al Kirk for his assistance and excellent suggestions. The initial work on the Station Stability Measurement project was done by Rudy Lay.

### References

1. Rutman, J., "Characterization of Phase and Frequency Instabilities in Precision Frequency Sources: Fifteen Years of Progress," *Proc. IEEE*, Vol. 66, pp. 1048-1075, Sept. 1978.
2. Hartop, R., Johns, C., and Kolbly, R., "X-Band Uplink Ground Systems Development," *DSN Progress Report 42-56*, pp. 48-58, Jet Propulsion Laboratory, Pasadena, Calif., Feb. 1980.

**Table 1. Block III Receiver/Exciter Measurement Points**

DSS 13 CTA 21	Blk III/rcvr/exciter assemblies	Estimated $\Delta f/f$ deviation for $\tau = 1000$ sec	Measured $\Delta f/f$ deviation
10 MHz	Rcvr output	} $\sim 2.0 \times 10^{-13}$	$1.02 \times 10^{-10}$ for $\tau = 1$ sec
10 MHz	Rcvr output (after mix)		$2.43 \times 10^{-11}$ for $\tau = 4$ sec
			$9.50 \times 10^{-12}$ for $\tau = 10$ sec
			$2.44 \times 10^{-12}$ for $\tau = 40$ sec
			$9.11 \times 10^{-13}$ for $\tau = 100$ sec
			$2.89 \times 10^{-13}$ for $\tau = 400$ sec
			(Estimate $1.0 \times 10^{-13}$ for $\tau = 1000$ sec)
50 MHz	Rcvr front-end output		$1.43 \times 10^{-14}$ for $\tau = 1000$ sec for 50 MHz
69 MHz	Rcvr RF loop		
66 MHz	S-band xltr in	$\geq 8.0 \times 10^{-14}$	
2105 MHz	S-band xltr	$\geq 8.0 \times 10^{-14}$	
	S-band xmtr		
2295 MHz	S-band xltr test sig	} $\sim 1.2 \times 10^{-13}$	
2295 MHz	S-band maser output		
2245 MHz	S-band lo	$\sim 1.0 \times 10^{-13}$	
7200 MHz	X-band uplink exciter output	$2.0 \times 10^{-15}$	
8400 MHz	X-X exc test sig	} $4.0 \times 10^{-15}$	
	X-X doppler ref		
2300 MHz	X-S exc test sig		
	X-S doppler ref		

Note: Expected  $\Delta f/f$  deviation for receiver translators is  $5 \times 10^{-15}$  and  $6.5 \times 10^{-16}$  for the X-band uplink translators.

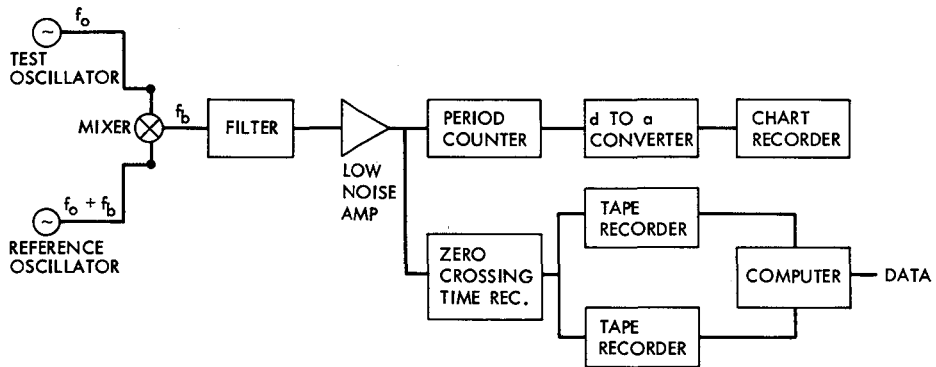


Fig. 1. Standard method of measuring frequency stability

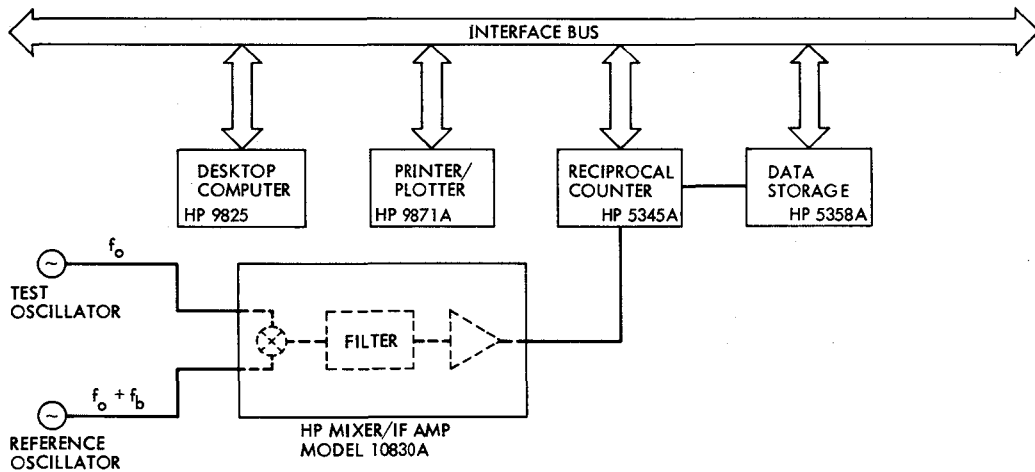


Fig. 2. Block diagram of the HP5390A frequency stability analyzer

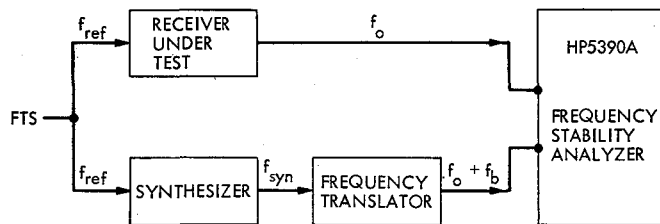


Fig. 3. Measurement method for DSS 13 and DSS 14

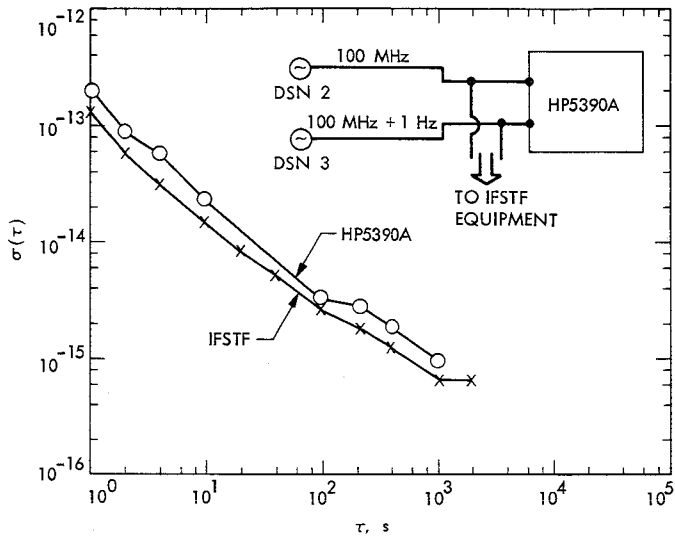


Fig. 4. Fractional frequency deviation noise floor of HP5390A

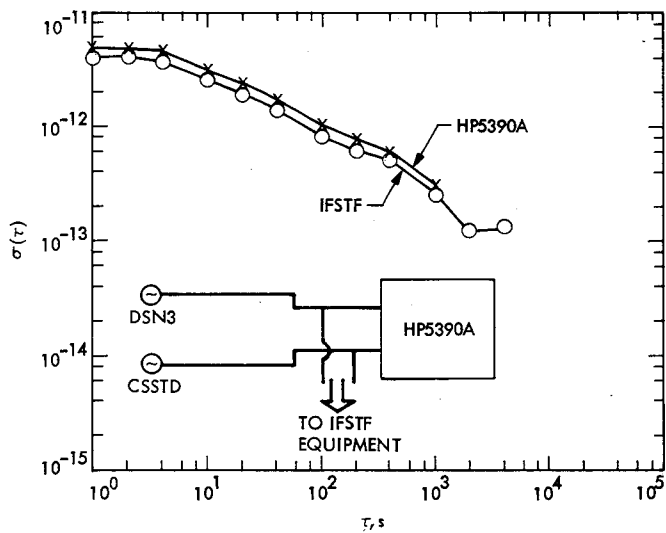


Fig. 5. A cesium standard measured with HP5390A and IFSTF equipment

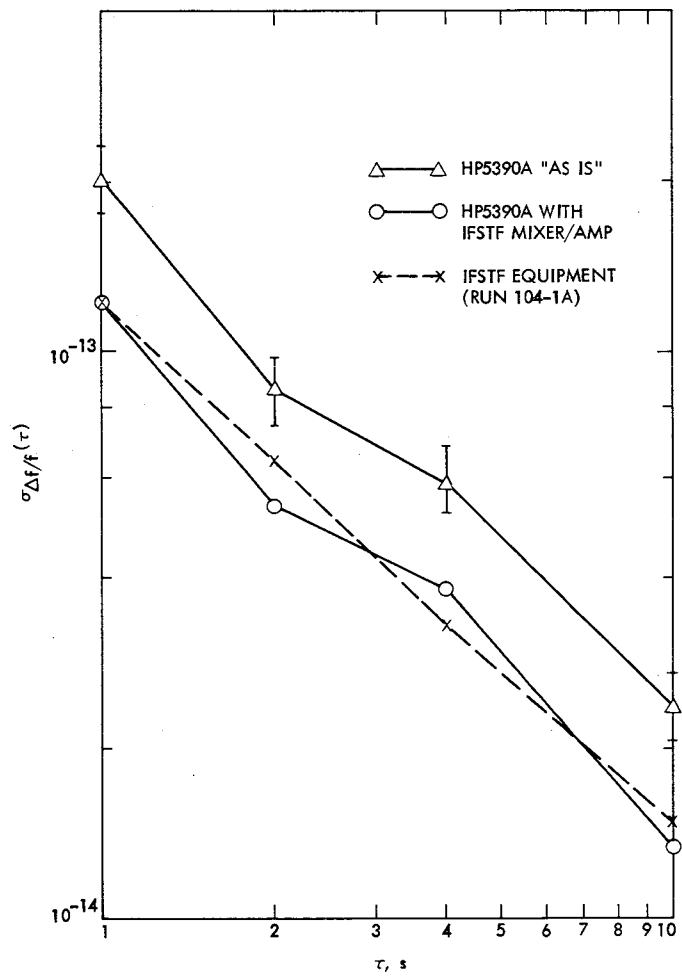


Fig. 6. The IFSTF mixer/amplifier unit eliminates systematic measurement error

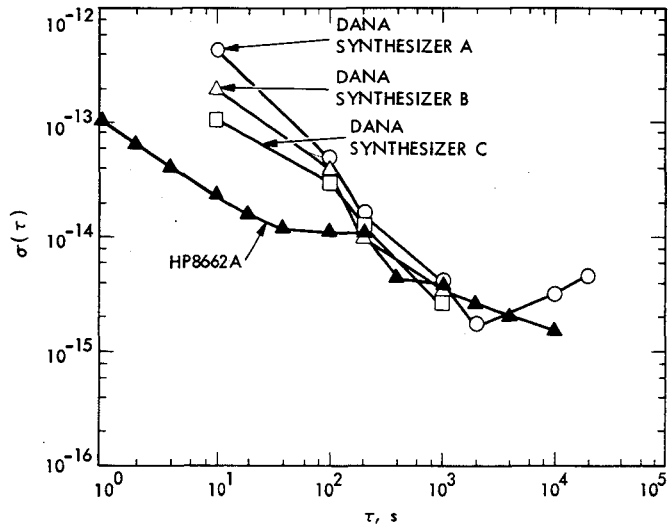


Fig. 7. The HP8662A exhibits a lower noise floor

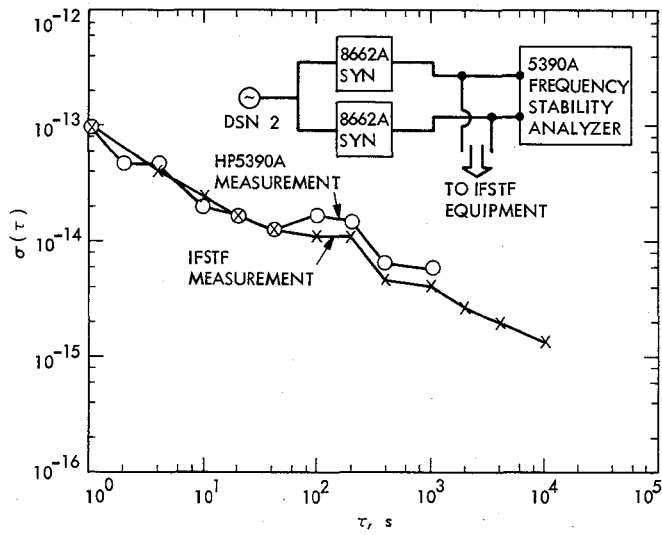


Fig. 8. Noise floor measurement of the HP8662A with the HP5390A

# High Speed Front End of the Multimegabit Telemetry Demodulator Detector

E. R. Wechsler

Communications Systems Research Section

*This article presents the high speed front end (HSFE) portion of the Multimegabit Telemetry Demodulator-Detector. The HSFE accepts in-phase and quadrature analog signals from the input signal conditioner. It samples them with analog-to-digital converters at a maximum rate of 64 megasamples per second. The samples are processed digitally and the integrals of  $I$ ,  $Q$  and of their crossproduct over one symbol period are supplied at symbol rate to the rest of the system.*

## I. Introduction

The purpose of the Multimegabit Telemetry project is to increase the symbol rate capability of the Deep Space Network from a maximum of 250 kilosymbols per second (ksps) to a range of symbol rates between 125 ksps to 32 msps.

A demodulator-detector which operates as a suppressed carrier Costas loop receiver is currently being developed at JPL. This article describes the high speed front end (HSFE) portion.

The HSFE accepts in-phase ( $I$ ) and quadrature ( $Q$ ) analog signals from the input signal conditioner described in Ref. 1 and samples them using high-speed arithmetic operations with the sampled values as described in Ref. 2.

The results of this fast processing are supplied to the rest of the system at the symbol rate. The signals which are supplied include the integrals of  $I$ ,  $Q$  and of  $\text{sgn}(I) \times Q$  over one symbol period and the symbol phase error samples. The digitally performed integral of  $I$  over one symbol period is the soft quantized output of the system and is equivalent to an analog "integrate and dump" output.

## II. System Description

Figure 1 is the block diagram of the HSFE. The  $I$  and  $Q$  signals are sampled by the converters  $A/D_1$  and  $A/D_2$  respectively. Each of them consists of two four-bit monolithic quantizers manufactured by Advanced Micro Devices, Inc. (AM 6688).

The two quantizers are clocked at half the desired sampling rate with 180 degrees phase shifted clocks. This gives more time for data processing by the accumulators,  $ACC_1$ ,  $ACC_2$ ,  $ACC_3$ ,  $ACC_4$  and  $ACC_5$ , the squarers  $SQ_1$  and  $SQ_2$  and the multiplier  $MULT_1$ .

The  $I$  and  $Q$  signals are sampled  $K$  times during one symbol period, where  $K$  can be selected to be 2, 4, 8 or 16. At the highest data rate of 32 msps,  $K$  has to be 2, but as the rate is reduced  $K$  can be increased, provided the sampling rate does not exceed 64 MHz.

A 64-MHz sampling rate means 32 MHz for the individual quantizers, which allows just 30 ns for arithmetic operations (accumulation, squaring, sign inversion, etc.). The  $I$  channel samples are accumulated by  $ACC_1$ , which supplies the integral

of  $I$  over a one-symbol period. The same samples are squared by  $SQ_1$  and the squares are accumulated by  $ACC_2$ .

The  $Q$  channel is processed in the same way. The sums:

$$\sum_{i=1}^k I_i^2 \text{ and } \sum_{i=1}^k Q_i^2$$

are used for lock detection.

The amplitudes of the  $I$  and  $Q$  signals are proportional to  $\cos \theta$  and  $\sin \theta$ , respectively, where  $\theta$  is the carrier phase, but the polarity is symbol-dependent.

Phase information of the carrier is obtained by multiplying  $Q$  and  $\text{sgn}(I)$ . This results in an output crossproduct proportional to  $\sin \theta$  having the right polarity.

There are two modes of operation: acquisition and tracking. During carrier acquisition the crossproduct is calculated by  $MULT_1$  using the  $Q$  samples and the sign of the  $I$  samples. The products are accumulated over one sample period by  $ACC_5$ .

When the system switches to tracking, the signal to noise ratio is increased by using the crossproduct of

$$\sum_{i=1}^k Q_i$$

and the sign of

$$\sum_{i=1}^k I_i.$$

This product is calculated by  $MULT_2$ . Switching between acquisition and tracking is done by the multiplexer  $MUX_1$  according to the condition of the IN LOCK DETECTOR.

The HSFE also detects symbol transitions and the transition output TR is "1" for one symbol period following a transition. This information is accumulated and used for loop parameter control. Another function of the HSFE is to supply the symbol phase necessary for symbol lock. This is done by sampling the  $I$  input at transition time with  $A/D_3$ , which consists of a single four-bit quantizer.

The symbol phase samples are multiplied by  $MULT_3$  with +1 or -1 depending upon the symbol transition polarity or

with zero when no transition has taken place. The symbol phase information is supplied at the phase output.

### III. Hardware Description

Since data must be processed at maximum rates of 32 MHz and some functions of the circuit are clocked at four times this rate, it was necessary to use emitter coupled logic (ECL) integrated circuits. The circuits used are mostly MECL 10,000 and some higher speed MECL III.

The 10,000 series has by design slower transitions at the outputs, while internally the propagation delays and transitions are kept very short. This allows the user to avoid stripline techniques when not absolutely necessary because of the reduced crosscoupling.

ECL circuits require a ground plane, a -5.2 V power plane and a -2 V power plane for the terminating resistors. Special boards are made for wire-wrapping ECL. They have pins 1 and 16 grounded on the board as required in order to avoid oscillations. For this development though, it was considered economical to use standard wire-wrap boards since all the hardware was already available for them. Standard wire-wrap boards have only two planes, so the -2 V plane was avoided by using Thevenin equivalent terminators.

In order to eliminate parasitic oscillations, ferrite beads were placed on pin 1 of most of the ECL circuits. Twisted pairs with the associated line drivers and receivers were used for long connections on board or between boards. The system was divided into four main boards:

- A – The converter and clock board
- B, B' – The  $I$  and  $Q$  channel processing boards
- C – The crossproduct board

Board A generates the clocks according to the  $K$  input and distributes them to the other boards of the HSFE and to the rest of the system. It also accepts the  $I$  and  $Q$  channels from the input signal conditioner and contains the five quantizers which convert the two signals digitally.

Boards B and B' are identical. They contain the accumulators and the squarers which perform  $I$ ,  $Q$ ,  $I^2$ ,  $Q^2$ . Board C contains the crossproduct multipliers and accumulators, the transition detectors, and the symbol phase circuits.

The quantizers used in board A require very short pulses and are sensitive to interference from the rest of the digital circuits. Therefore, decoupling components are very closely

connected. This excludes wire wrapping from the quantizer portion of the board. In this area, the wire-wrap board is cut out and a double-sided board is substituted. This board contains the quantizers and associated components as shown in Fig. 2. The ground and power planes were soldered at the junction in order to keep plane continuity. This permits ECL interconnections to be made with "wire above ground" transmission lines and avoids interruptions in the ground plane which would lead to waveform distortion.

## IV. Testing of the Hardware

The hardware was tested in two steps. The converter and clock board was tested first. The digital signal processing boards (B, B' and C) were tested independently of the converter and clock board. The reason for this two-step testing procedure is that it is very difficult to generate analog signals with predetermined values when sampled at a maximum frequency of 64 MHz.

### A. Testing of Board A (Converter and Clock)

The test setup is shown in Fig. 3.  $I$  and  $Q$  are the in-phase and quadrature inputs. CK is the clock input, which can be as high as 128 MHz.  $C_s$  is the symbol clock, which is distributed to the digital processing part of the system; it can be as high as 32 MHz.  $C_2$  is the sampling clock, it is distributed just to the high speed front end portion of the system, and it has one-fourth the frequency of CK.

The board has five digital outputs:  $I/C_1$ ,  $I/C_2$ ,  $I/C\phi$ ,  $Q/C_1$ ,  $Q/C_2$ . They are the 4-bit values of the  $I$  and  $Q$  inputs, sampled by the five analog-to-digital converters of the board synchronous with the internal clocks  $C_1$ ,  $C_2$  and  $C\phi$ . The test setup consists of three synchronized synthesizers (SYNTH 1, SYNTH 2 and SYNTH 3), a power splitter (PS), two 4-bit registers (Reg 1, Reg 2), two digital-to-analog converters ( $D/A_1$ ,  $D/A_2$  - computer labs HDS-0810E, 100-MHz converter) and an oscilloscope. The two registers can be connected to any of the five 4-bit outputs of Board A.

The sinewave output of SYNTH 1 is split by the PS and fed to the  $I$  and  $Q$  inputs. Its frequency is  $f_1$ . SYNTH 2 supplies the clock input CK with  $f_2$ , and SYNTH 3 triggers the oscilloscope externally at a frequency  $f_3$ . We set  $f_1 = 32.001$  MHz,  $f_2 = 128$  MHz and  $f_3 = 1$  kHz. All three signals are coherent because SYNTH 2 and SYNTH 3 are synchronized from SYNTH 1.

The frequency of  $C_2$  is one-fourth that of CK; therefore, the signal is sampled at  $f_2 \div 4 = 32$  MHz. Since the frequency of  $I$  and  $Q$  is  $f_1 = 32.001$  MHz, the output samples  $I/C_1$  through  $Q/C_2$  will have a periodicity of 1 kHz.

The samples are strobed by Reg 1 and Reg 2 and then converted to 1-kHz sinewaves by  $D/A_1$  and  $D/A_2$ , which can be observed on the oscilloscope triggered by SYNTH 3 at  $f_3 = 1$  kHz.

This method allows testing of the analog-to-digital converters from two points of view at the same time; we can see the frequency response of the input stage of the A/D and whether the sampling frequency of the A/D is within the allowable range. Observing two channels at the same time allows us to see if the sampling clocks are in the correct phase relationship.

The board was tested and found to work well for full-scale sinewave inputs of 32 MHz and clock inputs exceeding 128 MHz.

### B. Testing of the Digital Processing Boards (B, B', C)

The testing of the B, B', and C boards is done by substituting the digital signals from Board A with preprogrammed bit patterns from a word generator. The test setup is shown in Fig. 4.

The word generator supplies two 4-bit inputs to the digital processing boards. It also has a strobe output which marks the beginning of a symbol. Since the High Speed Front End generates its own clocks, including the symbol clock  $C_s$ , it was necessary to synchronize the strobe signal with the symbol clock from Board A. This was done by means of a phase-locked loop. The strobe output and the symbol clock phases are compared by the phase-sensitive detector PSD (MC 12040). The phase error controls a synthesizer in the search mode, which acts like a voltage-controlled oscillator (VCO). This VCO triggers a pulse generator which supplies the input clock CK to Board A. The delay line (DL) delays the digital outputs from the word generator approximately 14 ns relative to the symbol clock. This duplicates the conditions that exist when signals generated by Board A are used as input. A switching arrangement allows checking of all five inputs.

By feeding known bit patterns at various rates it was possible to extensively check the logic design, the wiring and the working speed. It was found that the system performs correctly at sample rates in excess of 32 MHz.

## V. Summary

The HSFE has been constructed and tested. It supplies other parts of the Multimegabit Telemetry System and the user with digital signals through differentially driven, shielded, twisted pairs with an impedance of 120  $\Omega$ . The clock supplied with the data is advanced 24 ns, which allows the clock to be distributed throughout the system with no difficulty.

## References

1. Stevens, G. L., "Input Signal Conditioner for the Multimegasympol Telemetry System Feasibility Model," in *The TDA Progress Report 42-58*, May-June 1980, Jet Propulsion Laboratory, Pasadena, Calif., Aug 15, 1980.
2. Wechsler, E. R., "Arithmetic Techniques Used in the High Speed Front End of the Multimegabit Telemetry Modem," in *The DSN Progress Report 42-56*, January-February 1980, Jet Propulsion Laboratory, Pasadena, Calif., April 15, 1980.

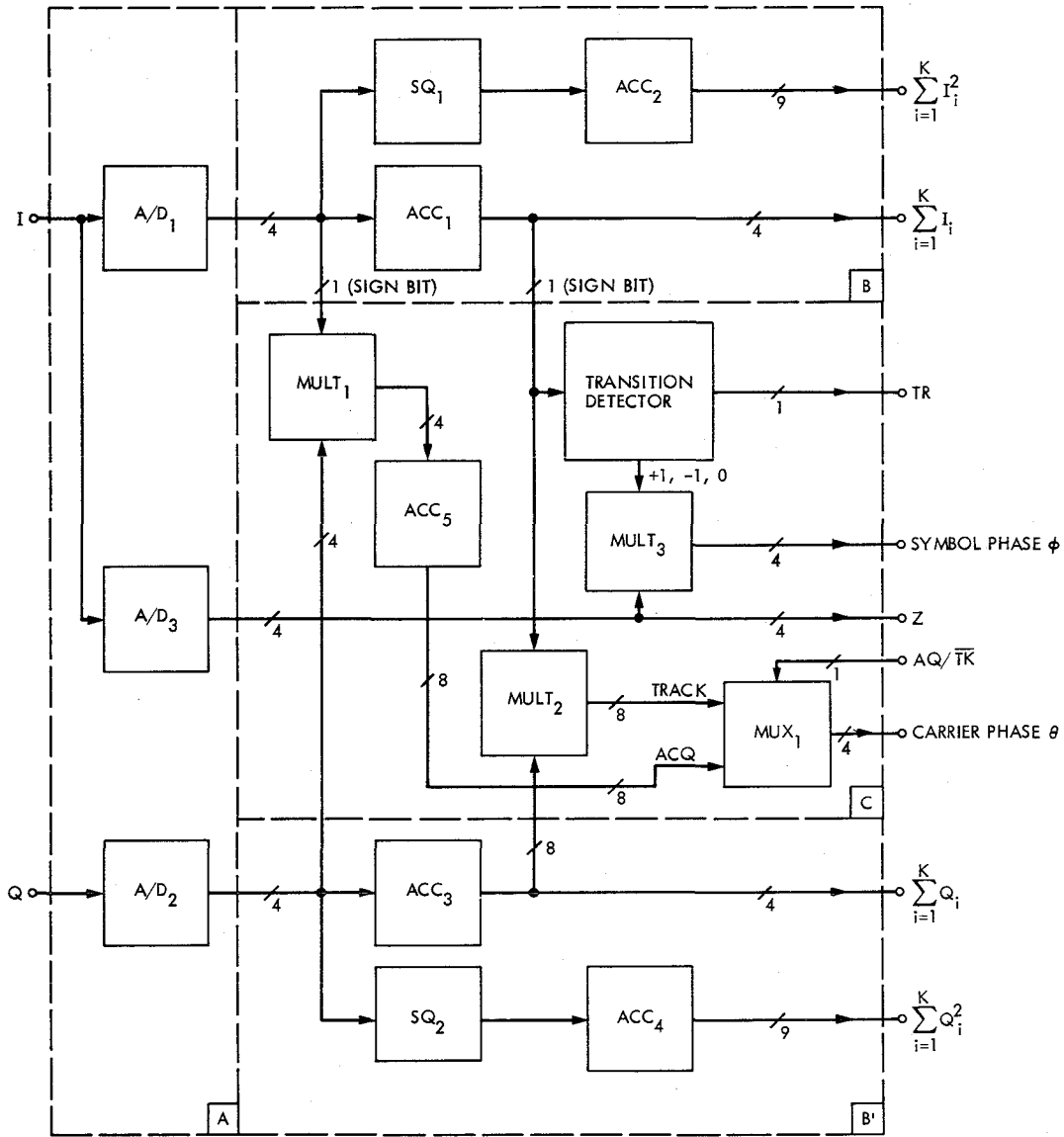


Fig. 1. Block diagram of the high speed front end

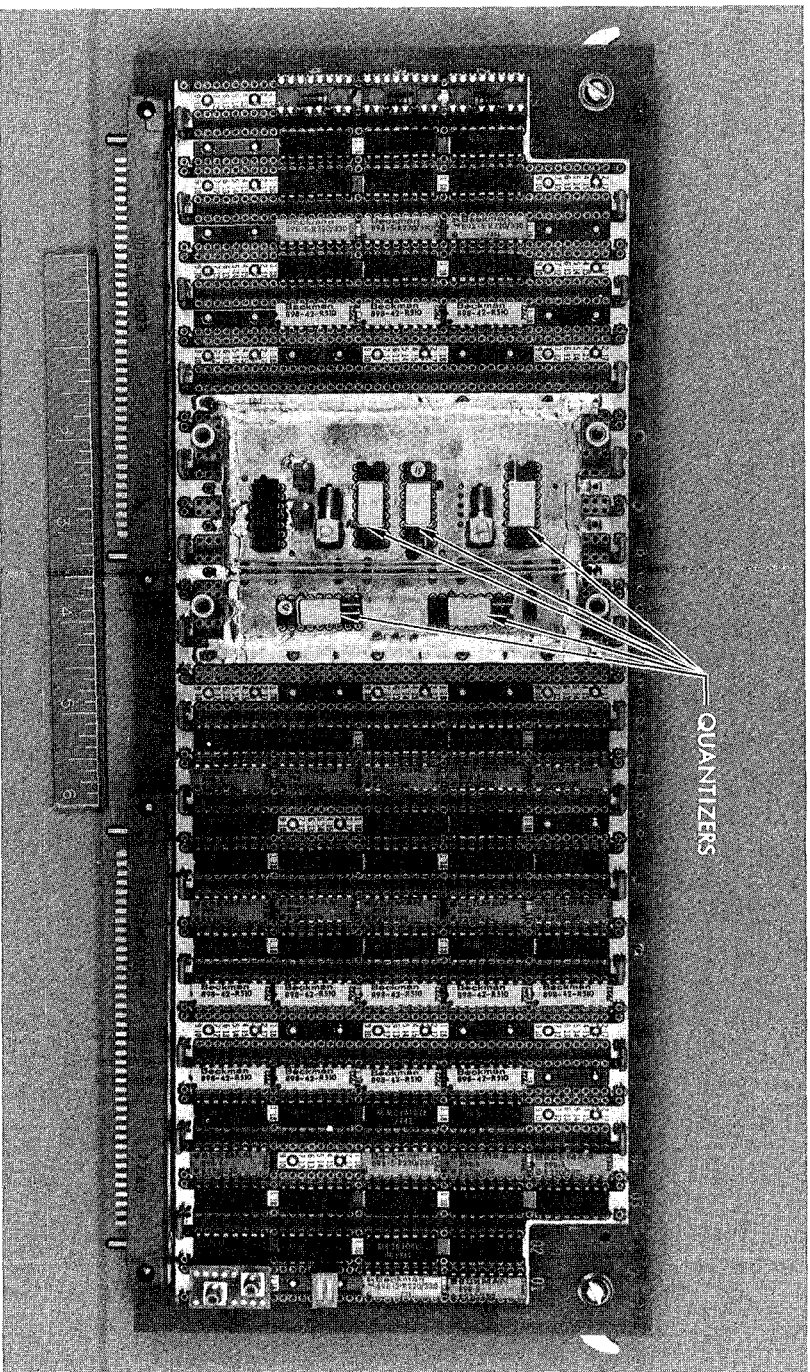


Fig. 2. Converter and clock board

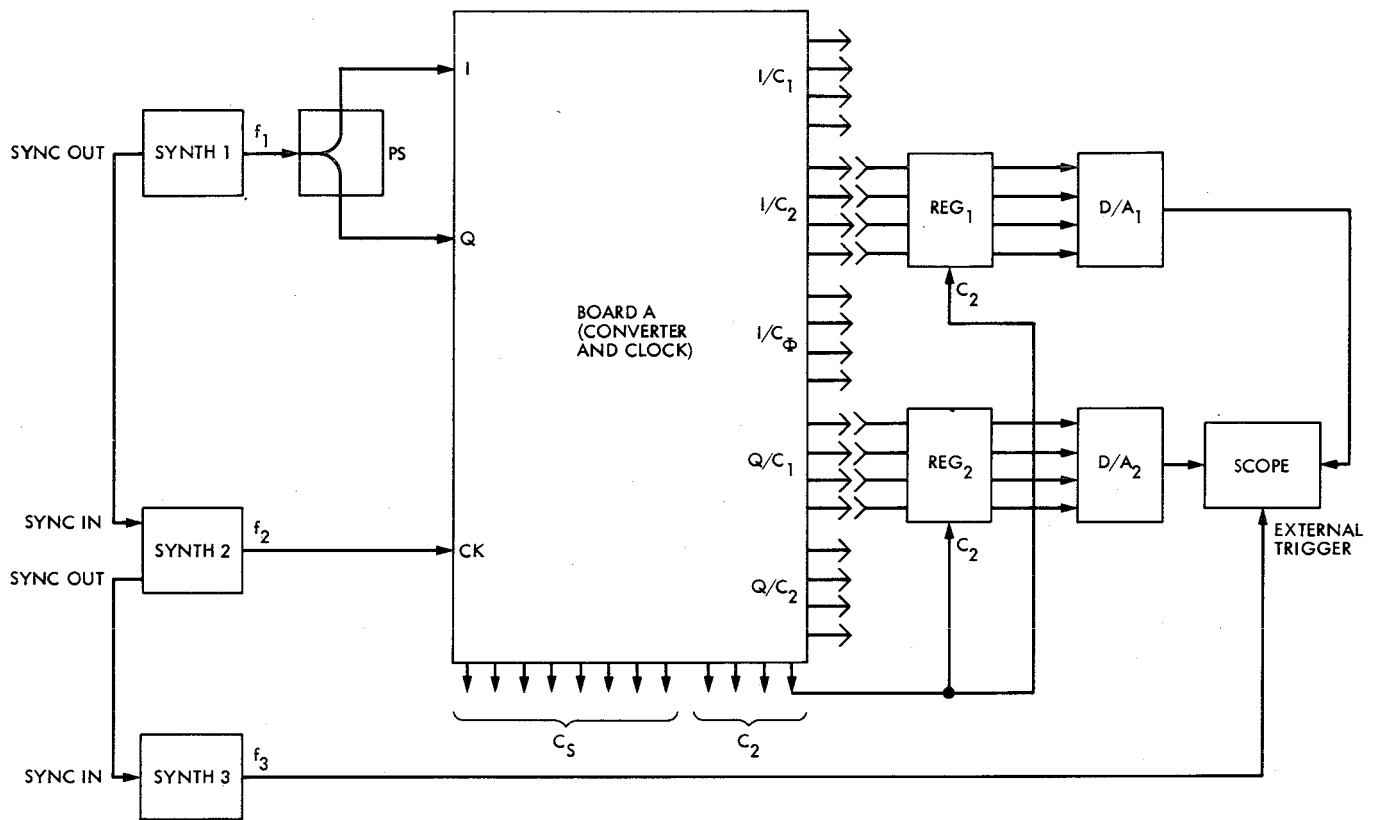


Fig. 3. Test setup for the converter and clock board

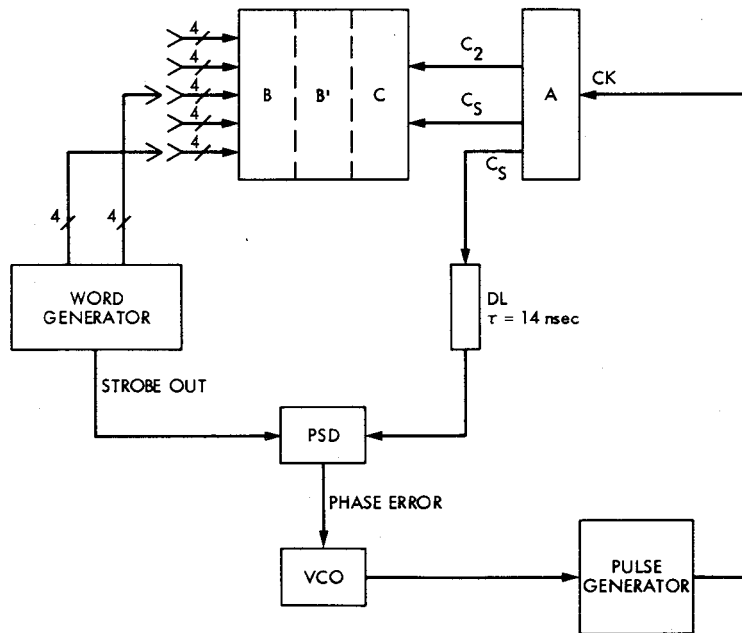


Fig. 4. Testing of the digital signal processing boards (B, B', C)

# ISPM X-Band Uplink Technology Demonstration

## Part I. Overview

T. A. Komarek and J. G. Meeker  
Telecommunications System Section

R. B. Miller  
TDA Mission Support Office

*This is the first of a series of articles on the X-band uplink system development. The ground and spacecraft hardware research, design and implementation will lead to an end-to-end in-flight technology demonstration on the International Solar Polar Mission spacecraft. This article gives an introduction to the overall effort and establishes the flight experiment objectives. The expected improvements in the telecommunications performance are summarized. Also presented is a conceptual mission operations plan. Subsequent articles will address the system design and performance, report on the implementation progress, and finally evaluate the flight experiment results.*

### I. Introduction

The X-band uplink technology demonstration was established by agreements among the NASA Offices for Space Science (OSS), Aeronautics and Space Technology (OAST), and Space Tracking and Data Systems (OSTDS). The agreement, documented by a Memorandum of Understanding in October 1980, provides for the support of a flight technology demonstration experiment on the International Solar Polar Mission (ISPM) spacecraft to be launched in 1985 (Ref. 1).

The engineering experiment will culminate the X-band uplink development phase with an end-to-end demonstration of new ground and spacecraft technology and an assessment of benefits for future deep space missions – in particular, possible future gravitational wave investigations (Ref. 2) and the proposed Starprobe mission.

The benefits of an X-band uplink over an S-band uplink are several. For one, it is possible to obtain a greater signal power density at the spacecraft receiver for a given ground transmitter power and given size of ground antenna. An equally important advantage is that the phase and group velocities of an X-band signal are less perturbed by charged particles in the signal path through the ionosphere, interplanetary space and especially near the sun. Finally, the bandwidth allocations at X-band are wider and in a spectral region less crowded than S-band and less exposed to radio frequency interference (RFI) at this time.

To assure proper coordination of all segments of the X-band uplink development, the JPL Telecommunications Science and Engineering Division formed a task and a design team under the programmatic leadership of the Telecommu-

nications and Data Acquisition Office (TDA). The design team represents all major implementation areas and interfaces with the ISPM project, TRW (the ISPM spacecraft system contractor), and possible future users in the radio science community. The ground and spacecraft hardware developments have been proceeding (Refs. 3-6).

## II. Scope and Responsibilities for the Flight Engineering Experiment

### A. Scope

The scope of the X-band uplink development and demonstration conforms to the following key guidelines:

- (1) The flight experiment will be a technology demonstration only. Operational X-band uplink use for spacecraft mission enhancement or science investigations would require additional implementation.
- (2) X-band uplink capability will be implemented only at the R&D Deep Space Station (DSS 13), and therefore the ISPM X-band uplink sequences will be supported from that station.

Also implied in the ISPM Project's acceptance of the X-band uplink experiment is that the inclusion of the X-band receive capability will not jeopardize spacecraft reliability, nor will it impair baseline operational functions, such as S-band uplink commanding or X-band telemetry. Furthermore, mission operations impact shall be minimized. For these reasons, the on-board X-band uplink hardware will be inserted in only one of the redundant S-band uplink paths and in only one of the X-band downlink paths. Also, the X- to S-band downconverter and the X-diplexer can be bypassed by direct or stored command when not in use, leaving only the incremental losses due to an added transfer switch and cabling in the X-band downlink path. Figure 1 shows the ground and Spacecraft Telecommunications System and Fig. 2 shows the spacecraft Radio Frequency Subsystem in some detail.

Similarly, an X-band uplink systems liaison has been established with the ISPM Mission Operations System (MOS) to integrate the X-band uplink requirements and mission sequences into the ISPM mission operations plan.

### B. Flight Hardware Responsibilities

JPL has the overall responsibility for the X-band uplink engineering experiment. The X-band uplink status is similar to that of the science experiments where the system contractor performs spacecraft integration of instruments furnished by the investigators. For the X-band uplink, TRW will integrate the hardware furnished by JPL. This is in contrast to all other spacecraft operational functions, including the S-band uplink

and X-band downlink, which are the responsibility of the system contractor.

The JPL X-band uplink task will supply to TRW one flight-model X- to S-band downconverter and one flight model X-band diplexer for integration aboard the NASA spacecraft. Consistent with its integration responsibility, TRW will specify and procure those components which lie in ISPM operational signal paths when the X-band uplink function is switched out. From Fig. 2 one can identify these components to be the coupler in the S-band uplink transponder Number 2 path and the transfer switch in the X-band downlink path from traveling-wave tube amplifier (TWTA) Number 1.

TRW will maintain the mass and power budget entries associated with the X-band implementation, and will also measure the circuit losses for the affected baseline ISPM links with the X-band uplink hardware passively switched in or out of the signal paths. TRW will account for these incremental losses in Design Control Tables for the baseline functions.

The JPL X-band uplink task will be responsible for all analysis, performance predictions and testing involving the X-band uplink. The pertinent links include commanding via X-band plus X-X and X-S doppler, ranging and coherent telemetry.<sup>1</sup> The task will also provide the liaison necessary to ensure that X-band uplink requirements become part of the ISPM Mission Plan, operational sequences, and DSN support plans.

### C. Ground Hardware Responsibilities

The focal point of the X-band uplink ground development has been the design and implementation of modified DSS 13 subsystems under the TDA Advanced Development program. The ground development is being integrated with the spacecraft portions by system engineering provided by the X-band uplink design team under the same TDA program.

The DSS 13 development was divided into four main areas: a 20-kW X-band transmitter and controller, a dual X-S antenna feed horn and X-band diplexer to be housed in a modified 26-meter antenna feed cone, a high-stability X-band exciter-doppler extractor using a hydrogen maser timing reference, and a Block III receiver upgrade. Temperature control will be employed throughout for critical components.

The high-power transmitter and the phase stable 7145-7235 MHz exciter-doppler extractor are being developed (Refs. 3 and 4) and will be compatible with a companion goal of

<sup>1</sup>A coherent X-uplink and X-downlink is abbreviated as X-X. Similarly, X-S means a coherent X-uplink and S-downlink.

achieving unattended operations. The stable reference depends upon hydrogen maser research and implementation (Ref. 5). The antenna feed design, development and testing has been proceeding, and it is planned for installation at DSS 13 in the fall of 1981 (Ref. 6).

In addition to the new station hardware under development, the X-band demonstration will require other ground equipment to be available at DSS 13 for the prelaunch and in-flight tests. Not all the planning has been completed at this time, and it will be necessary to coordinate with all other scheduled DSN activities. For example, a state-of-the-art hydrogen maser must be present during the crucial test and flight phases of the X-band demonstration. Likewise, all the data processing equipment needed for command modulation, telemetry acquisition and ranging measurements must be assured. The MU-2 ranging machine is desirable because of its dual-frequency capability, but its availability is subject at important times to high-priority users, such as Voyager at Uranus encounter.

The command and telemetry processing equipment may be shared between DSS 13 and the DSN Compatibility Test Areas located in JPL (CTA-21) and in the Merrit Island Launch Area (MIL-71). The equipment would reside at DSS 13 when needed by X-band uplink and would be transported to MIL-71 to support DSN launch commitments. However, this plan may be a problem depending on how the total mission set develops.

In the case of telemetry, another alternative may be to relay the demodulated subcarrier data from DSS 13 to DSS 12 via a microwave link for final processing as shown in Fig. 3, if the MIL-71 equipment were not available. The schedule for the support equipment, as well as the X-band uplink ground and space hardware, is given in Fig. 4. Resolution of the above issues will be part of the ongoing design team activity.

### **III. Flight Engineering Experiment Objectives**

The X-band uplink flight experiment will test the capabilities of all the pertinent telecom functions under the varied conditions applicable to future deep-space flight applications. In all cases the experimental results will be compared to preflight predictions, based upon analyses of the links.

#### **A. Flight Opportunities**

One of the significant uncertainties in our preflight knowledge of the X-band uplink flight performance is an incomplete understanding of the complex effects of the propagation medium, especially the tropospheric phase scintillations due to

water vapor variations, and fluctuations of signal amplitude and phase due to charged particles in the ionosphere, solar corona and solar wind. The tropospheric phase error may be a limiting factor in some future radiometric applications, such as gravitational wave searches. The charged particle effects are very important to near-sun communications, such as will be encountered by the projected Starprobe mission. The charged particle effects are also important to ultrastable doppler tracking in the antisolar direction for the possible future gravitational wave searches. Current understanding is that such detection experiments are only feasible at oppositions (i.e., viewing the spacecraft in the antisolar direction) with significant earth-spacecraft distances.

It is therefore important to test the X-band uplink in as many of the diverse propagation environments as possible. Fortunately, the ISPM trajectory provides flight opportunities which will enable separation of the dominant propagation effects. The propagation conditions range from nighttime spacecraft viewing with minimum solar plasma and ionospheric effects to the superior conjunction conditions when the sun is between the earth and spacecraft, less than 2 degrees off the line-of-sight propagation path.

It is also desirable to check out and calibrate the instrumentation stability of the end-to-end system early in the mission under strong signal conditions with minimal media effects, and to compare the performance again later at far distance under similar media conditions. These requirements suggest close-in and long-range X-band uplink sequences near solar oppositions. The long-range opposition gives the opportunity to obtain two types of data. First, it will show the advantages of X-X coherent telemetry vs S-X under weak signal, but "quiet" environmental conditions. Secondly, the quiet environment is precisely the one that gives an insight into the feasibility of gravitational wave search experiments by measuring the actual plasma noise floor in the antisolar direction using X-band uplink. The plasma noise floor will be one of ultimate limits (along with unmodelled tropospheric errors) until simultaneous uplinks are available for calibrating the plasma component.

Figure 5 shows two aspects of the ISPM trajectory, the range and the sun-earth-probe angle. Together, these plots illustrate the unique characteristics of the ISPM trajectory; viz., the two spacecraft (only one shown here) proceed out to Jupiter in the plane of the ecliptic, where they are deflected by Jupiter gravity up out of the ecliptic plane, and then fall back over the poles of the sun. While the out-of-ecliptic phase is prime for ISPM science, it is the outward bound part of the trajectory in the ecliptic plane that offers the X-band uplink all of the conditions needed to perform a good survey of X-band uplink capabilities.

## B. Data Acquisition Phases

The principal data acquisition phases providing for accomplishment of the demonstration objectives within the ISPM trajectory constraints are indicated in Fig. 5. The three experiment phases are (1) the system calibrations at the first opposition, (2) superior conjunction demonstration, and (3) long-range demonstration around the second opposition. As described in Table 1, each phase utilizes its unique propagation conditions for acquisition of different data types.

Each data acquisition phase consists of 30 to 40 spacecraft passes, a few of which are "fully dedicated" to the X-band uplink demonstration, while the rest may be performed concurrently with other ISPM data acquisition activities. The term "fully dedicated pass" means one in which not only the telecom system would be configured to accommodate the X-band uplink experiment but also the events and modes of the spacecraft would be maintained in a "quiet" or unchanging condition – both thermally and dynamically. Fully dedicated passes are required only for selected doppler stability measurements to establish the phase stability threshold.

## IV. Expected Improvement in Telecommunications Performance

The improvement in telecommunications functions expected from an X-band (approximately 7.2 GHz) vs S-band uplink (2.1 GHz) is due to two well-known advantages of high radio frequencies.

First, antenna gain is proportional to the square of frequency. The space loss, on the other hand, is also proportional to the square of frequency. Since two antennas are involved in a communications link, the net effect of a higher frequency will be a gain by a factor of approximately the square of the frequency ratio.<sup>2</sup> Thus the power received at the spacecraft increases by about 10.6 dB for the same ground transmitter power and given dimensions and efficiencies of the ground and spacecraft antennas. This advantage, in reverse, has been exploited by Voyager using X-band *downlinks* to increase telemetry rates substantially over previous S-band capabilities.

Secondly, X-band transmissions are much less affected by phase fluctuations induced by charged particles, locally in the ionosphere, and in the tenuous, but extended, solar corona or solar wind of interplanetary space. A small disadvantage is that X-band is more sensitive to weather effects than S-band.

## A. Doppler Stability Improvement

It is phase fluctuations due to charged particles that have become the limiting factor in discerning at S-band the minute doppler signatures below the  $10^{-14}$  level such as might be encountered in gravitational-wave searches of the future. Ultimately, a simultaneous dual-frequency uplink and simultaneous dual-frequency downlink will permit a much better calibration of the charged-particle contribution to the doppler error budget. Meantime, the X-band uplink, used with a dual-frequency downlink on ISPM, should reduce the error considerably. Figure 6 shows the expected improvement, first with X-band uplink on ISPM and, in the future, with a simultaneous dual-frequency uplink. The error budget of the next generation also anticipates advances in calibrating the wet troposphere fluctuations plus further improvements in the stabilities of timing reference and distribution systems.

The ISPM experiment will include as many of these link calibrations as practicable. A prime example is the planned use of a water vapor radiometer at DSS 13 for monitoring the tropospheric scintillations during X-band uplink experiment passes.

## B. Command Enhancement

Command enhancement at X-band derives from both the gain in EIRP and the reduction in phase fluctuations due to charged particles. The experiment will test this capability at low sun-earth-probe (SEP) angles. It is expected that reliable commanding should be possible down to an SEP angle of 2 degrees, with bit error rates of less than  $10^{-5}$ . This would reduce the command "blackout" zone now encountered with S-band uplink communications at solar conjunctions.

## C. Two-Way Coherent Telemetry Data-Rate Improvement

A demonstration of improved two-way coherent telemetry performance will be conducted under weak signal, but quiet environmental conditions selected to present unambiguously the advantage of using X-X vs S-X two-way coherent telemetry. These conditions are best met at the time of second opposition around September 1986, when both the spacecraft range and the SEP angle are large, approximately 4 AU and 177 degrees, respectively.

The telemetry performance improvement of an X-X link over an S-X link is realized from a reduction in radio loss, the term applied to the performance degradation in the received data due to imperfect tracking of the downlink carrier phase. It can be shown that the downlink carrier phase jitter in a two-way coherent link consists not only of the downlink jitter due to the ground receiver thermal noise and media-induced

<sup>2</sup> Stated in another way: the effective isotropically radiated power (EIRP) transmitted to the spacecraft increases by  $(f_x/f_s)^2$ .

signal fluctuations but also of all the noise accumulated on the uplink, multiplied by the turnaround frequency ratio of the transponder. Obviously, the X-X link gives an advantage in turnaround ratio (880/749 vs 880/221) over the S-X, plus an increase in uplink EIRP of approximately 10 dB.

The net improvement in data rate capability for convolutionally coded telemetry is approximately 3 dB for the long-range, weak-signal conditions that will exist at the mission time selected for these tests. In effect, the two-way X-X telemetry radio loss should approach that of a one-way telemetry link using the auxiliary oscillator as the downlink carrier reference.

#### **D. Ranging Improvement**

The ranging signal-to-noise ratio (SNR) as received at the DSN is determined by both the uplink and downlink parameters. Therefore, an X-X ranging link will demonstrate an improved SNR over its S-X counterpart as a direct beneficiary of the increased EIRP on the uplink. Added to this will be a somewhat smaller ranging radio loss for the same reasons that apply to two-way coherent telemetry.

Another approximately order-of-magnitude improvement in ranging accuracy should be realized by the reduction of errors caused by charged particles in the uplink path. The net improvement due to the X-band uplink will permit shorter integration times and therefore more data points with the same accuracy as that obtained with an S-band uplink.

#### **V. Conceptual Operations Plan**

ISPM is planning to operate throughout the mission in a "cruise mode," utilizing an 8-hour shift per day for each spacecraft, 5 days a week. The NASA MOS team will prepare for uplinking once a week the sequences necessary to program daily operations of the NASA spacecraft, including an 8-hour pass over an appropriate 34-meter station. It is important that the X-band uplink operations at DSS 13 do not seriously impact this routine.

The strategy presently planned for operations during the X-band uplink activity periods is to make the X-band uplink

experiment "nearly transparent" to the baseline operations of ISPM. This would be accomplished by incorporating into the sequences additional stored commands to configure the telecommunications system for two passes per day, one configuration to accommodate X-band uplink operations, using DSS 13, followed by a reconfiguration to execute normal ISPM operations at either DSS 42 or DSS 61. ISPM science data would continue to be recorded during the DSS 13 tracking. Thus, no ISPM data would be forfeited nor would 34-meter station activities be altered.

Let us consider a particular example, in this case a day's activities consisting of an X-band uplink doppler stability measurement conducted at DSS 13 followed by a routine ISPM data dump to DSS 42. The event sequences for these activities would have commenced just after the previous day's ISPM pass, at which time the spacecraft would have been configured for the upcoming X-band uplink from DSS 13. This mode would call for turn-on of the X- to S-band downconverter and for setting the telemetry modulation index at zero to maximize the downlink carrier power. These stored commands would have been executed sufficiently ahead of the DSS 13 pass to allow the spacecraft to come to thermal and dynamic equilibrium. Following the DSS 13 track, the telecommunications system would be reconfigured, again by stored command, to turn off the downconverter and reset the telemetry modulation index to execute the ISPM daily tape recorder playback to DSS 42. At the conclusion of that pass the spacecraft configuration would immediately be placed in the X-band uplink mode required for the next day. This dual-pass routine would be followed through the X-band uplink activity period.

There are several areas where further coordination with the ISPM Mission Operations System is necessary. The key MOS functions affected by the X-band uplink experiment are summarized in Table 2. The X-band uplink requirements and impacts will be worked as a continuing effort with the ISPM Mission Operations Design Team. Sequences accommodating the X-band uplink will be designed and tested before launch, as is the plan for all the NASA spacecraft sequences. Each sequence format will have sufficient flexibility to accept parametric changes during the mission.

## References

1. Miller, R. B., "International Solar Polar Mission," *TDA Progress Report 42-59*, Jet Propulsion Laboratory, Pasadena, Calif., October 15, 1980.
2. Berman, A. L., "The Gravitational Wave Detection Experiment: Description and Anticipated Requirements," *DSN Progress Report 42-46*, Jet Propulsion Laboratory, Pasadena, Calif., August 15, 1978.
3. Kolbly, R. B., "20 kW X-Band Uplink Transmitter Development," *TDA Progress Report 42-60*, Jet Propulsion Laboratory, Pasadena, Calif., December 15, 1980.
4. Hartop, R., Johns, C., and Kolbly, R., "X-Band Uplink Ground System Development," *DSN Progress Report 42-56*, Jet Propulsion Laboratory, Pasadena, Calif., April 15, 1980.
5. Kuhnle, P. F., "Hydrogen Maser Implementation in the Deep Space Network at the Jet Propulsion Laboratory," Proceedings of the 11th Annual PTTI Meeting, NASA Conf. Publication 2129, GSFC, Greenbelt, Md., 1979.
6. Williams, W., and Reilly, H., "A Prototype DSN X/S-Band Feed: DSS 13 Application Status, (Fourth Report), *TDA Progress Report 42-60*, Jet Propulsion Laboratory, Pasadena, Calif., December 15, 1980.

**Table 1. ISPM X-band uplink technology demonstration — flight experiment phases**

Experiment phase	Date <sup>a</sup>	Demonstration duration	Data required
Calibration at first opposition	July 1985	40 Passes (5 fully dedicated)	Carrier acquisition and tracking, ranging and two-way coherent telemetry vs uplink power level  Doppler stability, X-U/L vs S-U/L (strong-signal conditions, minimal solar wind environment, minimal ionosphere and troposphere effect)
Superior conjunction demonstration	Feb. 1986	30 Passes (5 fully dedicated)	Command demonstration, X-U/L vs S-U/L  Ranging demonstration and doppler, X-X and S vs S-X and S  System noise temp vs SEP angle (disturbed solar plasma environment)
Long-range demonstration	Around Sept. 1986	40 Passes (5 fully dedicated)	Two-way coherent telemetry, X-U/L vs S-U/L  Doppler demonstration X-X and S vs S-X and S (far range, quiet spacecraft, quiet natural environment)

<sup>a</sup>Based on tandem-launch trajectory data for March 29, 1985 launch.

**Table 2. Effects of X-band uplink on ISPM daily operations**

MOS function	Projected impact
DSN scheduling	Two-station per day coverage is implied during X-band uplink activity periods: DSS 13 for X-band uplink sequences, DSS 42 or DSS 61 for routine command, navigation and telemetry.
Stored command loads	Approximately 10 additional stored commands
Telemetry data rates	Downlink path losses are increased if X-diplexer is left in circuit during normal ISPM telemetry return. Option exists to switch X-diplexer IN/OUT for X-band uplink or telemetry, respectively. Desirability of this option is under study
Engineering data records	X-band uplink will require engineering records of spacecraft functions occurring during many X-band uplink passes. ISPM Ground Data System is required to provide such data within 24 hours (tapes and hard copy).

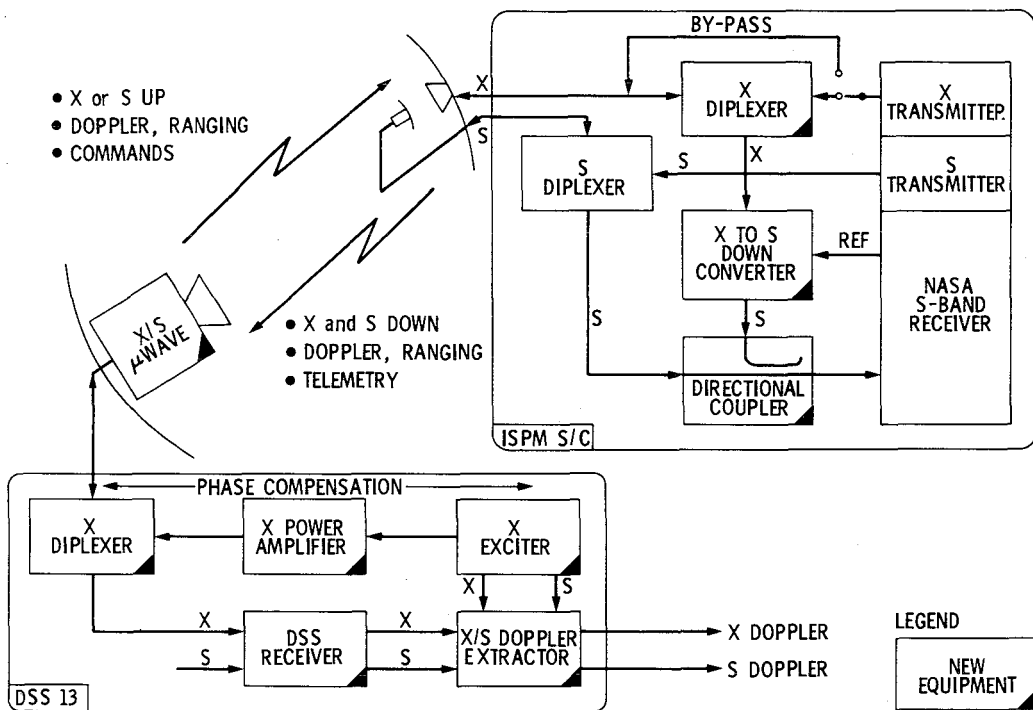


Fig. 1. Block diagram of the ISPM X-band uplink demonstration telecommunication system

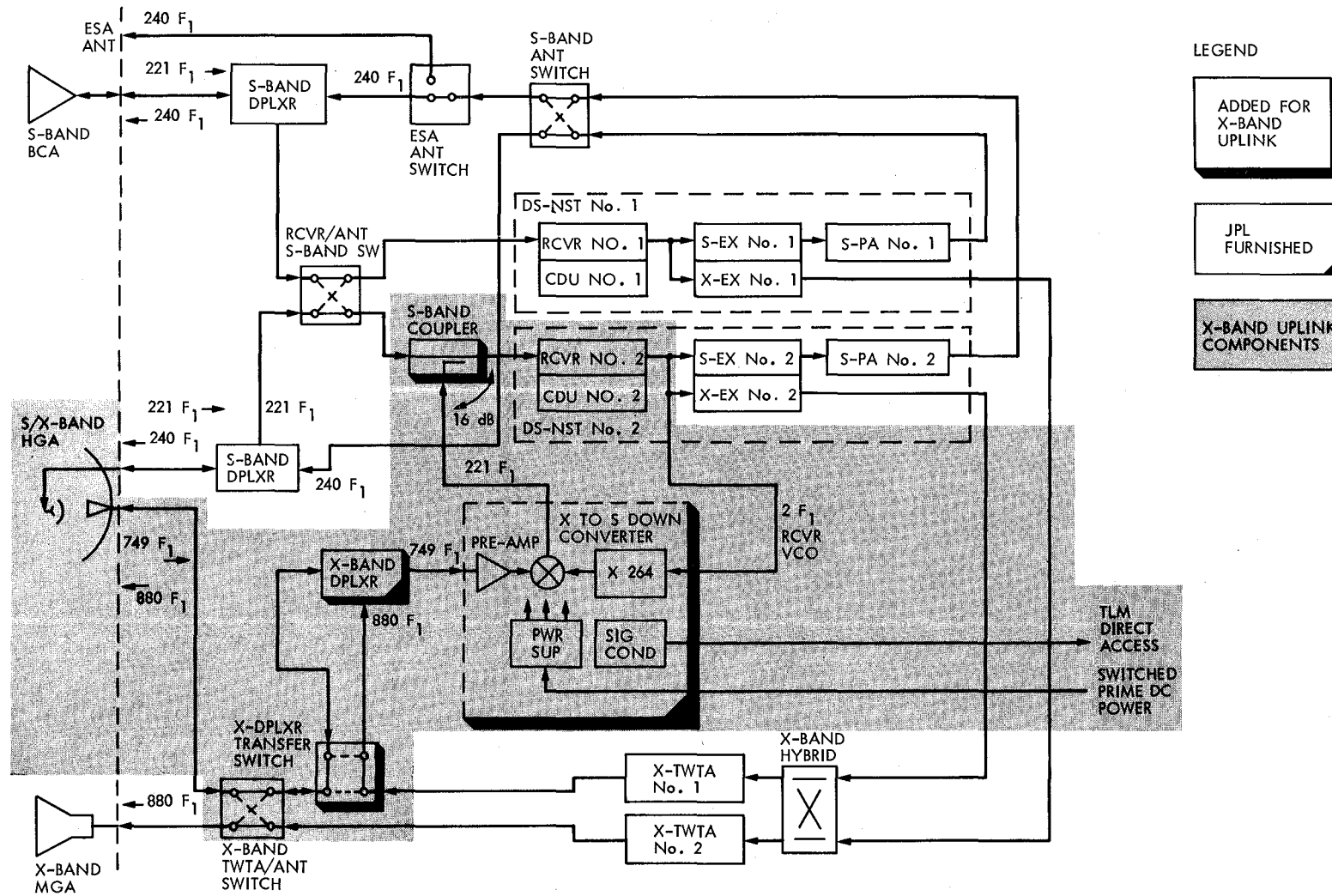


Fig. 2. ISPM spacecraft modifications for X-band uplink

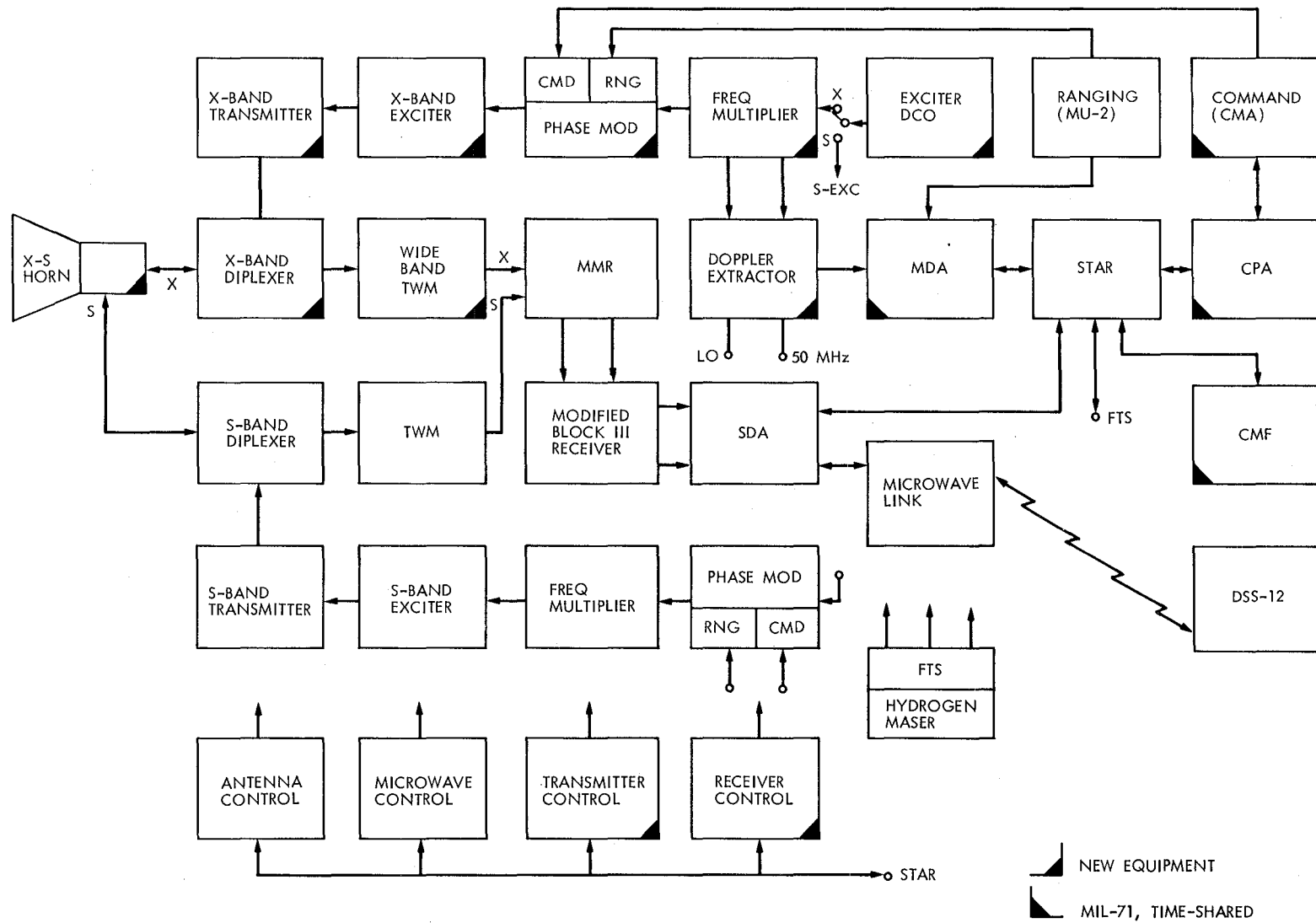


Fig. 3. Block diagram of DSS 13 X-band uplink elements

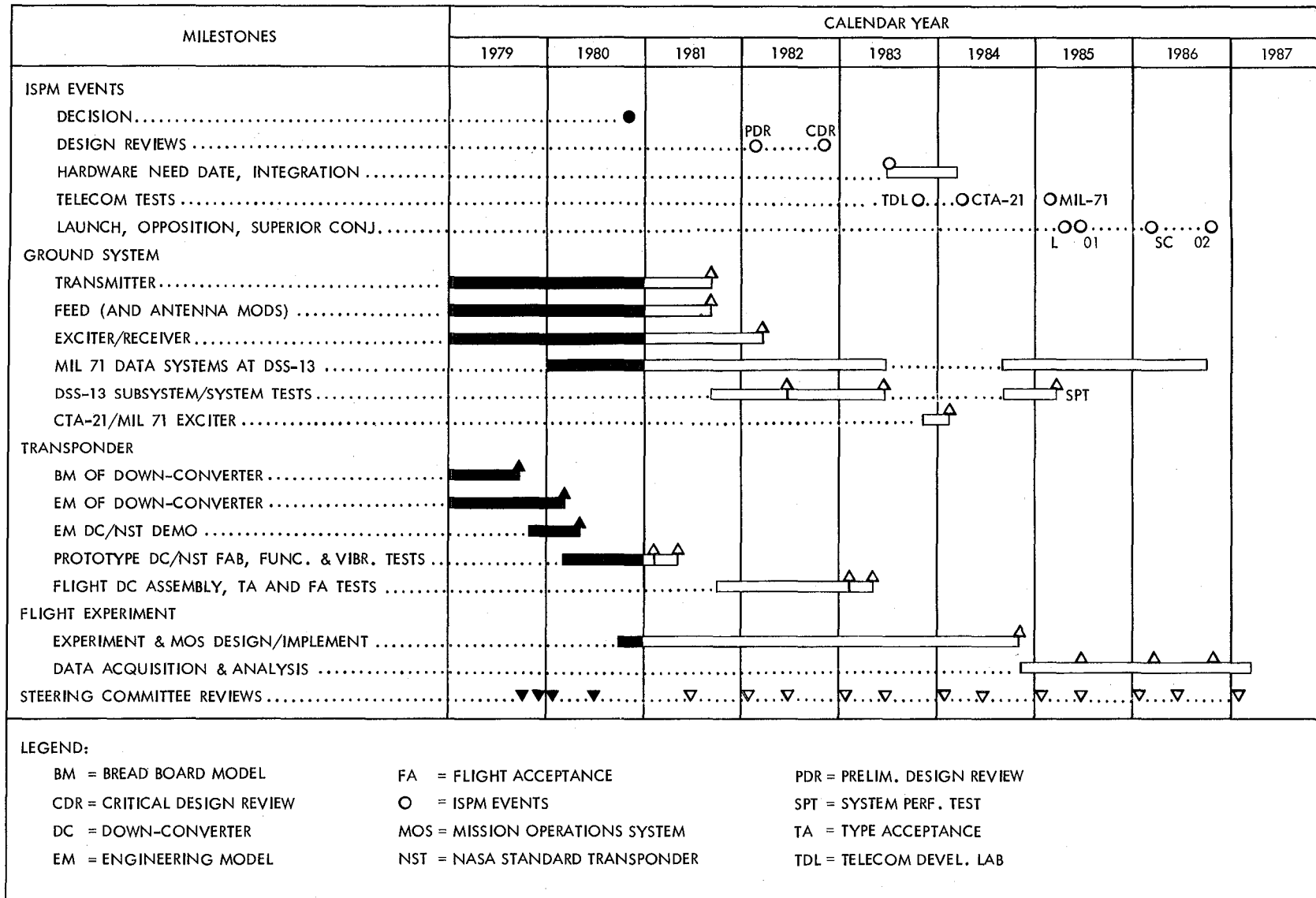
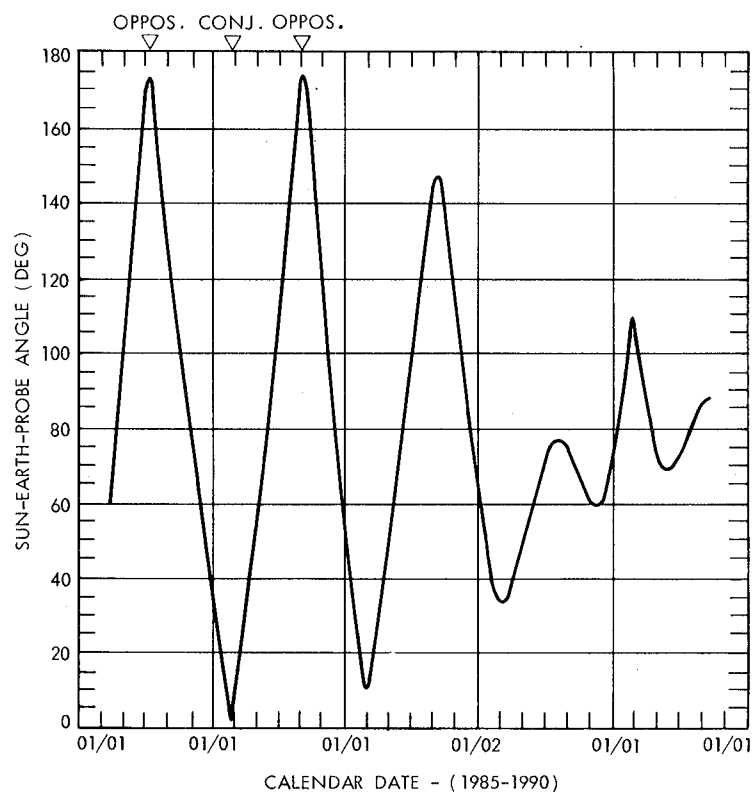
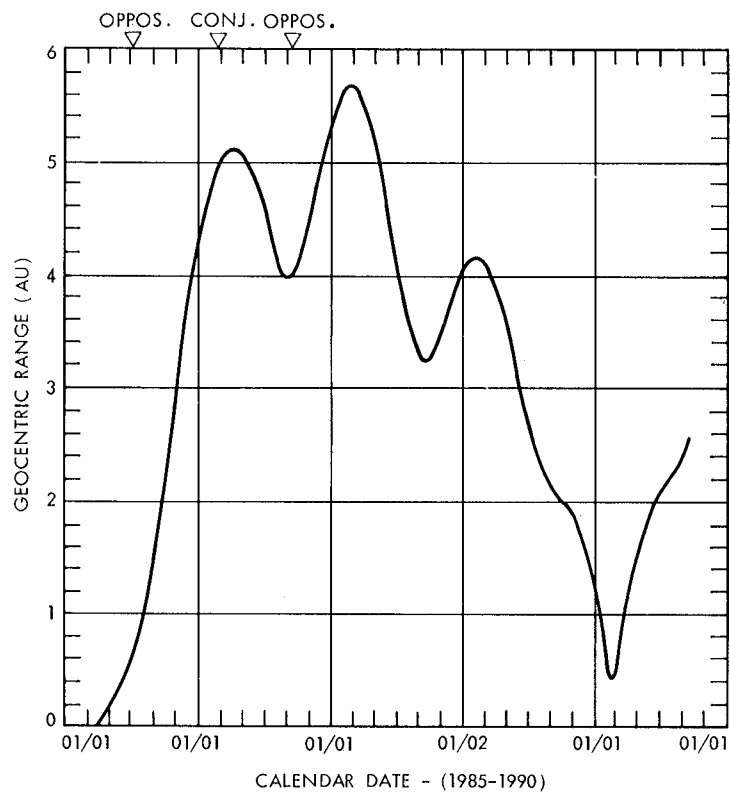
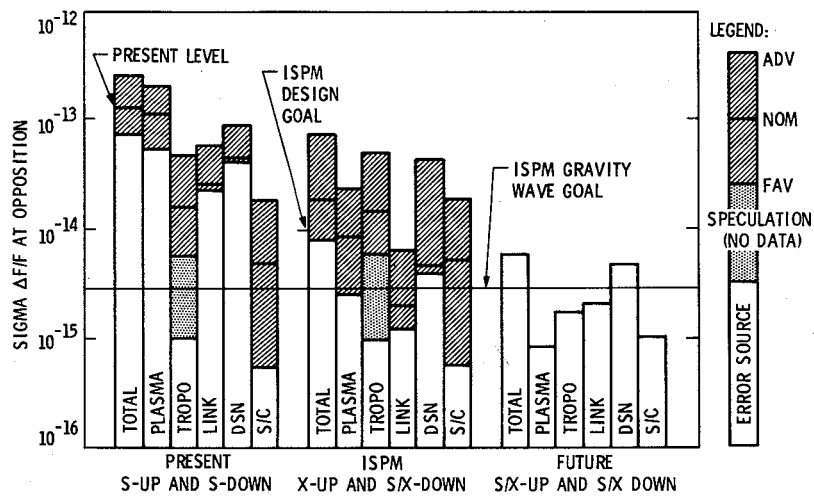


Fig. 4. ISPM X-band uplink demonstration schedule



**Fig. 5. Typical ISPM geocentric range and sun-earth-probe angle (3/29/85 launch)**



**Fig. 6. Doppler error reduction with X-band uplink at solar opposition with 1000 second sampling**

# End-to-End Quality Measure for Transmission of Compressed Imagery Over a Noisy Coded Channel

V. N. Korwar and P. J. Lee  
Communications Systems Research Section

*For the transmission of imagery at high data rates over large distances with limited power and system gain, it is usually necessary to compress the data before transmitting it over a noisy channel that uses channel coding to reduce the effect of noise-introduced errors. Both compression and channel noise introduce distortion into the imagery. In order to design a communication link that provides adequate quality of received images, it is necessary first to define some suitable distortion measure that accounts for both these kinds of distortion and then to perform various tradeoffs to arrive at system parameter values that will provide a sufficiently low level of received image distortion. This article uses the overall mean-square error as the distortion measure and describes how to perform these tradeoffs.*

## I. Introduction

For deep space missions to distant planets, the space loss is so high that it is usually necessary to compress the imaging data before transmission in order to meet the data rate requirements with the necessarily limited power levels and antenna gains normally available. Data compression or source coding introduces distortion into the received imagery, and so do errors on the noisy communication channel, even though their effect is reduced by channel coding.

In order to design the communication link, i.e., to choose the appropriate values of the several parameters that can be varied (within limits), we first need a reasonable measure of the distortion introduced into the imagery. This article defines one such measure—the overall mean-square error (MSE)—and describes how to perform the required parameter tradeoffs. The techniques used here apply to any concatenated channel coding scheme (Ref. 1) which uses an interleaver to interleave the 8-bit symbols of the outer code. As a specific example, the

coding scheme is assumed to be a Reed-Solomon outer code with 223 information symbols and 32 parity symbols, and a convolutional inner code with rate 1/2. Two interleaving schemes, denoted A and B in Ref. 2, are considered. The source coding scheme is assumed to be Rice's RM2 (Ref. 3).

Traditionally, the channel bit-error-probability (BEP) has been used at JPL as a measure of acceptability of the overall image communication system. For PCM-coded (uncompressed) images, the JPL rule-of-thumb is that a BEP of  $10^{-3}$  to  $5 \times 10^{-3}$  provides acceptable image quality. However, since there are very few images, simulated or otherwise, that include the effects of both channel errors and data compression (source coding) by some algorithm like the Rice algorithms (Refs. 3 and 4), it is not clear what value of BEP can be equated to "acceptable image quality" for compressed imagery. Some simulations of this kind have been done, but only for a compression ratio  $r$  (=uncompressed data rate/compressed data rate) of 2 and the BARC algorithm (Ref. 4), whereas

from link analysis it appears that higher values of  $r$  and the RM2 algorithm will be needed for missions to the outer planets under certain conditions.

Although it is true that the concatenated channel error rate drops off as the bit-energy-to-noise ratio increases, this increase requires an increased transmitting antenna diameter  $D_t$  or higher compression ratio. Beyond a certain point (see Ref. 5 or Eq. A-1 in the Appendix) increasing  $D_t$  does not help because pointing losses increase rapidly with  $D_t$ . Thus  $D_t$  is usually no more than 5 m (unless electronic pointing techniques can be used). The alternative of increasing  $r$  causes increased image distortion and there is a theoretical bound on how much  $r$  can be increased while keeping the distortion below a certain level, no matter how the distortion is defined and no matter what channel coding or data compression scheme is used. Therefore, it is necessary to perform an analysis that takes both channel and source coding errors into account.

A very large number of simulations of pictures compressed by the RM2 algorithm in the presence of channel errors would be needed before reliable subjective results can be obtained, and such simulations are not currently available and are obviously time-consuming. So we have obtained, instead, an estimate of overall mean-square error (MSE) in RM2-compressed images transmitted over the concatenated code channel. Much as the MSE and other objective measures of picture quality are looked down upon, the alternative is too time-consuming, and the authors of most papers describing a new compression scheme calculate the MSE or something related, in addition to performing a few simulations. See, for example, papers describing new compression schemes such as Blosser, et al. (Ref. 6), or statements about the popularity of MSE in articles dealing with image quality (Refs. 7 and 8); similarly, in the chapters describing various coding schemes, Pratt (Ref. 9) discusses MSE to a great extent. Besides, the correlation between subjective measures and MSE is of the order of 0.7 to 0.8 (Ref. 7), which is quite high, although not high enough to make MSE, in general, a very reliable measure.

Combining MSE calculations with link analysis, one can select the overall communication system parameter values.

## II. The System

Figure 1 shows the system block diagram.

The output of the source encoder is a stream of bits consisting of a continuously variable number of bits per pixel encoded. This stream is divided into 8-bit 'symbols' and a number  $k$  of these (which we will take to be 223) are encoded

into an  $n$ -symbol 'codeword' by the outer encoder ( $n$  is taken to be 255). A block of  $I$  (taken to be 16) codewords, called a 'code block' or CB is interleaved in the interleaver, and the output, again regarded as a stream of bits, is encoded by the rate 1/2 inner encoder. This is then modulated and transmitted to the receiving end, where the procedure is reversed.

For convenience, we assume that the imaging camera produces pictures consisting of 800 lines per picture, 800 pixels per line and 8 bits per pixel. The camera rate can then be defined as  $R_c$  = the number of pictures per hour, or  $R_d$  = bits/sec. The compression ratio  $r$  is defined as

$$r = \frac{8 \text{ bits/pixel}}{\text{average number of bits/pixel at source encoder output}}$$

We consider cases where  $r \leq 16$ . The quantities  $R_s, R_b, R_o, R_d$  are data rates (bits/sec) at the channel output, the inner decoder output, the outer decoder output, and the camera output respectively. They are related by:

$$R_d = r \times R_o, R_o = \frac{223}{255} R_b, R_b = \frac{1}{2} R_s$$

$E_s, E_b, E_o$  are the received energy per bit measured at the channel output, the inner decoder output, and the outer decoder output. They are related by:

$$E_o = \frac{255}{223} E_b, E_b = 2E_s$$

$P_b$  is the probability of a bit error on the inner channel, while  $P_o$  is the probability of a codeword error in the overall channel.

## III. Picture Quality

The picture quality measure defined here will be calculated in several steps. In Section III.A.1, below, the effects of a channel error, i.e., the basic equations describing the effect of an error in a codeword output by the outer decoder, will be considered. The procedure followed by Rice (Ref. 2) will be used, but slightly more refined calculations will be given. In Section III.A.2, these results are used to obtain a mean-square error,  $MSE^{(c)}$ , due to channel errors. Section III.B deals with the  $MSE^{(s)}$  due to source coding distortion. In Section III.C, the  $MSE^{(s)}$  due to source coding distortion is combined with the results of Section III.A to get an end-to-end picture quality measure, namely, the overall (normalized)  $MSE^{(t)}$

## A. Effect of Channel Errors on Picture Quality

1. **Basic equations.** The only property of the RM2 algorithm that we will use in this and the next subsection, is that RM2 divides each picture into  $64 \times 64$  pixel sub-pictures called "source blocks" (SB), encodes each of these independently, and serially outputs the pixels of each encoded SB, scanned row-wise. Some sort of synchronizing information is also assumed, which enables the start and finish of each encoded source block to be clearly recognized.

RM2 generates an encoded version of each SB by transforming the SB as a whole, so that a single bit error in the SB can conceivably spoil the whole SB. This may be a somewhat conservative assumption. We also assume that the beginning of a channel codeword need not be synchronized with the beginning of an SB, so that there is always a possibility that a single codeword error affects more than one SB, whatever the relative lengths of the codeword and SB. We assume that each SB spanned by an erroneous codeword is "lost" or unusable. This is reasonable if the erroneous bits in an erroneous codeword are distributed uniformly through the codeword, so that each SB spanned, with high probability gets at least one bad bit.

We now calculate the average number of SBs lost per codeword error.

Whenever a codeword error occurs, it affects only 223 consecutive information symbols. In interleaver scheme A (Ref. 2), these information symbols also correspond to contiguous portions of the picture encoded. However, interleaver B (Ref. 2) forms each codeword by choosing every 16<sup>th</sup> symbol output by the source coder as successive information symbols in the codeword. Because of this, a single codeword error can span a whole information code block (CB). Thus, the two cases (A and B) need to be treated separately.

*a. Interleaver A.* Suppose codeword No. 2 is in error, then the symbols labelled 224, 225, . . . 446 may be in error. Hence only one or two SBs are lost by a single codeword error for  $r \leq 16$ . The number of lost SBs per codeword error depends on the relative location of the SBs and the codeword. Figure 2(A) illustrates the situation for  $r = 4$ . One SB is lost in case A-1 and two in case A-2.

The number of bits per source block,  $b_r$ , after source coding with compression ratio  $r$ , is

$$b_r = \frac{8}{r} \times 64 \times 64 \quad \text{bits per compressed SB}$$

Let  $S_A$  be the number of bits affected by a codeword error, and let  $\delta_r$  be the probability that one compressed source block

with compression ratio  $r$  is lost by a codeword error. Then

$$S_A = 223 \times 8 = 1784 = (\text{bits affected by a codeword error})$$

$$\delta_r = \frac{b_r + 1 - S_A}{b_r}$$

Hence the average number of lost source blocks per codeword error when using interleaver type A and compression ratio  $r$ ,  $A_r$  is

$$A_r = 1 \times \delta_r + 2 \times (1 - \delta_r) = 2 - \frac{b_r + 1 - S_A}{b_r}$$

*b. Interleaver B.* Suppose codeword No. 2 is in error. Then the symbols labelled 2, 18, 34, . . . 3554, (in which consecutive symbols 1, 2, . . . represent the successive elements in an SB scanned row-wise) may be in error. Let  $S_B$  be the range in number of bits affected by a codeword error when using interleaver type B. Also let  $C_r$  be the smallest number of compressed source blocks which are affected by a codeword error, and  $\gamma_r$  be the probability that  $C_r$  source blocks are lost by a codeword error.

$$S_B = 3553 \times 8 = 28424 (\text{bits affected by a codeword error})$$

$$C_r = \lceil S_B / b_r \rceil$$

$$\gamma_r = \frac{C_r \times b_r + 1 - S_B}{b_r}$$

where  $\lceil x \rceil$  is the smallest integer greater than or equal to  $x$ . Figure 2(B) shows these situations ( $b_4 = 8192$  bits,  $C_4 = 4$ ). The case B-1, where four source blocks are lost, happens with probability  $\gamma_4$ . The only alternative case (B-2), where five source blocks are lost, happens with probability  $(1 - \gamma_4)$ . Hence, in general, the average number of lost source blocks per codeword error when using interleaver type B and compression ratio  $r$ ,  $B_r$  is

$$B_r = C_r \times \gamma_r + (1 + C_r) \times (1 - \gamma_r) = 1 + C_r$$

$$= \frac{C_r \times b_r + 1 - S_B}{b_r}$$

The values of  $A_r$  and  $B_r$  are shown in Table 1 for values of  $r$  between 2 and 16. These numbers are refined versions of those calculated by Rice (Ref. 2). For  $r = 1$ , i.e., the no compression case,

$$A_1 = B_1 = \frac{223 \times 8}{64 \times 64 \times 8}$$

since no source block structure is used.

**2. Average normalized mean-square error  $MSE^{(c)}/\sigma^2$  due to channel errors.** We now use the basic results obtained in the previous section to calculate the MSE contribution of channel errors.

*a. Average fraction of unusable part of a picture.* Let  $N_p$  be the average number of pictures transmitted between codeword errors. Then

$$\begin{aligned} N_p &= \text{Avg. \# of pictures per codeword error} \\ &= (\text{\# of pictures per SB}) \times (\text{\# of SBs per codeword}) \\ &\quad \times (\text{\# of codewords per codeword error}) \\ &= \frac{1}{157} \times \frac{223}{\frac{1}{r} \times 64 \times 64} \times \frac{1}{P_o} = \frac{1}{P_o} \times r \times \frac{223}{64 \times 64 \times 157} \end{aligned}$$

where

$$\begin{aligned} &\text{\# of source blocks per picture} \\ &= \left\lceil \frac{800 \times 800 \text{ pixels per picture}}{64 \times 64 \text{ pixels per SB}} \right\rceil = 157 \end{aligned}$$

and

$$\begin{aligned} &\text{\# of compressed source blocks per codeword} \\ &= \frac{223 \times 8 \text{ bits per codeword}}{64 \times 64 \times \frac{8}{r} \text{ bits per SB}} = \frac{223}{\frac{1}{r} \times 64 \times 64} \end{aligned}$$

Let's assume that the probability of more than one codeword error for each bad picture is very small, and hence ignored. Then  $N_p$  is equivalent to the average number of

pictures transmitted per bad picture, and  $A_r$  (or  $B_r$ ) is equivalent to the average number of lost source blocks in one bad picture when using compression ratio  $r$  and interleaver type A (or B). Here a bad picture means the picture is corrupted by channel errors, i.e., contains lost SBs.

The quality factor due to channel errors,  $Q_c$ , is defined as the average usable fraction of a picture. Then in terms of the user's choice parameter  $\beta$  (which we will soon explain) and with the terms already defined,  $Q_c$  can be expressed as:

$$\begin{aligned} Q_c &= \left( \frac{\text{\# of good pictures}}{\text{total \# of pictures}} \right) \\ &\quad + \beta \times \left( \frac{\text{\# of bad pictures}}{\text{total \# of pictures}} \right) \\ &\quad \times \left( \frac{\text{\# of good SB's in a bad picture}}{\text{total \# of SB's in a bad picture}} \right) \end{aligned}$$

where

$$\frac{\text{\# of bad pictures}}{\text{total \# of pictures}} = \frac{1}{N_p} = 1 - \frac{\text{\# of good pictures}}{\text{total \# of pictures}}$$

and

$$\frac{\text{\# of good SB's in a bad picture}}{\text{total \# of SB's in a bad picture}} = \frac{157 - A_r \text{ (or } B_r)}{157}$$

Therefore,

$$\begin{aligned} Q_c &= \left( 1 - \frac{1}{N_p} \right) + \beta \times \frac{1}{N_p} \times \left( 1 - \frac{A_r \text{ (or } B_r)}{157} \right) \\ &= 1 - P_o \times \frac{1}{r} \times \frac{64 \times 64}{223} \left\{ (1 - \beta) \times 157 + \beta \times A_r \text{ (or } B_r) \right\} \end{aligned}$$

The  $\beta$  is a user's choice parameter taking on values between 0 and 1. Here  $\beta = 0$  means the user throws away a bad picture however good some portions of it may be. This may not be reasonable since the user always wants to maximize his information return;  $\beta = 1$  means the user utilizes all of the good portion of a bad picture. But this may also be unreasonable because of edge effects of the lost source blocks and because when  $r = 1$  (no compression case), it is usually hard to tell which part of a bad picture is really bad. We will choose  $\beta = 0.99$  for later calculations.

We then define  $Q_c = 1 - Q_c$ , which is the average unusable fraction of a picture. In Fig. 3,  $1/Q_c$  in dB (at  $P_o = 10^{-4}$ ) is plotted for various values of  $r$  and  $\beta$ . It is noticeable that for  $r > 1$ , regardless of the value of  $\beta$ , the quality improves ( $Q_c$  decreases) when we compress more ( $r$  increases). This is due to the fact that the total number of pictures increases with  $r$  although the total number of lost SBs per codeword error remains almost the same or very slowly increases. The case of  $r = 1$  is quite interesting. For  $\beta = 1$ , the quality with  $r = 1$  is higher than with  $r \geq 2$ . But for  $\beta < 0.9$ , the quality with  $r = 1$  is worse than with  $r \geq 2$ ; and for  $\beta = 0.99$ , the quality with  $r = 1$  is almost the same as with  $r \geq 2$ .

*b. Calculation of  $MSE^{(c)}/\sigma^2$ .* The relationship between the average unusable fraction of a picture,  $Q_c$ , and the average normalized MSE due to channel error,  $MSE^{(c)}/\sigma^2$ , is now calculated. The subscript or superscript "c" is for channel error. The assumptions used in this calculation are that the gray level distribution of a pixel is uniform from 0 to 255, and that when a pixel is corrupted by channel errors, the gray level of the reproduced pixel is arbitrarily changed to one of these 256 levels. Then the average MSE (mean-square error) for that pixel is:

$$MSE = \frac{1}{256 \times 256} \times \sum_{i=0}^{255} \sum_{j=0}^{255} (i-j)^2 = 10922.5$$

The  $\sigma^2$  for the uniform 256 gray level distribution is:

$$\sigma^2 = \int_{-128}^{128} x^2 \times \frac{1}{256} \times dx = 5461.33$$

Now suppose we have one bad pixel among 1000 pixels. This is equivalent to  $Q_c = 10^{-3}$ . On the other hand, the average normalized MSE for those 1000 pixels with one bad pixel caused by channel errors is:

$$\frac{MSE^{(c)}}{\sigma^2} = \frac{1}{1000} \times \frac{10922.5}{5461.33} = 2.00 \times 10^{-3}$$

Generalizing from the above observation, we have the following simple relationship between  $MSE^{(c)}/\sigma^2$  and  $Q_c$ :

$$\frac{MSE^{(c)}}{\sigma^2} = 2 Q_c$$

## B. Average Normalized Mean-Square Error Due to Source Coding, $MSE^{(s)}/\sigma^2$

Even when there is no channel error, there usually exists a degradation due to source coding. Rice (Ref. 10) measured root mean-square error (RMSE) for a particular picture, where the value of  $\sigma$  was specified, for values of  $r$  between 4 to 16, using RM2. Hence the average normalized MSE due to source coding,  $MSE^{(s)}/\sigma^2$ , can be obtained from his results for those values of  $r$ . For  $r = 2$ , a rough value of RMSE was obtained by extending the graph of Rice's Fig. 1 (Ref. 10). For  $r = 1$ , the value of  $MSE^{(s)}/\sigma^2$  was calculated with the assumption of the source having a Gaussian distribution.

## C. End-to-End Picture Quality Measure $MSE^{(t)}/\sigma^2$

The total end-to-end normalized MSE,  $MSE^{(t)}/\sigma^2$  can be defined as the sum of average normalized MSEs for the usable portion of a picture and for the unusable portion of a picture. In the unusable portion, we assume the loss due to channel error dominates over the degradation due to source coding, and ignore the latter. On the other hand, in the usable portion of a picture, since there is no channel effect, only the degradation due to source coding is considered. Recall that  $Q_c = 1 - Q_c$  is the average usable fraction of a picture. Hence

$$\begin{aligned} \frac{MSE^{(t)}}{\sigma^2} &= \frac{MSE}{\sigma^2} \text{ for the usable parts of a picture} \\ &+ \frac{MSE}{\sigma^2} \text{ for the unusable parts of a picture} \\ &= \frac{MSE^{(s)}}{\sigma^2} \times (1 - Q_c) + \frac{MSE^{(c)}}{\sigma^2} \\ &= \frac{MSE^{(s)}}{\sigma^2} \times (1 - Q_c) + 2 \times Q_c \end{aligned}$$

Its inverse, i.e., signal-to-noise ratio (SNR), is a better representation of the quality measure, since quality improves with increasing SNR. Hence, we have the picture quality  $Q$  from the above results:

$$Q = SNR_{dB} = -10 \log_{10} \frac{MSE^{(t)}}{\sigma^2}$$

In Fig. 4, curves of the picture quality  $Q$  in  $SNR_{dB}$  versus codeword error probability  $P_o$  are shown, with compression

ratio  $r$  and interleaver-types as parameters. For very low error cases ( $P_o \leq 10^{-6}$ ), the channel error effects diminish, and  $MSE^{(t)} \approx MSE^{(s)}$ . Also, for these values of  $P_o$ , the use of interleaving scheme B is almost the same as that of scheme A. For high error rates ( $P_o \geq 10^{-3}$ ), the channel error effect term in the total end-to-end MSE dominates over the term of degradation due to source coding. Also, the order of acceptability in quality is the same as that of Fig. 3, since only channel error terms are considered in this region of  $P_o$ .

The SNRs for the 5-bit and 6-bit uniform Max (Ref. 11) quantizers are 24.6 dB and 29.8 dB respectively. Imagery quantized using the 5-bit uniform quantizer is generally considered to be "usable" (Ref. 9). Hence the desired quality  $Q$  in terms of SNR will be in the range of 25 to 30 dB.

#### IV. Using the Quality Measure in Overall System Design

Figure 4 gives the picture quality as a function of codeword error probability  $P_o$ , for the case where an  $n = 255$ ,  $k = 223$  outer code having 8 bits/symbol is concatenated with a rate

1/2 inner code. For any specific concatenated code with these parameters, we can relate  $P_o$  to the bit energy to noise ratio  $E_o/N_o$ . Then, using link analysis (see Appendix), we can relate  $E_o/N_o$  to system parameters by an equation such as Eq. (A-2). By this sequence of steps, the overall system parameters like antenna diameter, transmitter power, etc., can be chosen to obtain a desired level of picture quality for a given camera rate  $R_d$  (bits/sec) or  $R_c$  (pictures/hour).

#### V. Summary

We have shown how to obtain an end-to-end picture quality measure  $Q$  when compressed imagery is transmitted over a concatenated channel. Calculations are given for the specific case of an outer code with 223 information symbols and 32 parity symbols, 8 bits/symbol, and a rate 1/2 inner code, where the compression ratio is between 1 and 16. Similar calculations can be made for any other concatenated channel, to obtain quality  $Q$  as a function of codeword error probability  $P_o$  for various compression ratios. Link analysis, together with performance curves for the specific code used, enable  $Q$  to be incorporated into the overall system parameter design.

## References

1. Forney, G. D., *Concatenated Codes*, MIT Press, Cambridge, Massachusetts, 1966.
2. Rice, R. F., "Channel coding and data compression system considerations for efficient communication of planetary imaging data," Technical Memorandum 33-695, Jet Propulsion Laboratory, Pasadena, California, July 1974.
3. Rice, R. F., "An advanced imaging communication system for planetary exploration," *SPIE*, Vol. 66, pp. 70-89, Aug. 21-22, 1975.
4. Rice, R. F., et al., "Block adaptive rate controlled image data compression," *IEEE Conference Proceedings CH1514-9/79*, pp. 53.5.1-53.5.6, Sept. 1979.
5. Edelson, R. E., et al., "Telecommunications system design techniques handbook," Technical Memorandum 33-571, Jet Propulsion Laboratory, Pasadena, California, July 1974.
6. Blosser, R., and Rosenheck, B., "A comparative critique of two-dimensional imagery compression coding (spatial distance and spatial transform)," *IEEE Conference Proceedings CH1514-9/79*, pp. 53.3.1-53.3.8, Sept. 1979.
7. Parsons, J. R. and Tescher, A. G., "An investigation of MSE contributions in transform image coding schemes," *SPIE*, Vol. 66, pp. 196-206, Aug. 21-22, 1975.
8. Pearson, J. J., Millman, M. W., and Maitra, S., "Image quality considerations of compressed video imagery," *Proceedings of the International Telemetry Conference*, Los Angeles, California, pp. 51-57, Nov. 14-16, 1978.
9. Pratt, W. K., *Digital Image Processing*, Wiley, New York, 1978.
10. Rice, R. F., "RM2: rms error comparisons," Technical Memorandum 33-804, Jet Propulsion Laboratory, Pasadena, California, Sept. 15, 1976.
11. Max, J., "Quantizing for minimum distortion," *IRE Transactions on Information Theory*, Vol. IT-6, pp. 7-12, March 1960.

**Table 1. Average number of lost source blocks per codeword error**

$r$	2	4	8	16
$A_r$	1.109	1.218	1.435	1.871
$B_r$	2.735	4.470	7.939	14.88

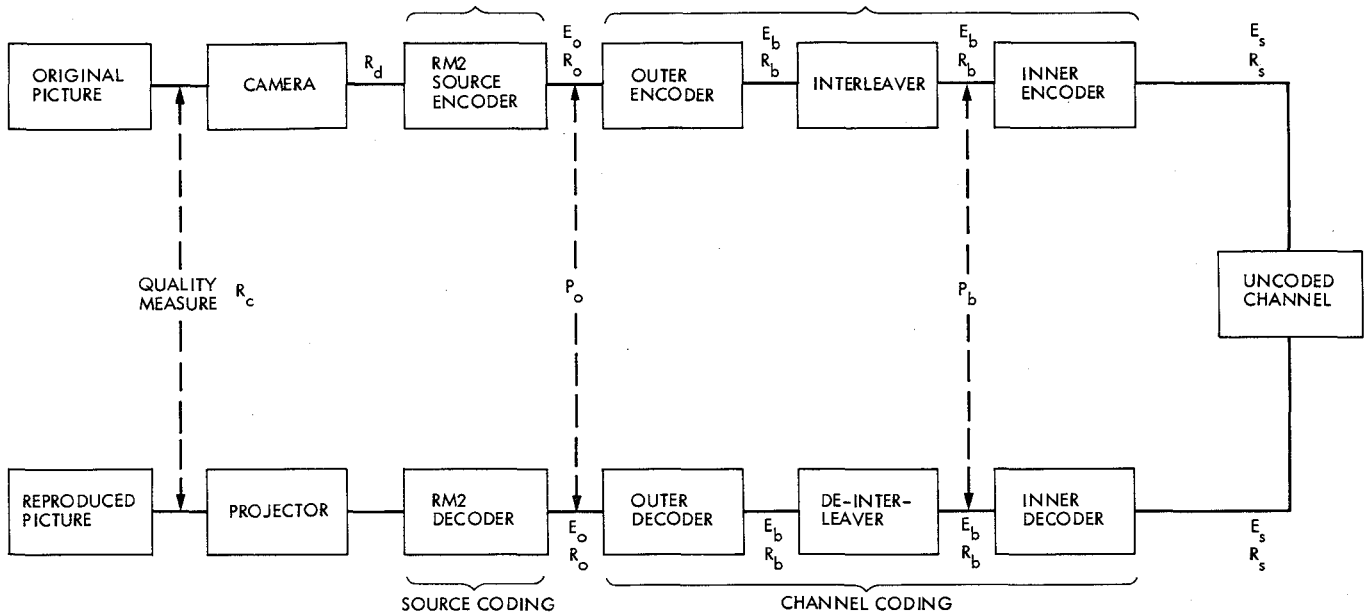


Fig. 1. System diagram

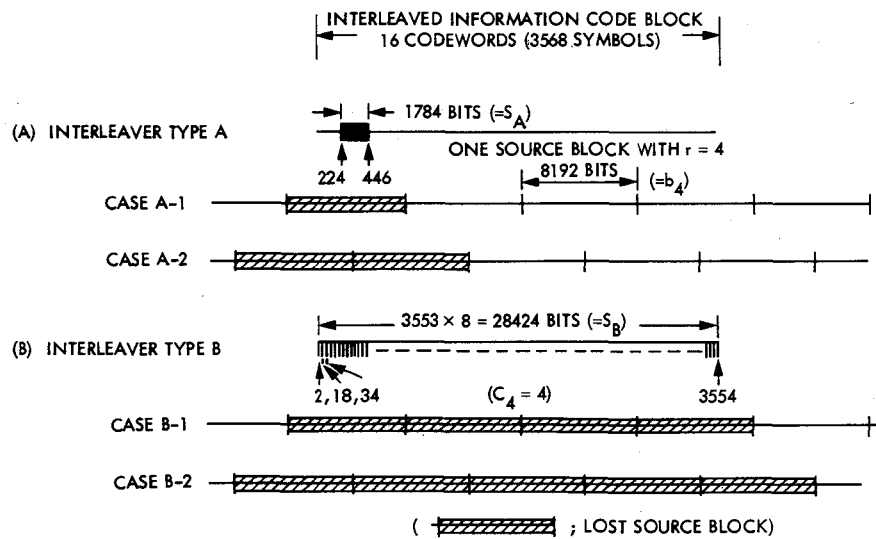


Fig. 2. Effect of a codeword error on the compressed source blocks;  $r = 4$ , codeword #2 in error

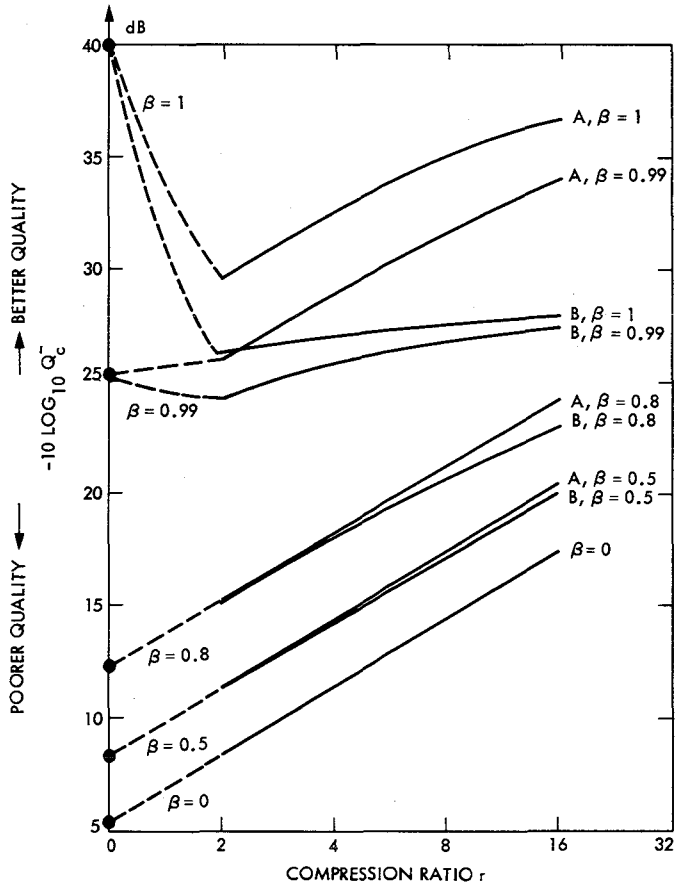


Fig. 3.  $1/Q_c$  at  $P_o = 10^{-4}$

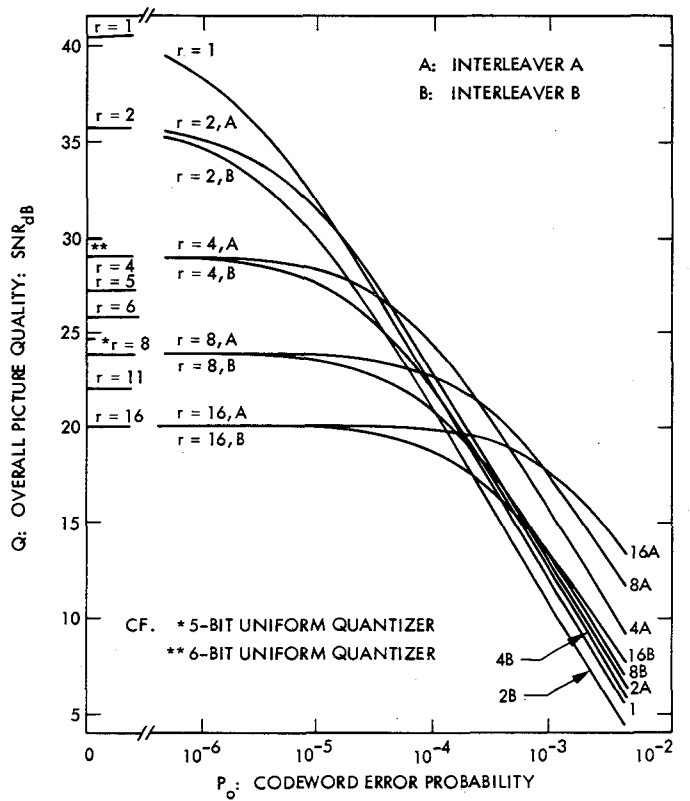


Fig. 4. Picture quality vs  $P_o$  with compression ratio  $r$  and types of interleaver A and B as parameters

## Appendix

Let

$S_t$  = Transmitter power

$f_o$  = carrier frequency

$L$  = earth-spacecraft separation

$\eta_t$  = transmitting antenna area efficiency

$N_o$  = one-sided noise spectral density of receiving system

$G_r$  = receiving antenna gain

$L_w$  = attenuation due to weather

$M_w$  = operating margin calculated from parameter tolerances

$D_t$  = transmitting antenna diameter

$L_p$  = transmitting antenna pointing loss which is a function of  $D_t$  given by

$$L_p = \frac{\sin^2 (2.78 \theta_{pt}/\theta_{Bt})}{(2.78 \theta_{pt}/\theta_{Bt})^2} \quad (\text{A-1})$$

where

$\theta_{pt}$  = pointing error in degrees

$\theta_{Bt}$  = antenna beamwidth in degrees

$$= 177.9259 \times \eta_t^{-1/1.96} \left( \frac{\pi D_t}{\lambda} \right)^{-2/1.96}$$

$L_1$  = all other system losses

We further assume that the spacecraft camera output rate  $R_d$  in bps is fixed, corresponding to  $800 \times 800$  pixels per picture, 8 bits/pixel, and  $R_c$  pictures per hour, so that the data compressor output rate is  $R_o = R_d/r$  bps. In terms of these parameters, the link performance equation is

$$\frac{E_o}{N_o} = \left( \frac{S_t}{R_d} \right) r (D_t^2 L_p) M_w L_w \left( \frac{\eta_t G_r L_1}{16 N_o L^2} \right) \quad (\text{A-2})$$

# Calculation of Atmospheric Loss From Microwave Radiometric Noise Temperature Measurements

C. Stelzried and S. Slobin

Radio Frequency and Microwave Subsystems Section

*Microwave propagation loss in the atmosphere can be inferred from microwave radiometric noise temperature measurements. The relevant equations are given and a derivation and calculation is made assuming various physical models. Comparison is made with the commonly used lumped element atmospheric model (isothermal and uniform loss) and the model with linear temperature and exponential loss distributions. The results are useful for estimating the integral inversion differences due to the model selection. This indicates that the commonly used lumped element atmospheric model is a very good approximation with judicious choice of the effective physical temperature. For the worst case comparison, the lumped element model agrees with the variable parameter model within 0.2 dB up to a propagation loss of 3 dB.*

## I. Summary

Microwave propagation loss in the atmosphere can be inferred from microwave radiometric noise temperature measurements. Conventionally, the total propagation loss ratio  $L$  is calculated from measurements of the noise temperature contribution  $T''$  using the relationship  $T'' = Tp(1 - 1/L)$  where  $Tp$  is a mean effective physical temperature of the atmosphere. This relationship assumes that the propagation loss and physical temperature can be treated as lumped constants. An "incorrect" choice for  $Tp$  results in an error in the determination of  $L$ . The equation for the radiometric noise temperature contribution due to the propagation path are derived for various combinations of loss and temperature contributions. These are useful to reduce the error in propagation loss determination. Although it may not be practical or necessary to use this technique in most applications, the analysis is valuable for estimating the integral inversion difference due to the model selection. Conversely, the technique can be used to improve the estimate of  $Tp$  required for computation of  $L$  using the lumped element model.

## II. Introduction

Radiometric microwave noise temperature measurements can be used to estimate atmospheric transmission loss (Refs. 1, 2, 3, 4). Treating the atmosphere as a lumped element, the noise temperature contribution is given by

$$T'' = Tp(1 - 1/L) \quad (1)$$

where

$L$  = propagation path loss (absorption only, no scattering), ratio  $[L(\text{dB}) = 10 \log_{10} L], \geq 1.0$

$Tp$  = atmosphere mean effective physical temperature, Kelvins

The atmospheric loss is usually calculated from radiometric measurements of  $T''$  using an assumed value for  $TP$  ( $\approx 260$ -

280 K). The purpose of this article is to compare values computed for  $L$  in this manner with those computed using a more realistic temperature and loss distribution. These results can either be used directly or as a measure of modeling error in the integral inversion.

### III. Theory

The translated radiometric noise temperature (Fig. 1) of a source at a temperature  $T$  (Ref. 5) propagating through a medium (such as the atmosphere or a transmission line) is given by (assuming  $hf \ll kT$ , so that the Rayleigh-Jeans law low-frequency approximation to Planck's radiation law is valid and the noise temperature is proportional to noise power)

$$T' = T'' + T/L \quad (2)$$

where

$T''$  = radiometric noise temperature contribution of the propagation path,  $K$

$$L = e^{\int_0^{\ell} \alpha(x) dx}$$

$\alpha(x)$  = transmission medium propagation constant<sup>1</sup> at  $x$ , nepers/m,  $[=(dB/m)/10 \log_{10} e]$

and

$$\begin{aligned} T'' &= \int_0^{\ell} \alpha(x) T(x) e^{-\int_x^{\ell} \alpha(x') dx'} dx \\ &= \frac{1}{L} \int_0^{\ell} \alpha(x) T(x) e^{\int_0^x \alpha(x') dx'} dx \end{aligned} \quad (3)$$

where

$T(x)$  = physical temperature at  $x$ , Kelvins

<sup>1</sup>This definition is consistent with radiative transfer theory (Ref. 6) and should not be confused with the transmission line voltage propagation constant  $(dB/m)/20 \log_{10} e$ .

### IV. Models

The first model is the simplest. Assume uniform temperature and propagation constant distributions

$$T(x) = Tp$$

$$\alpha(x) = \alpha$$

Then

$$L = e^{\alpha \ell}$$

and

$$\begin{aligned} T'' &= \frac{\alpha Tp}{L} \int_0^{\ell} e^{\alpha x} dx \\ &= Tp (1 - 1/L) \end{aligned} \quad (4)$$

This derivation agrees with Eq. (1).

The second model is the most realistic investigated. Assume for the propagation path linear temperature and exponential propagation constant distributions (Fig. 2)

$$T(x) = T_1 + (T_2 - T_1) x/\ell$$

$$\alpha(x) = \alpha_1 e^{ax} \quad (5)$$

where

$T_1, T_2$  = physical temperatures of the propagation path at  $x = 0$  and  $\ell$ , Kelvins

$\alpha_1, \alpha_2$  = propagation constants of the propagation path, at  $x = 0$  and  $\ell$ , nepers/m,

$$a = (1/\ell) \ln(\alpha_2/\alpha_1)$$

Then

$$T'' = \frac{\alpha_1}{L} \int_0^{\ell} e^{ax} [T_1 + (T_2 - T_1) x/\ell] e^{\int_0^x \alpha_1 e^{ax'} dx'} dx$$

and replacing  $x$  with  $\ell y$

$$T'' = \frac{\alpha_1 \ell}{L} \int_0^1 e^{\alpha_2 \ell y} [T_1 + (T_2 - T_1)y] e^{-\frac{\alpha_1}{\alpha_2} (e^{\alpha_2 \ell y} - 1)} dy \quad (6)$$

where

$$L = e^{\frac{\alpha_1 \ell [(\alpha_2/\alpha_1) - 1]}{\ln(\alpha_2/\alpha_1) - 1}}, \quad \alpha_1 \ell = \frac{\ln L \ln(\alpha_2/\alpha_1)}{(\alpha_2/\alpha_1) - 1}$$

These models and others are illustrated in Table 1. Computation of  $T''$  is possible in terms of  $L$ ,  $T_1$ ,  $T_2$  and the ratio  $(\alpha_2/\alpha_1)$  using numerical integration. Conversely, an estimate of the total atmospheric loss  $L$  may be calculated using a measured value of  $T''$  and an atmospheric model with parameters  $T_1$ ,  $T_2$  and the attenuation ratio  $(\alpha_2/\alpha_1)$  with iterative solutions. Models 1 and 2 are compared in Fig. 3 assuming  $(\alpha_2/\alpha_1) = 10$ ,  $T_1 = 250$  K,  $T_2 = 290$  K. For Model 1,

Case 1:

$$Tp = \frac{T_1 + T_2}{2} \quad (7)$$

This provides a rough estimate of the effective physical temperature as the mean of the upper and lower temperatures of the lossy propagation path.

Case 2:

$$Tp = \left( \frac{\alpha_1}{\alpha_1 + \alpha_2} \right) T_1 + \left( \frac{\alpha_2}{\alpha_1 + \alpha_2} \right) T_2 \quad (8)$$

This provides a judicious choice of effective physical temperature, weighted toward the region of higher loss, improving the agreement between models.

Case 3:

$$Tp \approx A \left( \frac{\alpha_1}{\alpha_1 + \alpha_2} \right) T_1 + B \left( \frac{\alpha_2}{\alpha_1 + \alpha_2} \right) T_2 \quad (9)$$

This formulation can be used for even closer agreement between models.  $A$  and  $B$  are chosen to minimize the model

difference with perturbations in  $T_1$  and  $T_2$ . For example, using  $(\alpha_2/\alpha_1) = 10$ ,  $L = 10$ , and  $T_1 = 270$  K (20 K increase) and  $T_2 = 290$  K (unchanged) we have from Eq. (6),  $T'' = 257.7$  K. Equation (1) is then satisfied with  $Tp = 286.3$  K. Similarly for  $T_1 = 250$  K (unchanged) and  $T_2 = 310$  K (20 K increase),  $T'' = 269.0$  K and  $Tp = 299.0$  K. Then from Eq. (9), solving two equations with two unknowns,

$$A \approx 2.0$$

$$B \approx 0.90$$

$$Tp \approx 282.7 \text{ K (for } T_1 = 250 \text{ K, } T_2 = 290 \text{ K)}$$

The effect of a different  $(\alpha_2/\alpha_1)$  or other changes in  $T_1$  or  $T_2$  requires modification of  $A$  and  $B$  or further refinement of Eq. (9) as a function of  $\alpha_1$ ,  $\alpha_2$ ,  $T_1$ , and  $T_2$ .

These three cases progressively improve the agreement with the variable parameter model (Model 2) at the expense of increasing complexity. The appropriate model can be selected on the basis of the accuracy required.

These models are all in good agreement at low loss (less than 3 dB). Moderate values of propagation loss can be determined with small error from noise temperature measurements up to about 200 K. At high loss ( $L > 10$  dB) the curve of  $T''$  vs  $L$  (Fig. 3) flattens out so that very small errors in noise temperature measurement or modeling will result in very large errors in the propagation loss computation.

Now consider the situation where it is desired to determine the total atmospheric loss from radiometric noise temperature measurements  $T''$ . For Model 2, Eq. (6) can be used with measured upper and lower temperatures  $T_1$  and  $T_2$  and an assumed attenuation ratio over the region  $x = 0$  to  $\ell$  ( $\ell \approx 30$  km for oxygen and  $\ell \approx 10$  km for water vapor). An iterative computer solution can be performed until the value of  $L$  is obtained to satisfy Eq. (6). This inversion may not always be practical. An alternative, simpler method uses the lumped element model (Model 1) with a corrected  $Tp$  as described before:

$$L = \frac{Tp}{Tp - T''} \quad (10)$$

This is evaluated using the same parameters as used in Fig. 3 and is compared with the variable parameter model (Model 2). The results are shown in Table 2 and Fig. 4 for  $Tp$  corrected using cases 1, 2, and 3. For the worst case comparison (Case 1), the lumped element model agrees with the variable parameter

model (Model 2) within 0.2 dB up to a loss of 3 dB. Again, Cases 2 and 3 provide better agreement of the expense of added complexity.

## V. Conclusion

It is shown that determination of atmospheric loss from microwave radiometric noise temperature measurements is not sensitive to temperature and loss distribution assumptions at low loss ( $L < 3$  dB). For the worst case comparison (Case 1),

the lumped element model agrees with the variable parameter model (Model 2) within 0.2 dB up to a total loss of 3 dB. With higher losses, accurate inversions can be made by using a model which is closer to reality. Techniques are suggested for improving the atmospheric loss determination from radiometric noise temperature measurements using the lumped element model with corrected  $T_p$  or iterative computation of the appropriate integral solution. Although these techniques have not been compared with field measurements, the model comparisons investigated provide an estimate of the atmospheric loss determination error from radiometric measurements.

## References

1. Stelzried, C. T., "RF Techniques: 90-GHz Millimeter Wave Work," *JPL Space Programs Summary 37-43*, Vol. 4, 1967, p. 354.
2. Stelzried, C. T., and Rusch, W. V. T., "Improved Determination of Atmospheric Opacity from Radio Astronomy Measurements," *Journal of Geophysical Research*, Vol. 72, No. 9, May 1, 1967, p. 2445.
3. Damosso, E. D., and De Padova, S., "Some Considerations about Sky Noise Temperature at Frequencies above 10 GHz," *Alta Frequenza*, Vol. XLV, No. 2, Feb. 1976, p. 11E-99.
4. Seidel, B. L., and Stelzried, C. T., "A Radiometric Method for Measuring the Insertion Loss of Radome Materials," *Microwave Theory and Techniques*, Vol. MTT-16, No. 9, Sept. 1968, p. 625.
5. Stelzried, C. T., "Microwave Thermal Noise Standards," *IEEE Transactions on Microwave Theory and Techniques*, Vol. MTT-16, No. 9, Sept. 1968, p. 646.
6. Marton, L., "Methods of Experimental Physics," *Astrophysics*, Academic Press, NY, Vol. 12, Part B, p. 142.

Table 1. Summary of propagation path noise temperature contribution ( $T''$ ) calculations

Model	Parameter $\alpha(x)$	$T(x)$	$L$	$T''$
1	$\alpha$	$T_p$	$e^{\alpha \ell}$	$T_p(1 - 1/L)$
2	$\alpha_1 e^{ax}$	$T_1 + (T_2 - T_1) \frac{x}{\ell}$	$e^{\frac{(\alpha_2 - \alpha_1)\ell}{\ln(\alpha_2/\alpha_1)}}$	$\frac{\alpha_1 \ell}{L} \int_0^1 e^{a\ell y + \frac{\alpha_1}{a}(e^{a\ell y} - 1)} [T_1 + (T_2 - T_1)y] dy$
3	$\alpha$	$T_1 + (T_2 - T_1) \frac{x}{\ell}$	$e^{\alpha \ell}$	$T_1(1 - 1/L) + (T_2 - T_1)(1 - 1/\ln L + 1/L \ln L)$
4	$\alpha_1 + (\alpha_2 - \alpha_1) \frac{x}{\ell}$	$T_p$	$e^{\frac{(\alpha_1 + \alpha_2)\ell}{2}}$	$T_p(1 - 1/L)$
5	$\alpha_2 \frac{x}{\ell}$	$T_1 e^{bx}$	$e^{\frac{\alpha_2 \ell}{2}}$	$T_1 \frac{(T_2/T_1) - 1/L}{[\ln(T_2/T_1)/\ln L] + 1}$
6	$\alpha_1 + (\alpha_2 - \alpha_1) \frac{x}{\ell}$	$T_1 + (T_2 - T_1) \frac{x}{\ell}$	$e^{\frac{(\alpha_1 + \alpha_2)\ell}{2}}$	$\frac{2 \ln L}{L \left(\frac{\alpha_2}{\alpha_1} + 1\right)} \int_0^1 \left[1 + \left(\frac{\alpha_2}{\alpha_1} - 1\right)y\right] e^{\frac{\ln L}{\alpha_2 + 1} \left[2y + \left(\frac{\alpha_2}{\alpha_1} - 1\right)y^2\right]} [T_1 + (T_2 - T_1)y] dy$

where  $y = x/\ell$

$$\alpha_1, \alpha_2 = \alpha(x) \text{ at } x = 0, \ell \text{ (} y = 0, 1 \text{)}$$

$$T_1, T_2 = T(x) \text{ at } x = 0, \ell \text{ (} y = 0, 1 \text{)}$$

$$a\ell = \ln(\alpha_2/\alpha_1)$$

$$b\ell = \ln(T_2/T_1)$$

$$\alpha, \ell = \frac{\ln L \ln(\alpha_2/\alpha_1)}{(\alpha_2/\alpha_1) - 1}$$

**Table 2. Comparison of atmospheric loss calculations using variable parameter and lumped element models**

$T''$ (K)	Calculated Atmospheric Loss, $L$ (dB)							
	Measured Atmospheric Noise Temperature	<sup>a</sup> Variable Parameter Model (Model 2)	<sup>b</sup> Lumped Element Model (Model 1)			Difference		
			Case 1	Case 2	Case 3	Case 1	Case 2	Case 3
57.1	1.0	1.0	1.0	1.0	0.0	0.0	0.0	
139.5	3.0	3.2	2.9	3.0	0.2	0.1	0.0	
210.6	6.0	6.7	5.8	5.9	0.7	0.2	0.1	
254.4	10.0	12.4	9.5	10.0	2.4	0.5	0.0	

<sup>a</sup> $T_1 = 250$  K,  $T_2 = 290$  K,  $(\alpha_2/\alpha_1) = 10$

<sup>b</sup>Case 1, 2, 3;  $T_p = 270$  K, 286.4 K and 282.7 K respectively.

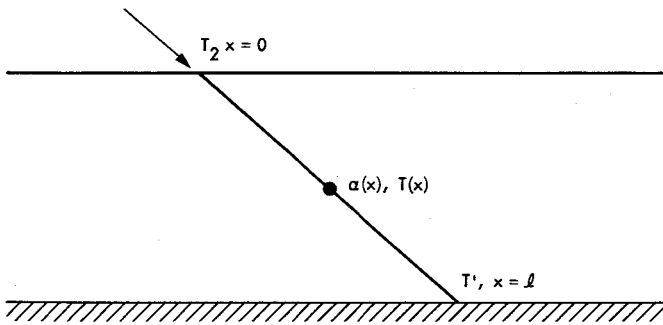


Fig. 1. Thermal noise source,  $T$ , with propagation constant  $\alpha(x)$  and physical temperature  $T(x)$  functions of position  $x$  along the propagation path, resulting in output noise temperature  $T'$

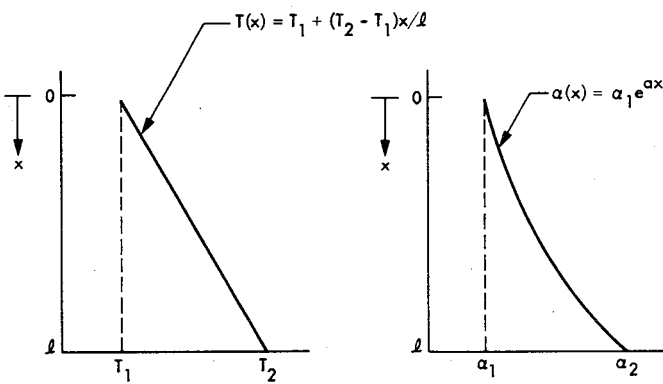


Fig. 2. Representations of temperature and propagation constant distributions in the propagation path for variable parameter model (Model 2)

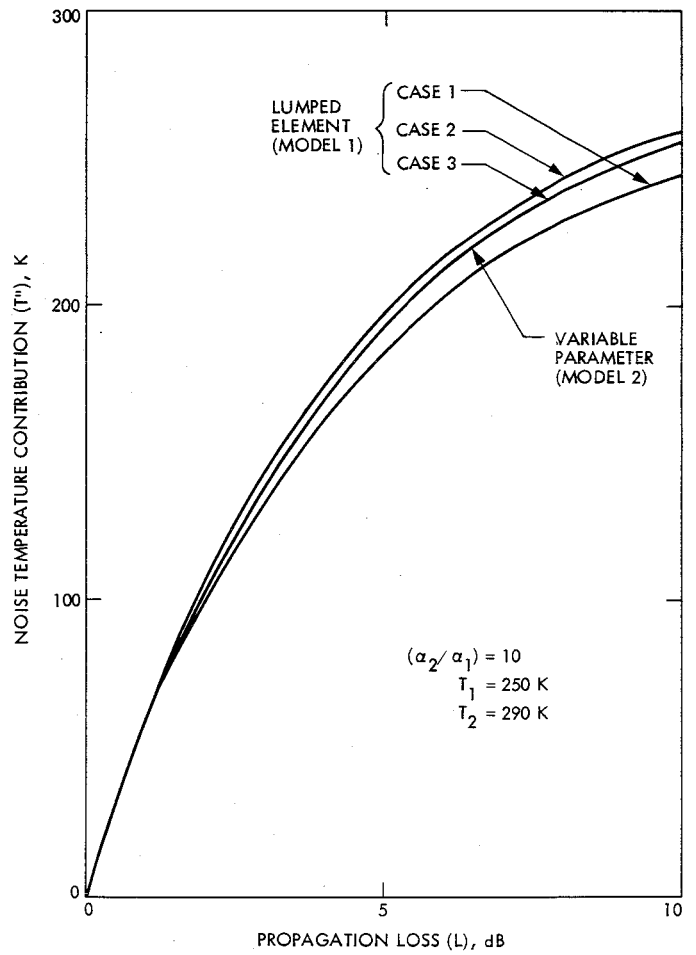
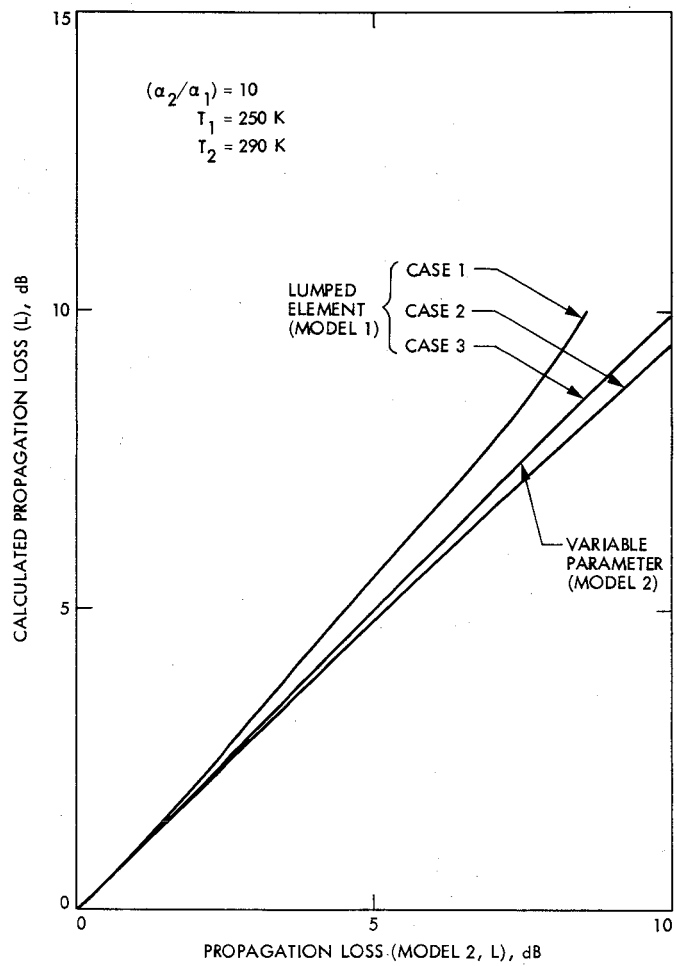


Fig. 3. Noise temperature contribution vs propagation loss



**Fig. 4. Propagation loss comparison**

# Maximizing Throughput Over an Average-Power-Limited and Band-Limited Optical Pulse Position Modulation Channel

D. Zwillinger

Communications Systems Research Section

*Given an optical pulse position modulation (PPM) channel, with an average power constraint and a bandwidth constraint, this article determines the word length needed to maximize the information throughput achievable by the channel. It is shown that, to achieve the maximal capacity, the channel must be operated with a high erasure probability. This implies that coding schemes capable of compensating for a high percentage of erasures are needed for the PPM channel.*

## I. Introduction

Many investigators have shown that pulse position modulation (PPM) is an effective method to use over the photon channel. PPM has been shown to maximize various channel parameters when the bandwidth goes to infinity (Refs. 1 and 2).

Because of the optimality of the PPM technique for infinite bandwidth, it has been thought of as a technique to use for a band-limited (realistic) channel. If it is decided to use PPM over a band-limited, average-power-limited photon channel, the PPM word size is still an arbitrary parameter. By selecting the PPM word size  $Q$ , we control the channel throughput (measured in nats/slot, which is equivalent to nats/sec since the bandwidth is fixed).

The question naturally arises as to the optimal choice of  $Q$  (denoted by  $Q^*$  for a specified system). The capacity of a channel and the  $R_{comp}$  (computation cutoff rate of the channel, also known as  $R_0$ ) of a channel are both valid measures of a channel's throughput.

Section II of this article determines the word size to maximize capacity; Section III determines the word size to maximize  $R_0$ . Section IV is a discussion.

## II. Maximizing Capacity

Let us suppose that the PPM channel allows an average power expenditure of  $P$  watts and permits us to send  $N$  slots per second. Given  $P$ ,  $N$  we would like to find the word size  $Q$  (slots/word) that maximizes the capacity  $C$  (nats/slot) of the channel. We can define the average energy (in photons) per slot  $\bar{s}$  by  $\bar{s} = P/Nh\nu$ , where  $h = 6.62 \times 10^{-34}$  j-sec is Planck's constant and  $\nu$  is the frequency of the optical radiation in Hz. Since  $P$  and  $N$  are fixed system parameters,  $\bar{s}$  is a known constant.

Let us define the following quantities:

$$W = N/Q = \text{word rate (words/sec)}$$

$$\bar{P} = \bar{s}N/W = \text{energy/word (photons/word)}$$

$$\epsilon = e^{-\bar{P}} = \text{erasure probability/word}$$

For a derivation of this formula for  $\epsilon$ , see Ref. 1. Recall that the  $Q$ -ary PPM channel is equivalent to a  $Q$ -ary erasure channel. A simple calculation gives for the  $Q$ -ary erasure channel:

$$C = \text{capacity} = (1 - \epsilon) \log Q \text{ nats/word}$$

Since there are  $W$  words/sec:

$$C = W(1 - \epsilon) \log Q \text{ nats/sec}$$

Since there are  $N$  slots/sec:

$$C = \frac{W}{N}(1 - \epsilon) \log Q \text{ nats/slot}$$

Substituting for  $W$  and  $\epsilon$  we find:

$$C = \left( \frac{1 - e^{-\bar{\nu}Q}}{Q} \right) \log Q \text{ nats/slot} \quad (1)$$

This is the form we must maximize by varying  $Q$ . Recall that  $\bar{\nu}$  is derivable from the given channel parameters.

It should be noted at this point that in Katz et al. (Ref. 3), an equation very similar to our Eq. (1) was developed to maximize the nats/photon of the channel, when the nats/sec of the channel was given. This study was conducted to minimize the power requirements of the system. The Katz paper can be viewed as a technique for the communications engineer to use when apportioning power on a spacecraft. The present paper is capable of determining the coding scheme *after* the power devoted to the communication system has been decided upon.

Figure 1 shows contours of constant  $C$  for varying  $Q$  and  $\bar{\nu}$  (utilizing Eq. 1). Note that for each  $\bar{\nu}$ , there is a best value of  $Q$ ,  $Q^*$ , such that Eq. (1) is maximized. This value can be found from Fig. 1 by drawing the line  $\bar{\nu} = \text{constant}$ , finding the  $C = \text{constant}$  curve that is tangent to this line, and, at the point of tangency, looking at the ordinate to read the value of  $Q^*$ . This has been done for various values of  $\bar{\nu}$ , and the result is Fig. 2 (which plots  $\bar{\nu}$  vs  $Q^*$ ). It is surprising how linear Fig. 2 appears. In the range  $Q^* \in [10, 1000]$  this relationship is well approximated by

$$Q^* \bar{\nu}^{0.817} = 1.36$$

Now recall that  $\epsilon$ , the erasure probability, is given by  $\epsilon = \exp(-\bar{P}) = \exp(-\bar{\nu}N/W) = \exp(-Q\bar{\nu})$ . Therefore, given an  $\bar{\nu}$  we can find  $Q^*$  and then we find  $\epsilon^* = \exp(-\bar{\nu}Q^*)$ . This value of

$\epsilon$ ,  $\epsilon^*$ , is the erasure probability that the channel must operate at to achieve the capacity given by  $\bar{\nu}$  and  $Q^*$ .

Figure 3 is a graph of  $Q^*$  vs  $\epsilon^*$  (note that  $Q^*$  implies  $\bar{\nu}$  by Fig. 2). Figure 3 shows that a value of  $\epsilon^*$  implies a single value of  $Q^*$ , and so also a value of  $\bar{\nu}$ . Therefore a value of  $\epsilon^*$  supplies all the necessary information to compute (1). Figure 4 shows this relationship between  $C$  and  $\epsilon^*$ .

### III. Maximizing $R_{comp}$

Using the same notation as in Section II for  $\bar{\nu}$ ,  $N$ ,  $\bar{P}$  and  $\epsilon$  we can obtain very analogous results for the computational cutoff rate  $R_{comp}$ . We easily find:

$$R_0 = R_{comp} = -\log \left[ \frac{1 - \epsilon}{Q} + \epsilon \right] \text{ nats/word}$$

Since there are  $W$  words/sec:

$$R_0 = -W \log \left[ \frac{1 - \epsilon}{Q} + \epsilon \right] \text{ nats/sec}$$

Since there are  $N$  slots/sec:

$$R_0 = -\frac{W}{N} \log \left[ \frac{1 - \epsilon}{Q} + \epsilon \right] \text{ nats/slot}$$

Substituting for  $W$  and  $\epsilon$  we find:

$$R_0 = -\frac{\log}{Q} \left[ \frac{1 - e^{-\bar{\nu}Q}}{Q} + e^{-\bar{\nu}Q} \right] \text{ nats/slot} \quad (2)$$

Now everything that was done in Section II for capacity can be done for  $R_{comp}$ . Specifically, Fig. 5 shows contours of constant  $R_0$  and Fig. 6 gives the value of  $Q^*$  that maximizes (2) for a given value of  $\bar{\nu}$ . Figure 7 is a graph of  $Q^*$  vs  $\epsilon^*$ , and Fig. 8 is a graph of  $R_0$  vs  $\epsilon^*$ .

It is worth noting how linear Fig. 6 appears. A good approximation in the range  $Q^* \in [30, 800]$  is given by

$$Q^* \bar{\nu}^{0.984} = 1.75$$

(An easier, still reasonable, approximation is  $Q^* \bar{\nu} = 1.56$ .)

## IV. Discussion

What Sections II and III have shown is that there is a triplet  $(\bar{s}, \epsilon^*, Q^*)$ , any one of which determines the other two. Since  $\bar{s}$  is determined by the channel, there is an optimal  $\epsilon$  and  $Q$  for each channel. This allows comparison of channels.

Suppose it had been decided to use a 256-ary PPM channel with an erasure probability of 0.01. This is within the realm of current thinking, and it is a *bad choice of parameters*. With  $Q = 256$ ,  $\epsilon = 0.01$  we have  $\bar{P} = -\log \epsilon = 4.61$  and  $\bar{s} = \bar{P}/Q = 0.018$ . From these values of  $Q$  and  $\bar{s}$  we obtain  $C = 0.021$  nats/slot (using formula 1).

We can do a lot better, however, with a different value of  $Q$  and the *same value of  $\bar{s}$* . With  $\bar{s} = 0.018$ , Fig. 2 gives  $Q^* = 35$ . Using  $Q^* = 35$  in Fig. 3 we find  $\epsilon^* = 0.53$ . Using  $\epsilon^* = 0.53$  in Fig. 4 we find  $C = 0.047$  nats/slot. Hence we see that by

changing  $Q$  from 256 to  $Q^* = 35$ , we increase the throughput from 0.021 nats/slot to 0.047 nats/slot, an increase of 124%! The peak power requirement also goes down from  $-\log(\epsilon) = 4.61$  to  $-\log(\epsilon^*) = 0.63$ , a decrease of 86%!

The only drawback is that this new set of parameters dictates the erasure probability to be  $\epsilon = 0.53$ . This means that coding schemes considered for this channel must have the capability of compensating for an unusually large number of erasures. Of course, the calculation above could also have been done for  $R_0$ , using Figs. 6, 7, and 8.

The conclusion is that, to effectively utilize the PPM channel, the erasure probability must be rather large. For example, associated with  $Q^* = 256$  is  $\epsilon^* = 0.68$  (utilizing Fig. 3). This high erasure probability forces the use of lower rate (and hence more complex) codes if one desires to use the channel optimally.

## References

1. McEliece, R. J., "Practical Codes for Photon Communication," *IEEE Trans. Information Theory* (to appear).
2. Tan, H. H., "Capacity of a Multi-mode Direct Detection Optical Communication Channel," (to be published in TDA Progress Report).
3. Katz, J., Butman, S. A., and Lesh, J. R., "Practical Limitations on Noiseless Optical Channel Capacity," in *The Deep Space Network Progress Report 42-55*, Jet Propulsion Laboratory, Pasadena, Calif., Feb. 15, 1980.

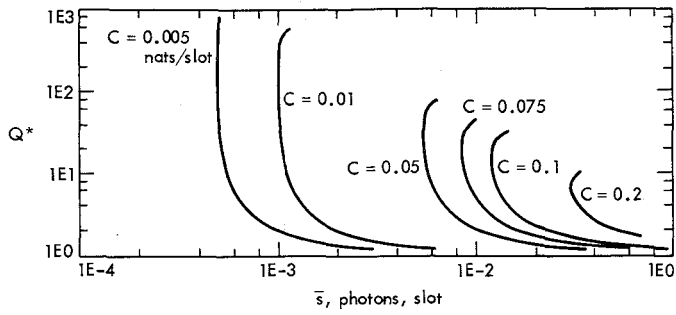


Fig. 1. Contours of constant  $C$

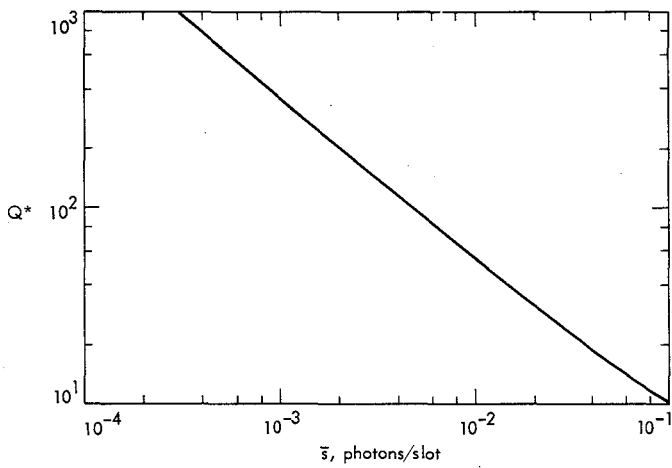


Fig. 2. Optimal  $Q^*$  such that  $C$  is maximal, given  $\bar{s}$

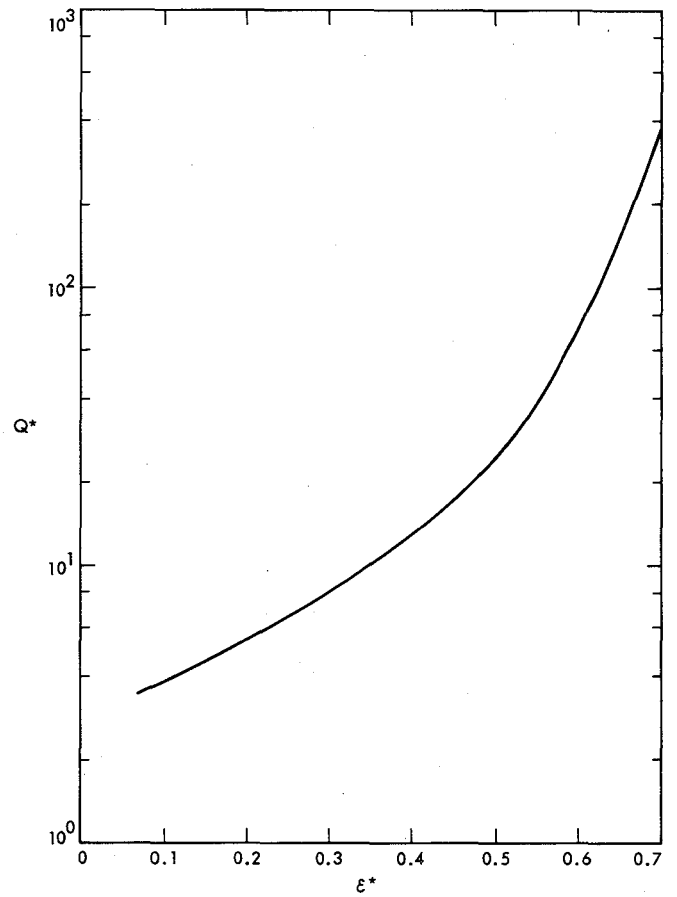


Fig. 3.  $Q^*$  vs  $\epsilon^*$  utilizing capacity as functional to be maximized

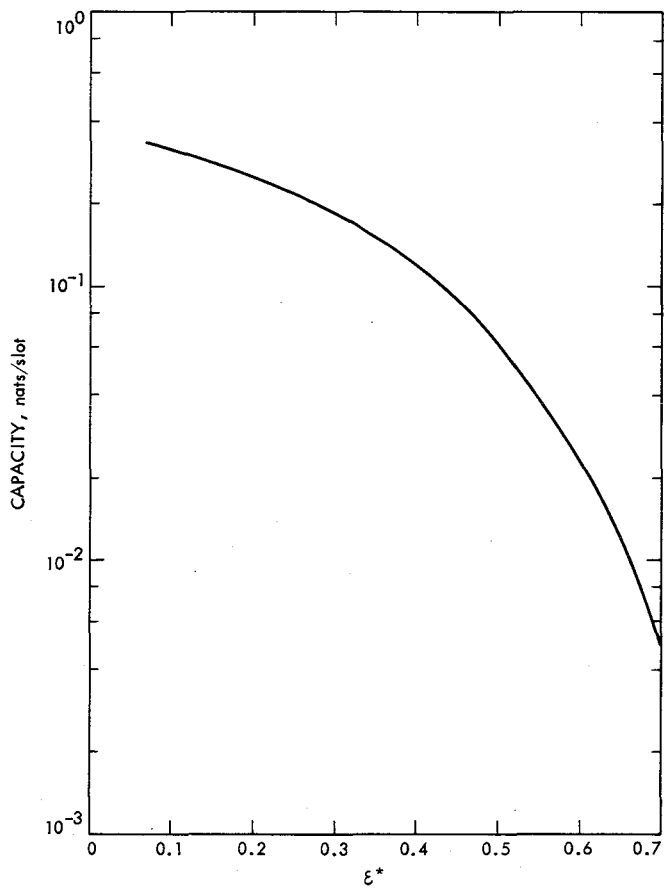


Fig. 4. Capacity given  $\epsilon^*$

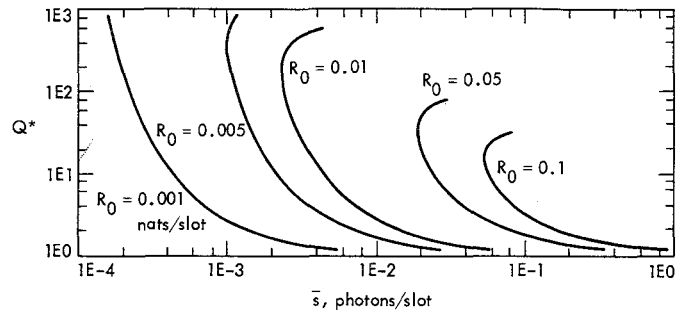


Fig. 5. Contours of constant  $R_{comp}$

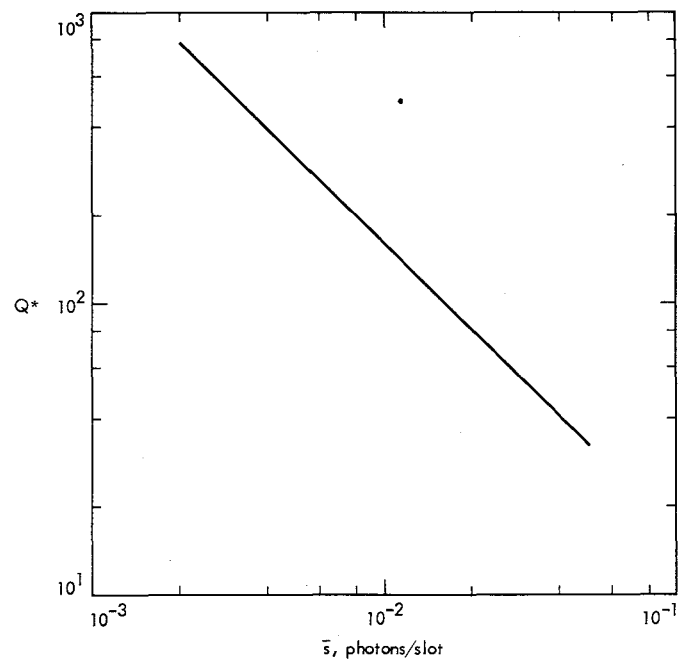


Fig. 6. Optimal  $Q^*$  such that  $R_0$  is maximal, given  $\bar{s}$

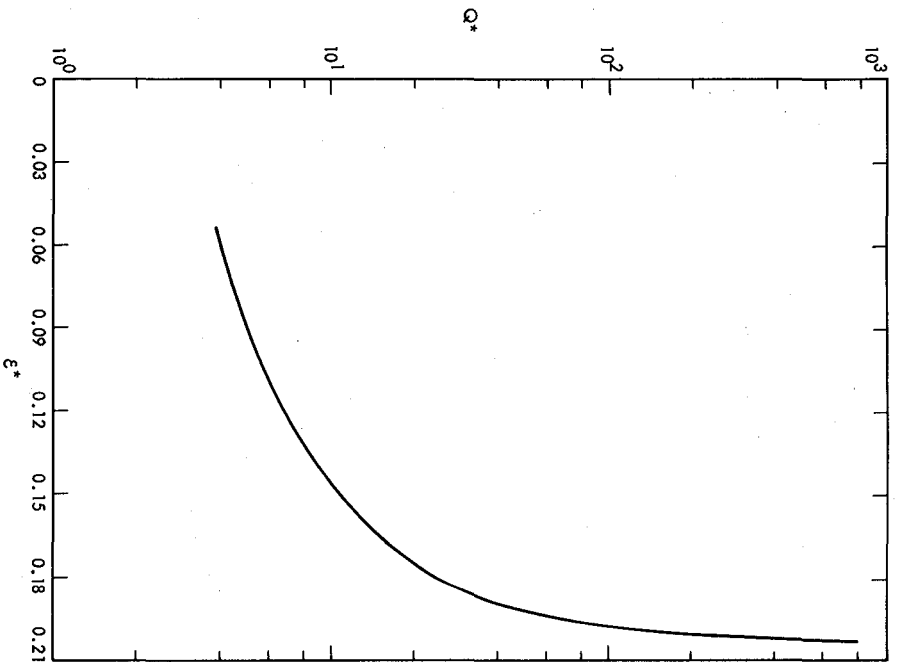


Fig. 7.  $Q^*$  vs  $\epsilon^*$  utilizing  $R_{comp}$  as functional to be maximized

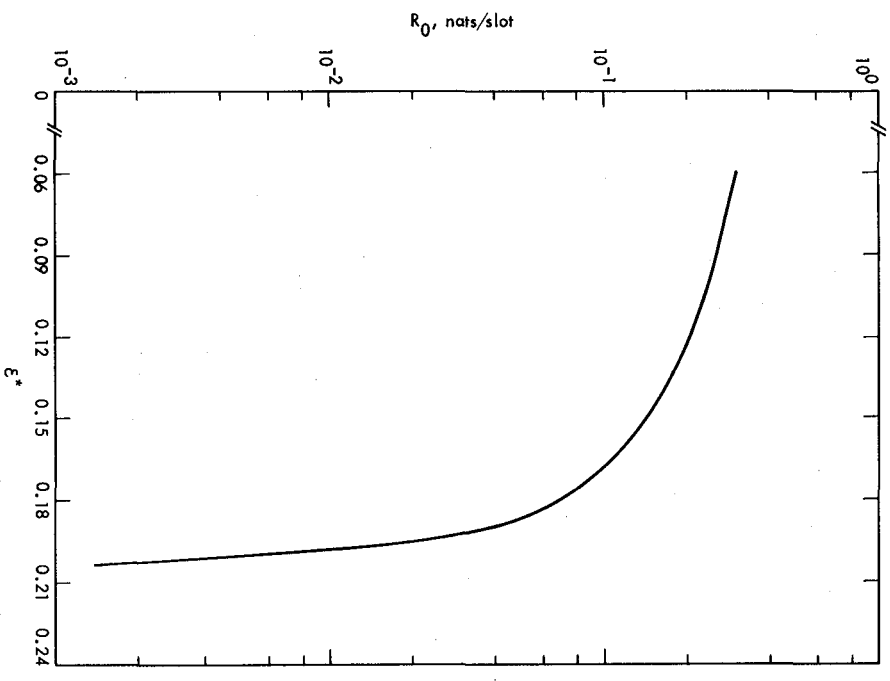


Fig. 8.  $R_{comp}$  given  $\epsilon^*$

# Optimum Design of Hybrid Phase Locked Loops

P. Lee and T. Yan

Communications Systems Research Section

*This article deals with the design procedure of phase locked loops in which the analog loop filter is replaced by a digital computer. Specific design curves are given for the step and ramp input changes in phase. It is shown that the designed digital filter depends explicitly on the product of the sampling time and the noise bandwidth of the phase locked loop. The technique of optimization developed in this article can be applied to the design of digital-analog loops for other applications.*

## I. Introduction

This article deals with the design of phase locked loops in which the analog loop filter is replaced by a digital computer. The optimum analog phase locked loop design, based on the Wiener filtering theory, has been analyzed by various researchers (Ref. 1). The effort described in this article is a procedure of digitizing the analog loop filters by properly designed digital filters. An applicable example is the tracking loop in the Multimegabit Telemetry System. Various techniques have been developed to replace the analog loop filters by their discrete counterparts (Ref. 2). However, Gupta (Ref. 3) pointed out that the optimum hybrid loop is not the discrete version of the analog loop. In this article, an optimum digital filter is designed to replace the conventional analog loop filter by putting an inequality constraint on the noise bandwidth of the phase locked loop. The Kuhn-Tucker theorem, together with the calculus of variation, is used to find the optimum structure of the digital filter. Both the interior optimum as well as the boundary optimum are evaluated. Based on the Kuhn-Tucker theorem, the interior optimum is computed as an unconstrained optimum while the boundary optimum is obtained via the Lagrange multiplier technique (Ref. 4).

## II. The Mathematical Model

The mathematical model of the analog-digital phase locked loop is shown in Fig. 1. The digital filter,  $D(z)$ , together with the sample and hold circuit replaces the conventional analog loop filter. A VCO is modelled by a pure integrator, and the output of the VCO is fed back to produce an error signal. The input  $\theta(t)$  is assumed to be deterministic and is corrupted by an additive white noise  $n_i(t)$  which has a one-sided power spectral density of  $N_o$  w/Hz. Let  $e(nT)$  be the sampled error between the actual input phase  $\theta(t)$  and the output phase of the VCO  $\psi(t)$  in the absence of noise. Then the sum squared sample error  $\sigma_e^2$  is defined as

$$\sigma_e^2 = \sum_{n=0}^{\infty} e^2(nT) = \sum_{n=0}^{\infty} [\theta(nT) - \psi(nT)]^2 \quad (1)$$

where  $T$  is the sampling period.

We want to minimize the  $\sigma_e^2$  subject to the constraint that the average power of the output noise  $n_o(t)$  is kept below a constant. Specifically, if  $B_N$  is the required noise bandwidth of

the phase locked loop, we want to solve the following problem.

Problem: Minimize  $\sigma_e^2$  subject to

$$\sigma_n^2 = E [n_o^2(t)] \leq N_o (\text{w/Hz}) \cdot B_N(\text{Hz}) \quad (2)$$

In the following sections, we first evaluate the quantities  $\sigma_n^2$  and  $\sigma_e^2$  in terms of the digital filter  $D(z)$ . Then we apply the Lagrange multiplier technique and the calculus of variation to minimize  $\sigma_e^2$  subject first to the equality constraint and then secondly to the strict inequality constraint. The resulting optimum digital filter  $\hat{D}(z)$  is then evaluated explicitly for the cases where  $\theta(t)$  are step and ramp inputs.

### III. The Optimum Digital Filter

Let  $G(s)$  be the transfer function of the cascaded system consisting of the zero order hold and the VCO. Then

$$G(s) = \frac{1 - e^{-sT}}{s} \frac{K}{s} \quad (3)$$

#### A. Evaluation of $\sigma_e^2$

Let  $E(z)$  be the  $z$  transform of the sampled error sequence  $e(nT)$ . Then

$$\begin{aligned} \sigma_e^2 &= \sum_{n=0}^{\infty} e^2(nT) = \sum_{n=0}^{\infty} e(nT) \left[ \frac{1}{2\pi j} \oint_C E(z) z^{n-1} dz \right] \\ &= \frac{1}{2\pi j} \oint_C E(z) \left[ \sum_{n=0}^{\infty} e(nT) z^n \right] \frac{dz}{z} \\ &= \frac{1}{2\pi j} \oint_C E(z) E(z^{-1}) \frac{dz}{z} \end{aligned} \quad (4)$$

where  $C$  is the counterclockwise closed contour in the region of convergence of  $E(z)$  and encircling the origin of the  $z$  plane.

Let  $G(z)$  be the  $z$  transform of the sampled impulse response of  $G(s)$ , and  $\theta(z)$ ,  $\psi(z)$  be the  $z$  transform of the sampled input sequence  $\theta(nT)$  and the output sequence  $\psi(nT)$ . Then

$$E(z) = [1 - W(z)G(z)] \theta(z) \quad (5)$$

where

$$W(z) = \frac{D(z)}{1 + D(z)G(z)} \quad (6)$$

Substituting Eqs. (5) and (6) in (4), we obtain  $\sigma_e^2$ .

#### B. Evaluation of $\sigma_n^2$

The average power of the output noise  $\sigma_n^2$  is given by

$$\sigma_n^2 = E \{n_o^2(t)\} = \frac{1}{2\pi j} \frac{1}{T} \int_0^1 dm \oint_{C'} \Phi_{n_o}(z, m) \frac{dz}{z} \quad (7)$$

where  $\Phi_{n_o}(z, m)$  is the modified pulse spectral density (Ref. 6) of the output noise  $n_o(t)$  and  $C'$  is the counterclockwise closed contour in the region of convergence of  $\Phi_{n_o}(z, m)$ ,  $0 < m < 1$ , and encircling the origin of the  $z$ -plane. Then, from Appendix A (with extensions to the modified  $z$  transforms),

$$\sigma_n^2 = \frac{1}{2\pi j} \frac{1}{T} \int_0^1 dm \oint_{C'} H(z, m) H(z^{-1}, m) \Phi_{n_i}(z) \frac{dz}{z} \quad (8)$$

where  $H(z, m)$  is the modified  $z$  transform of the system transfer function between the input  $n_i(t)$  and the output  $n_o(t)$ , and  $\Phi_{n_i}(z)$  is the pulse spectral density of the input noise  $n_i(t)$ .

From Fig. 1,

$$H(z, m) = W(z) G(z, m) \quad (9)$$

where  $W(z)$  is given by Eq. (6) and  $G(z, m)$  is the modified  $z$  transform of the impulse response of  $G(s)$ .

For white noise input

$$\Phi_{n_i}(z) = N_o$$

Hence

$$\sigma_n^2 = \frac{1}{2\pi j} \int_{C'} \frac{N_o}{T} A(z) W(z) W(z^{-1}) \frac{dz}{z} \quad (10)$$

where

$$A(z) = \int_0^1 G(z, m) G(z^{-1}, m) dm$$

### C. Constrained Optimum Digital Filter

Now we want to find an optimum  $W(z)$ , say  $\hat{W}(z)$ , that minimizes (2) with the equality constraint so that the optimum digital filter  $\hat{D}(z)$  is given by

$$\hat{D}(z) = \frac{\hat{W}(z)}{1 - \hat{W}(z)G(z)} \quad (11)$$

Define

$$J[W(z)] = \frac{1}{2\pi j} \oint_{\Gamma} [1 - W(z)G(z)] [1 - W(z^{-1})G(z^{-1})] \theta(z) \theta(z^{-1}) \frac{dz}{z} + \lambda \left[ \frac{1}{2\pi j} \oint_{\Gamma} A(z)W(z)W(z^{-1}) \frac{dz}{z} - B_N T \right] \quad (12)$$

where  $\lambda$  is the Lagrange multiplier and  $\Gamma$  is the counterclockwise closed contour in the region of convergence of both  $E(z)$  and  $\Phi_{n_o}(z, m)$  and encircling the origin in the  $z$  plane. Since contour integration is independent of path within the region of convergence, the contour  $\Gamma$  is taken as the unit circle which is the same as  $C$  or  $C'$ .

Using the calculus of variation and evaluating

$$\left. \frac{\partial}{\partial \epsilon} J[\hat{W}(z) + \epsilon V(z)] \right|_{\epsilon=0} = 0$$

we obtain

$$\begin{aligned} & \frac{1}{2\pi j} \oint_{\Gamma} \left[ \frac{1}{z} P(z) \hat{W}(z^{-1}) - \frac{1}{z} G(z) \theta(z) \theta(z^{-1}) \right] V(z) dz \\ & + \frac{1}{2\pi j} \oint_{\Gamma} \left[ \frac{1}{z} P(z) W(z) \right. \\ & \left. - \frac{1}{z} G(z^{-1}) \theta(z) \theta(z^{-1}) \right] V(z^{-1}) dz = 0 \end{aligned}$$

where

$$P(z) = G(z)G(z^{-1})\theta(z)\theta(z^{-1}) + \lambda A(z). \quad (13)$$

Defining

$$P(z) = P^+(z)P^-(z)$$

where  $P^+(z)$  has all the poles and zeroes inside the unit circle of the  $z$  plane and  $P^-(z)$  has all the poles and zeroes outside the unit circle of the  $z$  plane, we obtain the optimum  $\hat{W}(z)$  as

$$\hat{W}(z) = \frac{z}{P^+(z)} \left[ \frac{G(z^{-1})\theta(z)\theta(z^{-1})}{z P^-(z)} \right]_+ \quad (14)$$

where  $[\cdot]_+$  represents that part of the partial fraction expansion of  $[\cdot]$  whose poles are inside or on the unit circle.

In (14) the optimum  $\hat{W}(z)$  is a function of the Lagrange multiplier  $\lambda$ . By putting  $\hat{W}(z)$  in (10), and using

$$\sigma_n^2 = N_o B_N,$$

we can determine  $\lambda$  and hence the constrained optimum filter  $\hat{D}(z)$ .

### D. Unconstrained Optimum Digital Filter

Equation (14) defines the optimum filter  $\hat{W}(z)$  for the boundary minimum of (2). From the Kuhn-Tucker theorem, the interior minimum can be evaluated by forcing the Lagrange multiplier to zero in (12). In this case, the optimum digital filter given by (11) will satisfy the strict inequality of the constraint

$$\sigma_n^2 < N_o B_N$$

From (14) and (10), we obtain the unconstrained optimum digital filter,  $\tilde{D}(z)$ . The crossover point between the interior minimum and the boundary minimum is given by

$$(B_N T)_c = \frac{1}{2\pi j} \oint_{\Gamma} A(z) \tilde{W}(z) \tilde{W}(z^{-1}) \frac{dz}{z} \quad (15)$$

where  $\tilde{W}(z)$  is the unconstrained optimum of (2).

#### IV. Examples

In this section, the optimum digital filter  $\hat{D}(z)$  is evaluated for two types of inputs: the step and ramp change in phase inputs. Poles and zeroes of the optimum digital filter are described by the design curves for various time-bandwidth products.

##### Example 1. Step input

For step inputs,

$$\theta(t) = \begin{cases} 1 & t \geq 0 \\ 0 & t < 0 \end{cases}$$

Then

$$\theta(z) = \sum_{n=0}^{\infty} \theta(nT)z^{-n} = \frac{z}{z-1}$$

From the  $z$  transform table of Ref. 5, we obtain from (3)

$$G(z) = \frac{KT}{z-1}$$

and

$$G(z, m) = \frac{KT}{z} \left( m + \frac{1}{z-1} \right)$$

##### (i) Constrained optimum filter

From (13),

$$P(z) = \frac{\lambda K^2 T^2}{6} \frac{-(z^2 + z^{-2}) - 2(z + z^{-1}) + 6 + 6/\lambda}{(z-1)^2 (z^{-1}-1)^2}$$

$$= P^+(z)P^-(z)$$

where

$$P^+(z) = \sqrt{\frac{\lambda K^2 T^2}{6}} \frac{az^2 + bz + c}{(z-1)^2}$$

$$P^-(z) = \sqrt{\frac{\lambda K^2 T^2}{6}} \frac{az^{-2} + bz^{-1} + c}{(z^{-1}-1)^2}$$

and  $a, b, c$  satisfy the following equations

$$\begin{aligned} ac &= -1 \\ ab + bc &= -2 \\ a^2 + b^2 + c^2 &= 6 + 6/\lambda \end{aligned} \quad (16)$$

Then from (14)

$$\hat{W}(z) = \frac{a+b+c}{KT} \frac{z(z-1)}{az^2 + bz + c}$$

and from (12)

$$\hat{D}(z) = \frac{a+b+c}{KT} \frac{z}{az-c} = \frac{g_1}{KT} \frac{z}{z+P_1}$$

The constrained optimum digital filter for the step phase input is a single pole, single zero filter with pole located at  $c/a$ . Putting in the constraint that

$$B_N T = \frac{1}{2\pi j} \oint_{\text{unit circle}} A(z) \hat{W}(z) \hat{W}(z^{-1}) \frac{dz}{z}$$

we arrive

$$B_N T = \frac{(2a+2c-b)(a+b+c)}{3(a-c)(a+c-b)} \quad (17)$$

Therefore given any  $B_N T$ , we can determine the variables  $a, b, c$  and  $\lambda$  from (16) and (17) and hence the optimum filter  $\hat{D}(z)$ . Since  $B_N T \geq 0$ , and  $|c/a| < 1$  for a causal digital filter, only a range of values for  $a, b$ , and  $c$  can satisfy (17).

##### (ii) Unconstrained optimum filter

From (13)

$$P(z) = K^2 T^2 \frac{1}{(z-1)^2 (z^{-1}-1)^2} = P^+(z)P^-(z)$$

where

$$P^+(z) = KT \frac{z^2}{(z-1)^2}$$

$$P^-(z) = KT \frac{z^{-2}}{(z^{-1} - 1)^2}$$

Then

$$\tilde{W}(z) = \frac{1}{KT} \frac{z-1}{z}$$

$$\tilde{D}(z) = \frac{1}{KT}$$

and from (15),

$$(B_N T)_c = \frac{1}{2\pi j} \oint_{\Gamma} A(z) \tilde{W}(z) \tilde{W}(z^{-1}) \frac{dz}{z} = \frac{2}{3}$$

Figures 2 and 3 plot the gain coefficient  $g_1$  and the pole location of the optimum digital filter  $D(z)$  for the step phase input. Note that  $\hat{D}(z)$  becomes  $\tilde{D}(z)$  for  $B_N T \geq (B_N T)_c$ .

Example 2. Ramp input

For ramp inputs,

$$\theta(t) = \begin{cases} t & t \geq 0 \\ 0 & t < 0 \end{cases}$$

Then

$$\theta(z) = \frac{Tz}{(z-1)^2}$$

(i) Constrained optimum filter

From (13),

$$\begin{aligned} P(z) &= \frac{\lambda K^2 T^2}{b} \frac{(z^3 + z^{-3}) - 9(z + z^{-1}) + 16 + 6T^2/\lambda}{(z-1)^3 (z^{-1} - 1)^3} \\ &= P^+(z)P^-(z) \end{aligned}$$

where

$$P^+(z) = \sqrt{\frac{\lambda K^2 T^2}{6}} \frac{az^3 + bz^2 + cz + d}{(z-1)^3}$$

$$P^-(z) = \sqrt{\frac{\lambda K^2 T^2}{6}} \frac{az^{-3} + bz^{-2} + cz^{-1} + d}{(z^{-1} - 1)^3}$$

and  $a, b, c, d$  satisfy the following equations,

$$ad = 1$$

$$ac + bd = 0$$

$$ab + bc + cd = -9$$

$$a^2 + b^2 + c^2 + d^2 = 16 + 6T^2/\lambda$$

(18)

Then

$$\hat{W}(z) = \frac{1}{KT} \frac{z(z-1)(ez+f)}{az^3 + bz^2 + cz + d}$$

and

$$\hat{D}(z) = \frac{1}{KT} \frac{z(ez+f)}{(z-1)(az+d)} = \frac{g_2}{KT} \frac{z(z-z_2)}{(z-1)(z+p_2)} \quad (19)$$

where

$$e = 2a + b - d$$

$$f = -a + c + 2d$$

Unlike for the step change in phase, the optimum digital filter for the ramp change in phase is a double pole, double zero filter. Putting in the constraint that

$$B_N T = \frac{1}{2\pi j} \frac{2 + \sqrt{3}}{6} \oint_{\Gamma} F(z)F(z^{-1}) \frac{dz}{z}$$

where

$$F(z) = \frac{ez^2 + [(2 - \sqrt{3})e + f]z + (2 - \sqrt{3})f}{az^3 + bz^2 + cz + d}$$

Then

$$B_N T = \frac{1}{3} \frac{(2e^2 + ef + 2f^2)Q_0 - (e^2 + 4ef + f^2)Q_1 + efQ_2}{(a^2 - d^2)Q_0 - (ab - cd)Q_1 + (ac - bd)Q_2}$$

where

$$\begin{aligned} Q_0 &= a(a+c) - d(b+d) \\ Q_1 &= ab - cd \\ Q_2 &= b(b+d) - c(a+c) \end{aligned} \quad (20)$$

As in example 1, for any given  $B_N T$ , the variables  $a, b, c, d$  and  $\lambda$  are determined from (18) and (20). The optimum digital filter  $\hat{D}(z)$  is then given by (19).

(ii) Unconstrained optimum filter

From (13),

$$P(z) = \frac{K^2 T^4}{(z-1)^3 (z^{-1}-1)^3} = P^+(z) P^-(z)$$

where

$$\begin{aligned} P^+(z) &= KT^2 \frac{z^3}{(z-1)^3} \\ P^-(z) &= KT^2 \frac{z^{-3}}{(z^{-1}-1)^3} \end{aligned}$$

Then

$$\tilde{W}(z) = T \frac{2z-1}{(z-1)^2}$$

$$\tilde{D}(z) = \frac{1}{KT} \frac{2z-1}{z-1}$$

and from (15),

$$(B_N T)_c = \frac{1}{2\pi j} \oint_{\Gamma} A(a) \tilde{W}(z) \tilde{W}(z^{-1}) \frac{dz}{z} = \frac{8}{3}$$

Figures 4, 5 and 6 plot the gain coefficient  $g_2$ , the pole location and the zero location of the optimum digital filter for the ramp phase input. Again we see that  $\hat{D}(z)$  goes to  $\tilde{D}(z)$  when  $B_N T \geq (B_N T)_c$ .

## V. Conclusion

An optimum design procedure to replace the conventional analog loop filter in a phase locked loop by a digital computer is given. Specific examples of step and ramp change in phase have been described. In both cases, the filter gain coefficients, pole locations, and zero locations are plotted for various time-bandwidth products.

## References

1. Viterbi, A. J., *Principles of Coherent Communication*, McGraw Hill, New York, 1966.
2. Westlake, P. R., "Digital Phase Control Techniques," *IRE Trans. Com. Syst.*, Vol. CS-8, pp. 237-246, Dec. 1960.
3. Gupta, S. C., "On Optimum Digital Phase-Locked Loops," *IEEE Trans. Com. Tech.*, pp. 340-344, April 1968.
4. Kuhn, H. W., and Tucker, A. W., "Nonlinear Programming," *Proceedings 2nd Berkeley Symposium on Mathematical Statistics and Probability*, University of California Press, pp. 481-492, 1951.
5. Kuo, B. C., *Analysis and Synthesis of Sampled-Data Control Systems*, Prentice-Hall, Englewood Cliffs, N.J., 1963.
6. Mori, M., "Statistical Treatment of Sampled-Data Control Systems for Actual Random Inputs," *Trans. ASME*, pp. 444-456, Feb. 1958.

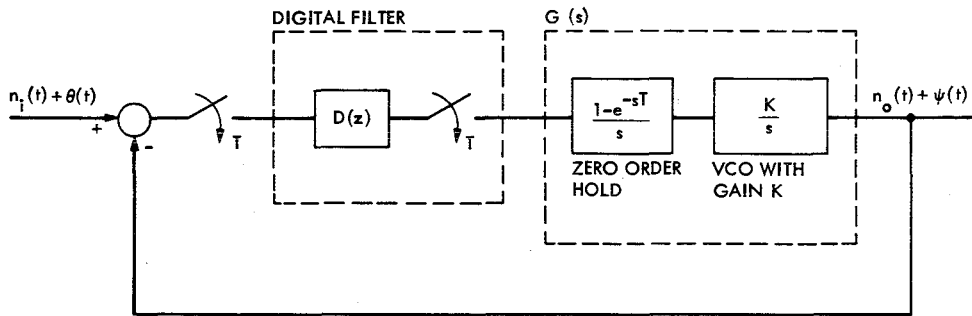


Fig. 1. Digital-analog phase locked loop

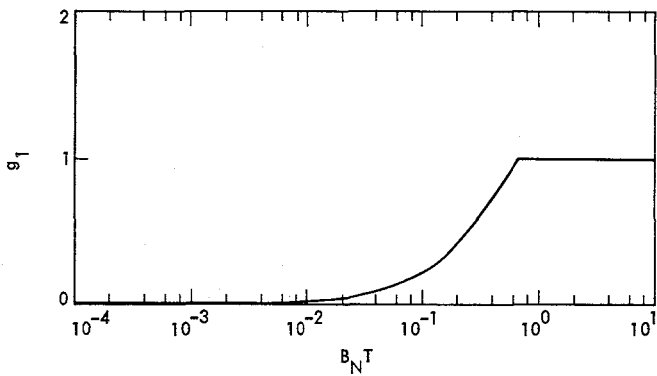


Fig. 2. Gain vs  $B_N T$  curve for loop with step change in phase

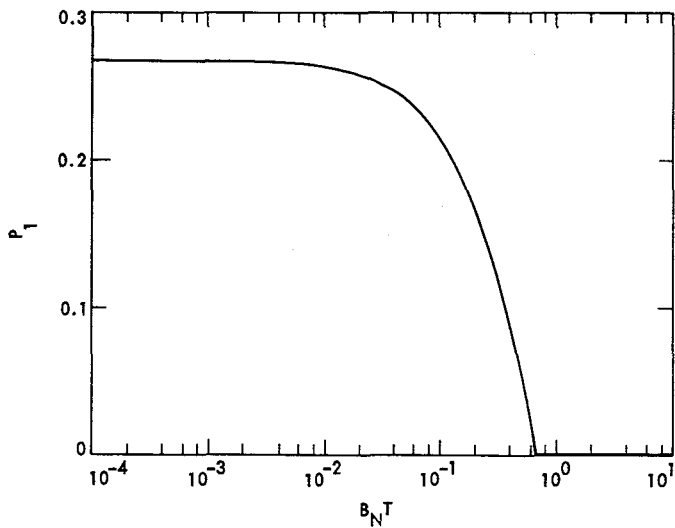


Fig. 3. Location of pole vs  $B_N T$  curve for loop with step change in phase

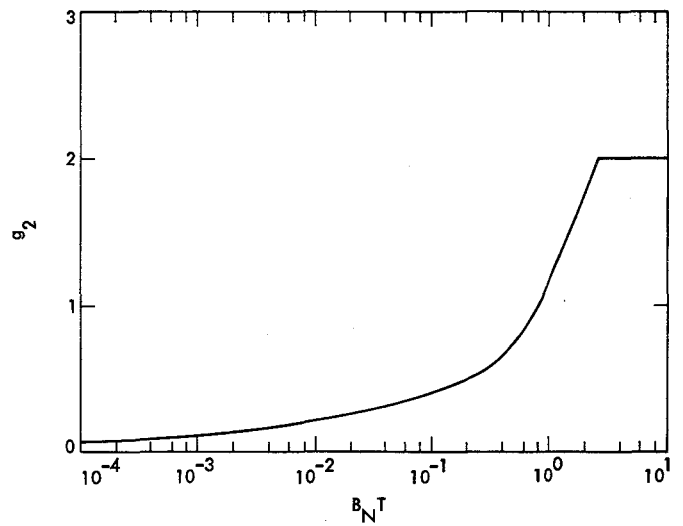


Fig. 4. Gain vs  $B_N T$  curve for loop with ramp change in phase

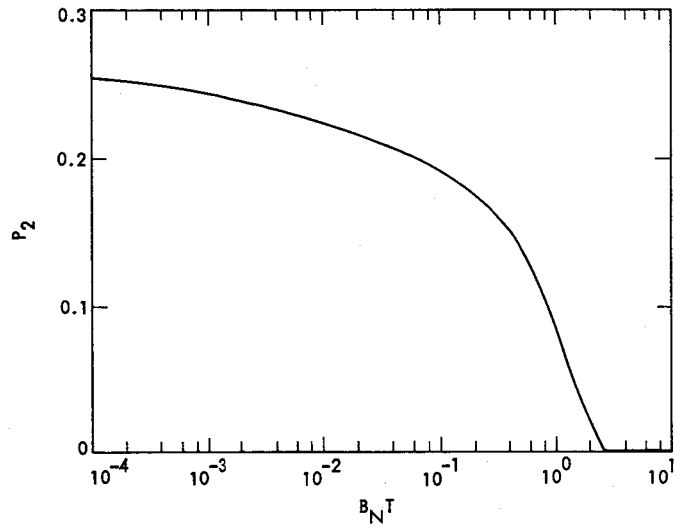


Fig. 5. Location of pole vs  $B_N T$  curve for loop with ramp change in phase

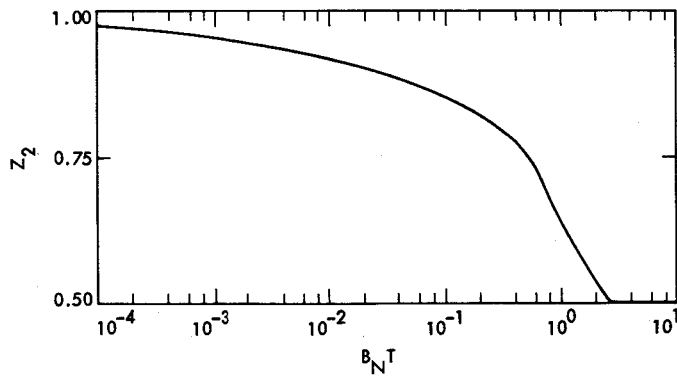


Fig. 6. Location of zero vs  $B_N T$  curve for loop with ramp change in phase

## Appendix A

### Evaluation of the Sampled Power Spectral Density for the Output of Digital Filters

Let  $[x_n]_{-\infty}^{\infty}$  be the stationary random sequence to the input of a digital filter having the impulse response  $[h_n]_{-\infty}^{\infty}$ . The output  $[y_n]_{-\infty}^{\infty}$  can be written as

$$y_n = \sum_{k=-\infty}^{\infty} h_{n-k} x_k$$

Then

$$\begin{aligned} E[y_n y_m] &= \sum_{k=-\infty}^{\infty} \sum_{l=-\infty}^{\infty} h_{n-k} h_{m-l} E[x_k x_l] \\ &= \sum_{k=-\infty}^{\infty} \sum_{l=-\infty}^{\infty} h_k h_l E[x_{n-k} x_{m-l}] \\ &= \sum_{k=-\infty}^{\infty} \sum_{l=-\infty}^{\infty} h_k h_l r_{(m-n) + (k-l)} \end{aligned}$$

where

$$r_k = E[x_n x_{n+k}]$$

Therefore  $[y_n]_{-\infty}^{\infty}$  is also a stationary sequence with

$$E[y_n y_{n+m}] = \sum_{k=-\infty}^{\infty} \sum_{l=-\infty}^{\infty} h_k h_l r_{m+(k-l)}$$

Defining the sampled power spectral densities of sequences  $[y_n]_{-\infty}^{\infty}$  and  $[x_n]_{-\infty}^{\infty}$  as

$$\Phi_y(z) = T \sum_{m=-\infty}^{\infty} E[y_n y_{n+m}] z^{-m}$$

and

$$\Phi_x(z) = T \sum_{j=-\infty}^{\infty} E[x_n x_{n+j}] z^{-j} \quad \text{for all } n$$

we obtain

$$\begin{aligned} \Phi_y(z) &= \sum_{k=-\infty}^{\infty} \sum_{l=-\infty}^{\infty} h_k h_l T \sum_{m=-\infty}^{\infty} r_{m+(k-l)} z^{-m} \\ &= \sum_{k=-\infty}^{\infty} \sum_{l=-\infty}^{\infty} h_k h_l z^{k-l} \Phi_x(z) \\ &= H(z) H(z^{-1}) \Phi_x(z) \end{aligned}$$

where  $H(z)$  is the  $z$  transform of the impulse response  $[h_n]_{-\infty}^{\infty}$

Hence

$$E[y_n^2] = \frac{1}{T} \cdot \frac{1}{2\pi j} \oint_c \Phi_y(z) \frac{dz}{z}$$

# The Reliability of Multistate, Multioutput Systems

E. J. Subelman

Communications Systems Research Section

*A system which can generate multiple signals such that each signal can have different quality states is modelled. A measure of the effectiveness of the system as a function of the status of its components is developed. Assuming only that the probability distribution of the status of each component is known, bounds on the probability distribution of the system's measure of effectiveness are developed.*

## I. Introduction

In the modelling of systems of many components to study their reliability, the usual assumption has been that each component can be in one of two states, either operating or failed, and that the system itself exhibits the same behavior. In many cases, and in particular in the case of NASA's Deep Space Network (DSN) these assumptions are too simplistic. For example, in the frequency and timing system (FTS) of a Deep Space Station (DSS) many different time signals and frequency standards are output, and it is quite possible that some of these may cease to be generated, due to equipment failure for example, while others are still available. In this situation, one cannot state that the system is failed or that it is operating, but rather that it is operating in a degraded mode, providing only some of the services it is intended to provide. One of the objectives of this article is to develop methodology to quantify the performance of systems with this characteristic.

A second complication is introduced by the fact that each of the outputs of the system may be available in different qualities as the system degrades and is repaired. For example in the FTS, the signals can originate from hydrogen masers, cesium standards, rubidium standards or crystal oscillators,

and the quality of each signal (accuracy and stability) will depend on which type of source is being used to generate it. Furthermore, as each signal is processed by the other components of the system, it may also be degraded in quality, depending on the state of the component. These varying qualities must be considered in the description of the system, since they influence the possible uses of the system's output. This article presents a method for the characterization of a system which can produce multiple outputs at multiple quality levels. The outputs are produced and processed by the components of the system.

We will assume that the components may be in different states and that these states can be assigned numerical values, with 0 representing a failed component. We will also assume that the state is a measure of the quality of the signal that the component can put out, if a signal of that quality or better is available as input to the component. Thus, we do not allow for a component to produce an output of better quality than its input.

In Section II we present a method of describing the quality of a single output as a function of the state of the components. Normally we are interested in predicting the system's

future behavior, and the state of the components will not be known with certainty. We thus proceed to assume that the states of the components are not precisely determined, but that we can give a probability distribution for the state of each component and determine from these distributions the probability distribution of the quality level of the output. Since the computations involved are easily seen to be quite elaborate, we also present upper and lower bounds on the distribution of the state of the output, which are easier to compute.

In Section III we extend these results to the case of multiple outputs by considering the different activities (e.g., telemetry, navigation, radio science) that require the signals output by the system as well as the minimal quality of each signal that each of these activities requires. It is thus possible to determine, from the state of the components, whether all the signals required by an activity are available at the necessary quality level so that the activity may be carried out. By assigning a value to each activity, it is then possible to arrive at an overall measure of the operation of the system as a whole. We develop bounds on the probability that each activity can be carried out, since the exact computation in many cases is not practical.

In Section IV we present an application of the method to a portion of the FTS.

## II. Analysis of a Single Output Multistate System

For a single signal, we define a *path set* as a set of components whose functioning will ensure that the signal is being produced. A *minimal path set* is a path that does not contain other paths. Thus, if all components are failed except those on a minimal path, the signal will be produced, but if any one of the minimal path components subsequently fails, the signal will cease to be produced.

We also define a *cut set* as a set of components whose failure causes the signal to cease to be produced, even if all other components are functioning. A *minimal cut set* is a cut set that does not contain other cut sets. Thus, if all components are functioning except those on a minimal cut set, the signal will not be produced, but repair of a single component of the minimal cut will cause the signal to be produced again.

We remark that the concepts of path and cut are of a binary nature and do not depend on the actual states of the components, except for the failed not failed distinction. We will initially consider only systems in which components can be in one of two states, and later extend our results to the more general case of multistate components. Corresponding to this binary conception, we may define the indicator variables  $x_i$  as

$$x_i = \begin{cases} 1 & \text{if component } i \text{ is functioning} \\ 0 & \text{if component } i \text{ is not functioning} \end{cases}$$

and the signal indicator variable  $\phi$  by

$$\phi = \begin{cases} 1 & \text{if the signal is being produced} \\ 0 & \text{if the signal is not being produced} \end{cases}$$

Clearly  $\phi$  depends only on the values of  $x_i$ ,  $i = 1, 2, \dots, n$ , where  $n$  is the number of components that generate the signal. We thus write  $\phi = \phi(x_1, x_2, \dots, x_n) \equiv \phi(\underline{x})$ . As discussed in Barlow and Proschan (Ref. 1), if  $\mathcal{P}_i$ ,  $i = 1, 2, \dots, p$  are the min path sets, and  $\mathcal{K}_i$ ,  $i = 1, 2, \dots, k$  are the min cut sets, then we can write

$$\begin{aligned} \phi(\underline{x}) &= \prod_{i=1}^k \left[ 1 - \prod_{j \in \mathcal{K}_i} (1 - x_j) \right] \equiv \min_{1 \leq i \leq k} \left\{ \max_{j \in \mathcal{K}_i} x_j \right\} \\ &= 1 - \prod_{i=1}^p \left( 1 - \prod_{j \in \mathcal{P}_i} x_j \right) \equiv \max_{1 \leq i \leq p} \left\{ \min_{j \in \mathcal{P}_i} x_j \right\} \end{aligned}$$

As discussed in Ref. 1, these expressions can be expanded into multilinear expressions. Furthermore since the  $x_i$  are binary variables,  $x_i^n = x_i$  for all  $n$ , so that no powers of the  $x_i$  appear.

If we now assume that components behave randomly, and let  $x_i$  be the state of component  $i$ , then  $\phi$  is also a random variable. Under the assumption that the  $x_i$  are independent, and letting  $p_i = P[x_i = 1] = E_{x_i}$ , we can show that

$$P[\phi(\underline{x}) = 1] = E\phi(\underline{x})$$

is a function only of the  $p_i$ . This is known as the reliability of the signal and we write

$$E\phi(\underline{x}) = h(p_1, p_2, \dots, p_n) \equiv h(\underline{P})$$

As explained in Ref. 1,  $h(\underline{P})$  can be obtained from the structure function by substituting for each  $x_i$  in the multilinear expansion of  $\phi(\underline{x})$  the corresponding  $p_i$ .

We remark that in the actual expansion of the structure  $\phi$  and the reliability  $h$ , not all components  $x_i$  or  $p_i$  will be present, since some components of the system will not be relevant to the production of the signal. We thus distinguish

between relevant and irrelevant components for the production of the signal.

We now proceed to extend the above results to the case where each component can be in any one of many states. Assume that the state of component  $j$  can be represented by a variable  $z_j$ . If we consider a minimal path of the signal, then, since all components in that path are necessary to process it, the best signal that path can produce is

$$\min_{j \in \mathcal{P}_i} z_j$$

Also, since any of the min paths is sufficient to generate the signal, the value of the actual signal produced will be

$$\Psi_p(z_1, z_2, \dots, z_n) = \max_{1 \leq i \leq p} \left\{ \min_{j \in \mathcal{P}_i} z_j \right\}$$

Similarly, since the signal must go through at least one component in a minimal cut set, the value of that cut set will be

$$\max_{j \in \mathcal{K}_i} z_j$$

and since the signal must traverse all minimal cut sets, we are led to the alternative

$$\Psi_k(z_1, z_2, \dots, z_n) = \min_{1 \leq i \leq k} \left\{ \min_{j \in \mathcal{K}_i} z_j \right\}$$

It is of course evident that if we restrict  $z_i$  to binary variables, we obtain precisely the structure  $\phi$  that details whether the signal is being produced or not.

A property of our definitions which will allow us to use the power of the binary system theory of Ref. 1 is the following. Consider a binary structure  $\phi$  with min path sets  $\mathcal{P}_i, i = 1, 2, \dots, p$ , and min cut sets  $\mathcal{K}_i, i = 1, 2, \dots, k$ . Assume component  $j$  operates for time  $t_j$  and then fails. Then the time until the structure fails is (See Ref. 1, pp. 12).

$$T = \min_{1 \leq i \leq k} \left\{ \max_{j \in \mathcal{K}_i} t_j \right\} = \max_{1 \leq i \leq p} \left\{ \min_{j \in \mathcal{P}_i} t_j \right\}$$

By comparing this expression with our definition of  $\Psi_p$  and  $\Psi_k$ , we conclude that they are both equal, and furthermore establish the following:

### Theorem

The state of the system is equal to the life of a binary system with the same min paths and min cuts, and whose component lifetimes are equal to the state of the individual components.

We will call the binary structure of the theorem the equivalent binary structure. With this property, most of the results known for binary structures extend easily to this more general representation. In particular all results on modular decompositions are valid. We can now assign probabilities to the states of the components, and obtain probabilistic results for the state of the system. If  $\bar{F}_i(z) = P[Z_i > z]$  then  $\bar{F}(z) = P[\Psi(Z) > z]$  is equal to the probability that the life of the equivalent binary structure exceeds  $z$  is thus (Ref. 1)

$$\bar{F}(z) = h[\bar{F}_1(z), \dots, \bar{F}_n(z)]$$

From this observation we immediately obtain versions of the IFRA and NBU closure theorems.

A distribution  $F(x) = 1 - \bar{F}(x)$  is called increasing failure rate average (IFRA) if it has the property that  $-1/x \log[1 - F(x)]$  is increasing in  $x$ . See Ref. 1, Section 4.2 for explanation and interpretation. The IFRA closure theorem states that a system whose components have IFRA distributions has itself an IFRA distribution (Ref. 1, Theorem 4.2.6).

If  $-\frac{1}{z} \log \bar{F}_i(z)$  is increasing in  $z$  for each  $i$ , then

$$-\frac{1}{z} \log \bar{F}(z) \text{ is increasing in } z.$$

A distribution is called new better than used (NBU) if it has the property that for all  $x_1$  and  $x_2$

$$1 - F(x_1 + x_2) \leq [1 - F(x_1)] [1 - F(x_2)].$$

See Ref 1, Section 6.2 for an explanation and interpretation. The NBU closure theorem is analogous to the IFRA closure theorem (Ref. 1, Theorem 6.5.1).

If  $\bar{F}_i(z_1 + z_2) \leq \bar{F}_i(z_1) \bar{F}_i(z_2)$  for each  $i$  for all  $z_1, z_2$ , then

$$\bar{F}(z_1 + z_2) \leq \bar{F}(z_1) \bar{F}(z_2) \text{ for all } z_1 \text{ and } z_2.$$

Another result that follows immediately is the reliability bounds of Ref. 1.

*Theorem*

Let  $p_i = P(Z_i > z)$  for a fixed  $z$ . Then if the components are independent

$$\prod_{i=1}^k \left[ 1 - \prod_{j \in \mathcal{K}_i} (1 - p_j) \right] \leq \bar{F}(z) \leq 1 - \prod_{i=1}^p \left( 1 - \prod_{j \in \mathcal{P}_i} p_j \right)$$

and

$$\max_{1 \leq i \leq p} \left\{ \prod_{j \in \mathcal{P}_i} p_j \right\} \leq \bar{F}(z) \leq \min_{1 \leq i \leq k} \left\{ 1 - \prod_{j \in \mathcal{K}_i} (1 - p_j) \right\}$$

Neither bound dominates so that in practice it is necessary to compute both pairs and select the best lower and upper bounds. Using modular decompositions, we can improve the bounds, as done in Ref. 1, pp. 39-44.

The concepts introduced thus far are stationary, and we will find it convenient to introduce time-varying states. If  $Z_i(t)$  is the state of component  $i$  at time  $t$ , we define

$$\bar{F}_i(t, z) = P[Z_i(t) > z]$$

Thus for fixed  $t$ ,  $\bar{F}_i(t, z)$  is the distribution of the state at time  $t$ . If  $T_{iz}$  is the first time at which the state of component  $i$  goes below  $z$ , then

$$P(T_{iz} > t) = P[Z_i(t) > z] = \bar{F}_i(t, z)$$

Thus for fixed  $z$ ,  $\bar{F}_i(t, z)$  is the distribution of the time until the components state first goes below  $z$ .

Therefore, for any  $t$  and  $z$  if the components are independent

$$\bar{F}(t, z) = h[\bar{F}_1(t, z), \dots, \bar{F}_n(t, z)]$$

and, for any fixed  $z$ , we have IFRA and NBU closure theorems for the passage times.

### III. Multiple Signals

A possible description of the state of a multisignal system would be the vector whose components describe the state of each signal. However, this has various drawbacks. The more serious one is of course that it becomes difficult to state

whether a particular state of the system is in some sense better or worse than another state. Furthermore, the number of possible states grows explosively with the number of signals, thereby obscuring the benefits of any analysis. The solution we have chosen to this dilemma is to consider the use to which the signals are put. We will assume that the outputs of the system are input to several users, which in the case of the DSN will be thought of as activities (e.g., telemetry, radio science, etc.). Each activity is assumed to require all of the signals, with a specified minimal quality level for each. Let

$m_{ij}$  = minimal acceptable level of signal  $i$  required by activity  $j$

It should be noted that we accept the possibility that  $m_{ij} = 0$ , which allows for the fact that signal  $i$  may actually not be required by activity  $j$ . Our formulation is preferable only because it leads to simpler notation. Note that this transforms each activity into a binary variable once more. Furthermore, we attach a value  $v_j$  to activity  $j$ , and we then measure the performance level of the system by the sum of the values of all the activities that can be performed. Thus, for activity  $j$ , we define, as an indicator of whether or not we are receiving the value of the activity, the binary random variable

$$Y_j = \begin{cases} 1 & \text{if } \Psi_i(z_1, z_2, \dots, z_n) \geq m_{ij} \text{ for } i = 1, 2, \dots, m \\ 0 & \text{otherwise} \end{cases}$$

where  $n$  is the number of components that produce the signals, and  $m$  is the number of signals. The application of the probabilistic notions to the experiment is complicated by the fact that the signals are not independent

$$P(Y_j = 1) = P[\Psi_i(\underline{Z}) \geq m_{ij}, i = 1, 2, \dots, m]$$

and since all the  $\Psi_i$  are functions of the random vector  $\underline{Z}$ , they are not independent. We thus are forced to either consider their interdependence, or to develop bounds on the probabilities that are relatively simple to compute.

The computation of bounds is relatively straightforward.

*Theorem*

$$\prod_{i=1}^m P(\Psi_i \geq m_{ij}) \leq P(Y_j = 1) \leq 1 - \prod_{i=1}^m [1 - P(\Psi_i \geq m_{ij})]$$

$$P(Y_j = 1) \leq \min_i P(\Psi_i \geq m_{ij})$$

*Proof*

Letting

$$\tau_i = \begin{cases} 1 & \text{if } \Psi_i(\underline{Z}) \geq m_{ij} \\ 0 & \text{otherwise} \end{cases}$$

We have that

$$Y_j = \begin{cases} 1 & \text{if } \tau_i = 1, i = 1, 2, \dots, m \\ 0 & \text{otherwise} \end{cases}$$

Hence  $Y_j$  is a series system of the  $\tau_i$ . Note that the  $\tau_i$  are not independent since they all depend on the same set of variables. However, since they are non-decreasing functions of the independent random variables  $\underline{Z}$ , they exhibit a special form of dependence known as association (see Ref. 1, Section 2.2 for definition and properties). Therefore, the reliability bounds for a series system of associated components (Ref. 1, Section 2.3) apply, yielding

$$\prod_{i=1}^m P(\tau_i = 1) \leq P(Y_j = 1) \leq 1 - \prod_{i=1}^m [1 - P(\tau_i = 1)]$$

which is the desired result.

The advantage of upper and lower bounds lies in that they provide an estimate of the error of each bound. We can use these approximations to compute bounds on the expectations of the value of all the activities. Since activity  $j$  is worth  $V_j$  we obtain

$$E \sum_{j=1}^l Y_j V_j = \sum_{j=1}^l P(Y_j = 1) V_j$$

and this can be bounded above and below by the bounds on each individual term.

The computation of the exact reliability can, at least in principle, be carried out along the following lines: Let  $\phi_i(\underline{x})$  be the binary structure of signal  $i$ . Let

$$\phi(\underline{x}) = \prod_{i=1}^m \phi_i(\underline{x})$$

be the structure of all activities (the activity can be performed if all signals are present). Although the product need only be taken over those signals that are actually used in activity  $j$ , the use of all signals will cause no problems once the minimal levels are introduced.

Corresponding to the structure  $\phi$  defined above we have the reliability function

$$h(\underline{P}) = P[\phi(\underline{x}) = 1] = h(P_1, \dots, P_n)$$

obtained as before by replacing  $x_i$  by  $p_i$  in the expansion of  $\phi$ . We now let

$$M_{kj} = \max_i \{m_{ij}\}$$

(where the maximization is carried out only over those signals  $i$  in which component  $k$  is relevant.)

Therefore  $M_{kj}$  is the minimal level of operation of component  $k$  that is compatible with the operation of activity  $j$ . It follows that the probability that activity  $j$  can be carried out is

$$\begin{aligned} P[\Psi_j(\underline{Z}) = 1] \\ = h[P(Z_1 \geq M_{1j}), P(Z_2 \geq M_{2j}), \dots, P(Z_n \geq M_{nj})] \end{aligned}$$

It should be evident that, even if the determination of  $\phi_i(\underline{x})$  could be carried out by analyzing every signal (and this is probably feasible from a practical point of view), the algebraic work necessary to obtain  $\phi(\underline{x})$  is probably beyond the realm of practicality due to the exponential growth in the number of terms (e.g., if each of 10 signals has 5 terms, a conservative estimate, we would have  $5^{10} \sim 9.75$  million terms in the expansion of  $\phi$ . This is what makes the possibility of using bounds so attractive. On the other hand, an alternative worth exploring is that of using symbol manipulation computer programs to expand and reduce these expressions, and this should be examined in the future.

#### IV. An Example

As an example, we will consider the generation of the 10.1-MHz frequency standard by the DSN. The block diagram (Fig. 1) is self-explanatory and is the basis of our analysis. From the block diagram we can easily deduce a logic diagram which specifies the binary structure of the system under consideration (see Fig. 2). By examining this diagram we can list the minimal path sets and minimal cut sets.

Minimal paths	Minimal cuts
1, 6, 7, 10	1, 3, 8
2, 3, 6, 7, 10	1, 3, 12
3, 4, 6, 7, 10	1, 2, 4, 5
3, 5, 6, 7, 10	1, 3, 4, 5
4, 6, 7, 8, 10, 12	7
5, 6, 7, 8, 10, 12	10
	6

Note that from the diagram, components 4 and 5 always appear in a parallel configuration and can thus be treated as a module, i.e., as a single larger component. Similarly, components 8 and 12 are in series and so are 6, 7 and 10.

Thus, if we let

$$X_A = X_4 + X_5 - X_4 X_5$$

$$X_B = X_8 X_{12}$$

$$X_C = X_6 X_7 X_{10}$$

we can rewrite the logic diagram as seen in Fig. 3. We obtain the following minimal path and minimal cuts

Minimal paths	Minimal cuts
1, C	1, 3, B
2, 3, C	1, 2, A
3, A, C	1, 3, A
B, A, C	C

Therefore, the structure function is (based on the minimal paths)

$$\phi(X) = 1 - (1 - X_1 X_C)(1 - X_2 X_3 X_C) \\ (1 - X_3 X_A X_C)(1 - X_A X_B X_C)$$

or, based on the minimal cut sets,

$$\phi(X) = [1 - (1 - X_1)(1 - X_3)(1 - X_B)] [1 - (1 - X_1) \\ (1 - X_2)(1 - X_A)] [1 - (1 - X_1)(1 - X_3)(1 - X_A)] X_C$$

Either expression can be reduced, after some painful algebra to

$$\phi(X) = X_1 X_C + X_2 X_3 X_C + X_3 X_A X_C + X_A X_B X_C \\ - (X_1 X_2 X_3 X_C + X_1 X_3 X_A X_C + X_1 X_A X_B X_C \\ + X_2 X_3 X_A X_C + X_3 X_A X_B X_C) \\ + (X_1 X_2 X_3 X_A X_C + X_1 X_3 X_A X_B X_C)$$

We emphasize that, even though this expression is easy to handle, we have not presented the algebra involved in obtaining it. Furthermore, the equivalent expression for a more complex system would be far harder both to obtain and to use. Therefore, the bounds developed will prove useful.

We now assume there are 5 qualities of signals:

- 0 No signal
- 6 Crystal standard quality
- 7 Rubidium standard quality
- 8 Cesium standard quality
- 9 Hydrogen maser standard quality

These numeric values were chosen as the logarithm of the  $Q$  value of typical devices of each kind. Any other assignment could, of course, be selected.

We will also assume known for some point in time  $t$ , values of the probabilities that different components are performing

Component 1: $P[Z = 0] = 0.40$	$P[Z = 9] = 0.60$
Component 2: $P[Z = 0] = 0.15$	$P[Z = 8] = 0.85$
Component 3: $P[Z = 0] = 0.05$	$P[Z = 6] = 0.95$
Components 4 and 5: $P[Z = 0] = 0.10$	$P[Z = 7] = 0.90$
Components 6-7-10: $P[Z = 0] = 0.01$	$P[Z = 6] = 0.02$
	$P[Z = 7] = 0.02$
	$P[Z = 8] = 0.05$
	$P[Z = 9] = 0.90$
Components 8-12: $P[Z = 0] = 0.01$	$P[Z = 7] = 0.99$

We can now compute

$$P_A = 0.9 + 0.9 - 0.9^2 = 0.99$$

and then proceed to compute the distribution of the state of the system. If we wanted  $P[\Psi(Z) \geq 7]$  we would use

$$\begin{array}{ll} P_1 = 0.6 & P_A = 0.99 \\ P_2 = 0.85 & P_B = 0.99 \\ P_3 = 0 & P_C = 0.97 \end{array}$$

to obtain

$$P[\Psi(Z) \geq 7] = 0.9623$$

The reliability lower bounds are

$$\begin{aligned} & [1 - (1-P_1)(1-P_3)(1-P_B)] [1 - (1-P_1)(1-P_2)(1-P_A)] \\ & [1 - (1-P_1)(1-P_3)(1-P_A)] P_C = 0.9617 \end{aligned}$$

and

$$\max \{P_1 P_C, P_2 P_3 P_C, P_3 P_A P_C, P_B P_A P_C\} = 0.9507$$

Thus a lower bound is 0.9617

The reliability upper bounds are

$$\begin{aligned} & 1 - (1 - P_1 P_C) (1 - P_2 P_3 P_C) (1 - P_2 P_3 P_C) \\ & (1 - P_A P_B P_C) = 0.9794 \end{aligned}$$

and

$$\begin{aligned} & \min [1 - (1-P_1)(1-P_3)(1-P_B), 1 - (1-P_1)(1-P_2)(1-P_A), \\ & 1 - (1-P_1)(1-P_3)(1-P_A), P_C] = 0.9700 \end{aligned}$$

Thus we obtain bounds of

$$0.9617 \leq P[\Psi(Z) \geq 7] \leq 0.9700$$

We can similarly compute bounds for the other states of the system

$$\begin{array}{ll} 0.9890 \leq P[\Psi(Z) \geq 6] \leq 0.9900 & (\text{true value } 0.9890) \\ 0.9617 \leq P[\Psi(Z) \geq 7] \leq 0.9700 & (\text{true value } 0.9623) \\ 0.5700 \leq P[\Psi(Z) \geq 8] \leq 0.5700 & (\text{true value } 0.5700) \\ 0.5400 \leq P[\Psi(Z) \geq 9] \leq 0.5400 & (\text{true value } 0.5400) \end{array}$$

From these bounds it is possible to compute bounds on information such as the expected state of the system ( $8.06 \leq E\Psi(Z) \leq 8.07$ ).

## V. Summary

We have examined a system which can produce multiple outputs each of which can be of many different qualities. We presented a method of modelling such system as a function of the state of each of its components, and, when that state is known only as a probability distribution, we have shown how to determine the probability distribution of the measure of the system's effectiveness. It was shown that the exact computation of this distribution could be an impossible task and that therefore it may be attractive to have available upper and lower bounds whose computation is easier to carry out.

## **Acknowledgment**

The author would like to acknowledge James Lesh for suggesting the problem and for the support and helpful discussions he provided.

## **Reference**

1. Barlow, R. E., and Proschan, R., *Statistical Theory of Reliability and Life Testing*, Holt Rinehart Winston, 1975.

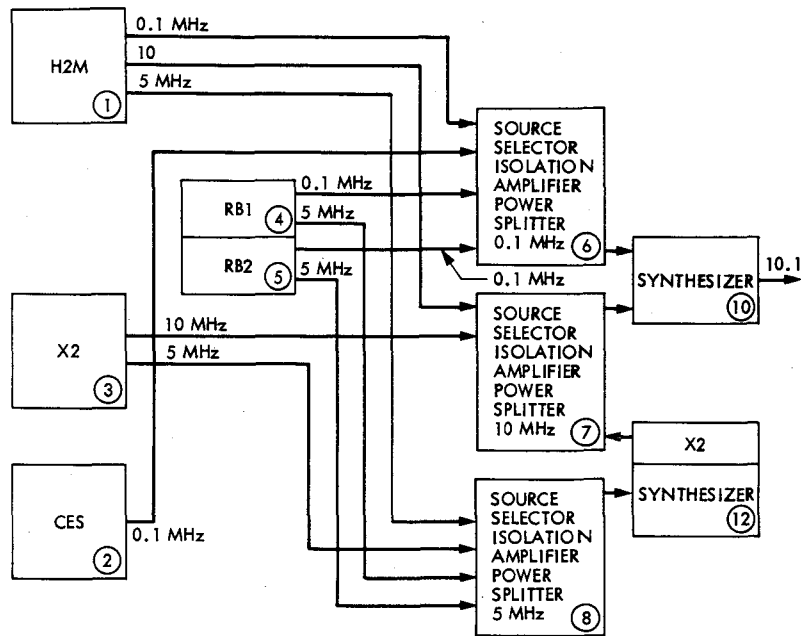


Fig. 1. Block diagram: 10.1 MHz frequency generation (numbers in circles are component numbers)

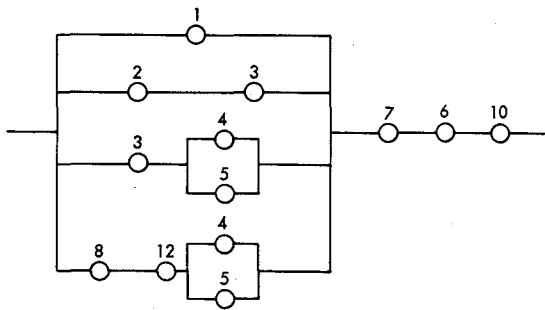


Fig. 2. Logic diagram

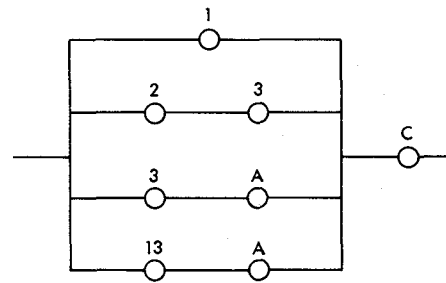


Fig. 3. Logic diagram including modules

# New Results on Antenna Arraying: Part 1

L. J. Deutsch, R. L. Miller, and S. A. Butman  
Communications Systems Research Section

*Baseband combining with and without combined carrier referencing for antenna arrays are compared under two scenarios for the Voyager 2 Uranus encounter. The combined carrier reference scheme is estimated to outperform the baseband-only scheme by less than 0.3 dB  $E_b/N_0$  at a bit error probability of  $5 \times 10^{-3}$ . These results were attained both with mathematical modeling and software Viterbi decoder simulations.*

## I. Introduction

Two methods have been proposed for the combining of signals received by an array of several antennas from deep space missions. The first, and by far the easier of the two, is known as "baseband-only combining." In this scheme, the receiver for each antenna heterodynes the incoming signal separately and the resulting baseband signals are simply added together. Since each receiver has its own phase lock loop for determining a reference phase for heterodyning, statistically independent phase errors (sometimes called "tracking errors") are introduced. This fact makes baseband-only combining awkward to model mathematically, and therefore its performance is difficult to estimate confidently without the use of a computer.

The second scheme is called "baseband combining with combined carrier referencing." In this scheme a single phase reference is determined by a single phase lock loop which examines the combined incoming signal. This reference is then used in every receiver for heterodyning to baseband. The difficulty in this scheme is that extremely accurate clocks are needed to synchronize the receivers. The amount by which this scheme will outperform baseband-only combining at Voyager 2 Uranus encounter is the subject of this article.

Figures 1 and 2 show simplified block diagrams of the two arraying schemes previously described. The delays are shown to compensate for the geometry of the array.

For the Voyager 2 Uranus encounter, arrays consisting of one 64-m antenna and one or more 34-m antennas are being considered. Arrays with two and three 34-m antennas will be considered in this article. An important question is whether baseband-only combining, which is less expensive and easier to implement, will suffice for this encounter or whether the addition of combined carrier referencing will be necessary.

A detailed analysis of baseband combined arrays is presently being undertaken and will be published in Part 2 of this study. The results presented here represent only a small portion of the intended effort, but they already show that, for the Uranus encounter, at most 0.3 dB channel  $E_b/N_0$  is gained by using combined carrier referencing.

## II. Theory of Baseband-only Combining

Suppose there are  $n$  antennas with a total area of unity. (This normalization is convenient for modeling purposes.) Let the

$i^{\text{th}}$  antenna have effective area  $w_i$  and let its phase lock loop signal-to-noise ratio (SNR) be  $\rho_i$ . Loop SNR is a measure of how well a phase lock loop can track the phase of a signal. It is known (Ref. 1) then that the  $i^{\text{th}}$  antenna's loop will generate phase errors  $\phi_i$  according to the distribution

$$p_i(\phi_i) = \frac{e^{\rho_i \cos \phi_i}}{2\pi I_0(\rho_i)}. \quad (1)$$

If a signal of (data) amplitude  $A$  is received by this array, the baseband combined signal will have amplitude

$$A' = \sum_{i=1}^n A w_i \cos \phi_i.$$

Hence, if the data signal-to-noise ratio of the array were equal to  $E_b/N_0$ , then the SNR seen at the output of the baseband combiner would be

$$\text{TOTSNR} = (E_b/N_0) \left( \sum_{i=1}^n w_i \cos \phi_i \right)^2. \quad (2)$$

Let  $x_i = \cos \phi_i$  and let

$$x = \sum_{i=1}^n w_i x_i.$$

Then, if the  $\phi_i$  vary slowly compared to the data rate of the signal (high rate model), the random variable  $x$  is distributed according to

$$\begin{aligned} f(x) &= \int_{-1}^1 \dots \int_{-1}^1 f_1(x_1) \dots f_{n-1}(x_{n-1}) \\ &\times f_n((x - w_1 x_1 - \dots - w_{n-1} x_{n-1})/w_n) \\ &\times dx_n \dots dx_1 \end{aligned}$$

where

$$f_i(x_i) = \frac{e^{\rho_i x_i}}{\pi I_0(\rho_i) \sqrt{1-x_i^2}}.$$

Voyager 2 uses a (7, 1/2) convolutional code for which the probability of bit error ( $p_{BIT}$ ) is known as a function of the channel  $E_b/N_0$ . Let this function be denoted by  $p_{BIT}(E_b/N_0)$ . Then the overall bit error performance of the baseband combined array is given as a function of  $E_b/N_0$  by

$$P_{ARRAY}(E_b/N_0) = \int_{-1}^1 p_{BIT}\left(\frac{E_b}{N_0} x^2\right) f(x) dx.$$

### III. The Relationship Between Loop SNR and Carrier Margin

The theory presented in Section II assumed knowledge of the loop SNRs of each receiver. In practice, carrier margin, and not loop SNR, is the known quantity. This section contains a method for computing loop SNR from carrier margin. Figure 4 shows the dependence of loop SNR on carrier margin for the expected receiver configurations at Uranus encounter.

The tracking loop SNR is given by

$$\rho = \frac{P_C}{N_0 B_L \Gamma}$$

where  $P_C$  is the carrier power,  $N_0$  is the one-sided noise spectral density,  $B_L$  is the loop bandwidth of the receiver, and  $\Gamma$  is the loop's bandpass limiter suppression factor. This formula can be rewritten as

$$\rho = m \frac{2B_{LO}}{B_L \Gamma}$$

where  $m$  and  $B_{LO}$  are the carrier margin and the threshold loop bandwidth respectively. In the case that  $2B_{LO} = 30$  Hz,  $B_L$  may be calculated from  $m$  by using Fig. 3.

The quantity  $\Gamma$  is often approximated by unity as it is always between 1 and 1.2. However,  $\Gamma$  can be better approximated in the following way. In Ref. 1 it is shown that

$$\Gamma \approx \frac{1 + \rho_H}{0.862 + \rho_H}$$

where  $\rho_H$  is the SNR of the receiver's bandpass hard limiter, and is given by

$$\rho_H = \frac{3m}{w_H \tau_2}$$

where  $w_H$  and  $\tau_2$  are known filter parameters. For the receivers that will be used at Uranus encounter,  $2B_{LO} = 30$  Hz,  $w_H = 4000$ , and  $\tau_2 = 0.05$ . Figure 4 indicates the dependence of the loop SNR  $\rho$  on the carrier margin  $m$  for these receivers.

#### IV. Application of Mathematical Model

The theory developed in Sections II and III can now be used to estimate the performance of any array proposed for the Uranus encounter by analyzing the appropriate mathematical model. For example, consider an array consisting of one 64-m antenna and two 34-m antennas. Suppose also that, of the two 34-m antennas in the array, one is a "listen only" (LO) antenna, while the other is a "transmit and receive" (T/R) antenna. The carrier margin and loop SNR of the LO antenna are greater than those for the T/R antenna. A lower bound to the performance of the array with baseband-only combining is obtained by assuming that both 34-m antennas are T/R.

An upper bound to the performance of the same array with combined carrier referencing is obtained by the performance of a single large antenna whose area equals the sum of the areas of the individual antennas. The carrier margin of this large antenna is the sum of the individual carrier margins. Although the loop SNRs are not additive, the cumulative loop SNR can be computed using Fig. 4. For example, two antennas with combined carrier referencing, each having  $\rho = 10$  dB, would perform no better than a single antenna with  $\rho = 12$  dB.

The expected carrier margins of the 64-m, 34-m (LO), and 34-m (T/R) antennas at Uranus encounter are 16.8 dB, 12.2 dB, and 11.0 dB respectively. The corresponding loop SNRs according to Fig. 4, are 13.4 dB, 10.1 dB, and 9.5 dB. The performance of this array with combined carrier referencing is bounded above by the performance of a single antenna with  $m = 18.9$  dB or  $\rho = 14.9$  dB.

The weights  $w_i$ , discussed in Section II, are proportional to the carrier margins of each antenna. For the lower bound to the baseband-only array performance,  $w_1 = 0.65$  and  $w_2 = w_3 = 0.175$ . Since the upper bound to the array with combined carrier referencing consists of only a single antenna,  $w_1 = 1$  for it.

Figure 5 shows the results of mathematical modeling applied to these parameters. It is clear from this figure that the array with combined carrier referencing performs at most 0.3 dB better than the baseband-only combined array at  $p_{BIT} = 5 \times 10^{-3}$ . For comparison, a graph of the ideal performance (i.e., no tracking losses) of the Viterbi decoder is shown in Fig. 6. The bit error rate of the Viterbi decoder is taken to be 1/2 at low channel SNRs, because the current DSN decoders lose node synchronization in this region.

#### V. Computer Simulations of Two Array Scenarios

In addition to mathematically modeling antenna array behavior, computer simulations were performed using a software Viterbi decoder.

The effective SNR seen by the Viterbi decoder was periodically updated according to Eq. (2) with each  $\phi_i$  being randomly generated according to Eq. (1). The results of these simulations for the array described in Section IV are shown in Fig. 7. Again the difference between baseband combining with and without combined carrier referencing is seen to be less than 0.3 dB. The overall performance indicated by the curves in Fig. 7 is better than that indicated in Fig. 5, because the software Viterbi decoder never loses node synchronization.

In the second scenario there is one 64-m antenna and three 34-m antennas. Of the three 34-m antennas, one is T/R and two are LO. The performance of this four-antenna array with and without combined carrier referencing was also simulated using the Viterbi software decoder. The results are shown in Fig. 8. The difference in performance between these two schemes for this array configuration is also seen to be at most 0.3 dB.

#### VI. Summary and Conclusions

It has been shown, both by mathematical modeling and by computer simulation, that a three-antenna array with combined carrier referencing will perform only 0.3 dB better than the same array with baseband-only combining. Similarly, computer simulations show that a four-antenna array with combined carrier referencing will perform at most 0.3 dB better than the same array with baseband-only combining. Since the difference between these two combining schemes is at most 0.3 dB, careful consideration should be given as to which scheme will be implemented for the Voyager 2 Uranus encounter.

## Acknowledgment

The authors wish to acknowledge several helpful discussions with Dr. C. A. Greenhall.

## Reference

1. Lindsey, W. C., and Simon, M. K., *Telecommunications Systems Engineering*, Prentice-Hall Inc., N.J., 1973.

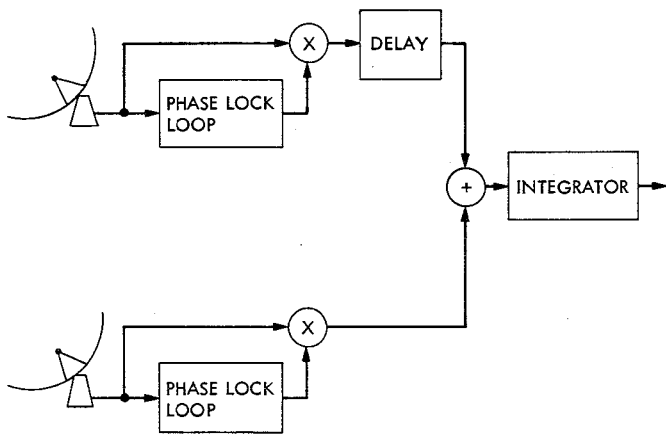


Fig. 1. Baseband-only combined arraying

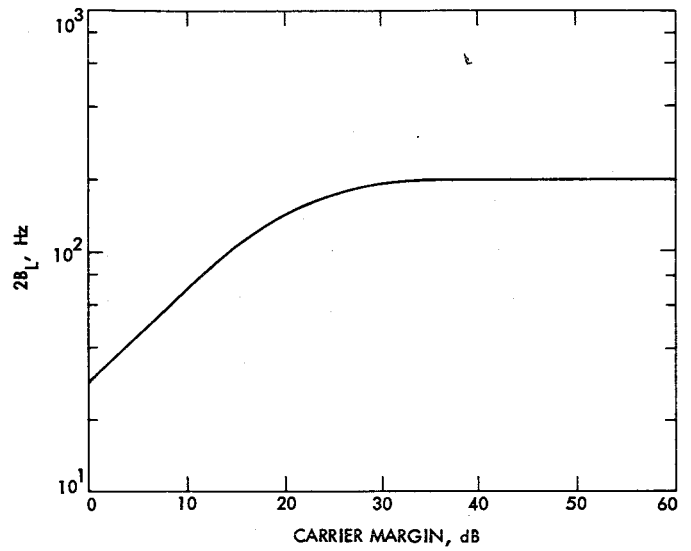


Fig. 3. Two-sided noise bandwidth as a function of carrier margin  
 $2B_{LO} = 30 \text{ Hz}$

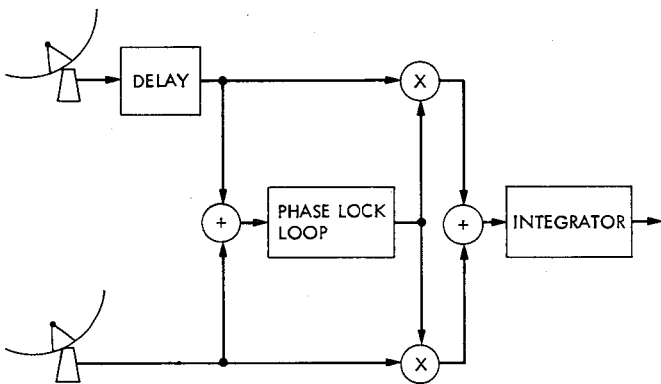


Fig. 2. Baseband combined arraying with combined carrier referencing

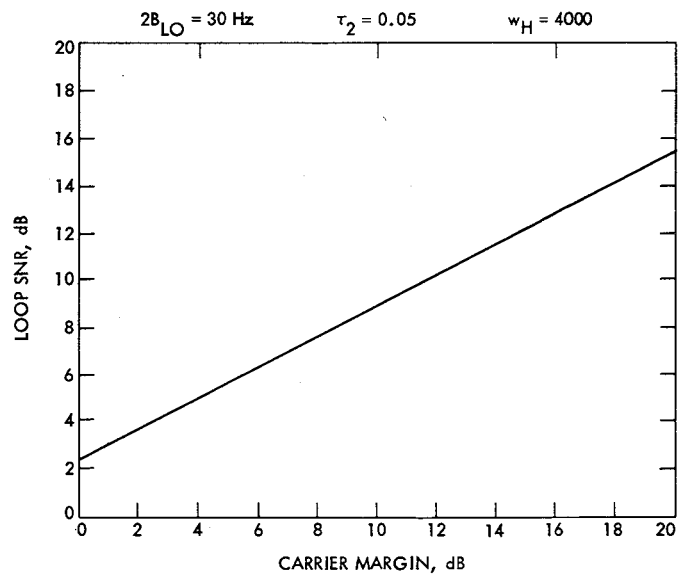


Fig. 4. Loop SNR as a function of carrier margin

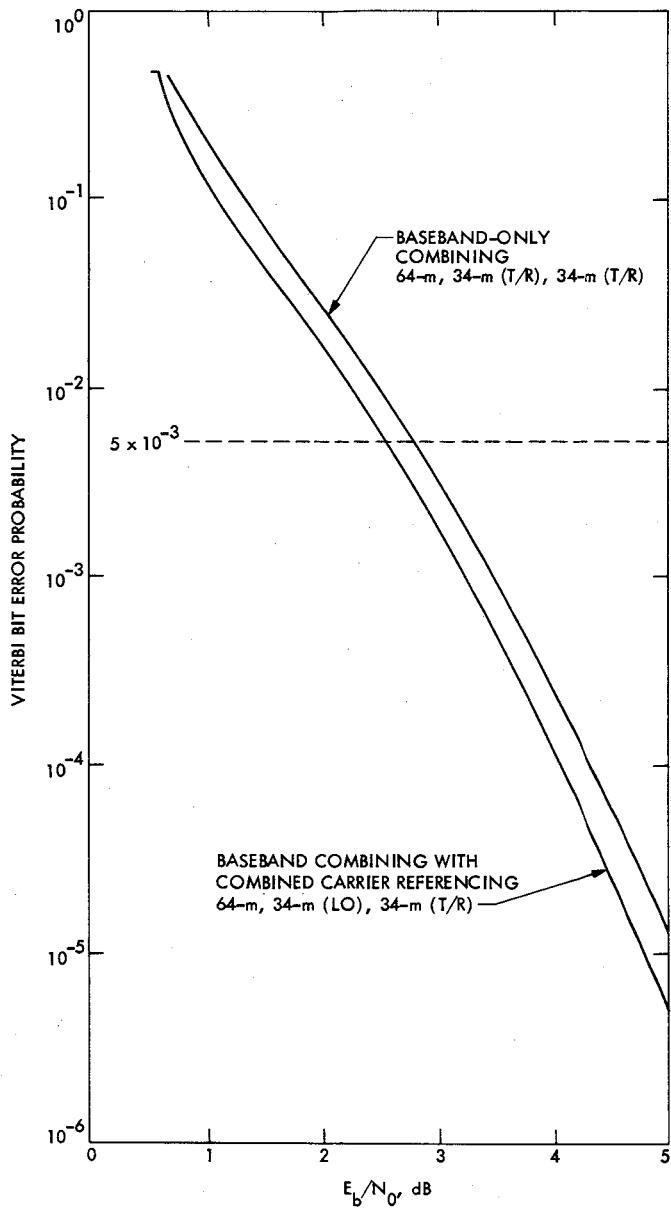


Fig. 5. Results of mathematical modeling for 64-m, 34-m, 34-m array at Uranus encounter

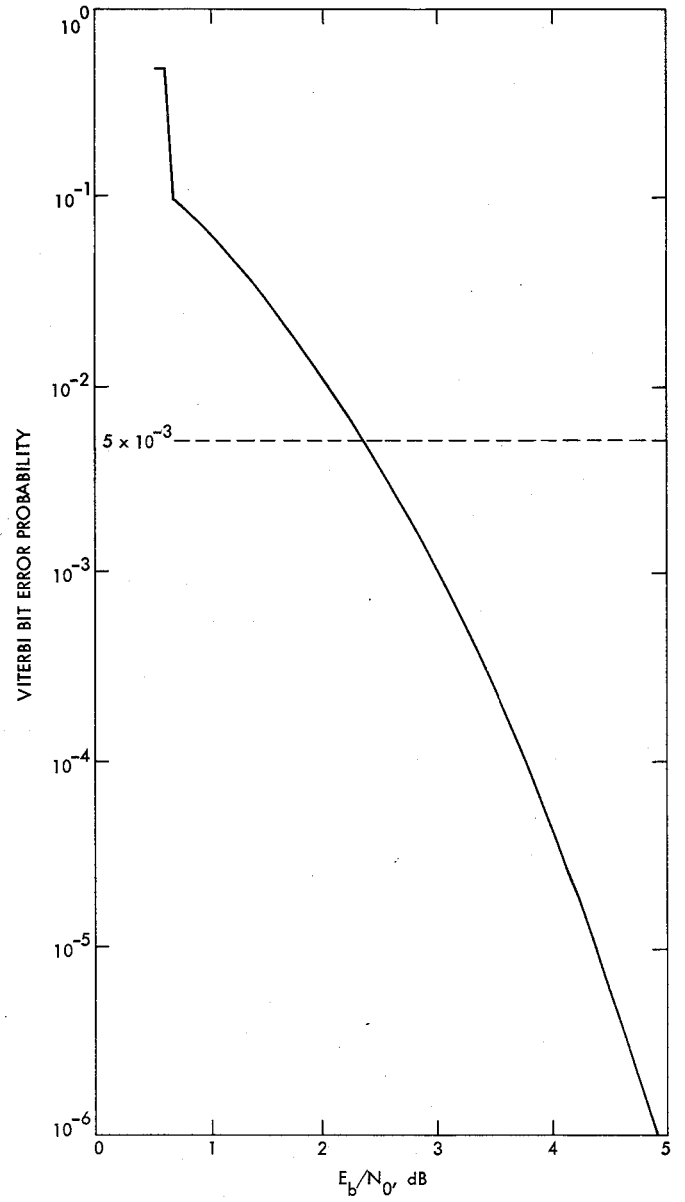


Fig. 6. Viterbi decoder performance without losses due to carrier tracking

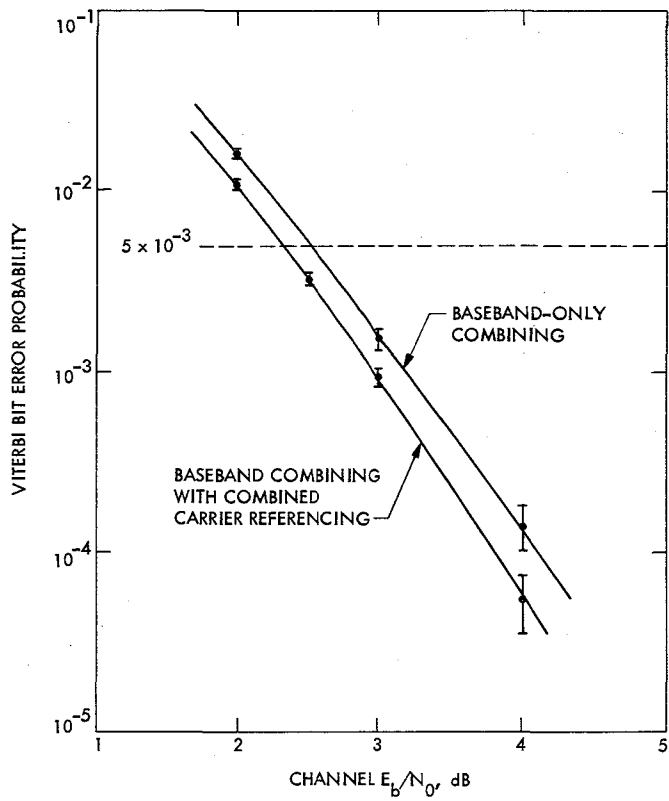


Fig. 7. Viterbi decoder simulations for 64-m, 34-m (LO), 34-m (T/R) array at Uranus encounter

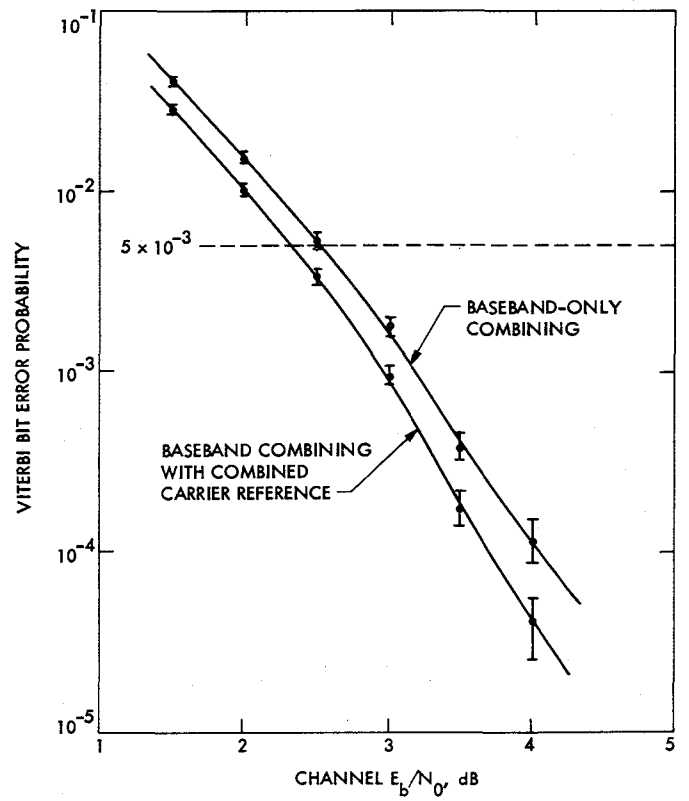


Fig. 8. Viterbi decoder simulations for 64-m, 34-m (LO), 34-m (LO), 34-m (T/R) array at Uranus encounter

# 34-Meter Antenna-Subreflector Translations to Maximize RF Gain

M. S. Katow  
DSN Engineering Section

*The extension of the 26-meter antenna to 34-meter diameter decreased the F/D ratio. This F/D change resulted in unacceptable gain losses due to the hyperboloid's lateral deflections. A three-direction translating mounting device was added to the hyperboloid. This device was controlled by a microprocessor to minimize the offsets of the phase centers in the cassegrain RF system and also compensated for boresight directions. This article discusses the use of the Radiation Program to predict the gain losses from displacements computed by a structural computing program using an analytical model of the 34-meter reflector structure. Field test results showed accurate predictions for the Y and Z hyperboloid translations. In the X-direction, the prediction value was low. However, the computed gain losses vs primary foci offsets by the radiation program were verified by field tests.*

## I. Introduction

The surface panels of the primary reflector and subreflector are rigged or set to the design positions with the 34-meter HA-DEC antenna pointing at 0 (zero) hour angle and -15 degrees declination angle. This rigging position minimizes the structural distortions as described in Ref. 1. When the antenna is moved from the rigged position, gravity loading deflections result in distorted radio frequency (RF) paths as shown in Fig. 1. Offsets of the phase centers occur. These offsets result in varying degrees of RF gain losses to the antenna system. The offsets at the RF feed result in negligible losses; however, the offsets between the focus of the best fit paraboloid and the virtual secondary phase center could result in unacceptable gain losses.

The value of the gain loss in dB per offset unit is a function of the focal-length-to-aperture diameter (F/D) of the primary

reflector and the operating RF frequency. For our case, the decrease in the F/D ratio resulting from increasing the aperture diameter from 26 to 34 meters tripled the gain loss in dB per expected offset of 5.08 cm (2 in.).

Focusing in the axial direction to minimize gain loss results in negligible boresight shift. However, lateral focusing will change the boresight direction. A control system interconnecting the lateral motion of the subreflector to the pointing system becomes a necessity.

## II. Solution Descriptions

A full or complete structural analytical model of the 34-meter HA-DEC reflector structure, which rotates about the elevation axis, was iteratively designed using the IDEAS Program (Ref. 2). Three 1.0 gravity loadings were applied and a

paraboloid was best-fitted to the distorted surface panel attaching points on the reflector structure. The three loading directions were:

- (1) Parallel to the elevation axis (X-direction) or also in the hour angle motion direction.
- (2) Normal to the elevation axis (Y-direction).
- (3) Parallel to the symmetric axis (Z-direction) or the RF boresight direction.

The deflections of the RF feed and the hyperboloid system were also obtained from the IDEAS answers (see Fig. 1 and Table 1). The gain losses from phase center offsets at the paraboloid's focus were evaluated by a version of the JPL-developed Radiation Program, as noted in Ref. 3, which was coded to accept three-component distortion vectors as computed by a structural computing problem (IDEAS).

As in the paraboloid best-fitting rms program (Ref. 4), the surface at a selected point on the paraboloid's surface is assumed to have moved parallel to the original surface. It follows that any distortion vector, OA of Fig. 2, can be normalized as OC. By geometric relationships, OB equals OD and the full pathlength error ODE equals  $OD(1 + \cos \psi)$  or  $2 \times OC \times \cos(\psi/2)$ .

The above-described algorithm permits the simulation of a phase center offset at the focus in the Radiation Program by moving the paraboloid as a unit with equal distortion vectors at each node under a stationary focus point. For maintaining computing accuracy during the integration in the Radiation Program, 341 nodes, approximately equally spaced over the paraboloid's surface, were used. The RF amplitude illumination input to the program was the same as measured for the 64-meter antenna (Fig. 3).

By inputs of varied axial and lateral offsets to the Radiation Program with different focal lengths, the curves shown in Fig. 4 were generated. The gain losses in dB's were converted to the equivalent rms distortion figure by the Ruze equation:

$$\text{Gain Loss} = e^{-16\pi^2 \frac{\text{rms}^2}{\lambda}}$$

where

rms = root-mean-square half-pathlength errors and

$\lambda$  = RF wavelength.

The gain loss conversion from dB to Ruze's rms equivalent loss resulted in RF frequency-independent curves. It should be

noted that the linear relationship between the offset and the gain loss in rms for any antenna resulted from the Radiation Program computations using a maximum of only three wavelengths offset. Figure 5 defines the computed or predicted gain loss in dB vs foci offset for the 34-meter HA-DEC antennas at the DSS stations.

### III. Field Results

The hyperboloid of the 34-meter HA-DEC was mounted to the apex of the quadripod with adjustable means to allow translational motions of plus or minus 7.62 cm (3 in.) in the X, Y, and Z directions. The control was by a microprocessor, which also compensated the pointing of the boresight change created by the lateral shifts.

A look-up table in the microprocessor was initially loaded with computed hyperboloid offset data. The data were computed by a modified program (Ref. 1) using the 1.0 gravity nominal offsets of Table 1. The nominal offsets were from the structural analysis results made initially in the project where the deflection characteristics of the controllable hyperboloid mounts were not known.

Field tests showed that both the Y and Z offsets were correctly predicted using the nominal offsets. However, the X offsets were much larger than predicted. The complete answer to this discrepancy is not known at present. However, by inspection, the X-direction stiffness of the hyperboloid mounting assembly is obviously less than in the Y-direction. The X offset of -4.83 cm of Table 1 was increased to -7.45 cm to maintain minimum gain loss. During the field tests, the gain losses vs offsets were measured. The field test results confirmed the correctness of the predicted curves of Fig. 5.

If an extreme eastward listening position of 0 deg declination and 75 deg hour angle is assumed (about 12.2 deg to ground) and the required lateral offset is 7.45 cm for 1.0 gravity in the X-direction, then the hyperboloid offset equals:

$$\begin{aligned} \text{Hyperboloid Offset} &= 7.45 \times \cos(35.2 \text{ (polar angle)}) \\ &\quad \times \sin 75 \text{ deg} \\ &= 5.9 \text{ cm} \end{aligned}$$

Since the foci offset itself is a little less than this number, as shown in Fig. 1, then by Fig. 5, about 1 dB gain was saved

using the hyperboloid automatic controls. It should be noted that the gravity and atmospheric losses are largest at these low angles to ground, which also reduces the overall gain.

The gain loss and the reflection factor can also be calculated from curves in Ref. 5, where Ruze has reduced the large amount of computed data by plotting the RF pattern characteristics against a quantity which is a function of the number of half-power beamwidths scanned and the F/D ratio. Although

the curves were necessarily small, it was possible to establish that our computed gain loss checked closely with Ruze's values.

The Radiation Program can use an input RF amplitude pattern as was done in this report, and can also include the feed phase errors if available. The program also accounts for the space loss within the antenna system. Analysis of offset primary reflectors can be made, and the computing costs are nominal for precise answers.

## Acknowledgments

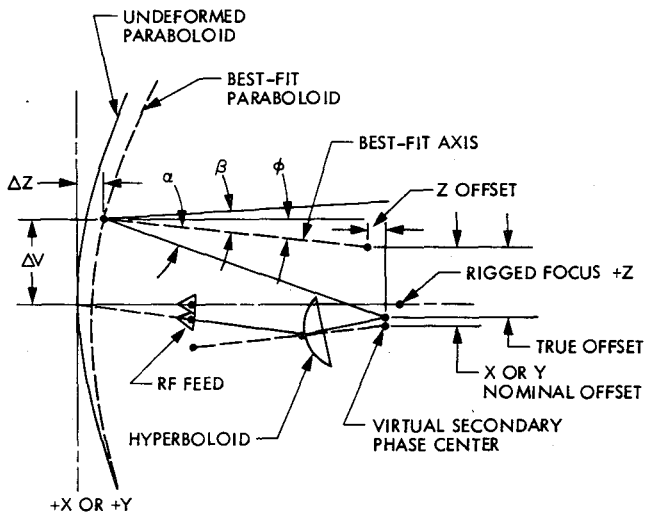
The author wishes to acknowledge the work of Kenneth Ng in developing the 34-meter HA-DEC analytical model and its IDEAS program analysis to output the hyperboloid's displacements. The microwave data furnished by Phil Potter and Dan Bathker and the field tests data verifying Fig. 5 values furnished by Dr. M. J. Klein are also gratefully acknowledged.

## References

1. Katow, M. S., "Minimizing the RMS Surface Distortions From Gravity Loadings of the 34-m HA-DEC Antenna for Deep Space Missions," in *The Deep Space Network Progress Report 42-52*, May and June 1979, pp. 94-98, Jet Propulsion Laboratory, Pasadena, Calif., Aug. 15, 1979.
2. Levy, R., "Iterative Design of Antenna Structures," in *The Deep Space Network Progress Report*, Technical Report 32-1526, Vol. XII, pp. 100-111, Jet Propulsion Laboratory, Pasadena, Calif., Dec. 15, 1972.
3. Bathker, D. A., "Radiation Pattern Programs," in *Computer Programs for Antenna Feed System Design and Analysis*, edited by A. Ludwig, Technical Report 32-979, Jet Propulsion Laboratory, Pasadena, Calif., 1967.
4. Katow, M. S., and Schmele, L. W., "Antenna Structures: Evaluation Techniques of Reflector Distortions," in *Supporting Research and Advanced Development, Space Programs Summary 37-40*, Vol. IV, pp. 176-184, Jet Propulsion Laboratory, Pasadena, Calif., Aug. 31, 1966.
5. Ruze, J., "Lateral-Feed Displacement in a Paraboloid," *IEEE Trans. Ant. Prop.*, pp. 660-665, Sept. 1965.
6. Silver, S., *Microwave Antenna Theory and Design*, Radiation Laboratory Series, Vol. 23, p. 173, McGraw-Hill Book Co., New York, N.Y., 1949.

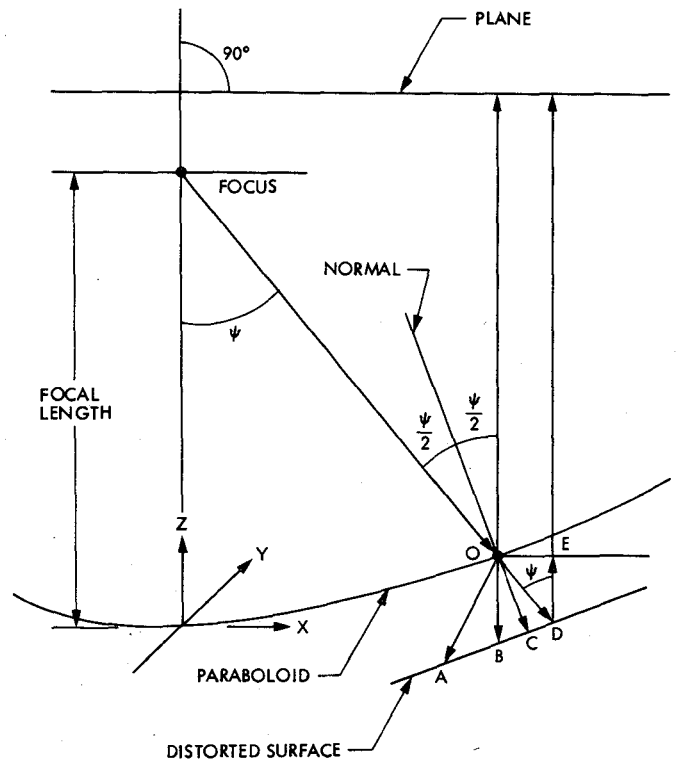
**Table 1. 34-meter antenna computed paraboloid and hyperboloid offsets**

1.0 gravity loading	Rotation $\phi$ , rad	$\Delta v$ vertex offset, cm	$\Delta z$ vertex offset, cm	Nominal offset, cm	Best-fit focal length, cm
X	0.004328	-9.40	0.0	-4.83	1097.280
Y	-0.004896	-7.89	0.0	-4.06	1097.280
Z	0.0	0.0	0.27	-0.51	1096.78



F - RIGGED FOCAL LENGTH = 10.9728 m (36 ft)  
 D - APERTURE DIAMETER = 34.0 m (111.6 ft)  
 F/D = 0.323  
 $\frac{\beta}{\alpha}$  - REFLECTION RATIO = 0.77

Fig. 1. 34-meter RF center ray tracing and hyperboloid offset for gravity distorted reflective surfaces



OA = DISTORTION VECTOR (CAN BE OUT OF PLANE OF VIEW)  
 OB = DELTA Z ERROR VECTOR  
 OC = NORMAL ERROR VECTOR  
 ODE = FULL PATHLENGTH ERROR

Fig. 2. RF pathlength error

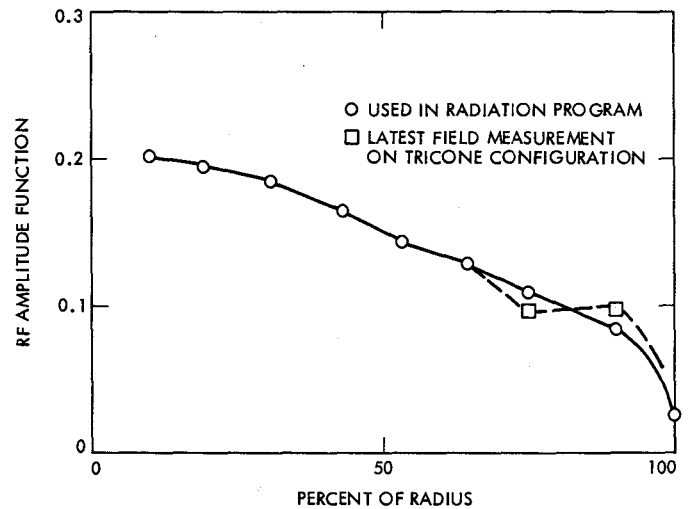


Fig. 3. RF feed amplitude pattern on 64-meter reflector surface

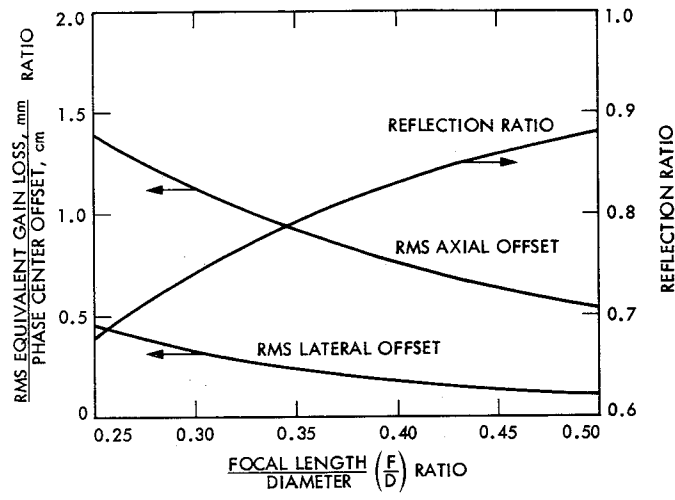


Fig. 4. Gain loss (rms equivalent, mm per cm offset) vs F/D ratio

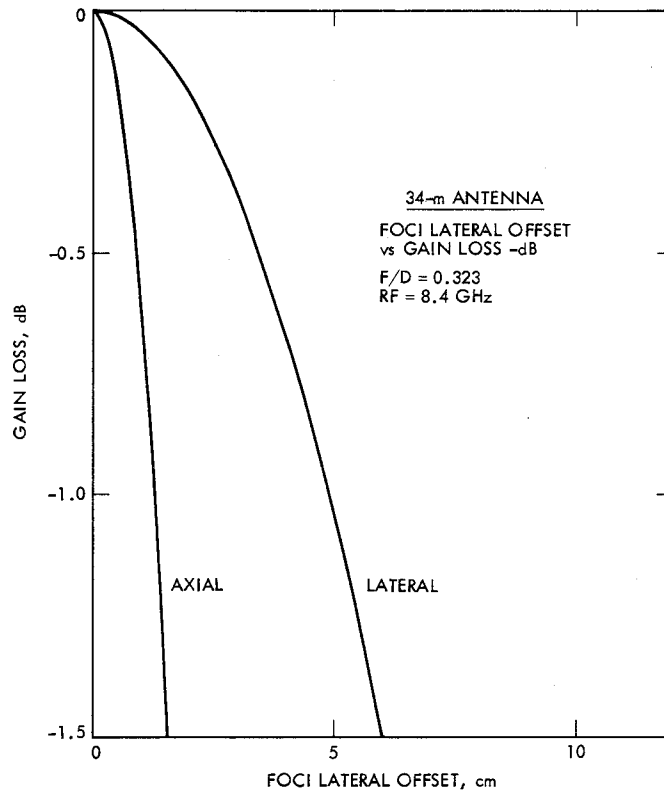


Fig. 5. Foci lateral offset vs gain loss - dB

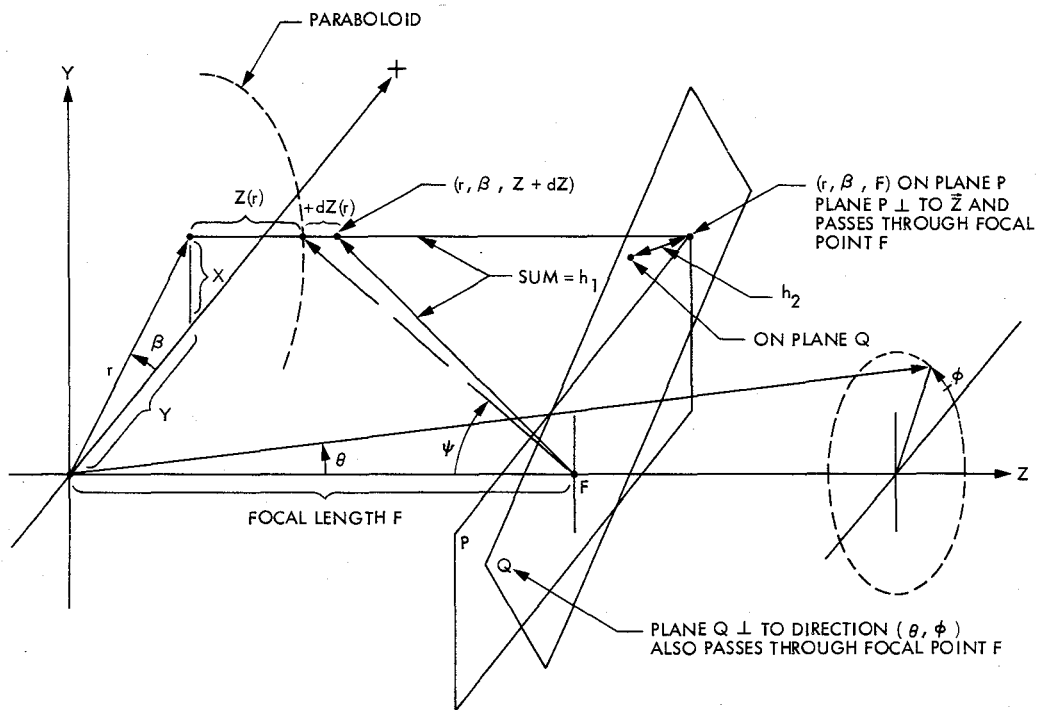


Fig. 6. RF path definitions and direction for the radiation program

## Appendix

An abridged initial reporting of the solution algorithms follows for completeness of this discussion. The solution algorithms were developed by P. Potter of the Microwave Subsystem Group and C. Lawson of the Numerical Analysis Group.

The Radiation Program numerically evaluates the following scalar far-field radiation pattern integral (Ref. 6) by the trapezoidal rule approximation:

$$G(\theta, \phi) = \int_0^{r \max} r w(r) dr \int_0^{360^\circ} e^{jh}(\theta, \phi, r, \beta, k) d\beta$$

where

$$G(\theta, \phi) = \text{RF gain in direction } (\theta, \phi) \quad (\text{Fig. 6})$$

$$h(\theta, \phi, r, \beta, k) = h_1(r, \beta, k) + h_2(\theta, \phi, \beta, r, k) + h_3(r, \beta)$$

$$h_1(r, \beta, k) = k(1 + \cos \psi) dz \quad (\text{Fig. 2})$$

$$= k \left| 1 + \frac{F - z(r)}{[F - z(r)^2 + r^2]^{1/2}} \right| dz(r, \beta)$$

$$z(r) = \frac{r^2}{4F}$$

$$h_2(\theta, \phi, r, \beta, k) = kr \sin \theta \cos(\phi - \beta)$$

$$h_3(r, \beta) = \text{feed phase errors}$$

$$k = \text{propagation factor } (2\pi/\lambda)$$

$$\lambda = \text{RF wavelength}$$

$$dz = \text{reflector surface error measured in Z-direction}$$

As shown in Fig. 6,  $h_1$  denotes the pathlength from the focus of the paraboloid to the reflector at the node  $(r, \beta, z + dz)$ , then to a reference plane  $P$  (which passes through the focal point perpendicular to the  $z$ -axis) at the point  $(r, \beta, F)$ ;  $h_2$  denotes the pathlength from the plane  $P$  to the plane  $Q$  in

the direction  $(\theta, \phi)$ . Plane  $Q$  passes through the focal point perpendicular to the direction  $(\theta, \phi)$ . The sum  $(h_1 + h_2)$  expresses the pathlength in radians minus the constant pathlength property of a paraboloid  $2kF$ .

As shown previously, the pathlength error in  $h_1$  resulting from the  $dz$  error is approximated closely by  $(1 + \cos \psi) dz$  (Fig. 2).

The paraboloid reflector surface is defined by

$$r^2 = x^2 + y^2 = 4Fz$$

The normal vector  $OC$  at the node  $(x, y, z)$  (Fig. 3) has components

$$n_1 = \frac{-2x}{c_1}$$

$$n_2 = \frac{-2y}{c_1}$$

$$n_3 = \frac{4F}{c_1}$$

where

$$c_1 = \sqrt{4x^2 + 4y^2 + 16F^2}$$

The projection of the distortion vector  $(u, v, w)$  on the normal has components

$$P_1 = c_2 n_1$$

$$P_2 = c_2 n_2$$

$$P_3 = c_2 n_3$$

where

$$c_2 = un_1 + vn_2 + wn_3$$

The length of the  $P$  vector is

$$\|P\| = \sqrt{\sum_{i=1}^3 P_i^2} = c_2$$

The magnitude of  $dz$  is

$$|dz| = \frac{\|P\|}{\cos(1/2 \psi)} = \frac{c_2}{n_3} = \frac{un_1 + vn_2 + wn_3}{n_3}$$

Angle  $\psi$  is defined as

$$\psi = \arccos \left| \frac{F - z(r)}{(F - z(r))^2 + r^2} \right|$$

The primary output of gain loss is the ratio of the magnitude  $G(\theta, \phi)$  to the normalizing factor or perfectly phased antenna value of:

$$G_0 = 36 \int_0^{r_{max}} r w(r) dr$$

# A Decoding Failure Test for the Transform Decoder of Reed-Solomon Codes

R. L. Miller and T. K. Truong  
Communications Systems Research Section

I. S. Reed  
Department of Electrical Engineering  
University of Southern California

*Using a finite field transform, a transform decoding algorithm is able to correct erasures as well as errors of any  $(n, k, d)$  Reed-Solomon code over the finite field  $GF(q)$ . This article discusses a pitfall of transform decoding and how to avoid it. A simple test is given so that the decoder will fail to decode instead of introducing additional errors, whenever the received word contains too many errors and erasures.*

## I. Introduction

Voyager, Galileo, and International Solar Polar Mission (ISPM) each have the capability to employ a coding scheme consisting of a  $(7, 1/2)$  convolutional inner code concatenated with a  $(255, 223)$  Reed-Solomon outer code. A Reed-Solomon decoding algorithm capable of correcting both errors and erasures was described in Ref. 1. This algorithm is called "transform decoding," since it resembles the Fast Fourier Transform (FFT). This feature allows an efficient software implementation. An additional advantage to transform decoding is that it is amenable to analysis by Fourier methods. This article proposes a modification of the algorithm which will essentially eliminate decoding mistakes.

Consider any  $(n, k, d)$  Reed-Solomon (RS) code over  $GF(q)$  Ref. 2. Then any combination of  $s$  erasures and  $t$  errors can be corrected if  $2t + s < d$ . In the event that  $2t + s \geq d$ , it is desirable to have the decoder respond with a decoding failure, i.e., with an alarm telling of the inability to decode. Unfortunately, in some cases it is also possible for a decoding error to

occur; this will happen if the received word is incorrectly decoded, thereby yielding the wrong code word.

Berlekamp and Ramsey (Ref. 3) showed that for the case  $s + 2t = d + 1$ , a lower bound to the probability of incorrectly decoding using any algorithm is given by

$$\binom{n-s-t}{t-1} (q-1)^{-(t-1)}$$

Recently, a simplified algorithm was developed (Ref. 1) for correcting erasures and errors of RS codes over  $GF(q)$ , using the finite field transform method. In this article, it is shown that with transform decoding, decoding errors will always occur if  $s + 2t \geq d$ , unless proper care is taken.

## II. Transform Decoding Algorithm

Suppose that  $c(X)$  is transmitted and  $r(X) = c(X) + e(X)$  is received, containing  $s$  erasures at locations  $\{Z_1, Z_2, \dots, Z_s\}$

and  $t$  (unknown) errors. Then transform decoding of the  $(n, k, d)$  Reed-Solomon code generated by

$$g(x) = \prod_{i=1}^{d-1} (x - \alpha^i)$$

(where  $\alpha$  is a primitive  $n^{\text{th}}$  root of unity) consists of the following steps:

Step 1. Compute the syndromes:

$$S_j = r(\alpha^j) \text{ for } 1 \leq j \leq d-1.$$

Step 2. Compute the erasure locator polynomial:

$$\tau(X) = \prod_{j=1}^s (X - Z_j) = \sum_{j=0}^s (-1)^j \tau_j X^{s-j}.$$

Step 3. Compute

$$T_i = \sum_{j=0}^s (-1)^j \tau_j S_{i+s-j} \text{ for } 1 \leq i \leq d-1-s.$$

Step 4. Compute the error-locator polynomial

$$\sigma(X)$$

from

$$T_1, \dots, T_{d-1-s}.$$

See Ref. 4 for details.

Step 5. Compute

$$\mu(X) = \sigma(X) \tau(X) = \sum_{i=0}^{s+t} (-1)^i \mu_i X^{s+t-i}.$$

Step 6. Compute the "extended" syndromes by

$$S_l = \sum_{i=1}^{s+t} (-1)^i \mu_i S_{l-i} \text{ for } d \leq l \leq n.$$

Step 7. Compute the error-erasure pattern

$$e(X) = \sum_{i=1}^{n-1} e_i X^i,$$

by

$$e_i = \frac{1}{n} S(\alpha^{-i}),$$

where

$$S(X) = \sum_{l=0}^{n-1} S_l X^l,$$

and

$$S_o = S_n.$$

Step 8. Decode  $r(X)$  to yield  $c(X) = r(X) - e(X)$ .

### III. A Transform Decoding Pitfall

This section discusses the proclivity of a transform decoder for making its own errors instead of flagging as uncorrectable a received word containing  $t$  errors and  $s$  erasures, when  $2t + s \geq d$ . It will be shown in the next theorem that a transform decoder does its task perhaps a little too well.

#### Theorem 1

The output of a transform decoder will always be a code word, regardless of the input.

#### Proof

Suppose that

$$f(X) = \sum_{i=0}^{n-1} f_i X^i$$

is input to the decoder, and

$$e(X) = \sum_{i=0}^{n-1} e_i X^i$$

is the output of Step 7 in the decoding algorithm. Then  $h(X) = f(X) - e(X)$  will be a code word for the following reason. If  $1 \leq j \leq d-1$ , then

$$\begin{aligned} h(\alpha^j) &= f(\alpha^j) - e(\alpha^j) \\ &= S_j - e(\alpha^j) \quad \text{by Step 1.} \end{aligned}$$

But,

$$\begin{aligned} e(\alpha^j) &= \sum_{i=0}^{n-1} e_i \alpha^{ij} \\ &= \sum_{i=0}^{n-1} \frac{1}{n} S(\alpha^{-i}) \alpha^{ij} \quad \text{by Step 7} \\ &= \frac{1}{n} \sum_{i=0}^{n-1} \left( \sum_{l=0}^{n-1} S_l \alpha^{-il} \right) \alpha^{ij} \\ &= \frac{1}{n} \sum_{l=0}^{n-1} S_l \sum_{i=0}^{n-1} \alpha^{(j-l)i} \\ &= S_j, \text{ since the inner sum vanishes unless } j = l. \end{aligned}$$

Thus,  $h(\alpha^j) = S_j - e(\alpha^j) = 0$  for  $1 \leq j \leq d-1$ , and  $f(X) - e(X)$  is a code word.

#### IV. A Simple Method for Detecting Decoding Errors

The previous theorem indicates that a transform decoder will allow errors to go undetected in the decoding process unless care is taken. The method to be presented here allows the decoder to detect when it makes a mistake, whenever it is theoretically possible. There are instances, as described in Ref. 3, when no decoder can detect that it has erred. For example, if  $d-1$  erasures occur, then the decoder will "correct" those positions yielding a code word, no matter how many additional errors are present. The next theorem provides a test so that decoding failures can be declared instead of allowing the decoder to output bad data unknowingly. Of course, when a decoding failure occurs, the best policy is to leave the received word unaltered.

##### Theorem 2

Suppose that  $t$  errors and  $s$  erasures have occurred, and that the Hamming weight of the error vector computed by the decoder is  $w$ . Then the decoder has erred if  $2w \geq d + s$ .

##### Proof

The decoder errs whenever  $2t + s \geq d$ . Unfortunately,  $t$  is unknown; only  $s$  and  $d$  are known by the decoder. Now since  $w = t + s$ , if

$$2t + s \geq d,$$

then

$$2(w - s) + s \geq d,$$

hence

$$2w \geq d + s.$$

## References

1. Reed, I. S., and Truong, T. K., "A Simplified Algorithm for Correcting Both Errors and Erasures of R-S Codes," *Deep Space Network Progress Report 42-48*, September and October 1978, Jet Propulsion Laboratory, Pasadena, Calif., Dec. 15, 1978.
2. McEliece, R. J., *The Theory of Information and Coding*, Addison-Wesley, London, 1977.
3. Berlekamp, E. R., and Ramsey, J. L., "Readable Erasures Improve the Performance of Reed-Solomon Codes," *IEEE Trans. Information Theory*, Vol. IT-24, No. 5, Sept. 1978.
4. Reed, I. S., Scholtz, R. A., Truong, T. K., and Welch, L. R., "The Fast Decoding of Reed-Solomon Codes Using Fermat Theoretic Transforms and Continued Fractions," *IEEE Trans. Information Theory*, Vol. IT-24, No. 1, Jan. 1978.

# Radio Frequency Interference Protection of Communications Between the Deep Space Network and Deep Space Flight Projects

D. W. H. Johnston  
TDA Mission Support Office

*The increasing density of electrical and electronic circuits in Deep Space Station systems for computation, control, and numerous related functions has combined with the extension of system performance requirements calling for higher speed circuitry along with broader bandwidths. This has progressively increased the number of potential sources of radio frequency interference (RFI) inside the stations. Also, the extension of spectrum usage both in power and frequency as well as the greater density of usage at all frequencies for national and international satellite communications, space research, earth resource operations and defense, and particularly the huge expansion of airborne electronic warfare (EW) and electronic countermeasures (ECM) operations in the Mojave area have greatly increased the potential number and severity of radio frequency interference incidents. This article describes the various facets of this problem and the efforts to eliminate or minimize the impact of interference on Deep Space Network support of deep space flight projects.*

## I. Introduction

At the inception of the Deep Space Network (DSN), one of the prime criteria considered in the location of a network communications station was the requirement for a completely radio frequency (RF) noise free environment. In the past several years the DSN capability to operate at progressively weaker signal levels, coupled with the greater use of the entire radio frequency spectrum by aircraft, satellites, etc., has resulted in an increasing number of radio frequency interference (RFI) incidents experienced by the Network. At the Goldstone Deep Space Communications Complex (Mojave desert, California), the DSN currently operates what are probably the most sensitive receivers and antennas in the world to extract intelligence from extremely weak radio signals. When it is realized that the Goldstone Complex is located in

the center of one of the largest restricted areas in the United States, which is now used as a test and proving ground for intensive operations of the most sophisticated electronic warfare (EW) and electronic countermeasures (ECM) equipment specifically designed to prevent intelligence from being extracted from any radio/radar signals, it is surprising that the Deep Space Stations can operate at all.

Other common sources of RFI to the Network are military and civil aircraft communications and navigation transmitters, point-to-point microwave links, military ground radars and vehicles, military and other earth-orbiting satellites, as well as interference generated inside the Network Complex or the Deep Space Station (DSS) itself.

## II. United States Department of Defense and Goldstone Complex Compatible Operations

The original selection of Goldstone, in 1958, as the site for the NASA/JPL/DSN communication stations was influenced mainly by the remote location in valleys which were out of the "line of sight" of any other manmade dwellings or structures. The closest domestic dwellings were over 80 km away, and the barren desert terrain, in the Ft. Irwin restricted area, made the building of new domestic or commercial radio noise sources a very remote possibility. The Department of Defense (DOD) activities at that time consisted mainly of occasional ground vehicle and troop exercises at Ft. Irwin, sporadic aircraft bombing and gunnery exercises at Edwards Air Force Base (EAFB) and China Lake Naval Weapons Center gunnery and bombing ranges.

The 20 years between 1958 and 1978 saw a vast change in the Mojave area activities. The very reasons NASA used in selecting the Goldstone location were the same reasons used by DOD to move the bulk of their research and development, testing and training to the same area. The result was that the number and scope of the defense exercises increased as did the number and severity of interference incidents at the Goldstone complex. On many occasions, visiting aircraft using the ranges were not even aware of the existence of the Goldstone complex and inadvertently radiated the stations.

The big problem, however, was that the DSN did not have the communications, points of contact or monitoring equipment to determine what the interfering source was, and each interference event ended on many occasions in numerous fruitless phone calls trying to identify the culprit. These exercises also uncovered the fact that the Network was often not the only victim and that interference between the various branches of DOD was becoming more prevalent.

In December 1978, a Memorandum of Understanding was signed by DOD and NASA. Summarizing, the memorandum states in part:

"a. DOD and NASA jointly will:

- (1) Establish a Mojave Coordinating Group (MCG), with DOD and NASA membership, for operational coordination, scheduling, and problem resolution."

It also states in part that . . . "NASA will:

- c. (4) Pursue a program to reduce the electromagnetic interference susceptibility of the Goldstone facility.
- (5) Pursue a program to enhance the capability to detect, classify, and identify electromagnetic interference."

The Mojave Coordinating Group was formed and composed of representatives from each of the military bases and ranges, NASA, JPL, Goldstone Deep Space Communications Complex, Department of Energy (DOE), Federal Aviation Authority (FAA), and the Electromagnetic Compatibility Analysis Center (ECAC). The MCG meets at six-week intervals to coordinate DOD and NASA scheduled events to ensure compatible, interference-free operations in the area. During 1979-1980 the MCG has proved to be extremely effective, as demonstrated during the last three quarters of 1980 when relatively few interference events occurred during routine spacecraft cruise operations and no interference was experienced during any critical or semicritical operations.

The functions of the MCG, the classification of DSN events, and the analysis and real-time coordination of RFI events are dealt with in some detail in Ref. 1.

## III. Radio Spectrum Surveillance Station

### A. Background

In mid 1978, prior to the signing of the NASA-DOD Memorandum of Understanding, the RFI situation at Goldstone indicated a strong requirement for some form of monitoring or detection of interference signals to facilitate their identification and prevent their recurrence.

A relatively small, low-cost surveillance station was designed, built, and installed at Goldstone. The initial installation consisted basically of a rotating horn antenna, mounted on top of the Goldstone 26-meter antenna station collimation tower. The tower, approximately 4 km from the 26-meter site and normally used as a calibration target for the station, is located on a hilltop overlooking the Complex and surrounding area. The antenna was connected to a preamplifier, down-converter and spectrum analyzer at the collimation tower site. This original model was equipped with a camera which was triggered whenever a signal was observed above a preset amplitude threshold. Each time the camera was triggered, the time and azimuth were recorded on the photo, and a counter in the Frequency Coordinator's office at the 26-meter station site was updated.

### B. Operations

The prototype radio spectrum surveillance station became operational in late 1978 and immediately proved to be an extremely effective tool to detect and identify interfering signals, particularly when the spectrum photos were used in conjunction with the MCG meetings. On many occasions, a group member could identify the interfering signal source as coming from a particular aircraft, emitter, frequency and

operational mode. The type of aircraft and configuration would then be listed as a definite DSN interference threat with the understanding that future scheduled operations would be coordinated with the DSN operations to prevent a recurrence. Spectra not identified by the MCG would be submitted to the Electromagnetic Compatibility Analysis Center for identification by their Annapolis computer facility; results were reported back to the MCG.

On many occasions, Defense Department agencies were subjected to the same interference as the DSN. When identified, the interference proved to have originated either unknowingly from one of the Mojave agencies' equipment (spurious, harmonics, etc.) or from agencies outside the Mojave area, sometimes hundreds of miles from Goldstone. Thus the Surveillance System has proved to be beneficial to the total Mojave Coordination Group membership and has resulted in a much closer working relationship within the group.

### **C. Radio Spectrum Surveillance System Enhancement**

As noted above, the prototype Radio Spectrum Surveillance System was equipped with a camera to record an event. This was effective but extremely cumbersome and time consuming. When the counter updated (indicating the receipt of an interference event) or RFI was experienced at a station, or both, the Interference Coordinator would drive to the collimation tower site, remove the film cassette, and have it developed and printed before he could start to analyze and identify it.

In early 1979, a Radio Spectrum Surveillance System redesign was initiated to enhance system capabilities. Redesign was completed in mid-1979 and currently the radio spectrum analyzer signal is converted to a digital format, automatically transmitted to the 26-meter site, stored on magnetic tape and printed on a hard copy page print. It can be replayed and displayed on a cathode ray tube or printed on a page printer. The system was moved from the collimation tower site, to a more suitable location, previously occupied by a surveillance radar installation.

A decision will be reached in 1982 as to whether the final model will also be installed at the overseas DSN Complexes. A very detailed technical description of the Radio Spectrum Surveillance System is contained in Ref. 2.

## **IV. Deep Space Network Susceptibility to Radio Frequency Interference**

### **A. Background**

The DSN S-band masers are intended to support spacecraft downlinks in the *deep space only* portion of the S-band

spectrum between 2290 and 2300 MHz. However, they were originally designed to also accommodate Apollo mission frequencies from 2270 to 2290 MHz. As DSN spacecraft downlinks usually operate at extremely low received signal power, the ground stations are very susceptible to interference not only from other in-band signals but also from some specific out-of-band signals. Previous analysis has discovered that RFI at several out-of-band frequencies can resonate with the maser pump and cause in-band interference. The problem to date has been most severe at S-band but with the increasing use of X-band, the problem is expected to increase with time at the higher frequencies.

It should be borne in mind that in the current Memorandum of Understanding with the Department of Defense, NASA agreed to substantially decrease the DSN susceptibility to RFI.

### **B. Cryogenic Filters**

Current thinking is that the best approach to this problem is to design some form of RF filter to reject any other signals except the spacecraft downlink signal of interest at any given time. In late 1979 funding was made available to initiate an R&D task to produce a design for:

- (1) Fixed passband filters ahead of the masers to avoid in-band interference caused indirectly by interfering sources whose prime frequency is outside the maser passband.
- (2) Tunable bandpass filters ahead of the masers to reject interference signals inside the maser pass band. Both types of filter must be cryogenically cooled to avoid raising the system noise temperature and degrading the receiver threshold.

Work is presently concentrated on yttrium iron garnet (YIG) wafer filters and involves one engineer at JPL and one at MIT. However, this is very much in the field of new technology and an answer as to whether or not low-loss, cooled YIG filters are feasible will not be known until late 1981 at the earliest.

## **V. Deep Space Network Radio Frequency Interference from Non-Deep-Space Sources**

### **A. Background**

The S-band spectrum from 2290 to 2300 MHz is allocated to deep space only downlinks by the International Telecommunications Union (ITU) and the Consultative Committee for

International Radio (CCIR) with deep space defined as lunar distance from earth and beyond. The 2200 to 2290 MHz portion is shared by many users including earth-orbiting satellite downlinks used for space operations and research. This includes government uses such as military satellite communications, military surveillance, earth resources satellites as well as terrestrial fixed and mobile communications, and aircraft electronic warfare, electronic countermeasures and telemetry.

Most of these downlinks are comparatively powerful, with the signal strength at times in excess of -90 dBm at the output of a DSN 64-meter (62 dBi gain at S-band) antenna on bore-sight. So although a satellite may be radiating on a center frequency outside the deep space spectrum, its associated harmonics, subcarriers and spurious radiation often fall within the deep space band at a level much stronger than the spacecraft earth-received signal.

The effort expended by JPL in the field of RFI avoidance is intended to ensure that no interference is experienced by the DSN during mission-critical or semicritical events, and that interference during routine operations is minimized or coordinated so as to minimize the impact on operations.

The terms "critical" and "semicritical" are often referred to in the following text so they are defined here for better understanding:

Critical or Class I events are of such science-mission importance that failure to execute them exactly as planned would result in catastrophic loss of scientifically unique data or destruction of the spacecraft with complete or near-complete failure to meet the mission objectives. Class I (critical) events are typically of short duration (hours), though longer periods are possible, and are inflexibly fixed in time dictated by launch constraints or celestial geometry, e.g., planetary flyby, planetary landing, launch critical pass.

Semicritical or Class II events are extremely important in terms of science-mission objectives and are defined as periods when loss or interruption of communications with the spacecraft could severely impact the mission objectives or cause extended disorientation of the spacecraft. Class II (semicritical) events fall into two main categories: (1) relatively long periods (days or hours) prior to and immediately following a Class I critical flyby or landing, and (2) relatively short periods required to execute a station-keeping or trajectory correction maneuver. In the case of Class IIA, it is sometimes possible to move sequences within the total period, if necessary, to avoid predicted interference, or in the case of Class IIB, to reschedule the entire event.

## **B. Deep Space Network Radio Frequency Interference from Earth-Orbiting Satellites Supported by the NASA Goddard Space Flight Center, Space Tracking and Data Network**

For many years, JPL and Goddard Space Flight Center (GSFC) have had an informal working interface whereby GSFC passes to JPL prelaunch frequency, spectrum and trajectory information in a form which the DSN then uses as an input to the Deep Space Interference Prediction Program (DSIP2) to predict interference to the Network. The DSIP program is discussed in VI below. This interface has been working very satisfactorily, with only occasional occurrences of predicted and actual interference to the Network and no occurrence during Network critical or semicritical events. A formal Memorandum of Understanding between GSFC and JPL is currently being prepared.

## **C. Deep Space Network Radio Frequency Interference from European Space Agency Earth Orbiting Satellites**

On June 29, 1976, the European Space Agency and NASA agreed upon a formal document titled "Working Arrangement for Radio Frequency Coordination Between ESA and NASA." Comprehensive working agreements and procedures were published in the "ESA/NASA Frequency Coordination Manual" in September 1978. Representatives from both agencies formed the "ESA/NASA Frequency Coordination Group" which initially met frequently, and now meets annually, to discuss and resolve ESA/NASA RFI matters. Prelaunch satellite parameters are received by JPL from ESA and are used by the Deep Space Interference Prediction Program.

These agreements, procedures and relevant interfaces have been operating very satisfactorily, with very rare interference occurrences predicted.

## **D. Deep Space Network Radio Frequency Interference from US Department of Defense Satellites**

A formal Memorandum of Understanding between the Air Force Satellite Control Facility (AFSCF) Sunnyvale, California, and JPL was originated in December 1979. Comprehensive operating procedures have been in use since that time, and they were finalized in February 1980. In this instance, because of the classified nature of the satellite parameters, JPL supplied the Air Force Satellite Control Facility with software modules and training, and routinely supplies the Facility with DSN spacecraft parameters and updates; the Facility runs a prediction program. JPL also supplies the Satellite Control

Facility with schedules of DSN critical and semicritical events to enable their satellite operational sequences to be modified to avoid causing interference during a Network critical event.

This Memorandum of Understanding and interface have been operating very satisfactorily, particularly during 1980 when there have been only two instances of Air Force Satellite originated interference resulting in minimal Network data degradation, and no instances during Network critical or semi-critical events. This is a significant improvement over years prior to the advent of the Memorandum.

### **E. Deep Space Network Radio Frequency Interference from USSR Earth-Orbiting Satellites**

The only USSR satellites known to pose a potential interference threat to the Network are highly elliptic vehicles which compose a subset of early warning satellites in the overall Cosmos series. These satellites operate at various frequencies, some of which have extremely powerful spectral components in the 2290 to 2300 MHz band.

It has not been possible to establish a Memorandum of Understanding, procedures or interface between the USSR and NASA, similar to those with other agencies discussed in this section. When the DSN becomes aware of the launch of a satellite in this category, trajectory information is requested and supplied through established channels, and a NASA station is scheduled to perform a short tracking pass of the satellite to obtain the downlink spectral characteristics. These are then input to the Deep Space Interference Prediction Program and interference predicts generated as for any other satellites.

If interference is predicted during routine or semicritical Network events, the spacecraft project personnel concerned are notified and the spacecraft operational sequences rescheduled, if possible, to avoid the predicted interference. If interference is predicted during a Network Class I critical event, e.g., Voyager Saturn encounter, where the prime mission objectives would be jeopardized, the event time, station location and frequencies are passed to the USSR from JPL via NASA Headquarters and the US State Department with a request for protection. This has occurred on three occasions to date: Pioneer Venus encounter, Pioneer 11 Saturn encounter and Voyager Saturn encounter, and on each occasion the USSR has complied with the request.

Efforts are still being made to establish a more direct and more easily exercised interface with the USSR, though very little progress has been made to date.

### **F. Deep Space Network Radio Frequency Interference from Japanese Satellites**

To date there have been no DSN interference incidents caused by Japanese satellites, mainly because Japan has not operated satellites in the S-band spectrum. In the past, an informal ad hoc interface was successfully established between Japan and NASA/JPL in which the DSN was informed of the status of a Japanese launch vehicle second-stage (battery powered) transponder operating at S-band. This signal was "in view" of the Australian DSN stations for very short periods of time and caused no Network interference.

Recently, Japan announced two launches in the future (one a Deep Space Comet Mission - Planet A) which will operate at S-band frequencies. Japanese-NASA meetings have taken place and it is hoped that a Memorandum of Understanding and formal working interfaces may be achieved in 1981.

## **VI. The Deep Space Interference Prediction (DSIP2) Program**

Briefly, the Deep Space Interference Prediction Program provides the capability to predict degradation to a deep spacecraft S-band downlink, caused by an interfering S-band CW signal from an earth-orbiting satellite. When predicted, the degradation is output in terms of telemetry signal-to-noise ratio degradation and for receiver loss of phase lock. The program will currently handle up to 10 DSN stations, 10 interfering satellites and any number of spacecraft for any one run (see Refs. 3, 5 and 6).

This program has been operating successfully since 1977; however, continuing effort is needed to keep pace with expanding requirements, and need for prediction accuracy. For instance, if the prediction errs on the conservative side this could result in the unnecessary request to turn off an internationally used earth resources satellite, causing loss of revenue and/or data to many countries. On the other hand, no predicted interference indicated in the case where an event will actually occur could result in the loss of a mission's prime objectives.

Future plans include examining the need to predict "X", "K<sub>u</sub>" and "K<sub>a</sub>" band interference from spread spectrum and pulse types of interfering signals.

This is a rather large and quite complex program and a technical description detailing the functions and techniques used will be published in a future TDA Progress Report.

## VII. Deep Space Station Internal Radio Frequency Interference

The modern 64-meter-diameter-antenna Deep Space Station is an extremely large and complex facility bearing no resemblance to its humble ancestors of 20 years ago which comprised a few racks of equipment in a trailer. When one realizes that not only does a 64-meter station control room contain more than 100 RF oscillators but also numerous computers, etc., which operate at speeds into the GHz range, the 60-cycle hum-type problems of early years seem very insignificant.

It appears that the interference characteristics of "off-the-shelf" or Laboratory-designed equipment have not been formally factored into equipment design as the stations have grown, so that currently there is no comprehensive picture of the electromagnetic environment inside a Deep Space Station. Commercial or domestic interference specifications and standards are basically intended to protect the commercial broadcast industry and are completely unsuitable for Deep Space Network use. With a few exceptions, military specifications and standards have also been found unsuitable.

This means that the only Radio Frequency Interference qualifications applied to Network equipment from either a "victim" or "culprit" aspect, have been the application of good engineering practice based on past experience. However, the density and new technology of Network equipment is beginning to require something more than the application of past experience to optimize design from the aspects of susceptibility to, or generation of, RFI. Radio frequency interference specifications are required to qualify most of the various types of equipment already implemented or planned to be implemented in the Network. A proposal to generate specifications, make an inventory and validate all the equipment, as part of the Network's consolidation implementation, is under consideration at this time.

## VIII. Search for Extraterrestrial Intelligence Impact on Radio Frequency Interference Studies

All of the foregoing has discussed RFI avoidance for Network support of Deep Space Missions. The object here simplistically is to reject and avoid or predict and detect all other signals to ensure good reception of a single well-known downlink frequency. The Network will be starting to support Search for Extraterrestrial Intelligence (SETI) program operations in the near future, and this will involve scanning the spectrum initially from 1 to 10 GHz (eventually 25 GHz) to ensure reception of a *single* and completely *unknown* signal, and

rejecting all the known signals. Obviously, current RFI avoidance thinking and techniques will not apply to the SETI operation. It is only in recent months that this task has received attention, and at this time it is still under discussion.

## IX. Human Factors in Radio Frequency Interference Avoidance

The major requirement to ensure effective avoidance of interference is good (personal) relations between the parties concerned, and this applies equally at the local, national and international levels, i.e., the ITU/CCIR/WARC. Participating nations agree that a specific portion of the spectrum will be allocated for a certain type of activity. However, each nation has authority to allocate blocks of frequencies inside their own country, and their numerous agencies, and to assign specific frequencies to government or industry.

When one considers the use of radio communications and navigation on international aircraft flights, it quickly becomes apparent that without extremely tight international, national and local frequency agreements, regulations and management there would be chaos. Satellites, radiating while they pass over many countries every 90 minutes, could increase the chaos without proper frequency management. However, constant coordination between the participants is essential to make the agreements effective, and the preparation for and issuance of the agreements and regulations require dedicated, qualified people working on behalf of the DSN to ensure reasonable protection and to carry out highly technical analyses to provide data for the negotiations and coordinators (Refs. 3-6).

## X. Conclusions

Radio frequency interference is here to stay. The potential for interference has been growing over the past 20 years, and the potential for interference to the Deep Space Network will increase with time. This author feels that JPL has recognized the external interference problem and has taken corrective action, with the result that the number of external interference events have been decreasing, none being experienced during a deep space mission critical event in recent years. Unfortunately, internal interference prevention has not enjoyed the same attention and there have been several cases recently in which several months of troubleshooting have been expended to cure interference problems with new equipment. However, with sufficient qualified personnel and the proper tools to negotiate, coordinate, analyze, predict, detect and identify radio frequency interference, the Deep Space Network should be able to continue to operate compatibly with all the other users of the radio frequency spectrum.

## References

1. Gaudian, B. A., and Cushman, R. B., "Goldstone Radio Spectrum Protection," in *The TDA Progress Report 42-60*, p. 177, Jet Propulsion Laboratory, Pasadena, Calif., Dec. 15, 1980.
2. Hersey, D. R., "Interim Radio Spectrum Surveillance Station," in *The TDA Progress Report 42-52*, May-June 1979, Jet Propulsion Laboratory, Pasadena, Calif., Aug. 15, 1979.
3. Sue, M. K., "Block IV Receiver Tracking Loop Performance in the Presence of CW RFI," in *The TDA Progress Report 42-60*, p. 155, Jet Propulsion Laboratory, Pasadena, Calif., Dec. 15, 1980.
4. Peng, T. K., "RFI Prevention for Colocated Antenna," in *The TDA Progress Report 42-60*, p. 135, Jet Propulsion Laboratory, Pasadena, Calif., Dec. 15, 1980.
5. Low, P. W., "RFI Effects of Continuous Sinewave Signals on Telemetry Data," in *The DSN Progress Report 42-40*, p. 174, Jet Propulsion Laboratory, Pasadena, Calif., Aug. 15, 1977.
6. Low, P. W., "RFI Effects of Continuous Wave Signals on Telemetry Data, Part II," in *The DSN Progress Report 42-51*, p. 204, Jet Propulsion Laboratory, Pasadena, Calif., June 15, 1979.

# DSN Scheduling System

R. Durham  
Control Center Operations

*The Deep Space Network (DSN) Scheduling Group provides the operationally oriented administrative support necessary for the effective scheduling of the DSN. The scheduling system plus the levels of schedules will be explained in this article.*

## I. Introduction

The DSN Scheduling Group, assigned to the Control Center Operations Section, has the direct responsibility and authority for scheduling Network operational resources based upon allocations, constraints and guidelines as set forth by the National Aeronautics and Space Administration, the Office of Space Tracking and Data Systems, and the Telecommunications and Data Acquisition and Deep Space Network Management.

Effective utilization of Deep Space Network (DSN) resources depends upon the requirements and plans of all users being known far enough in advance to accomplish orderly planning. DSN Scheduling provides the users of the Network with the accumulated requirements in a logical and timely manner.

The accomplishment of this task requires the ability to forecast gross requirements for a minimum of three years by means of the DSN Forecast (Fig. 1), refine these requirements into a three-month schedule by means of the DSS Utilization Plan, and further refine these activities in an eight-week schedule (DSN 8-Week Operations Planning Schedule), thereby

resulting in a detailed conflict-free weekly schedule (DSN 7-Day Operations Schedule). Figure 2 is a functional flow chart for scheduling and depicts the sequence of events.

Resource allocation is accomplished through a scheduling system comprising three levels of schedules; long-, mid- and short-range.

## II. Long-Range Resource Allocation Schedule

The DSN Forecast, published quarterly, represents the combined resource requirements by the various network users for the upcoming three years. It also depicts one year of history comparing project requirements versus actual support provided. As the time approaches three months prior to the planned event, these requirements must be shown in greater detail. Whereas the DSN Forecast depicts Network user requirements in four-week increments by longitude and size of antenna, these requirements must now be delineated as to day and facility. This is accomplished via the DSS Utilization Plan, which is commonly referred to as the X-Chart, and the DSN/FPSO Conflict Resolution Operations Planning Schedule.

### III. DSN/FPSO Conflict Resolution Operations Planning Schedule

Multiple users independently submitting requests for tracking resources twenty-four hours a day, seven days a week, creates an environment that can result in scheduling concurrent activities at the same facility. A joint DSN/Flight Project Support Office (FPSO) Scheduling Board is convened weekly to resolve these conflicts. The board comprises a representative from FPSO, DSN, each flight project, and other users of DSN Resources, as required. DSN Scheduling publishes a weekly DSN and FPSO Conflict Resolution-Operations Planning Schedule. The objective of this publication is to identify these conflicts as far in advance as possible. The following information is provided:

- (1) A list of user codes that are used to identify each user. These codes ensure the consistency and uniformity that is essential in data manipulation (Table 1).
- (2) A station loading table (Table 2). Each station requires a minimum of twenty hours per week for preventive maintenance. These tables enable scheduling personnel to ascertain if adequate maintenance has been allocated and if there is any remaining time available.
- (3) A DSS Utilization Plan or X-Chart (Table 3). This plan outlines by month and day the prime activities that are scheduled at each station. It does not reflect noninterference-basis activities or maintenance not requiring facility downtime.
- (4) A DSS Delta X-Chart (Table 4). This chart reflects additions or deletions occurring to the Scheduling data base as compared to the last issue of the DSN and FPSO Conflict Resolution-Operations Planning Schedule.
- (5) A Data Base listing that is month, day, and time sensitive, listing each activity at each station (Table 5) with identified conflicts.

### IV. Mid-Range Resource Allocation Schedule

The X-Chart and the DSN/FPSO Conflict Resolution Planning Schedule have proven to be excellent vehicles for spanning the gross requirements outlined in the DSN Forecast and the refined requirements listed in the DSN 8-Week Operations Planning Schedule. The X-Chart depicts each activity by day and facility. Changes made to the X-Charts have varying degrees of impact on the users. The closer they are made to the scheduled event, the greater the impact on the facilities and projects with low priorities. The impact upon the facilities prohibits proper internal activity planning for personnel train-

ing, engineering change order implementation, and maintenance. Projects cannot properly utilize the residual time which is available after these last minute changes. Analysis has shown that, due to the dynamic nature of the various projects, the greatest number of changes normally occur five to six weeks prior to the scheduled event.

The primary objective of the DSN 8-Week Operations Planning Schedule is to assist all users of Network Resources in the refinement and development of the forthcoming 7-Day Schedule. It is published on a four-week cycle and contains current planned Network resource allocation planned for two weeks in advance of the publication date through the next sequential eight weeks.

### V. Short-Range Resource Allocation Schedule

The DSN 7-Day Operations Schedule provides for the control and accountability of all activities occurring in the DSN. As an operations schedule, it contains the resources and configuration requirements necessary for minute-to-minute DSN Operations Support. The objective of the 7-Day Schedule/Forecast are two-fold. The first and primary objective is that of providing a detailed, timed sequence of events for the operation of the Deep Space Network in the forthcoming week. The second objective is to provide all concerned parties with the latest projected tracking and support activities for the week following the published 7-Day Schedule. This Forecast provides the DSN Facilities and all other principals with the information required so that they may plan their manpower and other resource allocation in the most efficient manner. There are many factors affecting DSN resource allocation. There are those which are known and can be factored into the generation of the 7-Day Schedule; unfortunately there are also those which cannot be accurately predicted. Therefore, provision must be made for accomplishing orderly real-time changes to the published 7-Day Schedule. Real-time scheduling provides a controlled method for coordinating and documenting all real-time changes throughout the Network.

### VI. Real-Time Scheduling

Changes to the published 7-Day Operations Schedule may be disruptive and counterproductive to the Network Resource Allocation System if not closely monitored and controlled. Although each originator of a change request is attempting to maximize his productive use of the Network, the sum of all inputs may be a net loss for everyone. To minimize the impact on resource allocation and maintain high network productiv-

ity, all requested changes are reviewed, assessed for impact, and closely controlled. This is accomplished by the real-time scheduling process.

Change requests to the published 7-Day Operations Schedule are submitted to DSN Scheduling for approval. Scheduling reviews each request for impact to other users, verifying concurrence when required, and availability of Network resources. When these requirements are met, the change requests are

processed. Users of Network resources should only submit these changes to ensure achievement of operational objectives.

The only changes to the published schedule that are accomplished through the Network Operations Control Team are changes required as a result of real-time activities such as spacecraft emergencies, major Network failures, resource conflict resolution, and necessary adjustment to provide committed flight support.

**Table 1. User codes for the DSS Utilization Plan**

Code	Activity
VKG	Viking Project and related DSN preparation testing and training activities
VK1	Viking 1 tracking pass
PNV	Pioneer Project and related DSN preparation testing and training activities
P06	Pioneer 06 tracking pass
P07	Pioneer 07 tracking pass
P08	Pioneer 08 tracking pass
P09	Pioneer 09 tracking pass
P10	Pioneer 10 tracking pass
P11	Pioneer 11 tracking pass
P12	Pioneer 12 tracking pass
HEL	Helios Project and related DSN preparation testing and training activities
HE1	Helios 01 tracking pass
VGR	Voyager Project and related DSN preparation testing and training activities
VG1	Voyager 1 tracking pass
VG2	Voyager 2 tracking pass
R/A	Radio Astronomy: OSS, RAES, OSF and OSTA activities
A/S	Advance Systems: OSTDS activities
HRS	Host Country Radio Science – Spain or Australia
RRR	Downtime for maintenance/reconfiguration
ENG	DSN engineering support
DSN	DSN preparation testing and training activities

**Table 2. DSN/FPSO station loading for weeks 9, 10, 11, and 12**

Week	DSS	Total sched.	4 ± hr gaps	Maintenance	Special <sup>a</sup>	Conflicts
9	11	168:00	0:00	29:25	0:00	0:00
	12	168:00	0:00	168:00	0:00	0:00
	14	168:00	0:00	14:40	32:50	0:00
	42	168:00	0:00	17:45	0:00	0:00
	43	168:00	0:00	23:35	0:00	0:00
	44	168:00	0:00	20:50	0:00	0:00
	61	168:00	0:00	41:50	0:00	0:00
	62	168:00	0:00	47:55	0:00	0:00
10	63	168:00	0:00	29:40	0:00	0:00
	11	149:30	11:20	21:45	0:00	0:00
	12	168:00	0:00	168:00	0:00	0:00
	14	163:25	0:00	13:20	50:20	0:00
	42	151:00	9:25	26:00	0:00	0:00
	43	164:25	0:00	14:25	0:00	0:00
	44	163:30	0:00	19:00	0:00	0:00
	61	142:30	23:35	28:55	0:00	0:00
11	62	125:00	43:00	18:50	0:00	0:00
	63	163:30	0:00	26:30	0:00	0:00
	11	147:00	12:35	17:20	0:00	0:00
	12	168:00	0:00	168:00	0:00	0:00
	14	168:00	0:00	16:10	40:00	0:00
	42	142:00	15:25	25:30	0:00	0:00
	43	167:45	0:00	20:00	0:00	0:00
12	44	161:15	0:00	21:35	0:00	0:00
	61	155:25	4:25	23:10	0:00	0:00
	62	123:15	43:00	21:15	0:00	0:00
	63	164:35	0:00	19:05	0:00	0:00
	11	154:30	0:00	14:50	0:00	0:00
	12	168:00	0:00	168:00	0:00	0:00
	14	160:05	0:00	18:20	15:15	0:00
12	42	142:05	15:05	17:30	0:00	0:00
	43	168:00	0:00	18:15	0:00	0:00
	44	153:05	0:00	16:45	0:00	0:00
	61	147:15	8:50	17:00	0:00	0:00
	62	125:30	35:05	28:50	0:00	0:00
	63	161:40	0:00	16:10	0:00	0:00

<sup>a</sup>Special category consists of the following: sole plate maintenance, RTC array maintenance, and bearing maintenance.

Table 3. DSS Utilization Plan (generated 2/6/81)

Week	8							9							10							11							
Day	Mon	Tue	Wed	Thu	Fri	Sat	Sun	Mon	Tue	Wed	Thu	Fri	Sat	Sun	Mon	Tue	Wed	Thu	Fri	Sat	Sun	Mon	Tue	Wed	Thu	Fri	Sat	Sun	
Date	16	17	18	19	20	21	22	23	24	25	26	27	28	1	2	3	4	5	6	7	8	9	10	11	12	13	14	15	
Month	Feb	Feb	Feb	Feb	Feb	Feb	Feb	Feb	Feb	Feb	Feb	Feb	Feb	Mar	Mar	Mar	Mar	Mar	Mar	Mar	Mar	Mar	Mar	Mar	Mar	Mar	Mar	Mar	
DOY	47	48	49	50	51	52	53	54	55	56	57	58	59	60	61	62	63	64	65	66	67	68	69	70	71	72	73	74	
DSS-11	HE1 VG2	HE1 VG1	DSN P11 HE1	HE1 VG1	HE1 VG2	HE1 VG1	HE1 VG1	P12 HE1 VG1	DSN R/A P11 HE1	P11 P12 HE1	HE1 VG2	HE1 VG1	HE1 VG1	P12 HE1 VG2	HE1 VG2	P12 VG2	P11 P12	R/A P11 HE1	P12 VG1	VG2	P12 VG2	P12 HE1 VG2	P12 VG1 VG2	R/A P11 P12 VG1 VG2	P12 VG1 VG2	P12 VG1 VG2	VG1 VG2	HE1 VG2 VG2	
DSS-12	VG1	P11	RRR	RRR	RRR	RRR	RRR	RRR	RRR	RRR	RRR	RRR	RRR	RRR	RRR	RRR	RRR	RRR	RRR	RRR	RRR	RRR	RRR	RRR	RRR	RRR	RRR	RRR	RRR
DSS-14	DSN P11 P12 RRR	P12 P11 VG2 RRR	VGR P11 VG2 RRR	VGR P11 P12 RRR	P10 P12 P12	P10 P12 P12	P10 P11 P12	RRR	DSN P12 VG2	P10 P12 VG2	P12 RRR HE1	P12 RRR HE1	R/A P10 R/A P12	VGR P10 R/A P10	P12	P10 RRR	HE1 VG2	RRR VG2	P10 RRR	P10 P12	P11	VGR P09 P11 RRR	P09 P11	P10 P11 VG2	P10 RRR	P09 P11 P12	P10 P11 P12	R/A P11 P12	
DSS-42	DSN P11 P12 P12	P12 VG2	ENG P12	ENG P12	ENG P12	P12 VG2	P12 VG2	DSN P11 P12	P12 VG1	P12 VG1	P11 P12	P11 P12	P12 VG2	P11 P12	P11 P12	P12 P12	VG1	P11 P12	VG2 P12	VG2 P12	P12 VG2	P12 VG2	VG1 VG2	VG2 P12	VG2 P12	P11 P12	P11 P12	VG2 P12	VG2 P12
DSS-43	P12 VG1	ENG P12	P12 VG2	VGR P12 VK1 VG2	R/A P11	R/A P09 P12	DSN ENG R/A P12	R/A P12 VG2	P12 VG2	P12 VG2	R/A VG2	R/A VG2	P10 P12	VGR R/A P08 P10	R/A VG1	VG2	P12 VG2	R/A P10 VG2	R/A P12	R/A P12	R/A P11	R/A P12	R/A P12	P10 P12	P10 P12	P10 P12	R/A P12	R/A P12	
DSS-44	DSN P11	P11 HE1 HE1	VG1 P11 HE1	P11 HE1 HE1	HE1 VG1 HE1	P11 HE1 HE1	P11 HE1	HE1 VG1	P11 HE1	P11 HE1	P11 HE1	DSN P11 HE1	P11 HE1 VG1	HE1 HE1 VG1	HE1 HE1 VG1	P11 HE1 VG1	HE1 HE1 VG1	P11 HE1 VG1	HE1 HE1 VG1	P11 HE1 VG1	HE1 HE1 VG1	HE1 HE1 VG1	HE1 HE1 VG1	HE1 HE1 VG1	HE1 HE1 VG1	HE1 HE1 VG1	HE1 HE1 VG1	HE1 HE1 VG1	
DSS-61	VG1	DSN P11	P12 VG2	P12 VG1	VG2 VG2	P12 VG2	P12 VG2	DSN P11 P12	P12 VG1	VG2 VG1	P12 VG1	P12 VG1	P12 VG2	P12 VG2	P11 VG2	P11 VG1	P12 VG1	VG2 VG1	P12 VG2	P12 VG2	VG2 VG1	P12 VG2	P12 VG2	P12 VG2	P11 VG1	P12 VG1	P12 VG1	P12 VG1	P11 VG1
DSS-62	P11 P12	P12 VG1	DSN VG1	R/A P12	P11 P12	P12 VG1	VG1 VG1	VG1 P11	DSN P10	P10 VG2	P11 P10	P12 P10	P12 P11	R/A VG2	P11 VG1	P12 VG1	P12 VG1	VG1 VG1	VG1 VG1	VG1 VG1	P11 P12	P11 P12	P12 P12	P12 P12	P11 P12	P10 P12	P10 P12	P12 P12	P12 P12
DSS-63	P10 VG2	P10 VG2	VGR P10	ENG P10 VG2	P10 P11	P09 P11	ENG DSN P06 P10	ENG P10 P12 VG2	P10 VG2	P10 P10	ENG P10 VG2	P10 P11	DSN P09 P12	VGR P12	P10 VG1	P10 VG2	P10 VG2	P11 P12	P09 P12 VK1	P11 P12	P10 P12	P10 P12	VGR P10 VG2	P10 VG1	P10 P10	P10 P12 VG2	P06 P10 P12	ENG P10 P12	R/A P10 P12

**Table 4. DSS Delta X-Chart (generated 2/13/81)**

Week	9							10							11							12								
Day	Mon	Tue	Wed	Thu	Fri	Sat	Sun	Mon	Tue	Wed	Thu	Fri	Sat	Sun	Mon	Tue	Wed	Thu	Fri	Sat	Sun	Mon	Tue	Wed	Thu	Fri	Sat	Sun		
Date	23	24	25	26	27	28	1	2	3	4	5	6	7	8	9	10	11	12	13	14	15	16	17	18	19	20	21	22		
Month	Feb	Feb	Feb	Feb	Feb	Feb	Mar																							
DOY	54	55	56	57	58	59	60	61	62	63	64	65	66	67	68	69	70	71	72	73	74	75	76	77	78	79	80	81		
DSS-11																														
DSS-12																														
DSS-14															P12	ENG														
DSS-42															ENG															
DSS-43								ENG								ENG														

**Table 5. DSN 10-week operations schedule for all stations, conflicts flagged (week no. 6, 3 Feb 81 – 9 Feb 81)**

Line item	Day	Start-end	Facility	User	Activity	Pass no.	Pre-track hrs-min	AOS LOS	Post-track hrs-min	DSS config	Work category	DSN config	Conflict flag
(Sat. 7 Feb)													
455	38	0000-2400	DSS-12	DSS-12	Panel alignment		None	0000-2400	None	None	3A1	B700	
456	38	0025-0655	DSS-63	DSS-63	Maintenance		None	0025-0655	None	None	2A1	M700	
457	38	0035-0535	DSS-44	HEL-01	Tracking pass	2252	1 0	0135-0520	0 15	200063	1A1	I000	
458	38	0220-0820	DSS-11	DSS-11	Maintenance		None	0220-0820	None	None	2A1	A700	
459	38	0535-0825	DSS-44	PN-12	Tracking pass	995	0 30	0605-0755	0 30	800063	1A1	I000	
460	38	0650-1250	DSS-42	DSN	NEP RFI test		None	0650-1250	None	None	2C2	G700	
461	38	0650-1250	DSS-43	DSN	NEP RFI test		None	0650-1250	None	None	2C2	H700	
462	38	0655-1545	DSS-63	PN-12	Tracking pass	995	0 30	0725-1530	0 15	800063	1A1	M000	
463	38	0815-1250	DSS-43	DSS-43	Maintenance		None	0815-1250	None	None	2A1	H7C0	461
464	38	0820-1745	DSS-11	VGR-01	Tracking pass	1255	0 30	0850-1715	0 30	610063	1A1	A000	
465	38	1020-1520	DSS-61	DSS-61	Maintenance		None	1020-1520	None	None	2A1	K700	
466	38	1135-2250	DSS-44	VGR-02	Tracking pass	1271	1 0	1235-2220	0 30	610063	1A1	I000	
467	38	1250-2220	DSS-43	PN-11	Tracking pass	2872	0 30	1320-2205	0 15	000063	1A1	H000	
468	38	1540-2140	DSS-62	DSS-62	Maintenance		None	1540-2140	None	None	2A1	L700	

PROJECT	ANTENNA SIZE	HELIOS-1 11th PH		HELIOS-2 9th PH		VGR-2 SOLAR CONJ		HEL-1 12th PH		HEL-2 10th PH		HEL-2 11th PH		PN-11 SUP CONJ		VGR-2 SATURN ENC	
		VGR-1 SOLAR CONJ		PN-10 SUP CONJ		PN-11 SUP CONJ		VGR-1 SATURN ENC		PN-VEN SUP CONJ		HEL-1 13th PH		VGR-2 SATURN ENC			
		HEL-1 10th PH	HEL-1 11th PH	HEL-2 8th PH	PN-10 SUP CONJ	PN-11 SUP CONJ	VGR-1 SATURN ENC	VGR-2 SATURN ENC	PN-VEN SUP CONJ	HEL-1 13th PH	VGR-2 SATURN ENC						
PIONEER 10	26-METER	5	5	3				1	2	1							
	34-METER										1						
	64-METER	20	20	19	20	19	20	4	1	6	12	12	12	12	12	12	12
PIONEER 11	26-METER	4	19	19	18	19	18	19	19	13	19	19	18	19	19	18	19
	34-METER																
	64-METER	21	2	2	2	2	2	2	2	2	2	2	2	2	2	2	2
VIKING	26-METER	6	3	3	3	3	3	1	1	1	1	1	1	1	1	1	1
	34-METER																
	64-METER	3	5	5	6	5	1	2	2	2	2	1	1	1	1	1	1
HELIOS	26-METER	4	3	10	21	21	14	11	6	4	1	1	2	3	6	2	
	34-METER																
	64-METER	19	23	9	5	1	3	3	2	4	26	15	2	18	0	18	16
VOYAGER	26-METER	28	28	28	28	56	56	53	40	13	9	11	11	20	20	20	20
	34-METER																
	64-METER	4	4	4	4	4	4	1	3	4	4	17	28	28	28	28	28
PIONEER VENUS	26-METER	10	8	19	15	17	23	26	26	22	18	16	19	20	20	25	28
	34-METER																
	64-METER	28	28														
VLBI BLOCK 1 AND 2	26-METER																
	34-METER																
	64-METER	1	4	2	2	2	2			2	3	3	2	5	3	2	3
IMPLEMENTATION	26-METER																
	34-METER																
	64-METER																
RADIO ASTRONOMY	26-METER	2	2	2	2	2	2	2	2	2	2	2	2	2	2	2	2
	34-METER																
	64-METER	2	2	2	2	2	2	2	2	2	2	2	2	2	2	2	2
ADVANCED SYSTEMS	26-METER	3	3	3	3	3	3	3	3	2	2	1	1	2	1	2	1
	34-METER																
	64-METER	5	5	5	5	5	5	5	5	5	3	2	2	3	2	2	2
PIONEER 6-9	26-METER																
	34-METER																
	64-METER	1															
MULTI-MISSION SUPPORT	26-METER	1															
	34-METER																
	64-METER																
TOTAL PASSES REQUIRED	26-METER	43	55	102	101	129	127	125	106	64	65	62	60	71	73	76	71
	34-METER																
	64-METER	106	93	39	41	39	36	49	55	58	45	45	56	68	67	62	47
TOTAL PASSES AVAILABLE	26-METER	88	88	88	88	88	88	88	88	44	44	44	44	44	44	44	44
	34-METER																
	64-METER	40	40	40	40	40	40	40	40	40	40	40	40	40	40	40	40
REQUIREMENTS	WEEKS	39	43	47	51	3	7	11	15	19	23	27	31	35	39	43	47
	FISCAL YEAR	42	46	50	2	6	10	14	18	22	26	30	34	38	42	46	50
	CALENDAR YEAR	1980								1981							
* TESTS	MONTHS	1979				1980								1981			
	OCT	NOV	DEC	JAN	FEB	MAR	APR	MAY	JUN	JUL	AUG	SEP	OCT	NOV	DEC	JAN	FEB
	PH = PERIHELION    SUP CONJ = SUPERIOR CONJUNCTION    JUP = JUPITER    ENC = ENCOUNTER    VGR = VOYAGER    SOL CONJ = SOLAR CONJUNCTION																
HISTORY ← → PLANNED																	

Fig. 1. DSN forecast, Goldstone

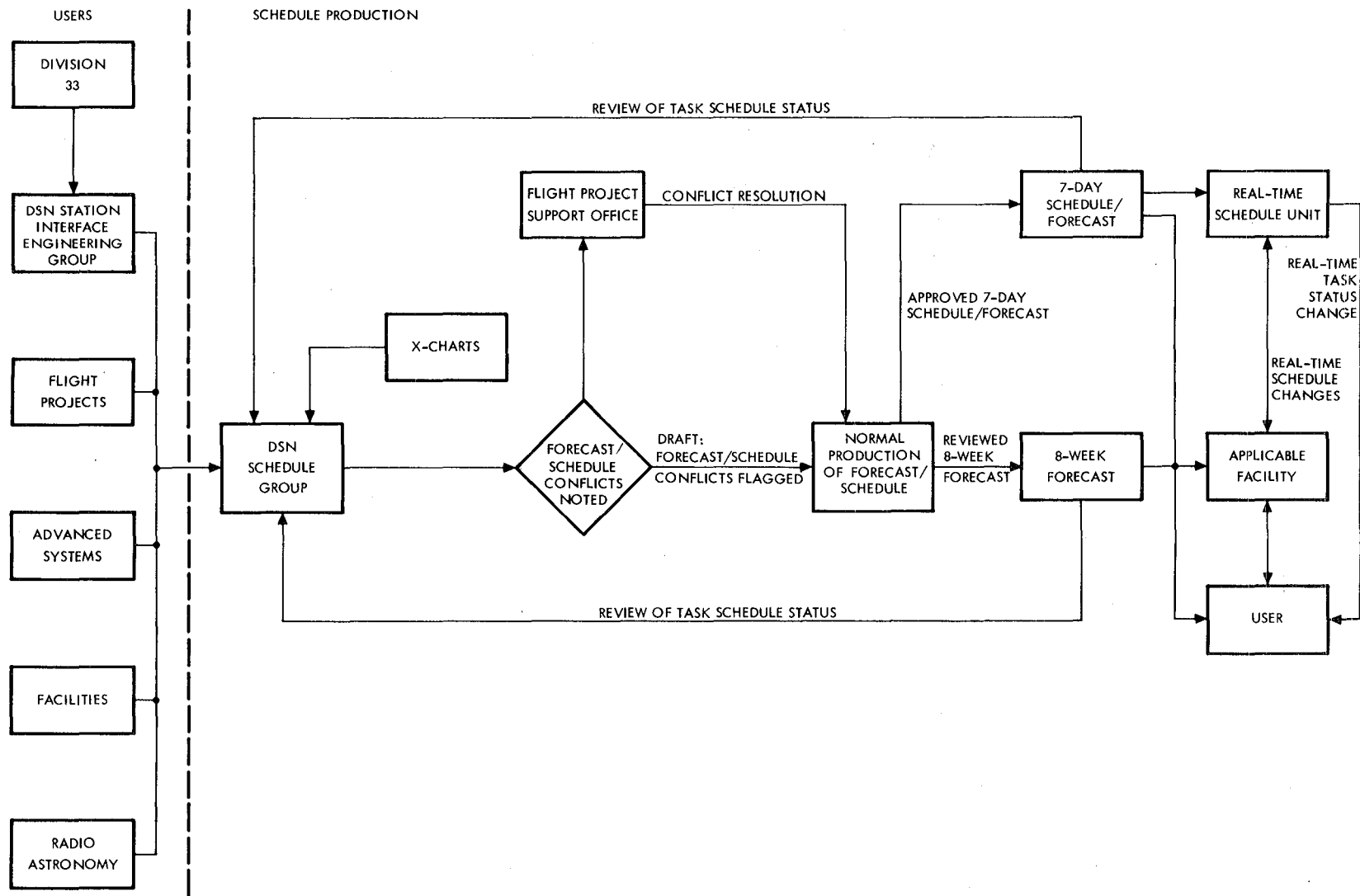


Fig. 2. Functional flowchart for scheduling

# Computer-Simulated Building Energy Consumption for Verification of Energy Conservation Measures in Network Facilities

B. Plankey  
DSN Engineering Section

*A computer program called ECPVER (for Energy Consumption Program – Verification) has been developed to simulate all energy loads for any number of buildings. The program computes simulated daily, monthly, and yearly energy consumption, which can be compared with actual meter readings for the same time period. Such comparison can lead to validation of the model under a variety of conditions, which allows it to be used to predict future energy saving due to energy conservation measures. Predicted energy saving can then be compared with actual saving to verify the effectiveness of those energy conservation changes. This verification procedure is planned to be an important advancement in the Deep Space Network Energy Project, which seeks to reduce energy cost and consumption at all DSN Deep Space Stations.*

## I. Introduction

Shortly after the 1973 oil embargo, the Goldstone Deep Space Communications Complex (GDSCC) initiated an energy management program following NASA guidelines. The Goldstone Energy Project formally started on July 1, 1975, with the objective of reducing the consumption of purchased energy by 50 percent within 10 years of the formal starting date. Total energy consumption during fiscal year 1973 was to be used as the baseline for calculating energy savings. In July 1977, a similar project was formally begun with the same goal for the overseas Deep Space Stations. The project then became known as the DSN Energy Project.

The project plan for the near term has involved, among other things, the reduction of energy consumed in existing equipment and building configurations. Before energy savings

could be realized, particularly from major equipment modifications, a reliable model capable of predicting energy consumption under various loading and operating conditions was needed. A computer program called ECP, for Energy Consumption Program, was first developed for this need in late 1977. The design and utility of ECP has been described in Refs. 1 and 2. Briefly, the program is designed to simulate all energy loads of a particular building and to compute the thermal and electrical energy consumption. It can be used to (1) monitor hourly, daily, monthly and yearly energy consumption, (2) identify and itemize energy consumption by equipment categories, and (3) predict future consumption levels. Since many equipment modification decisions must be made based on the results of the program, the accuracy of the model is of prime importance. The ECP program is continually being refined, updated and checked for flexibility, accuracy and additional features that are supportive to the design engineers.

## II. Need for Verification

The importance of the accuracy of any energy consumption model for building load simulation cannot be understated, and where possible the ECP model is compared with actual meter readings for validation and verification. However, many of the buildings at the DSN Complexes are not metered individually. Several buildings are often connected to a single meter. This can be seen, for example, in Fig. 1, which shows the electrical power and liquified petroleum gas (LPG) distribution systems with presently existing electrical and gas meters at DSS 12 at Goldstone. In order to compare simulated consumption with actual meter readings where buildings are not metered individually, a modified version of ECP is necessary to simulate more than one building at a time. The modified version (given the name ECPVER, for Energy Consumption Program – Verification) has been developed for this need.

In addition to accurately predicting future energy consumption levels due to planned conservation changes in equipment and operational procedure, the verification program is flexible enough to assist in identifying the causes behind unplanned consumption changes. These include unusual change due to (1) exterior environment such as outside air temperature, pressure, humidity, wind speed, cloud cover, etc., (2) interior building environment including occupancy levels, humidity, and lighting hours, and (3) equipment operation or procedure such as downtime or emergency use. It is necessary to track and explain these unexplained load changes in order to determine the accuracy of the model under all possible conditions that may arise.

## III. Description of Verification Model

The verification model (ECPVER) is designed to sum the energy consumption results for any number of buildings as needed for comparison with a particular meter configuration. For example, if four buildings are connected to a single meter, the simulated energy and cost profiles during a selected period of time are summed and printed for that meter. Input data have been grouped into three separate cataloged files for the three geographic locations: Goldstone, Canberra, and Madrid. Each cataloged file contains four program files identifying (1) all buildings included in the Complex by name, (2) all buildings included at each individual site, (3) all buildings monitored by each specifically numbered meter, and (4) each building with complete coded data needed by the program to simulate energy loads and consumption (see Ref. 2). The verification program can be run by declaring a Complex, site, meter, or single building option, and then identifying the site number, meter number, or building name. The program then prints out the summation of thermal and electrical consumption for all buildings included in the chosen option. A flow chart of the program logic is sketched in Fig. 2.

Implemented energy conservation changes produce two streams of data as shown in Fig. 3 which, when compared, lead to analyses of the effectiveness of those energy conservation measures. Multiple passes cause the model to more closely approximate actual consumption by allowing for update and also tend to minimize energy consumption by providing design feedback for further changes.

## IV. Application

To date, only a few runs have been made for the DSN Complexes. From these runs, preliminary verification analyses have been made and some update of the model has been effected. The major portion of the verification effort at Goldstone is awaiting the completion of the energy audit, which will yield updated information for all the building loads at the Complex. For the Complexes in Spain and Australia, the energy audits are completed for the major energy consumers. However, none of the overseas sites are now equipped with multiple watt-hour meters. A plan for installing several watt-hour meters and related logging instruments at both the Madrid and Canberra Complexes is underway. The verification procedure will proceed when their installation has been completed.

Another important application of the ECPVER program, not related to verification, is identifying total energy consumption by categories. The program output itemizes building energy consumption by the following categories: (1) heating equipment, (2) cooling equipment, (3) electric accessories, (4) thermal-powered accessories, (5) incandescent lighting, (6) fluorescent lighting, (7) electrical equipment, (8) mechanical equipment, and (9) thermal equipment. By applying the model for all the buildings at a particular site, the total energy consumption can be itemized on a percentage basis for each of the categories mentioned above. This has been tested for all the overseas sites. As an example, it is now known that cooling presently consumes approximately 19.5 percent of all energy used at DSS 61/63, as shown in Fig. 4.

## V. Summary

The effectiveness of energy conservation measures at all DSN facilities needs to be determined prior to and after implementation as accurately as possible. A computer program (ECPVER) has been developed to accomplish this verification by providing for direct comparison of actual meter readings with computer-simulated values. The verification program is planned to be an integral part of the DSN Energy Project and will be updated as more data from planning, engineering and operational sections become available.

## References

1. Stoller, F. W., Lansing, F. L., Chai, V. W., and Higgins, S., "Energy Consumption Program – A Computer Model Simulating Energy Loads in Buildings," in *The Deep Space Network Progress Report 42-45*, pp. 288-293, Jet Propulsion Laboratory, Pasadena, Calif., June 15, 1978.
2. Lansing, F. L., Strain, D. M., Chai, V. W., and Higgins, S., "The Updated Algorithm of the Energy Consumption Program (ECP) – A Computer Model Simulating Heating and Cooling Energy Loads in Buildings," in *The Deep Space Network Progress Report 42-49*, pp. 107-115, Jet Propulsion Laboratory, Pasadena, Calif., February 15, 1979.

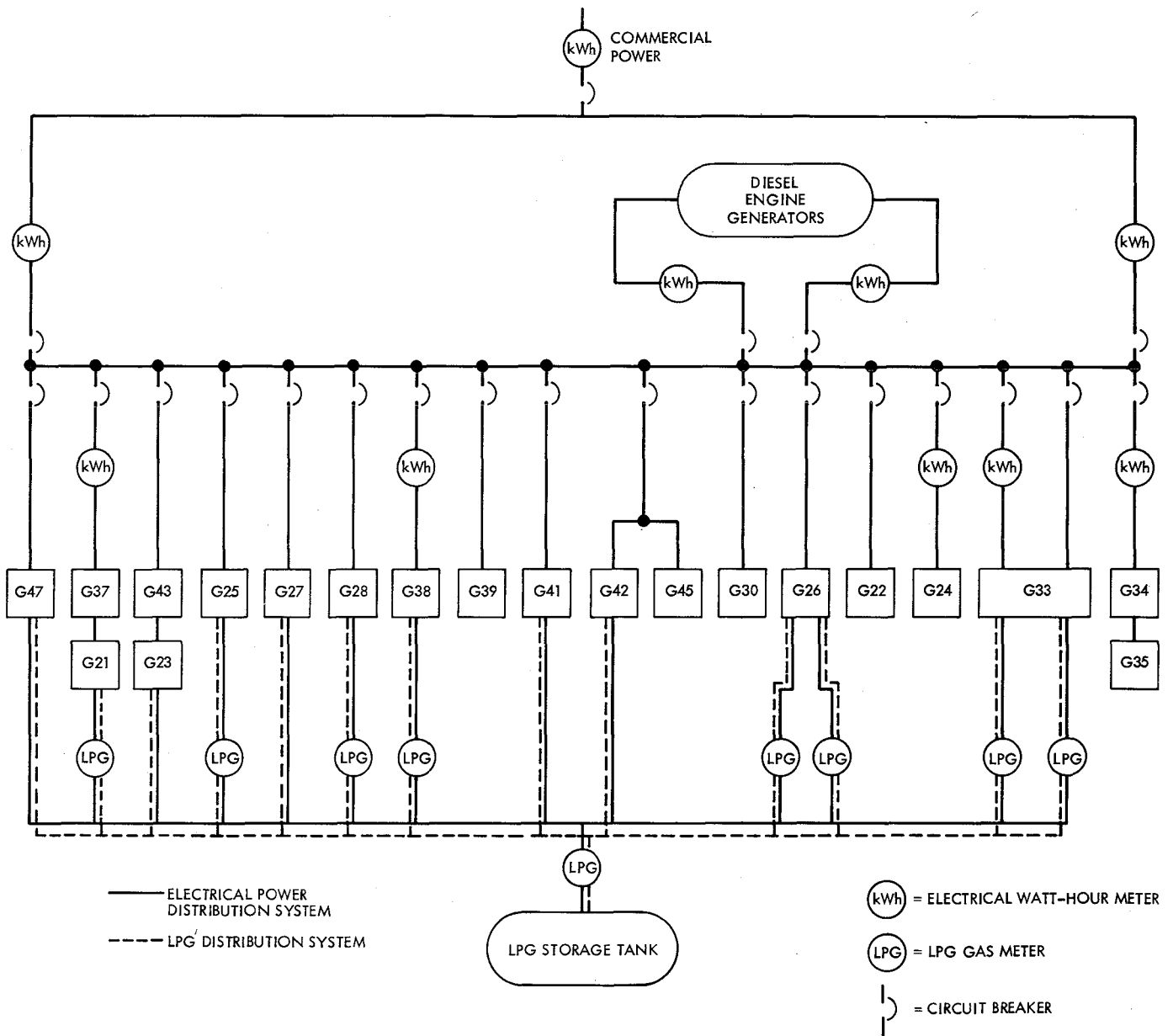


Fig. 1. Electrical power and LPG distribution systems at DSS 12

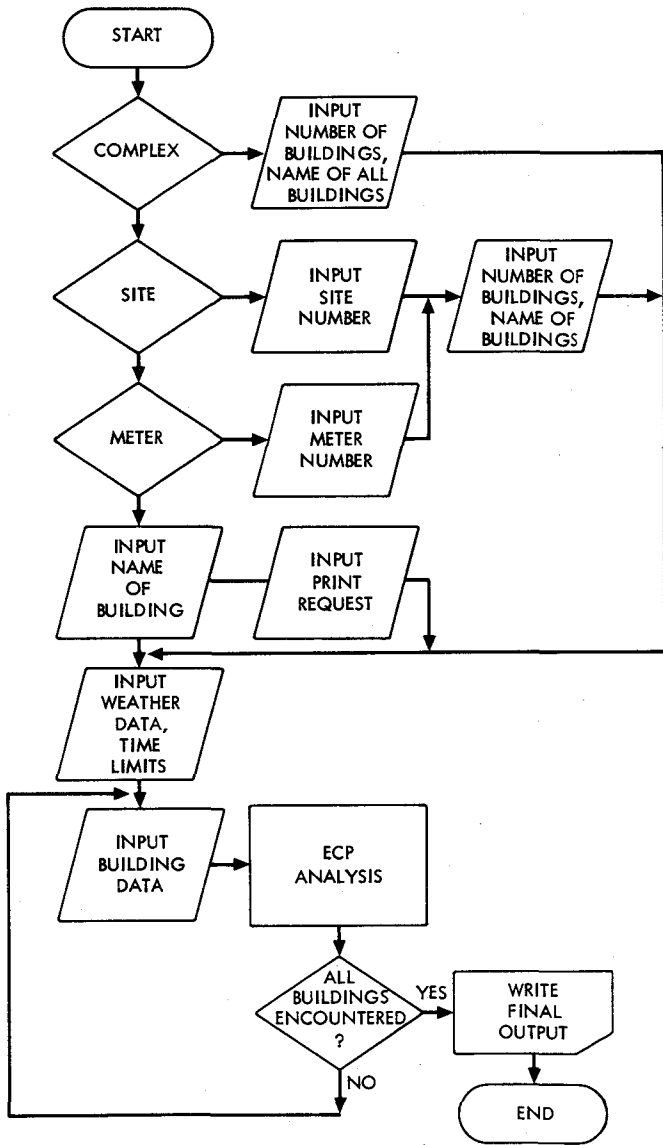


Fig. 2. Flow chart of ECPVER

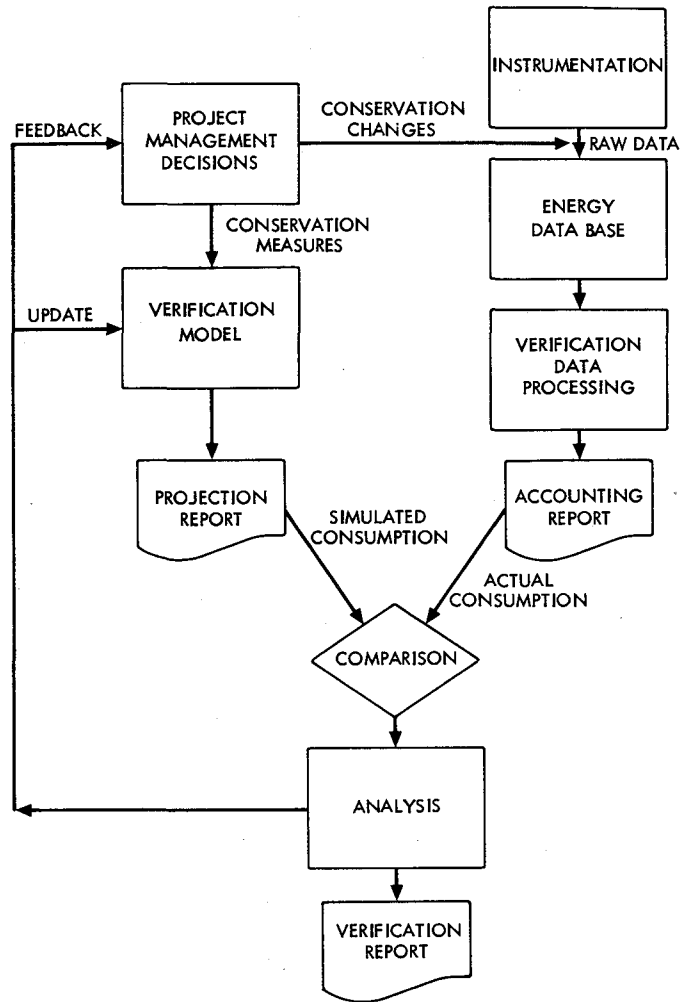


Fig. 3. Verification flow diagram

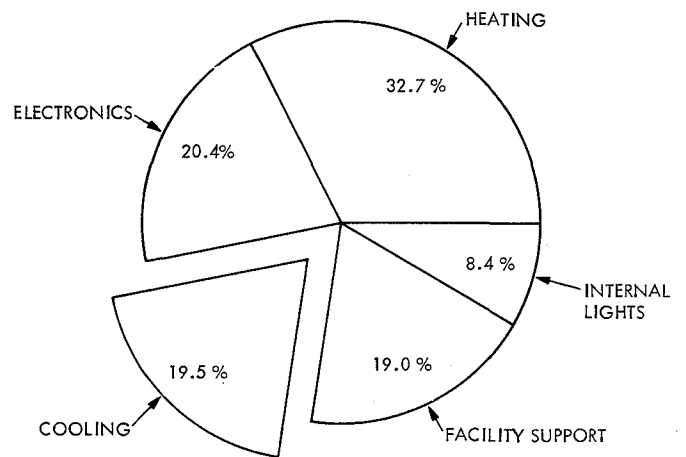


Fig. 4. Itemized DSS 61/63 consumption

# Reporting Capabilities and Management of the DSN Energy Data Base

R. D. Hughes and S. T. Boyd  
DSN Engineering Section

*The DSN Energy Data Base is a collection of computer files developed and maintained by DSN Engineering. The energy consumption data which it contains must be updated monthly and summarized and displayed in printed output as desired. The methods used to handle the data and perform these tasks are described in this article.*

## I. Introduction

The DSN Energy Data Base was implemented in 1976 at the request of the DSN Energy Conservation Project. Due to the significant amount of energy consumed by the DSN facilities and the increasingly important requirements for energy conservation, the Energy Data Base was designed to provide relevant and accessible information which would aid energy conservation engineering of the facilities. Reference 1 describes the initial design and details of the data base. However, as use of the Energy Data Base progressed, the need for a more efficient means of inputting monthly energy consumption data and for a method of presenting consumption data became apparent. Reorganization of some data base file groups and development of specialized computer programs were performed to achieve these needs.

## II. General Description of the DSN Energy Data Base

The DSN Energy Data Base is a collection of computer files developed, maintained, and used to support the DSN engineers, station operators, designers, and managers in monitoring

the progress of the Energy Conservation Project and providing engineering and environmental data for the evaluation of energy conservation measures. The DSN Energy Data Base contains energy consumption and engineering data for DSN facilities at Goldstone, Madrid, and Canberra. As described in Ref. 1, the functional objectives of the data base were to provide:

- (1) A readily available source of technical and descriptive data.
- (2) A central, standardized reference to augment engineering analysis and design.
- (3) Information for effective energy management.
- (4) A historical record for comparison of actual performance with project goals.
- (5) Information for preparing NASA Energy Program Reports.

The Energy Data Base currently consists of four master files:

- (1) Goldstone Energy Data (GED),
- (2) Madrid Energy Data (MED),

- (3) Canberra Energy Data (CED), and
- (4) Goldstone Energy Audit Information (GEA).

The GED file is made up of elements containing Goldstone Deep Space Communications Complex (GDSCC) data on exterior lighting, building air conditioning systems, building utilities, interior occupancy, interior electrical equipment, interior lighting, building architecture, power plants, weather, programmatic changes, and all forms of energy consumption. It is the last category, in which data is being continuously updated, which requires development of a more efficient means of performing these updates. The MED file for the stations in Spain contains monthly energy consumption data for the Robledo site (DSS 61/63) and the Cebreros site (DSS 62), as well as energy audit data for the major buildings as modeled by the Energy Consumption Program (ECP). The ECP computer program was developed in 1977 by the DSN Engineering Section to model building loads and make detailed energy consumption analyses. The CED file for the stations in Australia contains data elements analogous to the MED file; its energy consumption data is for the Honeysuckle site (DSS 44) and the Tidbinbilla site (DSS 42/43). The latter two files were the subjects of initial effort to develop a means of reporting consumption data, since structure of these files is much more simple than that of the Goldstone consumption files. The GEA file contains ECP input data for building models at Goldstone. It was separated from GED because of its large size. The data base now physically resides on computer tape, and files are copied to disk when data is needed or when energy consumption files are to be updated.

### III. Recent Modifications

The Madrid and Canberra MED and CED files were modified to facilitate the development of a reporting computer program which would extract, organize, display, and summarize data as required. The modifications began with consolidating separate file elements containing energy cost and consumption data into one element containing this data in a raw form. Thus, all energy consumption data now exists in one element for each DSS site, and summary data for either Madrid or Canberra is obtained as output from the reporting program.

The MED file element for the energy consumption at Cebreros (DSS 62) is shown in Table 1, as an example. Column headings were made brief for compactness. Of significance are data entries "NA" which indicate "not available" data and are recognized by the reporting program. Data consists of meter reading date, diesel fuel consumption, equivalent thermal energy of diesel fuel consumed, electrical energy produced,

fuel cost per liter in Spanish and American currency, currency conversion rate, and hours of antenna support.

### IV. Monthly Energy Consumption Reporting Techniques

It was desired to create a method of accessing, summarizing, and displaying data from both present and previous years on an annualized basis. Also, it was intended to automate the process of monthly reporting of purchased energy consumption for the DSN Energy Conservation Project management.

A computer program (called REPT) was developed which accomplishes these goals. REPT reads consumption period date, diesel fuel consumption, equivalent heat value, electrical production, fuel cost, and currency conversion data; it calculates unit energy cost, total monthly energy cost, and totals for the year or up to the most recent data point if the current year is being reported. This data is tabulated for each DSS site, and then summarized on a monthly and annual basis for the entire DSN Complex. A sample REPT output is shown in Table 2 for the Madrid Complex, for FY 1980 (September 1979 – August 1980). REPT was designed to be capable of reporting summaries for calendar years, fiscal years, or "energy years." An energy year is defined as the period July – June, which was the definition of a fiscal year prior to 1977.

The computer program logic was complicated by the fact that it had to read a line of data which represents one month's consumption, part of which would be numeric and part of which may be alphabetic in the form of a "NA" entry meaning "not available" data. This problem was handled by writing the program in FORTRAN and using FORTRAN's data conversion utilities. In REPT, data are read using the A-type format (alphanumeric) and the available (integer) data are converted from alphanumeric to computation-format binary integer. Any "not available" data which occurs on a data read triggers an appropriate flag which instructs following portions of the program to perform in a certain fashion. For example, if fuel consumption and fuel cost data are available but electrical production is not available, monthly energy cost can be calculated, but the unit energy cost cannot be calculated. Numerical data are then converted back to the alphanumeric format so that output formats can all be consistent, regardless of combinations of "not available" data.

In this fashion, the REPT program was designed to be completely general in terms of the data acceptance. It was decided not to use blanks or zeros for unavailable data (which would have permitted use of integers throughout the program) since zero is a valid data entry and blank is not specific enough.

Versions of REPT exist for use with both Madrid and Canberra data. A version will be developed soon to process the more abundant Goldstone data.

## V. Data Entry Methods

Energy consumption data for an overseas Complex consists of one line of data for each site; a total of four sites supply data which are entered into the data base manually each month. Automation of this procedure would only offer the advantage of allowing a nonformatted input, which is not significant.

However, the Goldstone energy data consists of LPG consumption, diesel fuel consumption, water consumption, and purchased electrical consumption metered at various locations in the Complex. These data must be inserted in proper locations in each data file element, not added to the end of the element as with the overseas files. Therefore, updating the Goldstone data manually was a cumbersome task, and an interactive computer program had been developed to perform this task. This interactive program was first written in MBASIC, using canned sorting and merging subroutines to insert the new data.

The first trial program seemed to be quite inefficient since it took about 20 minutes elapsed time at the computer terminal and cost about \$17 to process one month's data, which is about 70 data entries (data lines). It was decided to make a second trial and rewrite this program in FORTRAN, developing specialized subroutines to sort and merge the data. The second program (called ECD-UP) takes about 1 minute elapsed time and costs about \$3 to process one month's data.

Since specialized sorting and merging techniques were developed for ECD-UP, a block diagram and a functional description of the salient features of this program are presented in Appendix A.

## VI. Future Development

Programmatic changes in equipment and operating procedures are of high interest since energy consumption reporting techniques used by DSN Engineering take these changes into account. It is planned to develop an access program to process programmatic data.

Efforts are underway to couple the REPT program with advanced in-house graphics equipment, using a Hewlett-Packard graphics terminal and plotter to produce management reports, pie-charts, bar-charts and various plots which are used in monthly reporting to NASA.

In addition to the above, an expansion and a revision of the REPT program will be developed to process Goldstone energy consumption data in a fashion similar to the efforts made for overseas energy data.

Future development of the energy data base will be affected by new functional requirements of the Technical Facilities Controller (TFC) or the Configuration Control Assembly (CCA) Subsystem. Both may contain elements of the DSN Energy Data Base. However, since details concerning implementation of these systems are still under development, the Energy Data Base is being developed to best suit the current needs of engineers and management, with attention given to the development of the TFC and CCA.

## VII. Summary

The reorganization and automation of data processing of the DSN Energy Data Base has led to reduced effort, low cost, and better handling in working with the data. It is expected that future enhancement of automation will increase the efficiency of data base operations.

## Reference

1. Cole, E. R., Herrera, L. O., and Lascu, D. M., "DSN Energy Data Base Preliminary Design," in *The Deep Space Network Progress Report 42-51*, pp. 167-175, Jet Propulsion Laboratory, Pasadena, Calif., June 15, 1979.

Table 1. Energy data base file element "MED.ECM1502"

ECM/502 CEBREROS(DS362) CONSUMPTION\*

MO	YR	DATE	DIESEL (LITERS)	EQUIV (MWHT)	ELECT PROD (KWHE)	COST/ LITER PTS (\$US)	PTS/\$US	SUPPORT (HOURS)
07	73	0801	85000	913	NA	NA	NA	170
08	73	0901	90000	966	NA	NA	NA	210
09	73	1001	85000	913	NA	NA	NA	230
10	73	1101	83000	891	NA	NA	NA	180
11	73	1201	93000	999	NA	NA	NA	420
}}	}}	}}	}}	}}	}}	}}	}}	}}
07	79	0801	50575	543	172000	15 .23	66	563
08	79	0901	46966	504	NA	15 .23	66	426
09	79	1001	49515	532	154000	15 .23	66	429
10	79	1101	48387	519	144000	15 .23	66	422
11	79	1201	42700	458	147000	15 .23	66	484
12	79	0101	45124	484	153000	15 .23	66	580
01	80	0201	47704	512	164000	19 .29	66	590
02	80	0301	44446	477	152000	19 .29	66	585
03	80	0401	44995	483	154000	19 .27	70	555
04	80	0501	35232	378	112000	19 .27	71	214
05	80	0601	37650	404	124000	19 .27	71	286
06	80	0701	44322	476	149000	19 .27	70	504
07	80	0801	46078	494	153000	22 .27	71	536
08	80	0901	46877	503	159000	22 .27	71	541
09	80	1001	43396	465	144000	22 .31	71	482
10	80	1101	41796	449	138000	22 .29	75	413
11	80	1201	40477	435	132000	22 .29	75	326
}}	}}	}}	}}	}}	}}	}}	}}	}}

\* The period 10-79 to 9-80 is shown in Table 2 as REPT output.

Table 2. REPT output

ENERGY CONSUMPTION SUMMARY FOR MADRID DEEP SPACE STATIONS \*\*  
FOR FY 80

## ROBLEDO SITE (DSS 61/63)

MONTH	DIESEL FUEL CONSUMPTION (LITERS)	EQUIV HEAT VALUE * (MWHY)	ELECTRICAL PRODUCTION (KWHE)	FUEL COST /LITER PTS (\$US)	CURRENCY CONVERS. PTS/\$US	ENERGY COST /UNIT (\$/KWHE)	MONTHLY ENERGY COST (\$US)
OCT	210273	2258	618289	15 .23	66	.0782	48362
NOV	202019	2169	625454	15 .23	66	.0743	46464
DEC	216906	2329	662987	15 .23	66	.0752	49888
JAN	206341	2215	624133	19 .29	66	.0959	59838
FEB	196213	2207	578343	19 .29	66	.0984	56901
MAR	202726	2177	601600	19 .27	70	.0910	54736
APR	210883	2271	640000	18 .25	71	.0824	52720
MAY	196555	2110	591570	18 .25	71	.0831	49138
JUN	223823	2403	674482	22 .31	70	.1029	69385
JUL	239613	2573	721600	22 .31	71	.1029	74280
AUG	243793	2618	741600	22 .27	71	.0888	65824
SEP	231389	2484	716000	22 .31	71	.1002	71730
TOTAL	2580534	27814	7796058				699266

## CEBREROS SITE (DSS 62)

MONTH	DIESEL FUEL CONSUMPTION (LITERS)	EQUIV HEAT VALUE * (MWHY)	ELECTRICAL PRODUCTION (KWHE)	FUEL COST /LITER PTS (\$US)	CURRENCY CONVERS. PTS/\$US	ENERGY COST /UNIT (\$/KWHE)	MONTHLY ENERGY COST (\$US)
OCT	48387	519	144000	15 .23	66	.0773	11129
NOV	42700	458	147000	15 .23	66	.0668	9820
DEC	45124	484	153000	15 .23	66	.0678	10378
JAN	47704	512	164000	19 .29	66	.0844	13834
FEB	44446	477	152000	19 .29	66	.0848	12889
MAR	44995	483	154000	19 .27	70	.0789	12148
APR	35232	378	112000	19 .27	71	.0849	9512
MAY	37650	404	124000	19 .27	71	.0820	10165
JUN	44322	476	149000	19 .27	70	.0803	11966
JUL	46078	494	153000	22 .27	71	.0813	12441
AUG	46877	503	159000	22 .27	71	.0796	12656
SEP	43396	465	144000	22 .31	71	.0934	13452
TOTAL	526911	5653	1755000				140390

## MADRID COMPLEX TOTALS

MONTH	DIESEL FUEL CONSUMPTION (LITERS)	EQUIV HEAT VALUE (MWHY)	ELECTRICAL PRODUCTION (KWHE)	MONTHLY ENERGY COST (\$US)
JAN	258660	2777	762289	59491
FEB	244719	2627	772454	56285
MAR	262030	2813	815987	60266
APR	254045	2727	788133	73673
MAY	240659	2684	730343	69791
JUN	247721	2660	755600	66884
JUL	246115	2649	752000	62233
AUG	234205	2514	715570	59304
SEP	268145	2879	823482	81352
OCT	285691	3067	874600	86721
NOV	290670	3121	900600	78480
DEC	274785	2949	860000	85183
TOTAL	3107445	33467	9551058	839663

\* HEATING VALUE OF FUEL USED IS 10.74 KWHT/LITER.

\*\* THIS REPORT IS BASED ON MONTHLY INFO SUBMITTED BY OVERSEAS COMPLEX OPERATIONS

## Appendix A

### ECD-UP Program Description

The ECD-UP program updated Goldstone DSCC energy consumption file elements on a monthly basis by reading update data punched on computer cards. The existing data to be updated are contained on four computer file elements consisting of LPG, diesel fuel, water, and electrical consumption. ECD-UP first reads the updated data from the cards and inserts it into a single working array. This action is performed in the READIN subroutine (see Fig. A-1).

The SORTER subroutine is then called to sort and order the data in the array according to the four sort keys, listed in order of highest to lowest priority: station number, meter number, year, and date. The data array should be thought of as a matrix, with each row representing a line of data taken from a data card. A line of data contains a month's consumption data for a particular station, meter, year and date. This subroutine uses the "bubble sort" technique by indexing through the array line-by-line, comparing the sort keys of each line with the next line, and exchanging two lines if they are out of sequence. Several passes are made through the data until no exchanges are made, indicating that the data are ordered properly. For example, if three consecutive data lines contain the same site number, SORTER will then look at the

meter numbers and decide whether or not to exchange data lines, placing the line with the lowest numbered meter first.

The DIVIDER subroutine, called next, separates the updated data into four arrays corresponding to LPG, diesel fuel, water, or electrical consumption. The meter number is used to determine into which category each data line should be placed.

The MERGER subroutine then inserts the updated data into the existing data elements. It does this by reading the existing data, line-by-line, and comparing each line with the current line in the appropriate updated data array using the sort keys. If the updated data line should be inserted, it is written onto the new version of the data base file element; otherwise, the existing data line is written onto the new version of the element. The program reads through the existing data, in this fashion, indexing through the updated data, as it is inserted into the existing data.

When the end of either type of data is encountered, control passes to the FINFIL or FINAR subroutines, which write the remaining data onto the new file element and, finally, replace the old file element with the new element.

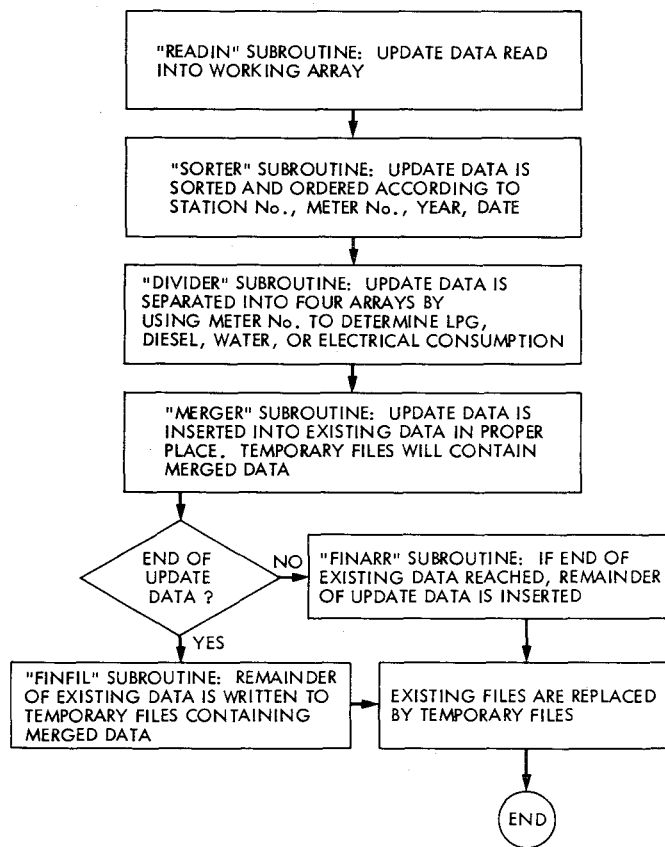


Fig. A-1. ECD-UP program block diagram

**End of Document**